

Kai Zhang

Multi-level Modelling of Plastic Anisotropy of Aluminium Alloys Using Crystal Plasticity Models and Advanced Yield Functions

Thesis for the degree of Philosophiae Doctor

Trondheim, June 2014

Norwegian University of Science and Technology
Faculty of Natural Science and Technology
Department of Materials Science and Engineering



NTNU – Trondheim
Norwegian University of
Science and Technology

NTNU

Norwegian University of Science and Technology

Thesis for the degree of Philosophiae Doctor

Faculty of Natural Science and Technology
Department of Materials Science and Engineering

© Kai Zhang

ISBN 978-82-326-0250-6 (printed ver.)
ISBN 978-82-326-0251-3 (electronic ver.)
ISSN 1503-8181

Doctoral theses at NTNU, 2014:164

IMT-Report 2014:207

Printed by NTNU-trykk

Preface

This thesis is submitted in fulfilment of the requirements for the doctor of philosophy at the Norwegian University of Science and Technology (NTNU). The work has been carried out at the Department of Materials Science and Engineering (DMSE), NTNU from March 2011 to March 2014. Professor Bjørn Holmedal at DMSE, NTNU was the main supervisor. Professor Odd Sture Hopperstad at the Department of Structural Engineering, NTNU, Dr. Stéphane Dumoulin at SINTEF Materials and Chemistry, and Professor Knut Marthinsen at DMSE, NTNU, were the co-supervisors. The thesis consists of two parts. The first part (Part I) includes the introduction, a short literature review and a summary of the work. The second part (Part II) contains articles which were published or prepared by the candidate during the PhD study. Four articles are listed in the main body of Part II, which present the main work, results and academic contributions of this PhD project. Two articles which were presented at international conferences are attached in the appendix of Part II.

The articles contained in this thesis:

1. “Multi-level Modelling of Mechanical Anisotropy of Commercial Pure Aluminium Plate: Crystal Plasticity Models, Advanced Yield Functions and Parameter Identification”, *International Journal of Plasticity*, 2014. DOI: 10.1016/j.ijplas.2014.02.003
2. “Use of Plane-strain Tension and Shear Tests to Evaluate Yield Surfaces for AA1050 Aluminium Sheet”, accepted after peer-review for the 14th International Conference on Aluminium Alloys (ICAA14). The conference proceeding will appear in the journal: *Materials Science Forum*.
3. “A Robust and Efficient Substepping Scheme for the Explicit Numerical Integration of a Rate-dependent Crystal Plasticity Model”, *International Journal for Numerical Methods in Engineering*, 2014. DOI: 10.1002/nme.4671
4. “Modelling the Plastic Anisotropy of Aluminium Alloy 3103 Sheets by Polycrystal Plasticity Models”, submitted to: *Modelling and Simulation in Materials Science and Engineering*.

The articles contained in the Appendix:

- I. “An Explicit Integration Scheme for Hypo-elastic Viscoplastic Crystal Plasticity”, 1st Asian Conference on Aluminium Alloys (ACAA-2013), accepted for publication in the journal: *Transactions of Nonferrous Metals Society of China*, 2014.

II. “Crystal Plasticity Calculations of Mechanical Anisotropy of Aluminium Compared to Experiments and to Yield Criterion Fittings”, 13th International Conference on Aluminium Alloys (ICAA13), Pittsburgh, USA, 3-7 June, 2012, doi: 10.1002/9781118495292.ch137.

Abstract

This thesis aims to accurately describe the plastic anisotropy of aluminium alloys through a hierarchical multi-level method. Robust and efficient integration schemes have been proposed for the explicit numerical integration of rate-dependent crystal plasticity models.

On the mesoscale, the plastic anisotropy is modelled by crystal plasticity models considering a representative volume element (RVE). The RVE consists of a number of single grains and inherits the microstructural information of the polycrystalline material, e.g. crystallographic texture, grain size and shape and grain boundary misorientation. Five crystal plasticity models have been used in this work, namely the full-constraint (FC) Taylor model, the Alamel model, the Alamel model with so-called type III relaxation (Alamel Type III), the visco-plastic self-consistent (VPSC) model and the crystal plasticity finite element method (CPFEM). The accuracy and applicability of these crystal plasticity models when predicting the plasticity anisotropy have been investigated for three different aluminium alloys. On the continuum scale, the yield surface of the material is represented by advanced yield functions. Two yield functions have been employed and investigated for this purpose, namely the Yld2004-18p yield function and the Facet yield function. The yield function is a key component of an anisotropic model in a finite element method (FEM) code, in addition to the flow rule and work hardening law, for simulating plastic deformations. Advanced yield functions, like Yld2004-18p, are conventionally identified by experiments, e.g. uniaxial tensile tests, biaxial tension/compression tests and shear tests. However, the number of available experimental tests is limited for sheet metals and most of the stress space is not covered by the experiments. The multi-level modelling was made through identifying the parameters of the advanced yield functions partially or fully by stress points at yielding provided by crystal plasticity calculations. The accuracy and applicability of this multi-level modelling scheme were evaluated for describing the plastic anisotropy of three aluminium alloy sheets in this thesis.

In **Article 1**, the plastic anisotropy of a fully annealed AA1050 aluminium sheet is studied by the use of five crystal plasticity models and two advanced yield functions. The in-plane uniaxial tension properties of the sheet were predicted by the FC-Taylor model, the Alamel-type models, the VPSC model and CPFEM. Results were compared with data from tensile tests at every 15° from the rolling direction (RD) to the transverse direction (TD) of the plate. Furthermore, all the models, except CPFEM, were used to provide stress points in the five-dimensional deviatoric stress space at yielding for 201 plastic strain-rate directions. The Facet yield surface was calibrated using these 201 stress points and compared to the in-plane yield loci and the planar anisotropy which were calculated by the crystal plasticity models. The anisotropic yield function

Yld2004-18p was calibrated by three methods: using uniaxial tension data, using the 201 virtual yield points in stress space, and using a combination of experimental data and virtual yield points (i.e., a hybrid method). Optimal yield surface exponents were found for each of the crystal plasticity models, based on calibration to calculated stress points at yielding for a random texture, and used in the latter two calibration methods. It was found that the hybrid calibration method could capture the experimental results and at the same time ensure a good fit to the anisotropy in the full stress space predicted by the crystal plasticity models.

Plane-strain tension and shear tests were carried out for the same AA1050 sheet and described in **Article 2**. The tests were simulated numerically with a commercial FEM code using an anisotropic plasticity model including the Yld2004-18p yield function, the associated flow rule and isotropic hardening. FEM simulations of the tests were made with parameters of Yld2004-18p identified in **Article 1** by three methods, i.e. using uniaxial tension data combined with FC-Taylor model predictions of the equibiaxial yield stress and r -value, using 201 virtual yield points in stress space provided by the Alamel Type III model, and using a combination of experimental data and virtual yield points. Predicted force-displacement curves were compared to the experimental data, and the accuracy of the parameter identification methods for Yld2004-18p was evaluated based on these comparisons. The results showed that the hybrid method captured the initial yielding most accurately for both the plane-strain tension and shear tests.

Similar studies as described in **Article 1** have been carried out on AA3103 sheets in the cold-rolled condition (H18 temper) and in the fully annealed condition (O temper) in **Article 4**. The plastic anisotropy of AA3103-H18 and AA3103-O sheets was studied experimentally and numerically. The microstructure and texture of the two materials were characterized and the anisotropic plastic behaviour was measured by in-plane uniaxial tension tests along every 15° from RD to TD of the sheets. The same five polycrystal plasticity models as used in **Article 1** were employed to predict the plastic anisotropy in the plane of the sheet. Experimentally observed grain shapes have been taken into consideration. In addition, a multi-level modelling method was employed where the advanced yield function Yld2004-18p was calibrated to stress points at yielding provided by CPFEM simulations along 89 strain-paths, and the plastic anisotropy was then produced by the yield function. Based on comparisons between the experimental and the predicted results, the multi-level fitting method was found to be the most accurate way of describing the plastic anisotropy. The Alamel Type III and Alamel models were also recommended as accurate and time-efficient models for predicting the plastic anisotropy of the AA3103 sheets in H18 and O tempers.

Article 3 describes the development of efficient and robust numerical integration schemes for rate-dependent crystal plasticity models. A forward Euler integration algorithm was first formulated. An integration algorithm based on the modified Euler method with an adaptive substepping scheme was then proposed, where the substepping was mainly controlled by the local error of the stress predictions within the time step. Both integration algorithms were implemented in a stand-alone code with the Taylor aggregate assumption and in an explicit finite element code. The robustness, accuracy and efficiency of the substepping scheme were extensively evaluated for large time steps, extremely low strain-rate sensitivity, high deformation rates and strain-path changes using the stand-alone code. The results showed that the substepping scheme is robust and in some cases one order of magnitude faster than the forward Euler algorithm. The use of mass scaling to reduce computation time in crystal plasticity finite element simulations for quasi-static problems was also discussed. Finally, simulation of the Taylor bar impact test was carried out to show the applicability and robustness of the proposed integration algorithm for the modelling of dynamic problems with contact.

Acknowledgements

First of all, I would like to express my deepest gratitude to my principal supervisor Prof. Bjørn Holmedal. Bjørn showed great patience when I was innocent of theories of crystal plasticity at the beginning of my PhD study. Together with my co-supervisors, Bjørn helped me find an interesting topic and made long-term plans for my PhD project. The well-defined topic and plans have made my research progress smoothly most of the time. During my study, Bjørn has provided very professional and academic guidance. I also enjoyed the time discussing with Bjørn and watching him illustrating his ideas on the whiteboard in his office. Prof. Odd Sture Hopperstad, Dr. Stéphane Dumoulin and Prof. Knut Marthinsen are my co-supervisors who have played important roles in my project and deserve my gratitude. Odd Sture is a prestigious scholar in the field of mechanics of materials, computational plasticity and fracture. He has broad knowledge covering topics of the PhD project. In particular, the substepping scheme was suggested by him. He works in an efficient, structural and careful manner which prompted the revision and publication of my articles. Stéphane possesses enormous experience on the development and application of CPFEM. He was very generous to provide the code and any help I asked. It was a great pleasure to work with him. Knut has played as a valuable discussion partner and provided many practical help, for example the workstation computer on which I performed most of the CPFEM calculations. Thank you, all my supervisors!

I would like to thank Dr. Jerzy Gawad, Prof. Albert Van Bael and Prof. Paul Van Houtte at MTM, KU Leuven, Belgium. I spent two weeks as a visiting scholar at their group. It was a short but fruitful visit, which improved my understanding about the Alamel model and the Facet method. They generously provided the Facet software package which had produced some interesting results.

Prof. Yanjun Li and Dr. Torodd Berstad are acknowledged for many inspiring discussions. I would like to thank the staff for their technical assistance: Trond Auestad, Yingda Yu, Torild Krogstad, and especially Pål Christian Skaret, with whom I did plenty of mechanical tests.

I want to thank my colleagues in the department who created an environment full of friendliness, knowledge and vigour. I enjoyed the time sitting in the same office with Dr. Ke Huang. Discussions with Dr. Qinglong Zhao and Dr. Tomáš Mánik contributed to my research. I knew more about Norwegian society and culture from Dr. Sindre Bunkholt. I had a lot of fun together with Dr. Ning Wang, Dr. Nagaraj Vinayagam Govindaraj and Dr. Emmanuel Hersent in our group. There are also many other colleagues and friends to be acknowledged: Min Zha, Sarina Bao, Zebin Xu, Shenbao

Jin, Xiaoguang Ma, Song Zhang, Yu Chen et al., who brought fun to my life in Trondheim.

Special thanks to my family. Although living in a tiny village of the enormous China, my parents always encouraged me to dream big and bigger. My wife Jingjing Gao showed great patience and always encouraged me during my PhD study. She makes me feel warm in the deep of my heart every day. Finally, the new-comer in my life, my beloved daughter Zhiting Zhang, needs a special acknowledgement. Thank you for all the adventures and fun we had together.

Contents

Preface	i
Abstract	iii
Acknowledgements	vii
Contents	ix
Chapter 1 Introduction	1
1.1 Background	1
1.2 Objectives, scopes and limitations of the thesis	1
Chapter 2 Literature review	3
2.1 Plastic anisotropy	3
2.2 Crystallographic texture	6
2.3 Crystal plasticity models	11
2.3.1 Schmid's law	11
2.3.2 Sachs model.....	12
2.3.3 Taylor-Bishop-Hill model	13
2.3.4 Relaxed-constraint Taylor models, Alamel and GIA	15
2.3.5 Visco-plastic self-consistent (VPSC) model	17
2.3.6 Crystal plasticity finite element method (CPFEM).....	19
2.3.7 Fast Fourier transformation based crystal plasticity (CPFEM)	20
2.3.8 Modelling the plastic anisotropy	21
2.4 Phenomenological plasticity theory	22
2.4.1 Yield functions	22
2.4.2 Flow rules and work hardening laws.....	26
Chapter 3 Experimental techniques	29
3.1 Mechanical testing	29
3.2 Structure characterization	29
Chapter 4 Summary and remarks	31
4.1 Summary	31
4.2 Suggestions for future work	33
References	35
Article 1	45
Article 2	103

Article 3.....	115
Article 4.....	155
Appendix.....	181
Article A-1	181
Article A-2	195

Chapter 1 Introduction

1.1 Background

Sheet forming processes are among the most common operations used in the industry. A large volume of products are produced by sheet forming, particularly in the automotive and packaging industries. Aluminium alloys are widely used nowadays in forming industries due to their high specific strength, good corrosion resistance and low recycling cost. International competition pushes all enterprises to shorten the manufacturing times and improve the quality of products, in order to maintain and better their position within the market. Numerical simulation of metal forming processes has a very important role in reducing the need for expensive and time consuming experiments for manufacturing good quality products. The finite element method (FEM) is currently the most widely used numerical procedure for simulating sheet metal forming processes. The accuracy of the simulation programs used in industry is influenced by the constitutive models of the material [1]. Sheet metals commonly exhibit plastic anisotropy which can have a major effect on the sheet metal forming processes and on in-service performance. Hence, the constitutive models used in FEM simulations of forming processes should describe the plastic anisotropy of the material accurately in order to give realistic predictions.

1.2 Objectives, scopes and limitations of the thesis

Crystal plasticity models at the mesoscale and advanced phenomenological yield functions at the macroscale are known as two principal methods for describing the plasticity, and its anisotropy, of engineering metallic materials. Combining these two methods through identifying yield functions by the help of crystal plasticity calculations, i.e. a multi-level modelling scheme, is a tendency in the forming industries. This work aims to find proper approaches to accurately describe the plastic anisotropy of aluminium alloys. Great efforts have been made to evaluate the accuracy and applicability 1) of existing models at both scales and 2) of the methods that bridge the two scales, i.e. the yield function identification procedures. The objectives of the thesis are summarized as:

1. Evaluate the accuracy and applicability of existing crystal plasticity models for predicting the plastic anisotropy of different aluminium alloys;
2. Compare the accuracy of two advanced yield function, i.e. the Yld2004-18p and the Facet yield functions, in terms of describing plastic anisotropy;

3. Evaluate different parameter identification procedures for advanced yield functions, especially the hybrid method where both experiments and crystal plasticity calculations are considered in the calibration procedure;
4. Improve the performance of CPFEM by proposing robust and efficient integration methods.

Three different aluminium sheets are studied in this thesis, including a fully recrystallized AA1050 sheet, a fully annealed AA3103-O sheet and a cold-rolled AA3103-H18 sheet. The anisotropic plastic behaviour is measured by in-plane uniaxial tension tests along every 15° from the rolling direction to the transverse direction of the sheet. The microstructure and texture of the two materials are characterized mainly using the electron back-scatter diffraction technique. Five crystal plasticity models are employed separately in the thesis to model the plastic anisotropy, which includes the full-constraint Taylor model, the Alamel model, the Alamel model with the so-called Type III relaxation, the visco-plastic self-consistent model and the crystal plasticity FEM (CPFEM). Grain morphology and/or grain boundary misorientation are considered in the crystal plasticity calculations. Two advanced yield functions employed in the thesis are the Yld2004-18p and the Facet criteria. Parameter identification procedures of the yield functions are evaluated by comparing the results obtained by the fitted yield surfaces to the experiments. The numerical integration schemes proposed in the thesis fall into the category of explicit integration methods.

The crystal plasticity models used in the thesis take the crystallographic texture as the main input. Dislocation populations and structures as well as their evolution during deformation are not considered. The grain size, constitutive particles and dispersoids are also neglected in the crystal plasticity modelling. As a consequence, the plastic anisotropy predicted from crystal plasticity calculations is mainly texture-based in this thesis.

Chapter 2 Literature review

The topics studied in this thesis mainly include plastic anisotropy, crystallographic texture (or texture for short), crystal plasticity models and phenomenological yield functions. Each of these topics will be introduced and briefly reviewed in the following of this chapter.

2.1 Plastic anisotropy

In the field of materials, anisotropy is the directional dependence of physical properties of the material. Among mechanical properties such as elastic modulus (Young's modulus), yield stress, ductility, ultimate tensile stress, the anisotropy of the yield stress and the flow pattern are of main concern in the forming industry. The anisotropic work hardening [2, 3] is also within the context of plastic anisotropy, but it is seldom used in the industry due to the complexity of the theory and the numerical implementation. Plastic anisotropy in terms of the yield stress and flow pattern is of main concern in this thesis.

Plastic anisotropy of materials greatly influences the final shapes and dimensions of the products in a forming process. As an example, the earing after deep drawing in Fig. 1(a) is due to plastic anisotropy of the material; the springback is also influenced by the plastic anisotropy [4]. Accurate numerical simulations of the plastic deformation, e.g. Fig. 1(b), are required for the purpose of predicting the final product shape and optimizing the operation processes.

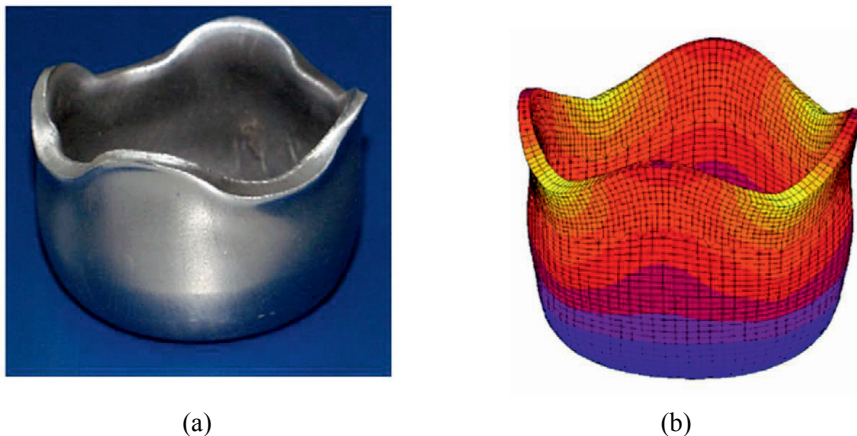


Fig. 1 Earing profile for a cube-textured aluminium sheet after cup drawing: (a) experiment and (b) CPFEM simulation [5].

Plastic anisotropy of a material can be measured by mechanical tests. The uniaxial tensile test is a widely used method. By conducting uniaxial tensile tests along various directions, the angular dependence of the initial yield stress (or the flow stress) and the flow pattern in terms of the Lankford value (r -value) can be obtained. The stress state corresponding to a uniaxial tensile test is known analytically and the strain state can be determined when the r -value is measured. Since both the stress and strain states are known, uniaxial tensile tests are very well suitable for calibration and validation of anisotropic plasticity models. The r -value can be measured according to the ASTM E517 standard. For in-plane tension at φ degrees from the rolling direction (RD) in the RD-TD plane, the corresponding stress tensor $\boldsymbol{\sigma}$ expressed in the material frame, see Fig. 2, can be represented as

$$\boldsymbol{\sigma} = \sigma_{\varphi} \begin{bmatrix} \cos^2 \varphi & \cos \varphi \sin \varphi & 0 \\ \cos \varphi \sin \varphi & \sin^2 \varphi & 0 \\ 0 & 0 & 0 \end{bmatrix} \quad (1)$$

The strain rate tensor \mathbf{D} for a uniaxial tensile test along RD is

$$\mathbf{D} = D_{11} \begin{bmatrix} 1 & 0 & 0 \\ 0 & -q & 0 \\ 0 & 0 & -(1-q) \end{bmatrix} \quad (2)$$

where D_{11} is the strain rate along RD and q -value is the contraction ratio proposed by Bunge [6], with $0 \leq q \leq 1$ and related to the r -value as $r = q / (1 - q)$.

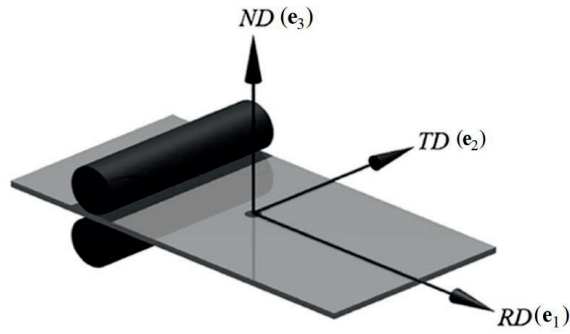


Fig. 2 Orthotropy axes of the rolled sheet metals: RD—longitudinal direction; TD—transverse direction; ND—normal direction, and the material frame with three base vectors \mathbf{e}_i ($i = 1, 3$) [1].

The coefficient of biaxial anisotropy [7, 8], defined as

$$r_b = \frac{\varepsilon_{22}}{\varepsilon_{11}} \quad (3)$$

can be measured by the disk compression test [7] or using a biaxial tensile testing machine [8].

Texture and microstructure, besides chemistry, are key factors that control properties of engineering materials. The plastic anisotropy exhibited by materials is mainly attributed to the existence of texture which is a preferred distribution of grain orientations. A single crystal of a metal is inherently anisotropic due to its lattice structure. If grains within a polycrystalline metal have randomly distributed orientations, the anisotropy at the single crystal level will ‘vanish’ due to the randomization. However, sheet metal commonly features stronger crystallographic texture than bulk metals due to the thermo-mechanical processing history, and exhibits anisotropy as a consequence. Anisotropic polycrystalline metals are thus merely reflecting the anisotropy of the single crystals they are composed of [9].

In addition to texture, other microstructural features can also influence the plastic anisotropy. Xie et al. [10] concluded that the initial grain shape has a clear effect on the q -value during tensile tests for three low carbon steels. Second-phase particles in aluminium alloys not only change the magnitude of the strength of an alloy, but also change its plastic anisotropy [11]. As an example, Bate et al. [12] showed changes in plastic anisotropy which accompany precipitation from a supersaturated solid solution in three different textured aluminium alloys, even though the crystallographic texture was not changed. Similar results were also found in [11]. Through-thickness variations of grain size and texture were observed in extruded aluminium profiles [13], and might have influence on the plastic anisotropy [14]. Chang et al. [15] examined the subgrain texture evolution of face-centered-cubic (FCC) metals under shear deformation by the help of CPFEM where the texture was the same but the grain boundary misorientation distribution (MD) was varied. It was found that the MD affected the evolution of texture. Hence, the MD may have influence on the evolution of texture-induced plastic anisotropy. During the deformation, the dislocation structure (substructure) evolves and may have influences on the plastic anisotropy. Juul Jensen and Hansen [16] measured the in-plane directional flow stress anisotropy of cold-rolled (to different plastic strains) polycrystalline high purity and commercially pure aluminium by uniaxial tension tests. The microstructure was also observed by transmission electron microscopy (TEM). Microbands (MB) and dense dislocation walls (DDWs) were found to arise after cold-rolling (especially at a low degree of deformation) and have preferred inclinations with respect to the sample frame. These DDW/MDs could act as obstacles to slip and hence influence the macroscopic flow stress anisotropy. Typical microstructure of FCC metals after plastic deformation and the relationship between grain orientation and the

substructure have been reported in the literature [17-21]. Landau et al. [22] investigated the evolution of the substructure during uniaxial compression of FCC metals from low to high stacking fault energy (SFE). Fig. 3(a) shows the dislocation boundaries formed following 3% strain, while Fig. 3(b) shows the dislocation cell structure following 70% strain. Latent hardening [16] and strain-path changes [23] may also contribute to the plastic anisotropy.

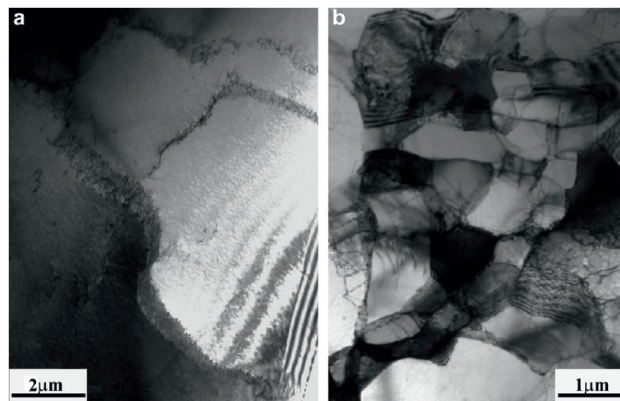


Fig. 3 TEM micrographs of aluminium compressed at room temperature showing dislocation boundaries and cell structure at different strains: (a) dislocation boundaries following 3% strain, (b) cellular structure following 70% strain [22].

Plastic anisotropy can be modelled by two different methods: crystal plasticity models and phenomenological anisotropic yield functions, which will be introduced later in this chapter.

2.2 Crystallographic texture

As illustrated schematically in Fig. 4, the crystallographic orientation of a grain is defined with respect to a reference frame, e.g. the RD-TD-ND sample frame of a rolled plate in Fig. 4. The orientation may be expressed by Miller indices $(h k l)[u v w]$, by Euler angles $(\varphi_1, \Phi, \varphi_2)$ or by an angle/axis of rotation [24]. The Miller indices can be interpreted as the $(h k l)$ crystallographic plane being parallel with the RD-TD plane while $[u v w]$ crystallographic direction being along RD.

There are several different conventions for expressing the Euler angles. The most commonly used are those formulated by Bunge, as shown in Fig. 5 [25]. In the angle/axis of rotation method, the crystal lattice will coincide with the sample

coordinate system by a rotation through a single angle θ , provided that the rotation is performed about a specific axis (r_1, r_2, r_3) .

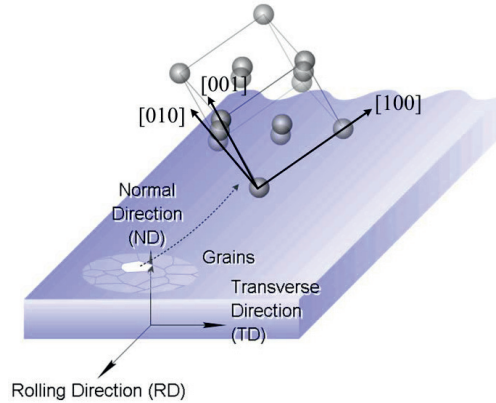


Fig. 4 Spatial orientation of the crystal lattice (FCC) of a grain relative to the rolled sheet [26].

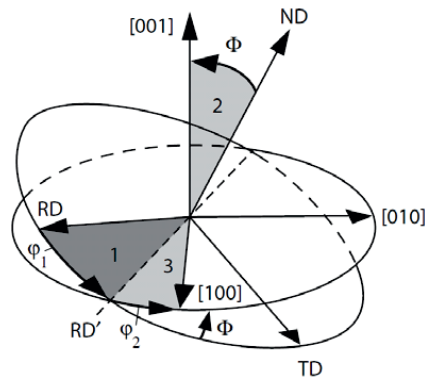


Fig. 5 Diagram showing the rotation between the specimen and crystal axes by rotation through the Euler angles φ_1 , Φ and φ_2 in that order [24].

The grain orientation can be illustrated by means of a pole figure, an inverse pole figure and the Euler space. In a pole figure, the orientation of the crystal coordinate system is represented in the specimen coordinate system, while the orientation of the specimen coordinate system can be projected into the crystal coordinate system in an inverse pole figure. It is noted that one single pole figure cannot describe all the orientation information; multi-poles are generally necessary for a full representation of the orientation. Inverse pole figures are commonly used for tracking the rotation of crystals

during deformation. The Euler space is a three dimensional (3D) coordinate system whose axes are spanned by the three Euler angles. Cubic-orthorhombic texture functions (e.g., of rolling textures) are conventionally represented in the Euler space with a range of 0° to 90° for φ_1 , Φ and φ_2 .

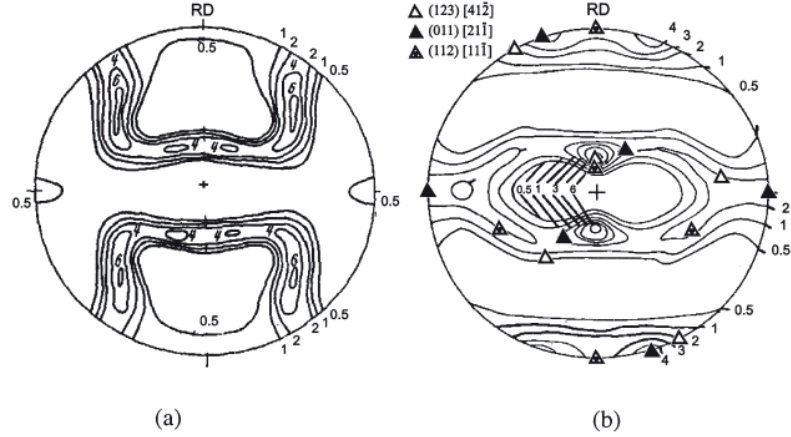


Fig. 6 Pole figures of 95% cold rolled aluminium, (a) {100} pole figure, (b) {111} pole figure [27].

A preferred distribution of grain orientations is called texture. As-cast materials are generally assumed to have a random texture, i.e. no texture. After different thermo-mechanical processing, the texture will arise. Typical cold-rolling texture of aluminium alloys are shown in Fig. 6.

In Fig. 6, one may perceive the difficulties of yielding unambiguously the entire texture information in a quantitative manner. To overcome these ambiguities and thus to permit a quantitative evaluation of the textures, it is necessary to describe the orientation density of grains in a polycrystal in an appropriate 3D representation, that is, in terms of its orientation distribution function $\bar{f}(g)$ (ODF) [28]. Typical cold rolling and recrystallization textures of aluminium alloys are illustrated in Fig. 7(a) and Fig. 7(b), respectively, in terms of ODFs.

It is necessary to compare two ODFs quantitatively for some circumstances, e.g. to examine the texture predicted by CP models, or to characterize the quality of the selected orientations in representing the measured texture. To compare two ODFs in a quantitative manner, the normalized difference texture index, ID_N , defined as

$$ID_N = \frac{\oint (\bar{f}(g) - \bar{f}_{\text{ref}}(g))^2 dg}{\oint (\bar{f}_{\text{ref}}(g))^2 dg} \quad (4)$$

with $dg = \sin \Phi d\varphi_1 d\Phi d\varphi_2$ can be used [29], where $\bar{f}_{\text{ref}}(g)$ is a reference ODF.

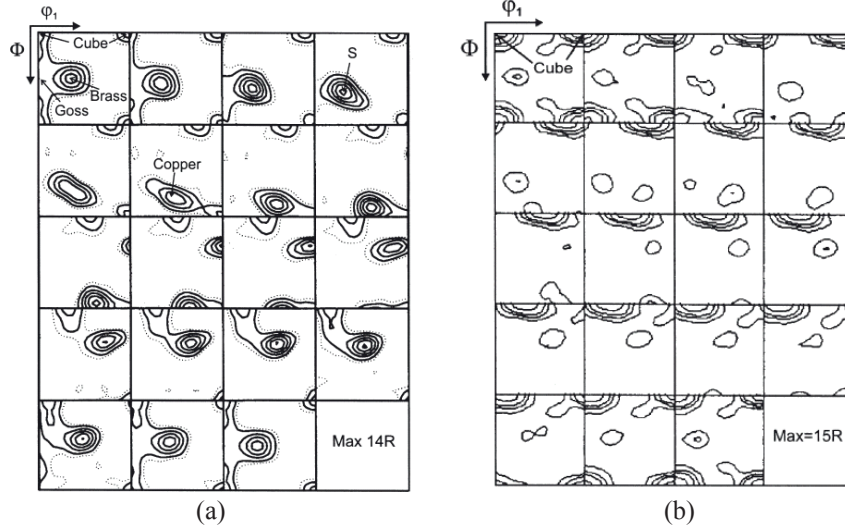


Fig. 7 (a) ODF of 90% cold rolled aluminium [30]; (b) recrystallization textures of coarse-grained Al-3%Mg after prior reduction 90% [31].

The coordinate transformation matrix \mathbf{Q} corresponding to a set of Euler angles $(\varphi_1, \Phi, \varphi_2)$ is expressed as

$$\mathbf{Q} = \begin{bmatrix} \cos \varphi_1 \cos \varphi_2 - \sin \varphi_1 \cos \Phi \sin \varphi_2 & \sin \varphi_1 \cos \varphi_2 + \cos \varphi_1 \cos \Phi \sin \varphi_2 & \sin \Phi \sin \varphi_2 \\ -\cos \varphi_1 \sin \varphi_2 - \sin \varphi_1 \cos \Phi \cos \varphi_2 & -\sin \varphi_1 \sin \varphi_2 + \cos \varphi_1 \cos \Phi \cos \varphi_2 & \sin \Phi \cos \varphi_2 \\ \sin \varphi_1 \sin \Phi & -\cos \varphi_1 \sin \Phi & \cos \Phi \end{bmatrix} \quad (5)$$

The misorientation matrix between two grains A and B is calculated as

$$\mathbf{Q}^{AB} = \mathbf{Q}_A \mathbf{Q}_B^{-1} \quad (6)$$

This misorientation is then expressed in axis-angle format and one obtains the rotation angle θ and the corresponding rotation axis (r_1, r_2, r_3) that makes A and B coincide by

$$\theta = \cos^{-1} \left[\frac{\text{tr} \mathbf{Q}^{AB} - 1}{2} \right] \quad (7)$$

$$r_1 = \frac{Q_{23}^{AB} - Q_{32}^{AB}}{2 \sin \theta}, \quad r_2 = \frac{Q_{31}^{AB} - Q_{13}^{AB}}{2 \sin \theta}, \quad r_3 = \frac{Q_{12}^{AB} - Q_{21}^{AB}}{2 \sin \theta}$$

Due to the crystal symmetry, there are multiple descriptions of the rotation (24 for cubic crystals) and the minimum angle from these equivalent angles is taken as the misorientation. In cubic metals, the maximum misorientation angle is given as 62.8° [32]. The distribution of the misorientation for a random texture case is shown in Fig. 8.

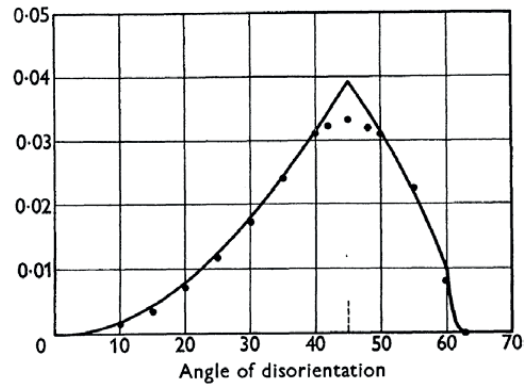


Fig. 8 Density function for the distribution of misorientation angles for a randomly textured polycrystal, from Mackenzie [32].

2.3 Crystal plasticity models

Deformation will happen in the material under external forces. Elastic deformation is reversible and occurs in the crystal by changing the mutual distance between atoms without breaking the atomic bonds. If the elastic limit is exceeded, non-reversible plastic deformation will take place. The main mechanisms for plastic deformations are slip and twinning, while slip is dominant for metals with high SFE, such as aluminium and its alloys. Slip happens through the dislocation movement on the slip systems which are defined by the most densely packed crystallographic planes and the most densely packed crystallographic directions. In body-centred-cubic (BCC) metals, the atoms are closest to each other along the $\langle 111 \rangle$ direction. Any plane in a BCC crystal that contains this direction is a suitable slip plane. Slip has been experimentally observed in $\{110\}$, $\{112\}$ and $\{123\}$ planes, leading to 48 potential slip systems in BCC metals. In FCC metals, there are 12 slip systems, i.e. the $\{111\}\langle 110 \rangle$ slip systems. These 12 slip systems are listed in Table 1, where \mathbf{m}^α is the unit vector of slip direction and \mathbf{n}^α is the slip plane normal vector.

2.3.1 Schmid's law

Crystal plasticity has as its origin in Schmid's law, which states that crystallographic slip is initiated when a critical resolved shear stress τ_c is reached on a slip plane in a slip direction. Fig. 9 illustrates crystallographic slip in uniaxial tension. The resolved shear stress for the uniaxial tensile stress state can be expressed as

$$\tau = \sigma \cdot \cos \lambda \cos \phi \quad (8)$$

where $\cos \lambda \cos \phi$ is known as the Schmid factor. For an arbitrary Cauchy stress tensor $\boldsymbol{\sigma}$, the resolved shear stress on slip system α can be defined as

$$|\tau^\alpha| = \left| \boldsymbol{\sigma} : \frac{1}{2}(\mathbf{M}^\alpha + \mathbf{M}^{\alpha T}) \right| = \left| \boldsymbol{\sigma} : \frac{1}{2}(\mathbf{m}^\alpha \otimes \mathbf{n}^\alpha + \mathbf{n}^\alpha \otimes \mathbf{m}^\alpha) \right| \leq \tau_c^\alpha \quad (9)$$

where $\mathbf{M}^\alpha = \mathbf{m}^\alpha \otimes \mathbf{n}^\alpha$ is the Schmid tensor and α is the label of slip systems.

Non-Schmid yield behaviour has been observed in some BCC metals [33] and intermetallic compounds [34], where not only the resolved shear stress on the primary slip system (the Schmid stress) controls the dislocation motion on that system, but other shear stress components also affect the mobility of dislocations. The generalization of Schmid's law and the flow rules accounting non-Schmid behaviour has been proposed in [34, 35].

Table 1 Slip direction \mathbf{m}^α and slip plane normal \mathbf{n}^α with respect to an orthonormal basis associated with the lattice for an FCC crystal (Bishop and Hill notation)

α	\mathbf{m}^α	\mathbf{n}^α	α	\mathbf{m}^α	\mathbf{n}^α
1	$\frac{1}{\sqrt{2}}(0,1,-1)$	$\frac{1}{\sqrt{3}}(1,1,1)$	7	$\frac{1}{\sqrt{2}}(0,1,-1)$	$\frac{1}{\sqrt{3}}(-1,1,1)$
2	$\frac{1}{\sqrt{2}}(-1,0,1)$	$\frac{1}{\sqrt{3}}(1,1,1)$	8	$\frac{1}{\sqrt{2}}(1,0,1)$	$\frac{1}{\sqrt{3}}(-1,1,1)$
3	$\frac{1}{\sqrt{2}}(1,-1,0)$	$\frac{1}{\sqrt{3}}(1,1,1)$	9	$\frac{1}{\sqrt{2}}(-1,-1,0)$	$\frac{1}{\sqrt{3}}(-1,1,1)$
4	$\frac{1}{\sqrt{2}}(0,-1,-1)$	$\frac{1}{\sqrt{3}}(-1,-1,1)$	10	$\frac{1}{\sqrt{2}}(0,-1,-1)$	$\frac{1}{\sqrt{3}}(1,-1,1)$
5	$\frac{1}{\sqrt{2}}(1,0,1)$	$\frac{1}{\sqrt{3}}(-1,-1,1)$	11	$\frac{1}{\sqrt{2}}(-1,0,1)$	$\frac{1}{\sqrt{3}}(1,-1,1)$
6	$\frac{1}{\sqrt{2}}(-1,1,0)$	$\frac{1}{\sqrt{3}}(-1,-1,1)$	12	$\frac{1}{\sqrt{2}}(1,1,0)$	$\frac{1}{\sqrt{3}}(1,-1,1)$

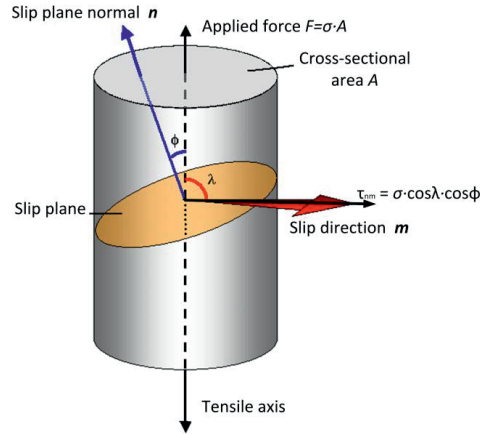


Fig. 9 Illustration of Schmid's law for a uniaxial tensile test. The resolved shear stress on the slip plane \mathbf{n} along the slip direction \mathbf{m} is: $\tau = \sigma \cdot \cos \lambda \cos \phi$ [36].

2.3.2 Sachs model

The oldest crystal plasticity model was proposed by Sachs [37] with the iso-stress assumption for all grains in the polycrystal. Under this assumption, adjacent grains will deform independently and lead to unrealistic overlaps and gaps at grain boundaries. Slip will happen on the slip system which features the largest resolved shear stress or Schmid factor according to Eq. (9). Hence, single slip is preferred in the Sachs model. The Sachs model is also known as the lower-bound model. Implementations of the standard or the modified Sachs models can be found in [38-40]. As a simple approximation of the Sachs model, the weighted mean value of the maximum Schmid

factor for all grains in the RVE can be used to investigate the strength anisotropy [41]. Sachs-type models were found to work well for some cases, e.g. simulating the early stage of development of rolling texture in Copper and Brass [42], and predictions of the strength anisotropy of AlZnMg materials [41]. Despite of these successes, the use of the Sachs model has been out of fashion in the last decades because the Taylor-type model has been considered much closer to reality [42, 43]. The Sachs model was not employed in the work of this thesis.

2.3.3 Taylor-Bishop-Hill model

The full-constraint (FC) Taylor model was originally proposed by Taylor in 1938 [44]. The plastic deformation rate tensor \mathbf{D}^p for a general plastic deformation of metals has only five independent components due to the incompressibility condition. The plastic deformation can then be accommodated by a least five independent slip systems as

$$\mathbf{D}^p = \sum_{\alpha} \frac{1}{2} (\mathbf{M}^{\alpha} + \mathbf{M}^{\alpha T}) \cdot \dot{\gamma}^{\alpha} \quad (10)$$

The spin of the crystal \mathbf{W}^p due to the slip can be expressed as

$$\mathbf{W}^p = \sum_{\alpha} \frac{1}{2} (\mathbf{M}^{\alpha} - \mathbf{M}^{\alpha T}) \cdot \dot{\gamma}^{\alpha} \quad (11)$$

In the Taylor theory, the single crystal is assumed to experience the same deformation as the macroscopic polycrystalline material, i.e. the iso-strain assumption is adopted, see Fig. 10. As mentioned above, there exist 12 potential slip systems for FCC metals at ambient temperature. The abundance of slip systems leads to multiple solutions of five active slip systems in Eq. (10) when \mathbf{D}^p is known, e.g. there are 792 combinations of 5 slip systems out of total 12. Taylor [44] proposed the second assumption that the solution with a minimum internal energy dissipation as

$$\sum_{\alpha} |\dot{\gamma}^{\alpha}| \cdot \tau_c^{\alpha} = \min \quad (12)$$

is a valid solution, where τ_c is assumed to be the same for all slip systems.

Bishop and Hill [45, 46] proposed a stress-based procedure for finding the active slip systems with the iso-strain assumption. Their stress-based approach sought to directly find stress states that could simultaneously operate at least five independent slip systems. By examining the yield criterion of each slip system, they found that any polyslip stress state that simultaneously operates at least five slip systems will actually operate six or eight. In total, there are 28 (56 with negatives) permissible FCC polyslip stress states. To accommodate an imposed deformation \mathbf{D}^p , the particular stress state can be found

by selecting from these total of 56 permissible ones, the one which maximizes the external work done, i.e.

$$dW = \sigma_{ij} D_{ij}^p = \max \quad (13).$$

This principle of maximum work was first derived rigorously by Bishop and Hill [45, 46]. It was also shown that the maximum work principle is equivalent to the minimum internal energy dissipation approach taken earlier by Taylor [45-47]. Hence, the FC-Taylor model also has the name as Taylor-Bishop-Hill model. A very concise and lucid introduction of the Taylor and the Bishop-Hill procedures can be found in [48] while comprehensive reviews are collected in [49-51].

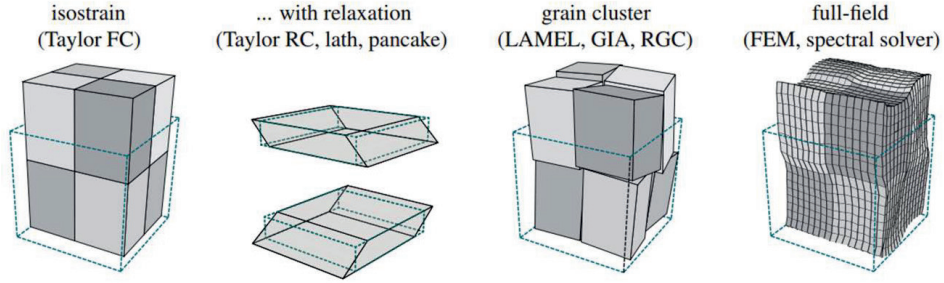


Fig. 10 Four commonly used homogenization schemes [52].

Eq. (10) with the constraint set by Eq. (12) can be solved effectively by the linear programming technique [50, 53]. However, the so-called Taylor ambiguity arises when multiple solutions that satisfy both Eqs. (10) and (12) are found. Physically, the Taylor ambiguity is attributed to using exactly the same critical resolved shear stress for all slip systems [49] and neglecting substructural anisotropy [54]. All valid basis solutions could be found by systematically changing the value of τ_c^α for single slip systems. Any non-negative linear combination (with sum of weighting factors equal to unity) of those basis solutions is also a valid solution. Hence, an additional criterion should be defined to select a valid solution for updating the orientation of the grains. One simple approach is a random choice of one of these basis solutions or an average of all basis solutions [50]. Delannay et al. [55] has tested two criteria for solving the Taylor ambiguity, by minimizing and by maximizing

$$T = \frac{\sum_{\alpha} (\dot{\gamma}^{\alpha})^2}{\left(\sum_{\alpha} \dot{\gamma}^{\alpha} \right)^2} \quad (14)$$

By minimizing T , slip will be distributed on as many as possible slip systems over all critically stressed slip systems, and the FC-Taylor model could reproduce a more realistic rolling texture than by maximizing T [55]. The method of minimizing T has also been found to be the best secondary criterion in [56] for solving the Taylor ambiguity. It is shown in [56] that the method for solving the Taylor ambiguity has significant influence on the texture predictions in the FC-Taylor model. By minimizing T , the FC-Taylor was found to perform similarly to other advanced crystal plasticity models in terms of predicting the rolling textures for an AA1050 material [56]. The minimization can be solved by the quadratic programming or by the singular value decomposition [57], while the latter method is widely employed when implementing rate-independent crystal plasticity (RICP) models in FEM codes. However, slip bands on pre-polished surfaces reveal that the inner core of the grain activates less than five slip systems [58], which contradicts the slip behaviour obtained by minimizing T .

Another way to solve the Taylor ambiguity is by the rate-dependent flow rule [59], which leads to the rate-dependent crystal plasticity (RDCP) models. The RDCP model assumes that all slip systems are active and that the slip activity is determined by a power-law type equation

$$\dot{\gamma}^\alpha = \dot{\gamma}_0 \left| \frac{\tau^\alpha}{\tau_c^\alpha} \right|^{\frac{1}{m}} \text{sgn}(\tau^\alpha) \quad (15)$$

where $\dot{\gamma}_0$ is a reference shearing rate, m is the instantaneous strain-rate sensitivity, τ_c^α represents the slip resistance which evolves during plastic deformation according to the hardening law, and τ^α is the resolved shear stress calculated from the current stress-state and crystallographic orientation. The RDCP models are commonly implemented into the FEM codes as CPFEM. A comprehensive review of the Taylor ambiguity can be found in [56].

2.3.4 Relaxed-constraint Taylor models, Alamel and GIA

The Taylor hypothesis violates stress equilibrium at grain boundaries and is in this sense as unrealistic as the Sachs hypothesis, although the deformation textures predicted by the Taylor model are generally closer to experiment [43]. Many models have been suggested with relaxations of the rigid strain constraint in the Taylor hypothesis, leading to the various relaxed-constraint (RC) Taylor models.

In ‘relaxed constraint’ (RC) Taylor models [60, 61], the full-constraint assumption, i.e. a uniform deformation throughout the aggregate, is partly abandoned based on grain-shape considerations. These models have for example been applied to rolled materials where grains are flattened and a significant proportion of the total grain-boundary area is parallel to the rolling plane. Along such boundaries, geometrical compatibility is not

hindered by heterogeneities in the shear components L_{13} and L_{23} of the global velocity gradient tensor \mathbf{L} . In the real material, the L_{13} and L_{23} can thus be assumed to be constrained only in the close neighbourhood of the boundaries but varied from grain to grain. The RC “pancake” model [50] neglects these small boundary regions and allows free variations of L_{13} (Type I relaxation) and L_{23} (Type II relaxation) from grain to grain. Due to the two degrees of freedom introduced, i.e. D_{13}^p and D_{23}^p are also relaxed, and only 3 independent slip systems need to be activated to fulfil the remaining 3 constraints. As shown mathematically in [50, 62], the stress components σ_{13} and σ_{23} will be zero, and hence partial stress equilibrium across grain boundaries will be satisfied. A schematic illustration of the RC-Taylor models is shown in Fig. 10.

The classical Taylor models, either with the FC or RC assumption, usually treat each single grain separately, i.e. no interaction between grains is considered in these 1-site models. However, the behaviour of single crystals in a real material is surely influenced by the neighbourhood grains, as experimentally observed in [17, 63] and from direct CPFEM simulations [64]. Hence, some advanced Taylor-type models have been proposed to consider more than one grain at the same time. The Lamel model [65] and the Advanced Lamel (Alamel) [29] model consider simultaneously two grains near a common boundary. The grain boundaries in the Lamel model are assumed to be parallel with the rolling plane while they are arbitrarily inclined in the Alamel model. Due to the configuration of grain boundaries, the Lamel model is only suitable for simulating rolling while the Alamel is applicable to any deformation modes. In the Lamel model, the in-plane shear strain component L_{12} can also be relaxed, which is termed Type III relaxation. It was found that the texture prediction for BCC metals cannot be improved by incorporating L_{12} in the Lamel model [66]. Li and Van Houtte [67] evaluated the predictions of cold-rolling texture by FC-Taylor, Lamel-type and CPFEM models, for the AA1200 and AA5182 alloys. It was found that the Lamel model performed better at higher reductions, while the Lamel + Type III model performed better at lower reductions. The Lamel type models gave better results than the FC-Taylor model and, were only inferior to the CPFEM at lower reductions. Rolling texture predictions for BCC and FCC materials showed that the Alamel model was among the best models. This suggested that the Alamel model, despite of all simplifications, captures the dominating mechanisms controlling the development of deformation textures in the materials studied [29]. The so-called Type III relaxation was introduced into the Alamel model in [68]. Due to the Type III relaxation, the deformation state of an Alamel cluster will deviate from the global deformation, hence leading to possible misfits between grains. The local coordinate system at the grain boundary should then be defined in a way that the reaction stresses from the surrounding material is minimum. The method for defining such an invariant grain boundary coordinate system has been proposed in

[68], where the grains (of a spherical shape before the deformation) and grain boundary will be deformed hypothetically by the global deformation gradient tensor \mathbf{F} . The major and minor axes of the ellipse intersected by the ‘deformed’ grains and updated boundary are taken as the two in-plane axes of the local coordinate system in an Alamel pair. With Type III relaxation, the performance of the Alamel model was found to be improved with respect to rolling texture prediction for two aluminium materials [68]. An extension of the Alamel model to an ‘ N -stack’ model was also proposed in the literature [69].

The grain interaction (GIA) model [70, 71] and a similar variant, the so called relaxed grain cluster (RGC) model [72], consider a volume element consisting of eight hexahedral grains which as a whole is aligned with the rolling direction. The entire cluster is forced to comply with the Taylor conditions but the grains in the cluster are allowed to deform freely and impose shears on next neighbour grains across these internal boundaries. This is illustrated in Fig. 10 and Fig. 11. However, this incompatibility has to be compensated for by the introduction of geometrically necessary dislocations. An energy minimization yields the activated slip systems and the respective shears, see also [73]. The computational cost of the GIA model is much higher than for the 2-point models, but with optimally chosen parameters it can predict rolling textures very well [29, 68, 73]. Similarly to the RC-Taylor and the Lamel models, the GIA model has been designed for rolling and not for general deformations. A modified GIA model which considers slip and twinning was proposed recently and applied to predict the texture evolution of Mg [74].

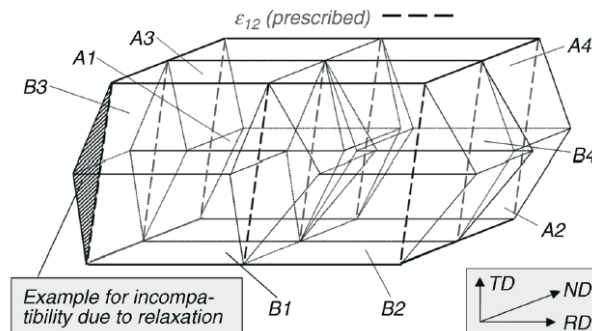


Fig. 11 The grain cluster model GIA considers an arrangement of eight grains and allows for interaction across their boundaries [75].

2.3.5 Visco-plastic self-consistent (VPSC) model

The self-consistent (SC) models regard each grain as an ellipsoidal inclusion in and interacting with a homogeneous effective medium (HEM). When a stress or deformation rate is applied to the outer boundary of the HEM, the inhomogeneity

induces local deviations of stress and strain rate in its vicinity. Such local field variations can be solved analytically using the Eshelby inclusion formulation when the local response of the medium is linear. Besides, stresses and strain rates are uniform within the ellipsoidal domain. This allows one to calculate the state of the grain without having to solve the local field outside the inclusion in the SC model [76]. When the relation between stress and strain rate is nonlinear it is usual to assume a linearized expression. The two common linear forms are the secant and the tangent approximations. It has been shown that for $n = \frac{1}{m} \rightarrow \infty$ the tangent approximation tends to a uniform stress state (Sachs or lower-bound approximation). On the other hand, it has been proved that the secant interaction is stiff and tends to a uniform state of strain rate (Taylor or upper-bound approximation) in the rate-insensitive limit. These two linearization schemes are schematically illustrated in Fig. 12. An intermediate approximation that gives polycrystal responses between the stiff secant and the compliant tangent approaches, can be obtained by introducing a tuning parameter n^{eff} , such that $1 < n^{\text{eff}} < n$. This intermediate approximation was termed a *relative directional compliance criterion* when originally proposed in [76].

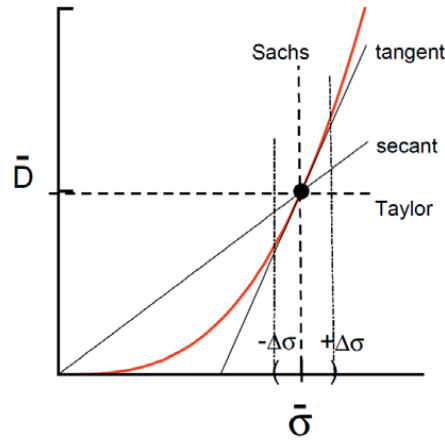


Fig. 12 Schematic one-dimensional representation of the linearization of the stress against strain-rate response in the vicinity of the overall magnitudes $(\bar{\sigma}, \bar{\dot{\epsilon}})$ for different types of interaction assumptions [76].

The visco-plastic self-consistent (VPSC) code developed by Lebensohn and Tomé [77] has been widely applied for simulating the plastic deformation and texture evolution of FCC and BCC materials as well as HCP metals and other materials of low symmetry crystallographic structures [10, 78]. The VPSC model has experienced continuous improvement in the last decades, e.g. second-order homogenization procedure [79], improved twinning models and work hardening laws [80, 81], finite

strain elastic–viscoplastic self-consistent (EPSC) model for polycrystalline materials [82, 83], and implementation of the VPSC model into an FEM code as the constitutive law at integration points [84].

2.3.6 Crystal plasticity finite element method (CPFEM)

The finite element (FE) method is commonly used to solve boundary-value problems in continua. Constitutive equations based on crystal plasticity have been implemented in FE simulations and applied to study a variety of material phenomena. Without Taylor ambiguity, RDCP models with power-law type flow rules, like Eq. (15), are widely employed in CPFEM [5, 62, 85-87], while rate-independent CPFEM implementations have also been proposed in the literature [57, 88]. The total deformation of a crystal is the result of two main mechanisms: dislocation motion within the active slip systems and lattice distortion. The general kinematics of the elastic-plastic deformation of crystals at finite strains were defined in the 1970s [89-91] and widely accepted in later research [5, 85, 92, 93]. The kinematic description may start from the additive decomposition of the velocity gradient tensor \mathbf{L} , generally associated with the hypoelastic assumption, or start from the multiplicative decomposition of the deformation gradient tensor \mathbf{F} where hyperelasticity is generally assumed. The two kinematic frames are practically identical for metals due to their small elastic deformations. The additive decomposition formulations have been described in **Article 3** and **Article A-1** of this thesis. Fig. 13 is a schematic illustration of the deformation of crystals according to the multiplicative decomposition of the deformation gradient. The details are not elaborated here and the reader is referred to e.g. [87, 94] for a complete description. In addition to slip, other deformation mechanisms such as twinning, phase transformation and non-crystallographic banding [95] can also be incorporated into CPFEM, see the comprehensive review of CPFEM in [5].

Since the 1980s, many research efforts have been made with CPFEM. Metals usually exhibit low value of strain-rate selectivity m in Eq. (15) at ambient temperature, which makes the resulting system of algebraic equations numerically extremely stiff. Hence, very small time step is commonly required when applying CPFEM in order to keep the stability. As a consequence, CPFEM is typical very time demanding. One research topic is **to propose efficient and robust numerical integration schemes**, to reduce the high computational cost due to the stress update algorithm. Some implicit integration schemes have been proposed, e.g. the slip-rate approach [85], the plastic deformation gradient \mathbf{F}^p approach [96], the stress approach [87], modified versions of the implicit slip-rate approach and of the implicit \mathbf{F}^p approach [86]. Examples of explicit integration schemes for integrating of RDCP models are the tangent modulus method [97], which was proposed first by Peirce et al. [91] using the Taylor series expansion of the flow rule to improve the numerical stability, and the fully explicit schemes proposed in [98] and [99]. Comparisons between different integration schemes for RDCP models,

with respect to efficiency, accuracy and robustness, have been presented in [86] and [94]. It was found that under the considered conditions the explicit methods were around 50 times faster than the implicit ones. However, the explicit method is only conditionally stable.

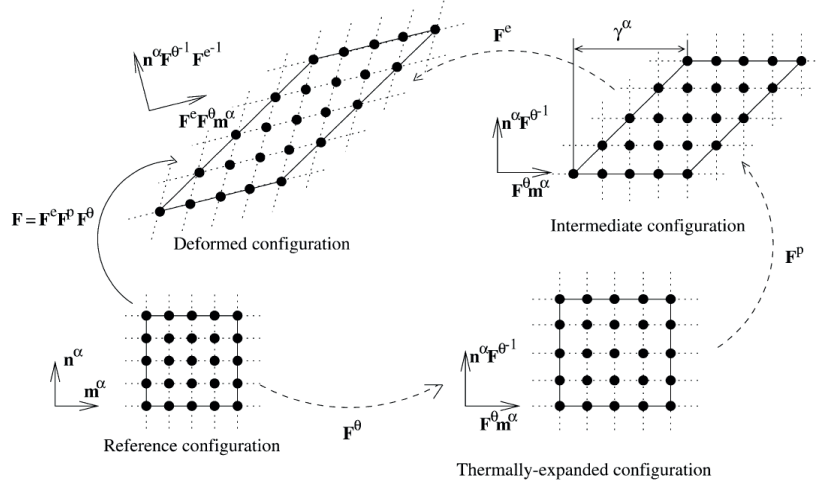


Fig. 13 Multiplicative decomposition of the total deformation gradient into thermal, plastic and elastic deformations. The rotation and stretching of the lattice are taken into account through the elastic deformation gradient \mathbf{F}^e [100].

Phenomenological constitutive models are commonly used in CPFEM, where the material state is only described in terms of the critical resolved shear stress τ_c^α . Dislocation populations and structures as well as their evaluation are not considered in these phenomenological constitutive models [5]. In recent years, **dislocation-based constitutive laws** in CPFEM have been proposed. Meissonnier et al. [100] have composed a strain-gradient theory based on the variation of dislocation density over a spatial area. Arsenlis and Parks [101] provided a model for plastic deformation based on the evolution of mobile dislocation density including individual analysis of various dislocation interactions. Temperature dependent dislocation density as well as dislocation blocks and walls were modelled in [102] and [103], mostly based on geometrically-necessary dislocation densities. Beyerlein and Tomé [104] used a multi-slip constitutive law for HCP materials with evolution of stored dislocation density, which is further extended in [105].

2.3.7 Fast Fourier transformation based crystal plasticity (CPFFT)

A spectral method operating in Fourier space was introduced in [106] and [107], as an alternative to the FEM for solving the system of partial differential equations resulting

from compatibility and static equilibrium in the context of computational homogenization. This spectral method is very efficient compared to FEM due to the repetitive use of a fast Fourier transforms (FFT) as part of an iterative solution algorithm. The FFT method has been extended to crystal plasticity models, leading to CPFFT models [108-110]. Compared with CPFEM [87], the CPFFT method has the advantage of higher efficiency [111], whereas one disadvantage is the requirement of periodic microstructures, making it less general than CPFEM. A CPFFT implementation is available in the open source Düsseldorf Advanced Material Simulation Kit (DAMASK) [112]. The CPFFT method is not used in the current project.

2.3.8 Modelling the plastic anisotropy

In 1970 Bunge [6] illustrated some applications of the FC-Taylor theory, for example to simulate uniaxial tensile and plane-strain tests and to predict the yield loci. Particularly, the method for determining the r -value was proposed, i.e. finding the contraction ratio q in Eq. (2) with a minimum Taylor factor. Bunge's method was widely used afterwards in the classical Taylor type models (e.g. FC/RC-Taylor, Alamel models) to conduct the virtual uniaxial tension tests, from which the angular dependence of yield stress and r -values can be observed, e.g. [10, 113-115]. Other type of tests, such as shear tests and biaxial tension/compression tests, can also be simulated by the FC-Taylor method. Virtual stress points at yielding along different applied strain rate directions are readily determined by Taylor-type models. These stress points at yielding can be employed to identify yield functions, e.g. [115-117]. These virtual experiments can be readily done by the VPSC code [77] where mixed boundary conditions can be prescribed, e.g. [118, 119].

Complex boundary conditions can be well prescribed in an FEM model. CPFEM is thus applicable to nearly any deformation type, from simple uniaxial tension, shear, plane-strain deformation [87] to real forming processes [98]. CPFEM has been applied to study the plastic anisotropy, e.g. conducting uniaxial tension tests along various in-plane directions [14] and providing stress-points at yielding for different loading directions [120].

Due to differences in underlying assumptions, different crystal plasticity models could perform differently for the prediction of plastic anisotropy. It is therefore worth investigating the accuracy and applicability of different CP models when predicting the plastic anisotropy. Such systematic investigations and comparisons are lacking in the existing literature and constitute a major part of this thesis.

2.4 Phenomenological plasticity theory

Computer simulations by means of FEM for large scale analysis of metal forming operations are used in the forming industry. Within FEM a constitutive model is required to describe the material response under general loadings. The constitutive model is commonly formulated under the framework of continuum mechanics. In continuum plasticity, the complexity of crystallographic deformation mechanisms and evolving dislocation substructures is disregarded and the plastically deforming material is replaced by a homogeneous continuum. The theory of plasticity has three main ingredients:

- the yield function, which defines the transition from elastic to plastic deformation.
- the flow rule, which defines the direction of the plastic deformation at yielding.
- the work hardening rule, which defines how the material hardens as a function of the imposed strain.

2.4.1 Yield functions

Mathematically the yield limit is described by the yield criterion, which is stated as

$$f(\boldsymbol{\sigma}) = 0 \quad (16)$$

where f is the yield function. The function f is assumed to be a continuous function of the stress tensor $\boldsymbol{\sigma}$, which takes negative values while the material is in the elastic region. The condition that $f(\boldsymbol{\sigma}) > 0$ is inadmissible. It is convenient to write the yield function in the form

$$f(\boldsymbol{\sigma}) = \varphi(\boldsymbol{\sigma}) - \sigma_Y \quad (17)$$

where $\sigma_{eq} = \varphi(\boldsymbol{\sigma})$ is the equivalent stress, measuring the magnitude of the stress state to which the material is subjected, and σ_Y is the yield stress of the material. The equivalent stress is assumed to be a positive homogeneous function of order one of the stress. For most metals and alloys, the yield function can be assumed to depend only on the deviatoric stress state \mathbf{S} and is expressed as $f(\mathbf{S}) = 0$.

For isotropic materials the yield function should depend only on either the principal stresses ($\sigma_1, \sigma_2, \sigma_3$) or the principal invariants ($I_\sigma, II_\sigma, III_\sigma$), and thus Eqs. (16) and (17) can be expressed as a function of the principal stresses or the principal invariants. The influence of hydrostatic pressure is usually neglected in classical metal plasticity. The Tresca criterion is the oldest yield criterion for isotropic materials. According to the Tresca criterion, yielding starts when the maximum shear stress reaches a critical value.

The von-Mises yield criterion is the most widely used isotropic yield function, and the equivalent stress is defined as

$$\begin{aligned}\sigma_{eq}^2 &= \frac{3}{2} S'_{ij} S'_{ij} \equiv \frac{1}{2} [(\sigma_1 - \sigma_2)^2 + (\sigma_2 - \sigma_3)^2 + (\sigma_3 - \sigma_1)^2] \\ &\equiv \frac{1}{2} [(\sigma_{11} - \sigma_{22})^2 + (\sigma_{22} - \sigma_{33})^2 + (\sigma_{33} - \sigma_{31})^2] + 3(\sigma_{23}^2 + \sigma_{31}^2 + \sigma_{12}^2)\end{aligned}\quad (18)$$

A non-quadratic formulation of the von-Mises yield criterion was introduced by Hershey [121] and used later by Hosford [122], expressed as

$$2\sigma_{eq}^a = (\sigma_1 - \sigma_2)^a + (\sigma_2 - \sigma_3)^a + (\sigma_3 - \sigma_1)^a \quad (19)$$

where a is the integer exponent which was shown to be connected to the crystal structure. Based on Taylor-Bishop-Hill calculations, it was found $a = 8$ for FCC metals, and $a = 6$ for BCC metals.

Anisotropic yield functions can be developed by generalizing the isotropic yield function into anisotropic cases, by adding coefficients to the isotropic yield function formulations [1] in a classical manner or by linear transformation [123]. It is important for any anisotropic yield function that the formulation reduces to isotropy when the material is isotropic and that convexity is preserved [119].

In 1948 Hill [124] proposed an anisotropic yield function by generalization of the von-Mises yield function. Later Hill proposed non-quadratic anisotropic yield functions [125-127]. However, the exponent in such yield functions should be determined numerically or by the r -values, and the yield loci obtained from these yield functions are distinct from Taylor-Bishop-Hill calculations [1].

Based on the Hershey isotropic yield function, Eq. (19), many anisotropic yield functions have been proposed, e.g. the renowned YLD series of yield functions proposed by Barlat and co-authors [7, 119, 128, 129] and the Banabic–Balan–Comsa (BBC) type yield function [130, 131].

Karafillis and Boyce [123] proposed the ‘Isotropic Plasticity Equivalent’ (IPE) theory, where a linear transformation ‘weights’ the different components of the stress tensor in order to account for the anisotropy. The ‘IPE stress transformation’ operates as

$$\tilde{\mathbf{S}} = \mathbf{L}^{4th} \boldsymbol{\sigma} \quad (20)$$

where \mathbf{L}^{4th} is a fourth order tensorial operator and $\tilde{\mathbf{S}}$ is the IPE stress tensor. Combining linear transformation with an isotropic yield function can be used to describe the anisotropy of materials. As pointed out by Aretz [132], the IPE procedure

has enormous advantages ‘From a mathematical point of view, this procedure is a very elegant way to arrive at a valid yield function for orthotropic materials. Most importantly, the use of a linear transformation ensures that the convexity of the isotropic yield function is preserved, which is the greatest problem in the development of orthotropic yield functions. Another advantage of this procedure is the fact that it is relatively easy to develop yield functions that can accommodate the full three-dimensional stress tensor, while most other developments in this field resulted in yield functions that can only account for planar stress-states’. Since the year 2000, several advanced yield functions have been proposed, which enable an accurate description of the anisotropic behaviour both of BCC and FCC metals, e.g. BBC2003 [131], Yld2004 [119], Yld2011 [132]. Two linear transformations are used in the Yld2004-18p yield function, and each \mathbf{L}^{4th} has 9 independent parameters. In total, there are 18 parameters for describing the anisotropy. The Yld2004-18p has been proven as an accurate model for describing the plastic anisotropy of aluminium alloys [51, 115, 119]. Fig. 14 and Fig. 15 are two such examples.

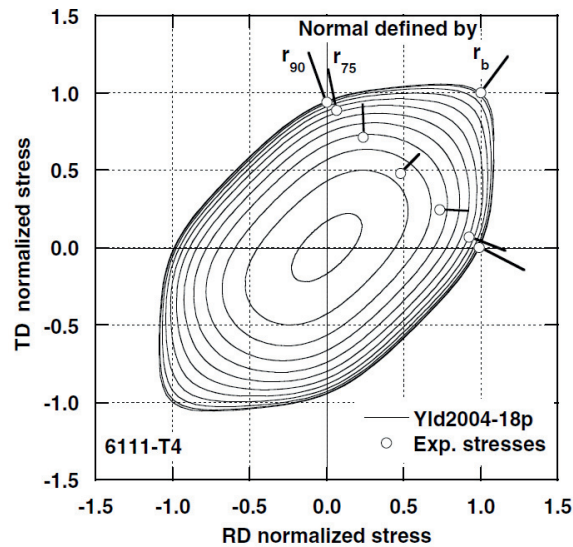


Fig. 14 Yld2004-18p yield surface represented by contours of normalized shear in 0.05 increments from zero, and projection of experimental data for 6111-T4 [119].

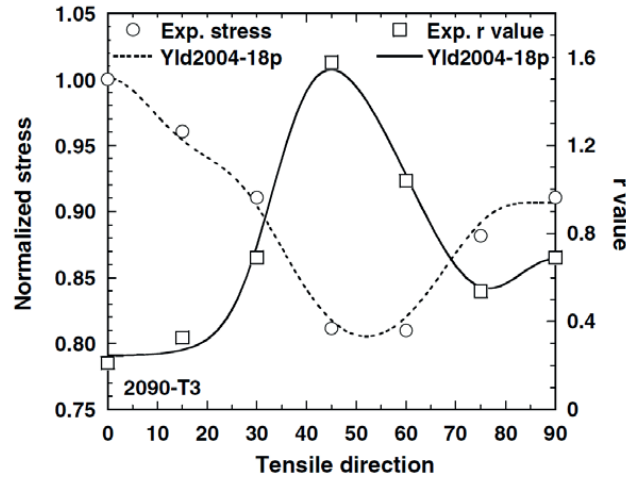


Fig. 15 Anisotropy of the flow stress (normalized by the RD uniaxial flow stress) and the r -value for 2090-T3, measured and calculated with Yld2004-18p [119].

A main drawback of advanced yield functions lies in the complexity of the parameter identification. For example, there are 18 parameters in Yld2004-18p to be identified in addition to the exponent, while there are even more in the Yld2011 criterion. These yield functions are generally calibrated by mechanical tests, e.g. uniaxial tensile tests and biaxial tension/compression tests. However, most of the stress space is left unexplored when fitting the parameters of the yield function due to severe experimental limitations [115], and biaxial tension/compression testing is not universally accessible. Hence, the crystal plasticity calculations have been employed to facilitate the yield function calibration. This can be done by conducting all or part of the required mechanical tests, such as uniaxial tensile tests, biaxial tests and/or shear tests virtually using CP models [29, 133]. For example, Kraska et al. [134] applied the CPFEM for the virtual uniaxial tensile, biaxial tensile, plane strain and shear tests, and calibrated the Vegter yield criterion [135]. However, it was found there the virtual tests lacked the important capability to predict the r -values correctly. If the r -values of the virtually fitted Vegter model were replaced by the measured r -values, the results of springback simulation were found to be improved. Alternatively, the virtual stress points at yielding along different strain-rate directions can be generated using CP models. The yield functions are then calibrated using these stress points [115, 117, 136]. Real mechanical tests and virtual stress points at yielding can be combined to identify parameters of advanced yield function. For example Grytten [115] evaluated three methods of identifying the Yld2004-18p by experiments, FC-Taylor stress points at yielding and a combination of experiments and FC-Taylor stress points (a hybrid method). By FEM simulation of plane-strain and shear tests, Grytten [115] concluded that the experiment-based method was the most reliable approach. However, the hybrid method was not

fully discussed in the work of Grytten [115]. It was also suggested there that advanced CP models in addition to the FC-Taylor model should be evaluated for the hybrid method.

An alternative yield function, again following the phenomenological plasticity approach, has been proposed by Van Houtte et al. [117] which is known as the Facet method. Dual plastic potentials described by means of a homogenous polynomial can be used either in the stress or strain-rate space. A large number of strain-rate/stress directions are generated by CP calculations to cover the total strain-rate/stress spaces, which permit a higher number of stress or strain modes than realizable in pure mechanical testing. As a consequence, a large number of parameters are usually contained in the Facet function. The Facet function was found to be flexible enough to represent the yield loci calculated by crystal plasticity models, and the texture evolution during the deformation can be taken into consideration under the hierarchy multi-scale (HMS) modelling scheme [136]. The comparison between Facet and other advanced yield functions is seldom done in the literature.

2.4.2 Flow rules and work hardening laws

The plastic flow rule defines the plastic strain-rate tensor \mathbf{D}^p in a way that ensures non-negative dissipation. In the most general case, the plastic flow rule is defined by

$$D_{ij}^p = \dot{\lambda} h_{ij} \quad \text{with} \quad h_{ij} = \frac{\partial g(\boldsymbol{\sigma})}{\partial \sigma_{ij}} \quad (21)$$

where $\dot{\lambda}$ is a non-negative scalar denoted the plastic multiplier and h_{ij} is the flow function which may be derived from a plastic potential function $g(\boldsymbol{\sigma})$. One particular choice is to assume that the plastic potential function $g(\boldsymbol{\sigma})$ is defined by the yield function $f(\boldsymbol{\sigma})$, in the sense that

$$D_{ij}^p = \dot{\lambda} \frac{\partial f(\boldsymbol{\sigma})}{\partial \sigma_{ij}} \quad (22)$$

This is called the associated flow rule or normality rule.

The loading/unloading conditions may be expressed by the Kuhn-Tucker conditions as

$$f \leq 0, \quad \dot{\lambda} \geq 0, \quad \dot{\lambda} f = 0 \quad (23)$$

which constitutes the constraints determining when plastic flow may occur in the elastic-plastic material. The concepts of yield surface, flow rule and loading/unloading conditions are schematically illustrated in Fig. 16.

Work hardening laws determine how the yield surface evolves during the plastic deformation. Isotropic and kinematic hardening laws are widely used in FEM, where the yield surface keeps the shape but expands or translates in the stress space, respectively. However, change of the shape of the yield surface has been observed in experiments. A distortional hardening law is then required to capture the change of shape of the yield function [2], which is now a very active research topic.

More details on the classical plasticity theories can be found in textbooks, e.g. [137].

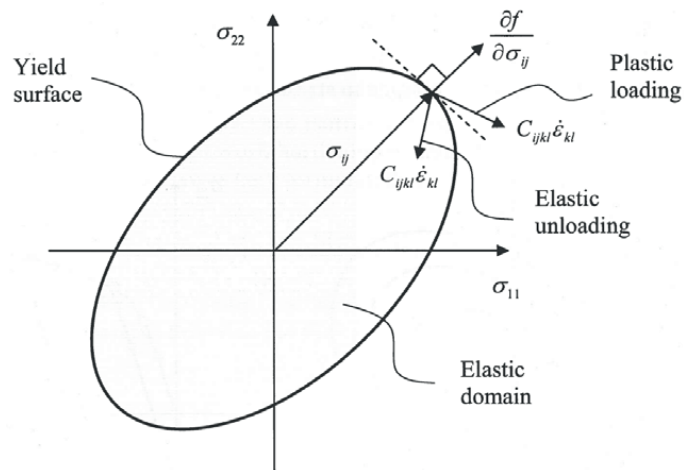


Fig. 16 Yield surface, normality rule and loading/unloading condition in the theory of plasticity [138].

Chapter 3 Experimental techniques

3.1 Mechanical testing

The **tensile test** is a standard technique to measure the mechanical properties of materials. Stress-strain curves and r -values are measured from tensile tests. The procedure of measurements is according to ASTM E517. In the present work the tests were performed at room temperature. The nominal strain rate was $\sim 10^{-3} \text{ s}^{-1}$.

3.2 Structure characterization

Materials science investigates the relationship between the processing, the structure and the properties. The structure encompasses atomic arrangements, the chemical structure and the grain-scale microstructure. The following instruments were used to characterize the structure.

The **optical microscopy**. Since in anisotropic crystals the grains with different orientations have different values of polarized light reflectivity, polarized light microscopy could be used to characterize the grain structure. However, aluminium has a cubic crystal structure, and is not sensitive to the polarization. Thus, a layer of anisotropic coating on the surface is required to reflect polarized light. An anodized aluminium surface displays contrast under polarized light. The anodization instrument is the same as the one used for electro-polishing where samples are connected to the anode. Anodization is performed at room temperature, at a voltage of 20-30 V for 2 min, using 5% HBF_4 solution.

The **scanning electron microscope (SEM)** is used for microstructure observation. The most common mode uses a secondary electron detector, which is generally used for the morphology of sample surface. Heavy elements reflect more backscattered electrons (BSE), so the BSE images can show chemical composition contrast. BSE imaging was used for observation of constitutive particles and dispersoids.

The **electron back-scatter diffraction (EBSD)** technique is used to characterize grain orientation, boundary misorientation and texture of crystalline materials. Zeiss Supra/Ultra 55 with EBSD detector was used in this work, and the results of EBSD were analysed by TSL software. To ensure a statistical soundness of the texture measured by EBSD, more than 5000 grains were generally covered in the scanning for the fully annealed sheets in this work. For the deformed material, the scanning area was large enough to ensure that the texture would change little if more scans were included. The Euler angles of all scanning points were then output to an external file. From the file, a number of orientations were then randomly chosen and compared to the measured texture in terms of ID_N defined by Eq. (4). The set of orientations that had a value equal

to or smaller than the user-set critical value of ID_N was then input into CP models for modelling the plastic anisotropy.

The **texture goniometer** is using X-ray diffraction to determine the crystallographic macrotexture of polycrystalline materials. This technique was used to determine the macrotexture of materials in this thesis. A Siemens D5000 X-ray diffractometer equipped with an Eulerian cradle was used. Four incomplete pole figures, namely {200}, {111}, {220} and {311}, were obtained for every sample, from which the ODFs were calculated by the series expansion method, generally using 22 terms in the expansion, and ghost-corrected. Compared with the EBSD technique, the texture goniometer is an economic and fast method to determine the texture. However, it is not straightforward in the texture goniometer to generate a set of Euler angles which is the input to CP models, even though it is possible, e.g. [139]. In this work, the texture measured by EBSD was compared to the macrotexture of the same material to check the statistical quality of measurements.

Chapter 4 Summary and remarks

4.1 Summary

Three different aluminium sheets were studied in this thesis, which included a fully recrystallized AA1050 sheet (in **Article 1**), a fully annealed AA3103-O sheet (in **Article 4**) and a cold-rolled AA3103-H18 sheet (in **Article 4**). The texture and microstructure of the three materials were characterized. Different textures and grain microstructures were observed in the three sheets. The AA1050 material featured a strong cube texture with a maximum ODF value of 18. The grain structure was almost equiaxed. In AA3103-O the texture was weak with a maximum ODF value of 6 and both cube and P orientations were dominant. The AA3103-H18 sheet exhibited a typical cold-rolling texture while the maximum ODF value was 10. A fibrous type microstructure was observed in AA3103-H18, while grains in AA3103-O were slightly elongated along the RD.

In-plane uniaxial plastic anisotropy was measured from uniaxial tensile tests along every 15° from the RD to the TD. Yield stresses and r -values for these 7 tensile directions were measured. Different anisotropic behaviours in terms of angular yield stresses and r -values were observed for the three materials. In all three materials, the anisotropy of the flow pattern was much stronger than the strength anisotropy.

Five crystal plasticity models, namely the FC-Taylor model, the Alamel model, the Alamel type III model, the VPSC model and the CPFEM, were employed to predict the plastic anisotropy through virtual uniaxial tension tests, and compared to experiments. Except the VPSC, the other four CP models have been implemented in an in-house code during the project. The main input for the CP calculations was the texture, which was represented by N single grain orientations. The measured grain boundary misorientation distribution was taken into consideration when making Alamel pairs for the AA1050 material, and for the AA3103-O and AA3103-H18 materials the observed grain morphology in terms of grain aspect ratios were taken into consideration when predicting the plastic anisotropy. For all three materials, the five crystal plasticity models could only predict qualitatively correct plastic anisotropy compared to the experiments. However, the predictions by high resolution CPFEM and the Alamel Type III model were found to be similar to each other and generally gave better results than the other three models. The Alamel Type III model is much more CPU-time efficient than CPFEM. Hence, the Alamel Type III model is recommended as an accurate and efficient model for predicting the plastic anisotropy of 1xxx and 3xxx series aluminium alloys.

Two advanced yield functions, namely Yld2004-18p and Facet, were employed in **Article 1** to describe the plastic anisotropy of the AA1050 sheet. Optimal exponents of Yld2004-18p for isotropic FCC metals (equivalent to the Hershey isotropic yield function) were determined for the FC-Taylor, Alamel, Alamel Type III and VPSC models, respectively. The optimized exponent according to the FC-Taylor model was 8, while an exponent of 6 was found for the other three CP models. Each of these four CP models provided a set of 201 virtual stress points at yielding along 201 equally distributed strain-rate directions. The Facet yield surface was calibrated using each of these four sets of 201 stress points and compared to the in-plane yield loci and the planar anisotropy calculated by the corresponding crystal plasticity models. The anisotropic yield function Yld2004-18p was calibrated by three methods: using uniaxial tension data, using the 201 virtual yield points in stress space, and using a combination of experimental data and virtual yield points (i.e., a hybrid method). The Facet yield function and the Yld2004-18p yield function based on virtual stress points only were found to be close to the predictions of the underlying CP models, but deviated from the experiments. The Yld2004-18p yield function identified mainly by experiments and by the hybrid method could accurately capture the experimental directional dependence of the yield stress and the r -value. By examining the yield loci involving out-of-plane stress components, it was found that the hybrid calibration method could capture the experimental results and at the same time ensure a good fit to the anisotropy in the full stress space predicted by the crystal plasticity models. Based on all these results for AA1050, the Yld2004-18p, the Alamel Type III model and the hybrid identification procedure were recommended as an accurate approach for describing the plastic anisotropy for the studied materials. Calibrating the Yld2004-18p yield surface for the AA1050 material by CPFEM calculations covering all the stress space has been done but not reported in this thesis. That will be published in a subsequent paper by the current author.

In **Article 2**, plane-strain tension and shear tests were conducted in laboratory and simulated numerically in an FEM code for the AA1050 sheet. In the FEM modelling, the Yld2004-18p functions calibrated in **Article 1** by three methods, i.e. by mainly experiments, by Alamel Type III stress points at yielding and by a combination of experiments and Alamel Type III stress points, were employed. Comparing the experimental and the predicted force-displacement curves, the Yld2004-18p calibrated by the hybrid method was found to be most accurate for describing the initial yielding of the material.

A multi-level modelling scheme involving the Yld2004-18p yield function and CPFEM was described and utilized in **Article 4**, to study the plastic anisotropy of AA3103 sheets which have non-equiaxed grain morphologies. The Yld2004-18p yield function was calibrated to 89 stress points at yielding provided by CPFEM calculations. This

method makes it convenient to predict plastic anisotropy while considering the real grain shapes even for non-equiaxed grain structures in the CPFEM simulations. The Yld2004-18p yield surface was able to represent quite accurately the plastic anisotropy determined from CPFEM calculations under this multi-level modelling scheme.

Article 3 and **Article A-1** in the appendix describe the efforts made to propose robust and efficient numerical integration schemes for a RDCP model. The kinematic framework in both articles started with additive decomposition of the velocity gradient tensor into elastic and plastic parts. The Cauchy stress was calculated by using a hypoelastic formulation applying the Jaumann stress rate. In **Article A-1**, an explicit integration scheme, similar to that used in [98], was proposed and implemented as “hypo-CPFEM”. It was compared to a well-evaluated “hyper-CPFEM” implementation [94] with the explicit integration method proposed in [98], through uniaxial tension and plane-strain compression simulations. It was found that the hypo-RDCP formulation was as accurate as the hyper-RDCP formulation, even though the Cauchy stress and the grain orientation were updated following different strategies. The integration scheme proposed in **Article A-1** was found to be slightly faster than the one proposed in [98]. In **Article 3**, the explicit integration scheme in **Article A-1** was improved by avoiding the update of Schmid tensor at each time step. An integration algorithm based on the modified Euler method with an adaptive substepping scheme was then proposed, where the substepping is mainly controlled by the local error of the stress predictions within the time step. Both integration algorithms were implemented in a stand-alone code with the Taylor aggregate assumption and in an explicit FEM code. The robustness, accuracy and efficiency of the substepping scheme were extensively evaluated for large time steps, extremely low strain-rate sensitivity, high deformation rates and strain-path changes using the stand-alone code. The results showed that the substepping scheme is robust and in some cases one order of magnitude faster than the forward Euler algorithm. The use of mass scaling to reduce computation time in crystal plasticity finite element simulations for quasi-static problems was also discussed. Finally, simulation of the Taylor bar impact test was carried out to show the applicability and robustness of the proposed integration algorithm for the modelling of dynamic problems with contact.

4.2 Suggestions for future work

1. The accuracy and applicability of these five CP models for describing the plastic anisotropy have been considered for typical 1xxx and 3xxx aluminium alloys in **Articles 1, 2** and **4**. Similar systematic studies should be extended to 5xxx, 6xxx and 7xxx aluminium alloys. This work could guide the industry and researchers to select the proper CP models for predicting the plastic anisotropy of aluminium alloys.

2. In **Article 2**, calibrations of the Yld2004-18p yield function were evaluated by plane-strain tension and shear tests. By these two tests, the biaxial tension and the pure shear regions of the yield surface were mainly tested. A more general evaluation can be done by formability tests and associated calculations.
3. Evolution of the directional flow stress, which is termed distortional hardening, was observed for the AA1050 material in the uniaxial tensile tests. The observed distortional hardening was not explained nor modelled in this thesis. Modelling of distortional hardening is suggested for further research efforts.
4. It would have been interesting to compare the efficiency of CPFEM with the substepping integration scheme to the CPFEM method.
5. As stated in Chapter 1.2, the CP models were employed in this thesis to deal with texture-induced plastic anisotropy of aluminium alloys. The secondary effects played by grain morphology and grain boundary misorientation distribution on the plastic anisotropy, in addition to the texture, have also been taken into consideration when predicting the plastic anisotropy by CP models. However, other important microstructural features, e.g. dislocation structures, particles and dispersoids, precipitates in heat-treatable aluminium alloys, are ignored in all CP models used here. Modelling the microstructure-based plastic anisotropy which considers all important microstructural features (including the texture of course) is recommended for future research. Dislocation-based CPFEM may be a promising candidate for that purpose.

References

1. Banabic, D., *Plastic Behaviour of Sheet Metal*, in *Sheet Metal Forming Processes*. 2010, Springer Berlin Heidelberg. p. 27-140.
2. Barlat, F., et al., *Extension of homogeneous anisotropic hardening model to cross-loading with latent effects*. *International Journal of Plasticity*, 2013. **46**(0): p. 130-142.
3. Barlat, F., et al., *An alternative to kinematic hardening in classical plasticity*. *International Journal of Plasticity*, 2011. **27**(9): p. 1309-1327.
4. Geng, L. and R.H. Wagoner, *Role of plastic anisotropy and its evolution on springback*. *International Journal of Mechanical Sciences*, 2002. **44**(1): p. 123-148.
5. Roters, F., et al., *Overview of constitutive laws, kinematics, homogenization and multiscale methods in crystal plasticity finite-element modeling: Theory, experiments, applications*. *Acta Materialia*, 2010. **58**(4): p. 1152-1211.
6. Bunge, H.J., *Some applications of the Taylor theory of polycrystal plasticity*. *Kristall und Technik*, 1970. **5**(1): p. 145-175.
7. Barlat, F., et al., *Plane stress yield function for aluminum alloy sheets—part 1: theory*. *International Journal of Plasticity*, 2003. **19**(9): p. 1297-1319.
8. Pöhlandt, K., D. Banabic, and K. Lange. *Equi-biaxial anisotropy coefficient used to describe the plastic behavior of sheet metal*. in *Proceedings of the ESAFORM Conference*. 2002. Krakow.
9. Hatherly, M. and W.B. Hutchinson, *An introduction to textures in metals*. 1979: Institution of Metallurgists.
10. Xie, Q., et al., *Polycrystal plasticity models based on crystallographic and morphologic texture: Evaluation of predictions of plastic anisotropy and deformation texture*. *Materials Science and Engineering: A*, 2013. **581**(0): p. 66-72.
11. Frédéric, B., L. John, and C.B. John, *Plastic anisotropy in precipitation-strengthened aluminium alloys deformed in uniaxial and plane strain deformation*. *Modelling and Simulation in Materials Science and Engineering*, 2000. **8**(4): p. 435.
12. Bate, P., W.T. Roberts, and D.V. Wilson, *The plastic anisotropy of two-phase aluminium alloys—I. Anisotropy in unidirectional deformation*. *Acta Metallurgica*, 1981. **29**(11): p. 1797-1814.
13. Fjeldbo, S.K., *Studies of the influence of strong through thickness texture variation on the plastic flow properties of extruded AA6063-W aluminium strips and tubes, with application to the modelling and simulation of tube hydroforming of T-shapes*, 2008, Norwegian University of Science and Technology.

14. Dumoulin, S., et al., *Description of plastic anisotropy in AA6063-T6 using the crystal plasticity finite element method*. Modelling and Simulation in Materials Science and Engineering, 2012. **20**(5): p. 055008.
15. Chang, H.J., et al., *Texture evolution in FCC metals from initially different misorientation distributions under shear deformation*. Metals and Materials International, 2010. **16**(4): p. 553-558.
16. Juul Jensen, D. and N. Hansen, *Flow stress anisotropy in aluminium*. Acta Metallurgica et Materialia, 1990. **38**(8): p. 1369-1380.
17. Huang, X. and G. Winther, *Dislocation structures. Part I. Grain orientation dependence*. Philosophical Magazine, 2007. **87**(33): p. 5189-5214.
18. Bay, B., et al., *Overview no. 96 evolution of f.c.c. deformation structures in polyslip*. Acta Metallurgica et Materialia, 1992. **40**(2): p. 205-219.
19. Hansen, N. and D.J. Jensen, *Development of microstructure in FCC metals during cold work*. Philosophical Transactions of the Royal Society of London. Series A: Mathematical, Physical and Engineering Sciences, 1999. **357**(1756): p. 1447-1469.
20. Winther, G. and X. Huang, *Dislocation structures. Part II. Slip system dependence*. Philosophical Magazine, 2007. **87**(33): p. 5215-5235.
21. Huang, X., *Grain Orientation Effect on Microstructure in Tensile Strained Copper*. Scripta Materialia, 1998. **38**(11): p. 1697-1703.
22. Landau, P., et al., *Universal strain-temperature dependence of dislocation structure evolution in face-centered-cubic metals*. Acta Materialia, 2011. **59**(13): p. 5342-5350.
23. Holmedal, B., P.V. Houtte, and Y. An, *A crystal plasticity model for strain-path changes in metals*. International Journal of Plasticity, 2008. **24**(8): p. 1360-1379.
24. *Descriptors of Orientation*, in *Introduction to Texture Analysis*. 2009, CRC Press. p. 15-50.
25. Bunge, H.J., *Texture Analysis in Materials Science: Mathematical Methods*. 1982: Butterworths.
26. Alumatter. <http://aluminium.matter.org.uk/>. 2005.
27. Grewen, J. and J. Huber, *Recrystallization of Metallic Materials*, F. Haessner, Editor. 1978, Dr. Riederer-Verlag: Stuttgart. p. 111.
28. *Evaluation and Representation of Macrotecture Data*, in *Introduction to Texture Analysis*. 2009, CRC Press. p. 123-172.
29. Van Houtte, P., et al., *Deformation texture prediction: from the Taylor model to the advanced Lamel model*. International Journal of Plasticity, 2005. **21**(3): p. 589-624.
30. Hirsch, J.R., *Correlation of deformation texture and microstructure*. Materials Science and Technology, 1990. **6**(11): p. 1048-1057.
31. Engler, O., *An EBSD local texture study on the nucleation of recrystallization at shear bands in the alloy Al-3%Mg*. Scripta Materialia, 2001. **44**(2): p. 229-236.

32. MACKENZIE, J.K., *SECOND PAPER ON STATISTICS ASSOCIATED WITH THE RANDOM DISORIENTATION OF CUBES*. Biometrika, 1958. **45**(1-2): p. 229-240.
33. Christian, J.W., *Some surprising features of the plastic deformation of body-centered cubic metals and alloys*. Metallurgical Transactions A, 1983. **14**(7): p. 1237-1256.
34. Qin, Q. and J.L. Bassani, *Non-schmid yield behavior in single crystals*. Journal of the Mechanics and Physics of Solids, 1992. **40**(4): p. 813-833.
35. Soare, S.C., *Plasticity and non-Schmid effects*. Proceedings of the Royal Society A: Mathematical, Physical and Engineering Science, 2014. **470**(2161).
36. DoITPoMS. *TLP Library, Slip in Single Crystals*. Available from: http://www.doitpoms.ac.uk/tlplib/slip/slip_geometry.php.
37. Sachs, G., *Zur ableitung einer filebedingung*. Zeitschrift des Vereines Deutscher Ingenieure, 1928. **72**: p. 734-736.
38. Ahzi, S., R.J. Asaro, and D.M. Parks, *Application of crystal plasticity theory for mechanically processed BSCCO superconductors*. Mechanics of Materials, 1993. **15**(3): p. 201-222.
39. Clausen, B., *Characterisation of Polycrystal Deformation by Numerical Modelling and Neutron Diraction Measurements*, in *Department of Solid Mechanics 1997*, Department of Solid Mechanics: Risø.
40. Pedersen, O.B., et al., *Modelling of Plastic Heterogeneity in Deformation of Single-Phase Materials*, in *Constitutive Relations and Their Physical Basis*, B. Ralph, Editor 1987, Risø National Laboratory: Roskilde. p. 147-172.
41. Fjeldly, A. and H.J. Roven, *Comparison of Anisotropy and Flow Behaviour in Two AlZnMg Extrusions - Recrystallized versus Nonrecrystallized*. Materials Science Forum, 1996. **242**.
42. Leffers, T. and D.J. Jensen, *The Early Stages of the Development of Rolling Texture in Copper and Brass*. Textures and Microstructures, 1988. **8**: p. 467-480.
43. Delannay, L., *Observation and modelling of grain interactions and grain subdivision in rolled cubic polycrystals* in *Departement Metaalkunde en Toegepaste Materiaalkunde 2001*, KU Leuven.
44. Taylor, G.I., *Plastic strain in metals*. Journal of Institute of Metals, 1938. **62**: p. 307-324.
45. Bishop, J.F.W. and R. Hill, *XLVI. A theory of the plastic distortion of a polycrystalline aggregate under combined stresses*. Philosophical Magazine Series 7, 1951. **42**(327): p. 414-427.
46. Bishop, J.F.W. and R. Hill, *CXXXVIII. A theoretical derivation of the plastic properties of a polycrystalline face-centred metal*. Philosophical Magazine Series 7, 1951. **42**(334): p. 1298-1307.

47. Van Houtte, P., *On the equivalence of the relaxed Taylor theory and the Bishop-Hill theory for partially constrained plastic deformation of crystals*. Materials Science and Engineering, 1982. **55**(1): p. 69-77.
48. Piehler, H.R., *Crystal-plasticity fundamentals*. ASM handbook A, 2009. **22**: p. 232-38.
49. Gil Sevillano, J., P. van Houtte, and E. Aernoudt, *Large strain work hardening and textures*. Progress in Materials Science, 1980. **25**(2-4): p. 69-134.
50. Van Houtte, P., *A Comprehensive Mathematical Formulation of an Extended Taylor-Bishop-Hill Model Featuring Relaxed Constraints, the Renouard&-Wintenberger Theory and a Strain Rate Sensitivity Model*. Textures and Microstructures, 1988. **8**: p. 313-350.
51. Yoon, J.W., et al., *Prediction of six or eight ears in a drawn cup based on a new anisotropic yield function*. International Journal of Plasticity, 2006. **22**(1): p. 174-193.
52. Roters, F., et al., *DAMASK: the Düsseldorf Advanced Material Simulation Kit for studying crystal plasticity using an FE based or a spectral numerical solver*. Procedia IUTAM, 2012. **3**(0): p. 3-10.
53. Press, W., et al., *Numerical Recipes in Fortran: The Art of Scientific Computing*. 1992: Cambridge University Press.
54. Peeters, B., et al., *Taylor ambiguity in BCC polycrystals: a non-problem if substructural anisotropy is considered*. Scripta Materialia, 2001. **45**(12): p. 1349-1356.
55. Delannay, L., S.R. Kalidindi, and P. Van Houtte, *Quantitative prediction of textures in aluminium cold rolled to moderate strains*. Materials Science and Engineering: A, 2002. **336**(1-2): p. 233-244.
56. Mánik, T. and B. Holmedal, *Review of the Taylor ambiguity and the relationship between rate-independent and rate-dependent full-constraints Taylor models*. International Journal of Plasticity, 2013(0).
57. Anand, L. and M. Kothari, *A computational procedure for rate-independent crystal plasticity*. Journal of the Mechanics and Physics of Solids, 1996. **44**(4): p. 525-558.
58. Essmann, U., M. Rapp, and M. Wilkens, *Die versetzungsanordnung in plastisch verformten kupfer-vielkristallen*. Acta Metallurgica, 1968. **16**(10): p. 1275-1287.
59. Hutchinson, J.W., *Bounds and Self-Consistent Estimates for Creep of Polycrystalline Materials*. Proceedings of the Royal Society of London. A. Mathematical and Physical Sciences, 1976. **348**(1652): p. 101-127.
60. Honneff, H. and H. Mecking, *A method for the determination of the active slip systems and orientation changes during single crystal deformation*. Textures of Materials, 1978. **1**: p. 265-275.
61. Kocks, U.F. and H. Chandra, *Slip geometry in partially constrained deformation*. Acta Metallurgica, 1982. **30**(3): p. 695-709.

62. Peirce, D., R.J. Asaro, and A. Needleman, *An analysis of nonuniform and localized deformation in ductile single crystals*. Acta Metallurgica, 1982. **30**(6): p. 1087-1119.
63. Winther, G., *Slip systems, lattice rotations and dislocation boundaries*. Materials Science and Engineering: A, 2008. **483–484**(0): p. 40-46.
64. Kanjarla, A.K., P. Van Houtte, and L. Delannay, *Assessment of plastic heterogeneity in grain interaction models using crystal plasticity finite element method*. International Journal of Plasticity, 2010. **26**(8): p. 1220-1233.
65. Van Houtte, P., L. Delannay, and I. Samajdar, *Quantitative Prediction of Cold Rolling Textures in Low-Carbon Steel by Means of the Lamel Model*. Textures and Microstructures, 1999. **31**(3): p. 109-149.
66. Van Houtte, P., L. Delannay, and S.R. Kalidindi, *Comparison of two grain interaction models for polycrystal plasticity and deformation texture prediction*. International Journal of Plasticity, 2002. **18**(3): p. 359-377.
67. Li, S. and P. Van Houtte, *Performance of statistical (Taylor, Lamel) and CP-FE models in texture predictions of aluminium alloys in cold rolling*. Aluminium, 2002. **78**: p. 918-922.
68. Mánik, T. and B. Holmedal, *Additional relaxations in the Alamel texture model*. Materials Science and Engineering: A, 2013. **580**(0): p. 349-354.
69. Arul Kumar, M., S. Mahesh, and V. Parameswaran, *A 'stack' model of rate-independent polycrystals*. International Journal of Plasticity, 2011. **27**(6): p. 962-981.
70. Crumbach, M., et al., *A Taylor type deformation texture model considering grain interaction and material properties. Part I - Fundamentals*. Recrystallization and Grain Growth, Vols 1 and 2, ed. G. Gottstein and D.A. Molodov. 2001, Berlin: Springer-Verlag Berlin. 1053-1060.
71. Crumbach, M., M. Goerdeler, and G. Gottstein, *Modelling of recrystallisation textures in aluminium alloys: I. Model set-up and integration*. Acta Materialia, 2006. **54**(12): p. 3275-3289.
72. Tjahjanto, D.D., P. Eisenlohr, and F. Roters, *A novel grain cluster-based homogenization scheme*. Modelling and Simulation in Materials Science and Engineering, 2010. **18**(1): p. 015006.
73. Engler, O., M. Crumbach, and S. Li, *Alloy-dependent rolling texture simulation of aluminium alloys with a grain-interaction model*. Acta Materialia, 2005. **53**(8): p. 2241-2257.
74. Mu, S., F. Tang, and G. Gottstein, *A cluster-type grain interaction deformation texture model accounting for twinning-induced texture and strain-hardening evolution: Application to magnesium alloys*. Acta Materialia, 2014. **68**(0): p. 310-324.

75. Gottstein, G., *Through-Process Modeling of Materials Fabrication: Philosophy, Current State, and Future Directions*, in *Microstructural Design of Advanced Engineering Materials*. 2013, Wiley-VCH Verlag GmbH & Co. KGaA. p. 1-17.
76. Tomé, C.N., *Self-consistent polycrystal models: a directional compliance criterion to describe grain interactions*. *Modelling and Simulation in Materials Science and Engineering*, 1999. **7**(5): p. 723.
77. Lebensohn, R.A. and C.N. Tomé, *A self-consistent anisotropic approach for the simulation of plastic deformation and texture development of polycrystals: Application to zirconium alloys*. *Acta Metallurgica et Materialia*, 1993. **41**(9): p. 2611-2624.
78. Oppedal, A.L., et al., *Anisotropy in hexagonal close-packed structures: improvements to crystal plasticity approaches applied to magnesium alloy*. *Philosophical Magazine*, 2013. **93**(35): p. 4311-4330.
79. Lebensohn, R.A., C.N. Tomé, and P.P. Castañeda, *Self-consistent modelling of the mechanical behaviour of viscoplastic polycrystals incorporating intragranular field fluctuations*. *Philosophical Magazine*, 2007. **87**(28): p. 4287-4322.
80. Proust, G., et al., *Modeling the effect of twinning and detwinning during strain-path changes of magnesium alloy AZ31*. *International Journal of Plasticity*, 2009. **25**(5): p. 861-880.
81. Proust, G., C.N. Tomé, and G.C. Kaschner, *Modeling texture, twinning and hardening evolution during deformation of hexagonal materials*. *Acta Materialia*, 2007. **55**(6): p. 2137-2148.
82. Wang, H., et al., *A finite strain elastic-viscoplastic self-consistent model for polycrystalline materials*. *Journal of the Mechanics and Physics of Solids*, 2010. **58**(4): p. 594-612.
83. Agnew, S.R., D.W. Brown, and C.N. Tomé, *Validating a polycrystal model for the elastoplastic response of magnesium alloy AZ31 using in situ neutron diffraction*. *Acta Materialia*, 2006. **54**(18): p. 4841-4852.
84. Knezevic, M., et al., *Integration of self-consistent polycrystal plasticity with dislocation density based hardening laws within an implicit finite element framework: Application to low-symmetry metals*. *Journal of the Mechanics and Physics of Solids*, 2013. **61**(10): p. 2034-2046.
85. Cuitino, A.M. and M. Ortiz, *Computational modelling of single crystals*. *Modelling and Simulation in Materials Science and Engineering*, 1993. **1**(3): p. 225.
86. Ling, X., M.F. Horstemeyer, and G.P. Potirniche, *On the numerical implementation of 3D rate-dependent single crystal plasticity formulations*. *International Journal for Numerical Methods in Engineering*, 2005. **63**(4): p. 548-568.

87. Kalidindi, S.R., C.A. Bronkhorst, and L. Anand, *Crystallographic texture evolution in bulk deformation processing of FCC metals*. Journal of the Mechanics and Physics of Solids, 1992. **40**(3): p. 537-569.
88. McGinty, R.D. and D.L. McDowell, *A semi-implicit integration scheme for rate independent finite crystal plasticity*. International Journal of Plasticity, 2006. **22**(6): p. 996-1025.
89. Asaro, R.J. and J.R. Rice, *Strain localization in ductile single crystals*. Journal of the Mechanics and Physics of Solids, 1977. **25**(5): p. 309-338.
90. Hill, R. and J.R. Rice, *Constitutive analysis of elastic-plastic crystals at arbitrary strain*. Journal of the Mechanics and Physics of Solids, 1972. **20**(6): p. 401-413.
91. Peirce, D., R.J. Asaro, and A. Needleman, *Material rate dependence and localized deformation in crystalline solids*. Acta Metallurgica, 1983. **31**(12): p. 1951-1976.
92. Nemat-Nasser, S. and T. Okinaka, *A new computational approach to crystal plasticity: fcc single crystal*. Mechanics of Materials, 1996. **24**(1): p. 43-57.
93. Asaro, R.J. and A. Needleman, *Overview no. 42 Texture development and strain hardening in rate dependent polycrystals*. Acta Metallurgica, 1985. **33**(6): p. 923-953.
94. Dumoulin, S., O.S. Hopperstad, and T. Berstad, *Investigation of integration algorithms for rate-dependent crystal plasticity using explicit finite element codes*. Computational Materials Science, 2009. **46**(4): p. 785-799.
95. Jia, N., et al., *Non-crystallographic shear banding in crystal plasticity FEM simulations: Example of texture evolution in α -brass*. Acta Materialia, 2012. **60**(3): p. 1099-1115.
96. Maniatty, A.M., P.R. Dawson, and Y.S. Lee, *A time integration algorithm for elasto-viscoplastic cubic crystals applied to modelling polycrystalline deformation*. International Journal for Numerical Methods in Engineering, 1992. **35**(8): p. 1565-1588.
97. van der Giessen, E. and K.W. Neale, *Analysis of the inverse Swift effect using a rate-sensitive polycrystal model*. Computer Methods in Applied Mechanics and Engineering, 1993. **103**(1-2): p. 291-313.
98. Grujicic, M. and S. Batchu, *Crystal plasticity analysis of earing in deep-drawn OFHC copper cups*. Journal of Materials Science, 2002. **37**(4): p. 753-764.
99. Rossiter, J., et al., *A new crystal plasticity scheme for explicit time integration codes to simulate deformation in 3D microstructures: Effects of strain path, strain rate and thermal softening on localized deformation in the aluminum alloy 5754 during simple shear*. International Journal of Plasticity, 2010. **26**(12): p. 1702-1725.

100. Meissonnier, F.T., E.P. Busso, and N.P. O'Dowd, *Finite element implementation of a generalised non-local rate-dependent crystallographic formulation for finite strains*. International Journal of Plasticity, 2001. **17**(4): p. 601-640.
101. Arsenlis, A. and D.M. Parks, *Modeling the evolution of crystallographic dislocation density in crystal plasticity*. Journal of the Mechanics and Physics of Solids, 2002. **50**(9): p. 1979-2009.
102. Ma, A., F. Roters, and D. Raabe, *Numerical study of textures and Lankford values for FCC polycrystals by use of a modified Taylor model*. Computational Materials Science, 2004. **29**(3): p. 353-361.
103. Ma, A., F. Roters, and D. Raabe, *A dislocation density based constitutive model for crystal plasticity FEM including geometrically necessary dislocations*. Acta Materialia, 2006. **54**(8): p. 2169-2179.
104. Beyerlein, I.J. and C.N. Tomé, *A dislocation-based constitutive law for pure Zr including temperature effects*. International Journal of Plasticity, 2008. **24**(5): p. 867-895.
105. Hansen, B.L., et al., *A dislocation-based multi-rate single crystal plasticity model*. International Journal of Plasticity, 2013. **44**(0): p. 129-146.
106. Moulinec, H., P. Suquet, and C.R. Acad, Sci. Paris II, 1994. **318**: p. 1417.
107. Moulinec, H. and P. Suquet, *A numerical method for computing the overall response of nonlinear composites with complex microstructure*. Computer Methods in Applied Mechanics and Engineering, 1998. **157**(1-2): p. 69-94.
108. A. Lebensohn, R., *N-site modeling of a 3D viscoplastic polycrystal using Fast Fourier Transform*. Acta Materialia, 2001. **49**(14): p. 2723-2737.
109. Lebensohn, R.A., A.K. Kanjarla, and P. Eisenlohr, *An elasto-viscoplastic formulation based on fast Fourier transforms for the prediction of micromechanical fields in polycrystalline materials*. International Journal of Plasticity, 2012. **32-33**(0): p. 59-69.
110. Eisenlohr, P., et al., *A spectral method solution to crystal elasto-viscoplasticity at finite strains*. International Journal of Plasticity, 2013. **46**(0): p. 37-53.
111. Prakash, A. and R.A. Lebensohn, *Simulation of micromechanical behavior of polycrystals: finite elements versus fast Fourier transforms*. Modelling and Simulation in Materials Science and Engineering, 2009. **17**(6): p. 064010.
112. DAMASK. *Düsseldorf Advanced Material Simulation Kit*. Available from: <http://damask.mpic.de/>.
113. Fjeldly, A. and H.J. Roven, *Observations and calculations on mechanical anisotropy and plastic flow of an AlZnMg extrusion*. Acta Materialia, 1996. **44**(9): p. 3497-3504.
114. Li, S., O. Engler, and P. Van Houtte, *Plastic anisotropy and texture evolution during tensile testing of extruded aluminium profiles*. Modelling and Simulation in Materials Science and Engineering, 2005. **13**(5): p. 783.

115. Grytten, F., et al., *Evaluation of identification methods for YLD2004-18p*. International Journal of Plasticity, 2008. **24**(12): p. 2248-2277.
116. Barlat, F. and O. Richmond, *Prediction of tricomponent plane stress yield surfaces and associated flow and failure behavior of strongly textured f.c.c. polycrystalline sheets*. Materials Science and Engineering, 1987. **95**(0): p. 15-29.
117. Van Houtte, P., S.K. Yerra, and A. Van Bael, *The Facet method: A hierarchical multilevel modelling scheme for anisotropic convex plastic potentials*. International Journal of Plasticity, 2009. **25**(2): p. 332-360.
118. Choi, S.H., et al., *Macroscopic anisotropy in AA5019A sheets*. Acta Materialia, 2000. **48**(8): p. 1853-1863.
119. Barlat, F., et al., *Linear transformation-based anisotropic yield functions*. International Journal of Plasticity, 2005. **21**(5): p. 1009-1039.
120. Saai, A., et al., *Simulation of yield surfaces for aluminium sheets with rolling and recrystallization textures*. Computational Materials Science, 2013. **67**(0): p. 424-433.
121. Hershey, A., *The plasticity of an isotropic aggregate of anisotropic face centred cubic crystals*. Journal of Applied Mechanics, 1954. **21**: p. 241-249.
122. Hosford, W.F., *A Generalized Isotropic Yield Criterion*. Journal of Applied Mechanics, 1972. **39**(2): p. 607-609.
123. Karafillis, A.P. and M.C. Boyce, *A general anisotropic yield criterion using bounds and a transformation weighting tensor*. Journal of the Mechanics and Physics of Solids, 1993. **41**(12): p. 1859-1886.
124. Hill, R., *A Theory of the Yielding and Plastic Flow of Anisotropic Metals*. Proceedings of the Royal Society of London. Series A, Mathematical and Physical Sciences, 1948. **193**(1033): p. 281-297.
125. Hill, R., *Theoretical plasticity of textured aggregates*. Mathematical Proceedings of the Cambridge Philosophical Society, 1979. **85**(01): p. 179-191.
126. Hill, R., *A user-friendly theory of orthotropic plasticity in sheet metals*. International Journal of Mechanical Sciences, 1993. **35**(1): p. 19-25.
127. Hill, R., *Constitutive modelling of orthotropic plasticity in sheet metals*. Journal of the Mechanics and Physics of Solids, 1990. **38**(3): p. 405-417.
128. Barlat, F. and K. Lian, *Plastic behavior and stretchability of sheet metals. Part I: A yield function for orthotropic sheets under plane stress conditions*. International Journal of Plasticity, 1989. **5**(1): p. 51-66.
129. Barlat, F., D.J. Lege, and J.C. Brem, *A six-component yield function for anisotropic materials*. International Journal of Plasticity, 1991. **7**(7): p. 693-712.
130. Banabic, D., et al., *Non-quadratic yield criterion for orthotropic sheet metals under plane-stress conditions*. International Journal of Mechanical Sciences, 2003. **45**(5): p. 797-811.
131. Banabic, D., et al., *An improved analytical description of orthotropy in metallic sheets*. International Journal of Plasticity, 2005. **21**(3): p. 493-512.

-
132. Aretz, H. and F. Barlat, *New convex yield functions for orthotropic metal plasticity*. International Journal of Non-Linear Mechanics, 2013. **51**(0): p. 97-111.
 133. Inal, K., R.K. Mishra, and O. Cazacu, *Forming simulation of aluminum sheets using an anisotropic yield function coupled with crystal plasticity theory*. International Journal of Solids and Structures, 2010. **47**(17): p. 2223-2233.
 134. Kraska, M., et al., *Virtual material testing for stamping simulations based on polycrystal plasticity*. Computational Materials Science, 2009. **46**(2): p. 383-392.
 135. Vegter, H., et al., *Characterisation and modelling of the plastic material behaviour and its application in sheet metal forming simulation*, in *COMPLAS VII, 7th International Conference on Computational Plasticity 2003*: Barcelona, Spain.
 136. Gawad, J., et al., *Hierarchical multi-scale modeling of texture induced plastic anisotropy in sheet forming*. Computational Materials Science, 2013. **66**(0): p. 65-83.
 137. Khan, A.S. and S. Huang, *Continuum Theory of Plasticity*. 1995, New York: John Wiley & Sons.
 138. Hopperstad, O.S. and T. Børvik, *Plastic theory lecture notes*. 2012.
 139. Toth, L. and P. Van Houtte, *Discretization Techniques for Orientation Distribution Functions*. Textures and Microstructures, 1992. **19**(4): p. 229-244.

Article 1

Multi-level Modelling of Mechanical Anisotropy of Commercial Pure Aluminium Plate: Crystal Plasticity Models, Advanced Yield Functions and Parameter Identification

K. Zhang¹, B. Holmedal¹, O.S. Hopperstad^{2,3}, S. Dumoulin⁴, J. Gawad^{5,6},
A. Van Bael⁷, P. Van Houtte⁷

1. Department of Materials Science and Engineering, Norwegian University of Science and Technology, NO-7491 Trondheim, Norway

2. Department of Structural Engineering, Norwegian University of Science and Technology, NO-7491 Trondheim, Norway

3. Structural Impact Laboratory (SIMLab), Center for Research-based Innovation, Norwegian University of Science and Technology, NO-7491 Trondheim, Norway

4. SINTEF Materials and Chemistry, NO-7465 Trondheim, Norway

5. KU Leuven, Department of Computer Science, Celestijnenlaan 200A, 3001 Leuven, Belgium

6. AGH University of Science and Technology, Department of Applied Computer Science and Modeling, al. Mickiewicza 30, 30-059 Krakow, Poland

7. KU Leuven, Department of Metallurgy and Materials Engineering, Kasteelpark Arenberg 44 bus 2450, 3001 Heverlee, Belgium

International Journal of Plasticity, 2014

DOI: 10.1016/j.ijplas.2014.02.003

Multi-level Modelling of Mechanical Anisotropy of Commercial Pure Aluminium Plate: Crystal Plasticity Models, Advanced Yield Functions and Parameter Identification

Abstract

The mechanical anisotropy of an AA1050 aluminium plate is studied by the use of five crystal plasticity models and two advanced yield functions. In-plane uniaxial tension properties of the plate were predicted by the full-constraint Taylor model, the advanced Lamel model (Van Houtte et al., 2005) and a modified version of this model (Mánik and Holmedal, 2013), the viscoplastic self-consistent model and a crystal plasticity finite element method (CPFEM). Results are compared with data from tensile tests at every 15° from the rolling direction (RD) to the transverse direction (TD) in the plate. Furthermore, all the models, except CPFEM, were used to provide stress points in the five-dimensional deviatoric stress space at yielding for 201 plastic strain-rate directions. The Facet yield surface was calibrated using these 201 stress points and compared to in-plane yield loci and the planar anisotropy which were calculated by the crystal plasticity models. The anisotropic yield function Yld2004-18p (Barlat et al., 2005) was calibrated by three methods: using uniaxial tension data, using the 201 virtual yield points in stress space, and using a combination of experimental data and virtual yield points (i.e., a hybrid method). Optimal yield-surface exponents were found for each of the crystal plasticity models, based on calibration to calculated stress points at yielding for a random texture, and used in the latter two calibration methods. It is found that the last hybrid calibration method can capture the experimental results and at the same time ensure a good fit to the anisotropy in the full stress space predicted by the crystal plasticity models.

Keywords: crystal plasticity models; Yld2004-18p; Facet method; parameter identification; hierarchy multi-level modelling

1. Introduction

During thermo-mechanical processing, crystallographic texture will evolve in sheet metals. Texture, i.e. preferred crystallographic orientations of the grains, is the primary source of plastic anisotropy. This anisotropic plastic behaviour should be taken into account in finite element simulations of metal forming processes and in predictions of sheet formability.

Two main approaches exist to describe the plasticity of polycrystalline metallic metals. In the first, a phenomenological yield function is used. The Tresca (1864) and the von Mises (1913) yield criteria are widely used for isotropic materials. Hill (1948) proposed a quadratic yield function for materials with orthotropic symmetry, while Hosford (1972) introduced a non-quadratic yield function with a variable exponent for isotropic polycrystalline metals. Based on full-constraint (FC) Taylor model calculations of metals with random textures, the exponent was suggested as 6 and 8 for body-centered cubic (BCC) and face-centered cubic (FCC) metals, respectively. This criterion was then generalized to anisotropic materials by Hosford (1979). Barlat and Lian (1989) further extended Hosford's criterion. Later on, Barlat et al. (1991, 1997, 2003a, 2005), Karafillis and Boyce (1993), Banabic et al. (2003, 2005) and Aretz and Barlat (2013) proposed yield functions, where anisotropy is introduced by means of linear transformations of the stress tensor. A detailed overview of linear transformation-based yield functions can be found in Barlat et al. (2007). Nowadays, phenomenological yield functions are commonly used in finite element simulations by the sheet forming industry. One drawback by applying a flexible yield function is that a significant number of material tests is required (Barlat et al., 2005). Among the linear transformation-based yield functions, the Yld2004-18p criterion, proposed by Barlat et al. (2005) and implemented by Yoon et al. (2006) into a finite element code, has been proven as an accurate and flexible yield function capable of predicting six or eight ears in deep drawing of aluminium plates. Due to severe experimental limitations, a fundamental problem with the phenomenological approach is that most of the stress space is left unexplored when fitting the parameters of the yield function.

The other approach is to use polycrystal plasticity models. The oldest one was proposed by Sachs (1928) with the iso-stress assumption for all grains in the polycrystal representative volume element. In contrast, the full-constraint Taylor model (Taylor, 1938; Bishop and Hill, 1951 a,b) assumes that each grain experiences the same deformation as the aggregate, and the deformation is accommodated by at least five slip systems according to the principle of maximum plastic work or the complementary minimum principle, which follows from the yield criterion at the slip system level. Some relaxed-constraint Taylor models have also been developed to increase the freedom of single grains (Kocks and Chandra, 1982; Van Houtte, 1982, 1988). The Lamel model (Van Houtte et al., 1999, 2002) is also a relaxed-constraint Taylor model particular for the rolling process which considers two grains at the same time. Since the model considers a pair of grains, it is called a two-site model.

Over the past few decades, materials scientists have become more aware of the important role played by the distribution and connectivity of different grain boundary types in governing various mechanical and functional properties of materials (Patala et al., 2012). It has been shown that the grain boundary can be of importance to texture and microstructure evolution during deformation (Chang et al., 2010). Grain boundary

characteristics can be expressed by five degrees of freedom, i.e., the misorientation between the two neighbouring grains (three parameters) and the boundary plane normal (two parameters). It is now possible to obtain complete three-dimensional boundary information owing to the development of three-dimensional X-ray diffraction methods and automated serial sectioning methods combined with Electron Backscatter Diffraction (EBSD). The Taylor-type advanced Lamel model (ALAMEL) (Van Houtte et al., 2005) was developed to account for grain boundary orientations and general deformation modes. Recently, a modified version has been suggested, taking into account the so-called Type III strain constraint relaxation (Mánik and Holmedal, 2013). There are also other similar N -site Taylor-type models, such as the GIA model (Crumbach et al., 2001) and the N -‘stack’ model (Arul Kumar et al., 2011). In these N -site rate-independent crystal plasticity models, the local interaction at the grain boundary is introduced by relaxation of strain components and stress equilibrium is partially obtained.

Another popular class of polycrystal plasticity models is based on the self-consistent approach, originally proposed by Kröner (1958) for the elastic case and later extended to elastoplasticity (Hill, 1965) and viscoplasticity (Hutchinson, 1976). The viscoplastic self-consistent (VPSC) model regards each grain of the polycrystalline material as an ellipsoidal inclusion embedded in a homogeneous effective medium whose mechanical response corresponds to the volumetric average of all grains. Among various self-consistent plasticity models, the VPSC model developed by Molinari et al. (1987), and extended by Lebensohn and Tomé (1993, 1994) to account for anisotropy, has been widely used to simulate large strain behaviour and texture evolution. In addition to various first-order linearization schemes, a second-order approximation scheme is also available now (Lebensohn et al., 2007).

Since it was first introduced by Peirce et al. (1982), the crystal plasticity theory implemented in the finite element method (CPFEM) has matured into a whole family of constitutive and numerical formulations that has been applied to a broad variety of crystal mechanics problems (Roters et al., 2010). The CPFEM has both theoretical and practical advantages. Firstly, grains are represented by single or multiple elements where both stress equilibrium and strain compatibility are fulfilled at the boundaries. Secondly, complex boundary conditions are easily specified in the FEM code. Hence, the CPFEM is applicable to simulations of engineering processes. One main drawback of CPFEM is the huge computational time cost (Dumoulin et al., 2009). Recently, a full-field method based on the Fast Fourier Transform algorithm has been developed for polycrystal plasticity (Lebensohn, 2001; Lebensohn et al., 2012; Eisenlohr et al., 2013). Compared with the CPFEM, it shows much higher time efficiency (Prakash and Lebensohn, 2009).

To combine the strength of phenomenological yield functions and crystal plasticity models, hierarchical modelling schemes have recently become of interest. In such context, virtual experiments are performed using crystal plasticity models to provide data points; advanced yield functions are then identified using virtual experimental data. Barlat et al. (2005) used experimental data plus some out-of-plane stress points calculated by the VPSC model to identify the parameters of the Yld2004-18p yield function. Grytten et al. (2008) evaluated different methods for identifying the parameters of the Yld2004-18p yield function, including only experimental data, only virtual experiments with the FC-Taylor model and a combination of these methods. A similar study has also been done by Zhang et al. (2012). The hierarchical modelling approach has also been used by Inal et al. (2010), An et al. (2011) and Saai et al. (2013) with different yield functions or crystal plasticity models. Extra data provided by crystal plasticity calculations, in addition to the experimental, is believed to improve the fitting of yield functions, although Grytten et al. (2008) claimed that fitting only to experimental data was most reliable for one case where the FC-Taylor model was employed.

Another well-established hierarchical modelling scheme was proposed by Van Houtte et al. (2009), where the Facet yield surface and the FC-Taylor or the ALAMEL model are used. The Facet method (Van Houtte et al., 2009) applies convex plastic potentials in the stress and strain-rate spaces using the simple analytical Facet polynomials. Owing to the large number of coefficients, the Facet yield surface is optimal in combination with crystal plasticity models. The texture evolution occurring during deformation can optionally be captured by lower-scale crystal plasticity models and used to update the Facet yield function. This hierarchical modelling scheme has been successfully applied in simulations of cup drawing, see Van Houtte et al. (2011) and Gawad et al. (2010; 2013a).

Following the work of Grytten et al. (2008), identification methods for the Yld2004-18p yield function will be evaluated in this paper for an AA1050 aluminium plate, employing four different crystal plasticity models. The two ALAMEL-type models, the VPSC model and the FC-Taylor model are applied. A detailed comparison of the yield surfaces obtained by the different calibration methods will be made. The capability of crystal plasticity models to capture the experimentally observed mechanical anisotropy will be discussed. The Facet yield surface for the aluminium alloy AA1050 will be identified using these crystal plasticity models. A primary comparison will be made between the Facet and Yld2004-18p yield functions using the hierarchical modelling scheme. CPFEM will also be used here for modelling of the plastic anisotropy, although not extensively for fitting of the yield functions. Calibrations of the Yld2004-18p yield function by means of CPFEM has been presented recently by Saai et al. (2013) for plane stress states.

In Section 2 of this paper, the crystal plasticity models used in this study, namely the FC-Taylor model, the ALAMEL-type models, the VPSC model and CPFEM, will be summarized. In particular, a new misorientation fitting algorithm for ALAMEL-type models will be introduced. Virtual experiments performed to obtain uniaxial tensile properties and stress points on the yield surface are also described in this part. In Section 3, the advanced yield function Yld2004-18p and the Facet method are recalled, and relevant calibration methods are presented. Section 4 deals with material characterization and experimental mechanical tests. The results obtained from the experiments, the crystal plasticity simulations and the different calibration methods of the Yld2004-18p yield function and the Facet method are presented in Section 5 and discussed in Section 6. The main conclusions of the experimental and numerical study are provided in Section 7.

2. Crystal plasticity modelling

2.1 FC-Taylor model

A strain-rate independent FC-Taylor model was implemented and applied here. Elastic deformations are neglected. This model is briefly outlined below while more theoretical details can be found in the literature (Van Houtte, 1988; Van Houtte et al., 2005).

For a single crystal, the plastic deformation rate tensor \mathbf{D}^p is related to the shear rate on the slip systems by

$$\mathbf{D}^p = \sum_{\alpha} \frac{1}{2} \dot{\gamma}^{\alpha} (\mathbf{b}^{\alpha} \otimes \mathbf{v}^{\alpha} + \mathbf{v}^{\alpha} \otimes \mathbf{b}^{\alpha}) \quad (1)$$

where $\dot{\gamma}^{\alpha}$ is the shear rate of slip system α . Each slip system is uniquely defined by its slip plane normal \mathbf{v}^{α} and slip direction \mathbf{b}^{α} . Among all solutions of Eq. (1), the solution that minimizes the internal plastic power is defined as a valid basis solution, i.e.

$$\sum_{\alpha} |\dot{\gamma}^{\alpha}| = \min \quad (2)$$

By lack of other experimental data, it is assumed here that the critical resolved shear stress τ_c is identical for all slip systems.

The following yield criteria for the slip systems provide an equivalent alternative to Eq. (2)

$$|\tau^{\alpha}| = \left| \frac{1}{2} (\mathbf{b}^{\alpha} \otimes \mathbf{v}^{\alpha} + \mathbf{v}^{\alpha} \otimes \mathbf{b}^{\alpha}) : \mathbf{S}_{\xi} \right| \leq \tau_c \quad (3)$$

where τ^α is the resolved shear stress on slip system α and \mathbf{S}_ξ is the deviatoric Cauchy stress tensor of grain ξ . For FCC crystals where $\{111\}\langle 110\rangle$ are the dominant slip systems, Bishop and Hill (1951a; 1951b) have summarized 56 stress states which can activate 6 or 8 slip systems simultaneously, fulfilling Eq. (3). These stress states constitute the corners of the poly-slip yield surface in the five-dimensional deviatoric stress space. The deviatoric Cauchy stress tensor \mathbf{S} of the grain aggregates is calculated as the simple average of the stress response of each grain ξ , viz.

$$\mathbf{S} = \frac{1}{N} \sum_{\xi=1}^N \mathbf{S}_\xi \quad (4)$$

where N is the number of grains.

2.2 ALAMEL-type models

2.2.1 ALAMEL theory and additional Type III relaxation

The ALAMEL model was proposed by Van Houtte et al. (2005). Interactions between two neighbouring grains are taken into account by introducing strain constraint relaxations at the grain boundaries. A brief introduction to the ALAMEL model will be given in the following paragraphs for the sake of completeness. Comprehensive theoretical descriptions can be found in Van Houtte et al. (1999, 2005) and Mánik and Holmedal (2013).

Figure 1 shows parts of two neighbouring grains, denoted ‘grain 1’ and ‘grain 2’, respectively, which share the grain boundary segment AB. Region 1 and region 2, which belong to grain 1 and grain 2, respectively, are in the vicinity of AB. The two regions and the grain boundary segment compose an ALAMEL pair. A Cartesian coordinate system y_1, y_2, y_3 is attached to the grain boundary segment where the y_3 axis is along the normal direction (ND) of the boundary surface defined by the y_1, y_2 plane. This coordinate system is called the ‘grain boundary reference frame’ and is given by the Euler angles of its three axes with respect to the macroscopic frame. These Euler angles constitute the only microstructural description available in the ALAMEL model. If nothing else is stated, all vector and tensor components in this section are expressed in the grain boundary reference frame. Note that the ALAMEL model is invariant with respect to rotations of the reference system around the y_3 axis, while the modified version with the Type III relaxation is not.

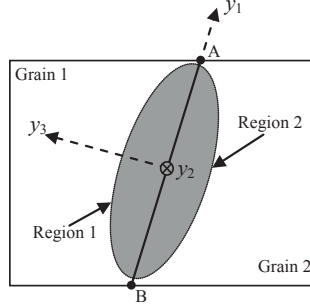


Figure 1 Schematic illustration of one ALAMEL pair consisting of Region 1 in Grain 1, Region 2 in Grain 2 and the grain boundary AB.

Three relaxations are considered, as illustrated in Figure 2, and denoted Type I, II and III. The velocity gradient \mathbf{l}_x felt by grain x ($x=1,2$) is expressed as

$$\mathbf{l}_1 = \mathbf{L} + \sum_{r=1}^2 \tilde{\mathbf{K}}_r \dot{\gamma}_r^{\text{RLX}} + \tilde{\mathbf{K}}_3 \dot{\gamma}_3^{\text{RLX}}, \quad \mathbf{l}_2 = \mathbf{L} - \sum_{r=1}^2 \tilde{\mathbf{K}}_r \dot{\gamma}_r^{\text{RLX}} + \tilde{\mathbf{K}}_3 \dot{\gamma}_3^{\text{RLX}} \quad (5)$$

where \mathbf{L} is the global velocity gradient tensor, $\dot{\gamma}_r^{\text{RLX}}$ is the relaxation shear rates and the tensors $\tilde{\mathbf{K}}_r$ are expressed as

$$\tilde{\mathbf{K}}_1 = \begin{bmatrix} 0 & 0 & 1 \\ 0 & 0 & 0 \\ 0 & 0 & 0 \end{bmatrix}, \quad \tilde{\mathbf{K}}_2 = \begin{bmatrix} 0 & 0 & 0 \\ 0 & 0 & 1 \\ 0 & 0 & 0 \end{bmatrix}, \quad \tilde{\mathbf{K}}_3 = \begin{bmatrix} 0 & 1 & 0 \\ 0 & 0 & 0 \\ 0 & 0 & 0 \end{bmatrix} \quad (6)$$

Then Eq. (5) is transformed into

$$\begin{aligned} \mathbf{d}_1 &= \sum_{\alpha} \frac{1}{2} \dot{\gamma}_1^{\alpha} (\mathbf{b}_1^{\alpha} \otimes \mathbf{v}_1^{\alpha} + \mathbf{v}_1^{\alpha} \otimes \mathbf{b}_1^{\alpha}) + \sum_{r=1}^2 \tilde{\mathbf{M}}_r \dot{\gamma}_r^{\text{RLX}} + \tilde{\mathbf{M}}_3 \dot{\gamma}_3^{\text{RLX}} \\ \mathbf{d}_2 &= \sum_{\alpha} \frac{1}{2} \dot{\gamma}_2^{\alpha} (\mathbf{b}_2^{\alpha} \otimes \mathbf{v}_2^{\alpha} + \mathbf{v}_2^{\alpha} \otimes \mathbf{b}_2^{\alpha}) - \sum_{r=1}^2 \tilde{\mathbf{M}}_r \dot{\gamma}_r^{\text{RLX}} + \tilde{\mathbf{M}}_3 \dot{\gamma}_3^{\text{RLX}} \end{aligned} \quad (7)$$

where \mathbf{d}_x is the symmetric part of \mathbf{l}_x and $\tilde{\mathbf{M}}_r$ is the symmetric part of $\tilde{\mathbf{K}}_r$. The internal plastic power due to slip is to be minimized for the two grains simultaneously, and, therefore, Eq. (2) is transformed into

$$\sum_{x=1}^2 \sum_{\alpha} |\dot{\gamma}_x^{\alpha}| = \min \quad (8)$$

in which the subscript x refers to the grains in the pair. This minimization, subject to the constraints defined in Eq. (7), is carried out by the simplex method. The deviatoric stresses in the two grains are computed by solving the following set of linear equations:

$$\begin{aligned}
 \frac{1}{2}(\mathbf{b}_1^\alpha \otimes \mathbf{v}_1^\alpha + \mathbf{v}_1^\alpha \otimes \mathbf{b}_1^\alpha) : \mathbf{S}^1 &= \tau_{c1} \text{sgn}(\dot{\gamma}_1^\alpha) & \text{if } \dot{\gamma}_1^\alpha \neq 0 \\
 \frac{1}{2}(\mathbf{b}_2^\alpha \otimes \mathbf{v}_2^\alpha + \mathbf{v}_2^\alpha \otimes \mathbf{b}_2^\alpha) : \mathbf{S}^2 &= \tau_{c2} \text{sgn}(\dot{\gamma}_2^\alpha) & \text{if } \dot{\gamma}_2^\alpha \neq 0 \\
 S_{13}^1 &= S_{13}^2 & \text{if } \dot{\gamma}_1^{\text{RLX}} \neq 0 \\
 S_{23}^1 &= S_{23}^2 & \text{if } \dot{\gamma}_2^{\text{RLX}} \neq 0 \\
 S_{12}^1 &= -S_{12}^2 & \text{if } \dot{\gamma}_3^{\text{RLX}} \neq 0
 \end{aligned} \tag{9}$$

where τ_{c1} and τ_{c2} are the critical resolved shear stress of grain 1 and grain 2, respectively. From Eq. (9) it can be shown that, as far as the shear stresses S_{13}^x and S_{23}^x are concerned, stress equilibrium is guaranteed at the interface. When the Type III relaxation occurs, S_{12}^x will have the same magnitude but opposite signs in the two grains. Thus, S_{12}^x in one ALAMEL cluster will not contribute to the internal plastic power.

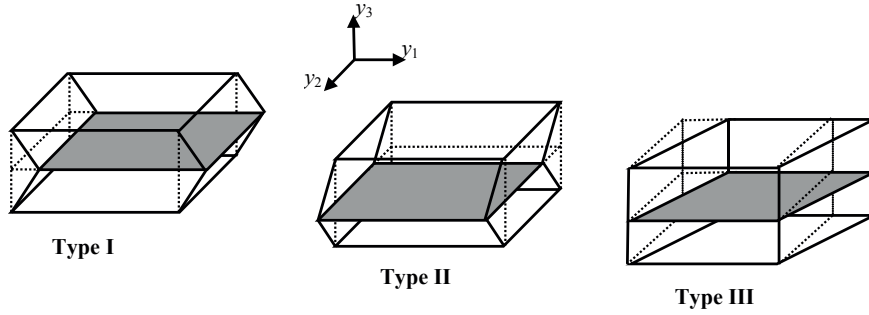


Figure 2 Illustration of Type I (L_{13}), Type II (L_{23}) and Type III (L_{12}) relaxation in the grain boundary frame of one ALAMEL pair. The grey face indicates the grain boundary, while Grain 1 and Grain 2 are positioned at the upper and lower sides of the boundary, respectively.

More details on the original ALAMEL model and the ALAMEL model with Type III relaxation can be found in Van Houtte et al. (2005) and Mánik and Holmedal (2013).

In the original implementation of the ALAMEL model (Van Houtte et al., 2005), ALAMEL pairs are created by random selection of a grain boundary interface orientation from the microstructure file and a random choice of two crystal orientations from the discretized orientation distribution functions (ODF). In this work, both the original ALAMEL, and the one with the additional Type III relaxation, denoted ALAMEL Type III in the following, have been implemented. Instead of randomly

choosing the ALAMEL pairs, a fitting procedure is proposed for obtaining the measured misorientation distribution function (MDF) which will be described in the following.

2.2.2 Grain boundary misorientation distribution in ALAMEL

When only the relative misorientation between crystallites is concerned, two-dimensional EBSD measurements are sufficient to provide a statistical description by suitably defined probability density functions (Zhu et al., 1999; Miodownik et al., 1999). This is also the case for the ALAMEL model, since the grain boundary inclination has been specified through Euler angles recorded in the microstructure file. The grain boundary MDF represents the number fraction vs. misorientation angle as measured by EBSD.

The MDF of the list of ALAMEL clusters can be obtained by calculating the misorientation angle of each pair and by converting all the misorientation angles into a continuous distribution. The difference between the MDF of the list of grains and the experimental one is called e_{MD} and expressed as

$$e_{\text{MD}} = \int_{\theta} |P - P^{\text{exp}}| d\theta \quad (10)$$

where θ is the misorientation angle, P is the MDF from ALAMEL, and P^{exp} is the experimental one. The fitting procedure starts with making ALAMEL pairs by randomly choosing two orientations from the input. Then the density function P and the error e_{MD} are computed. If the error e_{MD} is sufficiently small, $e_{\text{MD}} < e_{\text{MD}}^{\text{max}}$, then the solution fulfils the MDF requirement and can be used for further calculations. Otherwise, two pairs are randomly selected and two orientations, one from each pair, are interchanged. If the new value of e_{MD} is smaller than the previous one, the exchange of orientations will be recorded, else it is discarded. This process is repeated until the targeted accuracy is reached.

2.3 Viscoplastic self-consistent crystal plasticity model (VPSC)

The viscoplastic self-consistent model regards each grain of the polycrystal as an ellipsoidal inclusion embedded in a homogeneous effective medium whose mechanical response corresponds to the volumetric average of all grains. This assumption considers the long-range interaction between a single grain and the matrix.

Inspired by Eshelby (1957), the partitioning of strains between matrix and inclusions is computed by assuming that the matrix can be characterized by a uniform, effective compliance operator. Elasticity is neglected and the treatment of plasticity follows Eq. (1), where slip activity is derived from the resolved shear stress using a viscoplastic exponential law:

$$\dot{\gamma}^\alpha = \dot{\gamma}_0 \left| \frac{\tau^\alpha}{\tau_c^\alpha} \right|^{\frac{1}{m}} \text{sgn}(\tau^\alpha) \quad (11)$$

Here $\dot{\gamma}_0$ is a reference shearing rate, m is the instantaneous strain-rate sensitivity, τ^α is the resolved shear stress defined by Eq. (3), and τ_c^α will evolve during the plastic deformation of single grains.

Several formulations exist for the interaction equation that linearly relates stress and strain rates in the grain with the overall stress and strain rates of the effective medium, such as the secant approach (Hutchinson, 1976), the tangent approach (Lebensohn and Tomé, 1993) and the intermediate approximation with one adjustable parameter n^{eff} (Tomé, 1999). The last approximation approach gives a response of the polycrystal which lies in-between the stiff secant and the compliant tangent approaches. Further details about the VPSC are not given here, but can be found in the references (Lebensohn and Tomé, 1993, 1994; Tomé, 1999; Lebensohn et al., 2007).

2.4 Crystal plasticity finite element method (CPFEM)

The formulation of single crystal plasticity models is well documented by several authors (e.g. Kocks et al., 2000). CPFEM accounts for both short and long-range grain interactions in the polycrystal and ensures both stress equilibrium and strain compatibility, at least in a weak form. The model which has been implemented into the commercial finite element code LS-DYNA (LSTC, 2007) through a user subroutine is briefly described in the following.

The velocity gradient tensor \mathbf{L} is additively decomposed into symmetric and skew-symmetric parts:

$$\mathbf{L} = \mathbf{D} + \mathbf{W} \quad (12)$$

where \mathbf{D} is the symmetric deformation rate tensor and \mathbf{W} is the skew-symmetric spin rate tensor. The tensors \mathbf{D} and \mathbf{W} can be further decomposed into lattice and plastic parts:

$$\mathbf{D} = \mathbf{D}^e + \mathbf{D}^p \quad (13)$$

$$\mathbf{W} = \mathbf{W}^* + \mathbf{W}^p \quad (14)$$

where \mathbf{D}^e is the elastic deformation rate and \mathbf{D}^p is the plastic deformation rate due to crystallographic slip. The spin tensors \mathbf{W}^* and \mathbf{W}^p represent the lattice and plastic spins, respectively. The plastic deformation rate and spin tensors depend on the slip rates for the active slip systems by Eq. (1) and by

$$\mathbf{W}^p = \sum_{\alpha} \frac{1}{2} \dot{\gamma}^{\alpha} (\mathbf{b}^{\alpha} \otimes \mathbf{v}^{\alpha} - \mathbf{v}^{\alpha} \otimes \mathbf{b}^{\alpha}) \quad (15)$$

respectively, where the slip activity $\dot{\gamma}^{\alpha}$ is described by Eq. (11). The vectors \mathbf{b}^{α} and \mathbf{v}^{α} are not affected by crystallographic slip but will be rotated by the lattice spin \mathbf{W}^* as:

$$\dot{\mathbf{b}}^{\alpha} = \mathbf{W}^* \mathbf{b}^{\alpha}, \quad \dot{\mathbf{v}}^{\alpha} = \mathbf{W}^* \mathbf{v}^{\alpha} \quad (16)$$

A hypoelastic relation is used here and the rate of the Cauchy stress tensor $\boldsymbol{\sigma}$ is defined as

$$\dot{\boldsymbol{\sigma}} = \boldsymbol{\sigma}^{\nabla J} + \mathbf{W}^* \boldsymbol{\sigma} - \boldsymbol{\sigma} \mathbf{W}^* \quad (17)$$

where the Jaumann stress rate tensor $\boldsymbol{\sigma}^{\nabla J}$ is computed as

$$\boldsymbol{\sigma}^{\nabla J} = \mathfrak{R} \left[\hat{\mathbf{C}} : (\mathfrak{R}^T \mathbf{D}^e \mathfrak{R}) \right] \mathfrak{R}^T \quad (18)$$

In Eq. (18), $\hat{\mathbf{C}}$ is the fourth-order elasticity tensor which is constant in the co-rotational lattice frame, whereas \mathfrak{R} is the rotation tensor from the initial crystal frame to the current co-rotational frame and is updated as

$$\dot{\mathfrak{R}} = \mathbf{W}^* \mathfrak{R} \quad (19)$$

Work hardening is captured at the slip system level by the slip resistance functions τ_c^{α} in Eq. (11). The hardening rule used in this work, assumes that the critical resolved shear stress, τ_c^{α} , equals τ_0 initially, and then evolves according to

$$\dot{\tau}_c^{\alpha} = \sum_{\beta} h^{\alpha\beta} |\dot{\gamma}^{\beta}| \quad (20)$$

where $h^{\alpha\beta}$ is the instantaneous strain hardening matrix. In this work, $h^{\alpha\beta}$ is described phenomenologically by a Voce-type rule:

$$h^{\alpha\beta} = \left[\theta_1 + \left(\theta_0 - \theta_1 + \frac{\theta_0 \theta_1}{\tau_1} \Gamma \right) \exp \left(-\frac{\theta_0}{\tau_1} \Gamma \right) \right] \left[q_0 + (1 - q_0) \delta^{\alpha\beta} \right] \quad (21)$$

where θ_0 is the initial hardening rate, while θ_1 and τ_1 describe the asymptotic hardening. Γ is the accumulated plastic shear strain defined by

$$\dot{\Gamma} = \sum_{\alpha} |\dot{\gamma}^{\alpha}| \quad (22)$$

The parameter q_0 represents latent hardening, while $\delta^{\alpha\beta}$ is the Kronecker delta function.

2.5 Virtual experiments by crystal plasticity models

A total of 1000 orientations selected from the measured crystallographic texture, i.e. an aggregate of $N=1000$ grains, were used as input to the five crystal plasticity models described above. The N representative orientations out of texture measurement can be gathered either by random selection from scanning points in the EBSD measurement or by discretization techniques for ODFs calculated based on X-ray diffraction measurement (Toth and Van Houtte, 1992). To characterize the quality of the selected N orientations in representing the measured texture, the normalized difference texture index, ID_N , proposed by Van Houtte (Van Houtte et al., 2005) for comparing two textures, is adopted here as

$$ID_N = \frac{\int (f^R(g) - f^{\text{exp}}(g))^2 dg}{\int (f^{\text{exp}}(g))^2 dg} \quad (23)$$

where $f^R(g)$ and $f^{\text{exp}}(g)$ are the ODFs of the selected N orientations and the experimental measurements, respectively. The integral is taken over the entire orientation space. This criterion does not only consider the major texture components, but also the minor ones. Ideally, ID_N should be equal to zero, which means that the texture defined by the N orientations is identical to the experimental one, but practically this is hardly ever the case. Since plastic anisotropy can be significantly affected by a large number of minor texture components, ID_N should be kept at a very low level.

In this work, the texture was measured by EBSD which covered more than 8000 grains and $N=1000$ orientations were randomly selected from all scanning points. The functions $f^{\text{exp}}(g)$ and $f^R(g)$ were computed using the series expansion method with $l_{\text{max}} = 22$ and $\psi_0 = 5^\circ$ (see Engler and Randle, 2009, for further details). The orientation selection used here has $ID_N = 4.42 \times 10^{-3}$, which indicates a rather good representation of the experimental ODF.

The list of grains used for the virtual experiments with ALAMEL or ALAMEL Type III consists of 500 ALAMEL clusters. The MDF fitting, which has been discussed in Section 2.2.2, was used to obtain $e_{\text{MD}}^{\text{max}} = 6.5 \times 10^{-3}$.

For the VPSC model, the instantaneous strain-rate sensitivity m in Eq. (11) was set equal to 0.02 and an intermediate linearization with $n^{\text{eff}} = 10$ was used.

For the CPFEM model, a cube of volume $1.5 \times 1.5 \times 1.5 \text{ mm}^3$ was considered as the representative volume (RVE), and Voronoi tessellation (Quey et al., 2011) was used to generate a random grain structure made of 1000 grains. It was then discretized with 64000 cubic eight-node element with eight integration points, i.e. about 64 elements per grain in average, as shown in Figure 3. This mesh represents the microstructure of the fully-recrystallized AA1050 sheet with a high resolution. In order to reproduce the experimental conditions during tensile testing in CPFEM, periodic boundary conditions were applied on the faces of the RVE. To simulate tensile testing in different directions with respect to the RD, the mesh and the boundary conditions remained fixed in space, while the texture was rotated. This is a reasonable approach for the actual equi-axed grain structure. The material parameters were fitted through trial and error to the stress-strain curve of the same AA1050 sheet along the rolling direction. All parameters are given in Table 1. Uniaxial tensile tests were simulated by CPFEM with loading rates at 10^{-2} s^{-1} . The Lankford coefficients (r -values) were determined between 5% and 10% elongations, whereas yield stresses were determined at 0.2 MPa specific plastic work which was calculated based on the predicted stress-strain curves.

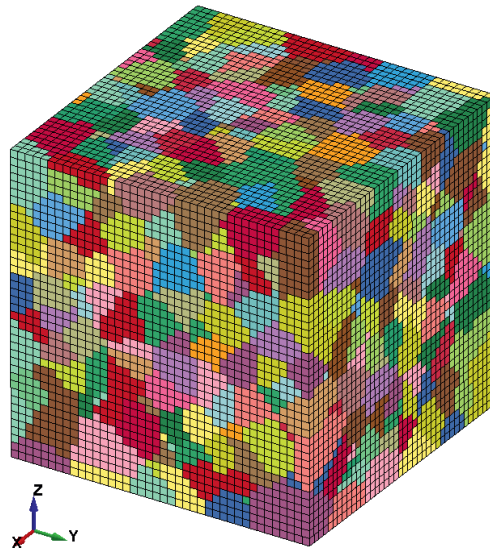


Figure 3 CPFEM model with 64000 eight-node elements representing a random microstructure with 1000 grains.

Table 1 Material parameters for CPFEM simulations of AA 1050.

$\dot{\gamma}_0$	m	θ_0	θ_1	τ_0	τ_1	q_0	\hat{C}_{11}	\hat{C}_{12}	\hat{C}_{44}
		(MPa)	(MPa)	(MPa)	(MPa)		(GPa)	(GPa)	(GPa)
10^{-3}	0.02	300	16.5	12.9	138.8	1.0	106.75	60.41	28.34

Two types of virtual experiments were conducted. In the first case, in-plane uniaxial tension tests at different angles from RD to TD were simulated by the five CP models. The r -value and the normalized yield stress computed by the CP models were then compared to experimental data to evaluate the quality of the predictions. The calculation of the r -value and the yield stress for an in-plane uniaxial tensile test using aggregate models, i.e. FC-Taylor, ALAMEL-type models and VPSC, is done by imposing strain-rate components which are iteratively adjusted until the average stress is uniaxial along the tensile axis. In the second case, 201 stress states at initial yielding in the five-dimensional strain-rate space were calculated with the FC-Taylor, ALAMEL, ALAMEL Type III and VPSC models. A uniform distribution of strain-rate directions is convenient, since the deformation rate tensor is the prescribed input of these models. However, the yield points will not be evenly distributed in stress space, but will be condensed where the gradient of the yield surface changes most rapidly. This provides a natural adaptive distribution of the stress directions.

The problem of obtaining a uniform distribution of strain-rate directions can be reduced to finding a uniform distribution of points on a five-dimensional hypersphere. However, such a uniform distribution is hard to find in higher dimensions, even by numerical iteration schemes. Van Houtte et al. (2009) proposed to extend the Miller indices from three-dimensional to five-dimensional spaces by adding two extra indices so that the strain-rate directions can be represented by five-dimensional Miller indices. This approach is adopted here. A total of 402 directions could be made from [00001], [00011], [00111], [01111], [11111] and the additional [11113], plus all permutations, plus those obtained by changing the sign of one or several of them. Since the stress differential effect was not considered, only one-half of these, i.e. 201 directions, were used when fitting the parameters of the Yld2004-18p and Facet yield surfaces.

For fitting the exponent of the Yld2004-18p yield surface to the various CP models, 5832 random crystal orientations together with 1241 strain-rate directions (generated in the same way as above) will be employed. Stress states along 1241 strain-rate directions at yielding for AA1050 were also calculated for the purpose of evaluating Facet fittings based on 201 points.

3. Continuum yield functions and fitting methods

3.1 Yld2004-18p and its three fitting procedures

The analytical yield function, denoted Yld2004-18p, was proposed by Barlat et al. (2005) as

$$\bar{\sigma}(\boldsymbol{\sigma}) = \frac{1}{4^{1/a}} \left(|S'_1 - S_1''|^a + |S'_1 - S_2''|^a + |S'_1 - S_3''|^a + |S'_2 - S_1''|^a + |S'_2 - S_2''|^a + |S'_2 - S_3''|^a + |S'_3 - S_1''|^a + |S'_3 - S_2''|^a + |S'_3 - S_3''|^a \right)^{1/a} \quad (24)$$

where $\bar{\sigma}$ is the equivalent stress and a is the exponent of the yield function. S'_i and S''_i , $i = 1, 2, 3$, are the principal values of the tensors $\mathbf{S}' = \mathbf{C}'\mathbf{S}$ and $\mathbf{S}'' = \mathbf{C}''\mathbf{S}$, where \mathbf{S} is the stress deviator. Using Voigt notation, the two fourth-order transformation tensors are expressed in the principal axes of anisotropy as

$$\mathbf{C}' = \begin{bmatrix} 0 & -c'_{12} & -c'_{13} & 0 & 0 & 0 \\ -c'_{21} & 0 & -c'_{23} & 0 & 0 & 0 \\ -c'_{31} & -c'_{32} & 0 & 0 & 0 & 0 \\ 0 & 0 & 0 & c'_{44} & 0 & 0 \\ 0 & 0 & 0 & 0 & c'_{55} & 0 \\ 0 & 0 & 0 & 0 & 0 & c'_{66} \end{bmatrix}, \quad \mathbf{C}'' = \begin{bmatrix} 0 & -c''_{12} & -c''_{13} & 0 & 0 & 0 \\ -c''_{21} & 0 & -c''_{23} & 0 & 0 & 0 \\ -c''_{31} & -c''_{32} & 0 & 0 & 0 & 0 \\ 0 & 0 & 0 & c''_{44} & 0 & 0 \\ 0 & 0 & 0 & 0 & c''_{55} & 0 \\ 0 & 0 & 0 & 0 & 0 & c''_{66} \end{bmatrix} \quad (25)$$

In addition to the exponent a , the yield function has 18 coefficients which are used to describe the plastic anisotropy of the material. Among these, 14 parameters are related to the in-plane properties of the sheet, while the remaining 4 parameters are associated with out-of-plane properties (Yoon et al., 2006). A possible approach to determine the in-plane parameters is to use data from uniaxial tension tests at every 15° from RD to TD, where the directional yield stresses and the r -values are measured. The out-of-plane properties cannot easily be measured for sheet materials, but they can either be set to their isotropic values as a first approximation or calculated by crystal plasticity models when the crystallographic texture is known. When the coefficients are all equal to one, this yield function reduces to Hershey's isotropic yield function (1954).

The main role of the exponent a of the yield function is to determine the radius of curvature of the corners of the yield locus, which most often cannot be properly resolved by mechanical tests due to the limited number of experimentally available strain paths. Alternatively, the exponent a can be fitted through a multi-scale modelling scheme, i.e. using CP models to provide stress points along uniformly distributed strain-rate directions. In general anisotropic cases the curvature of the yield surface can be different in different corners in the five-dimensional deviatoric stress space. The value

of a corresponding to the best fit of the isotropic case with a random texture will be used. The case when the 18 anisotropy coefficients are all set to unity corresponds to a random texture. A total of 5832 almost uniformly distributed orientations were applied, for which 1241 strain-rate directions were prescribed and the FC-Taylor, ALAMEL, ALAMEL Type III and VPSC models were run to generate corresponding stress points. The exponent a was chosen so that the error function

$$e(a) = \sum_{q=1}^{N_{cp}} \left(\bar{\sigma}(\mathbf{S}_q^{\text{cp}}) - 1 \right)^2 \quad (26)$$

is minimised by a least squares method. Here N_{cp} is the number of yield points from the virtual experiments and takes the value 1241. \mathbf{S}_q^{cp} is the normalized deviatoric stress tensor at yielding in a virtual experiment, where the yield stress obtained in a virtual uniaxial tension test in the RD is used for normalization.

In the following, experimental data, virtual experimental data, i.e. stress states at yielding along 201 strain directions, and their combination will be used to determine the coefficients of the Yld2004-18p yield function. It is assumed that the equivalent stress $\bar{\sigma}$ equals unity at yielding. The experimental yield stresses at every 15° from RD to TD were normalized by the yield stress in the RD direction. Stress states along 201 strain-rate directions at yielding were normalized by the yield stress for a virtual uniaxial tension test along the RD. The error function to be minimized by a non-linear least squares method is

$$e(c'_{ij}, c''_{ij}) = \sum_{p=1}^{N_{\text{exp}}} \left(w^{\text{YS}} \left(\frac{\sigma_p^{\text{pr}}}{\sigma_p^{\text{exp}}} - 1 \right)^2 + w^{\text{R}} \left(\frac{r_p^{\text{pr}}}{r_p^{\text{exp}}} - 1 \right)^2 \right) + \sum_{q=1}^{N_{cp}} w^{\text{cp}} \left(\bar{\sigma}(\mathbf{S}_q^{\text{cp}}) - 1 \right)^2 + w^0 \left(\bar{\sigma}(\boldsymbol{\sigma}_0) - 1 \right)^2 \quad (27)$$

where N_{exp} is the number of in-plane directional uniaxial tensile tests (equal to 7 in this work) and N_{cp} is equal to 201 in the following of this work. σ_p^{exp} and r_p^{exp} are the normalized yield stress and the r -value for direction p from the experiments, while σ_p^{pr} and r_p^{pr} are the counterparts predicted from the yield function (see Barlat et al., 2005 for details). \mathbf{S}_q^{cp} is the normalized deviatoric stress tensor at yielding from a virtual experiment, while $\boldsymbol{\sigma}_0$ is the unit stress tensor corresponding to uniaxial tension along the RD. The term containing $\boldsymbol{\sigma}_0$ in Eq. (27) is added to force yielding to occur at an equivalent stress equal to unity in uniaxial tension along the RD. Finally, w^{YS} , w^{R} , w^{cp}

and w^0 are weighting factors for the different contributions to the error function. By selecting different sets of weighting factors, different fitting procedures are obtained. Three procedures for fitting the anisotropy parameters of Yld2004-18p are evaluated while keeping the exponent a constant.

The first approach is to use only the seven yield stresses and the seven r -values measured from the uniaxial tensile tests to fit the 14 in-plane anisotropy parameters. The coefficients governing the out-of-plane properties, i.e. c'_{44} , c'_{55} , c''_{44} , c''_{55} , were then set to unity. Since only experimental data are used, this approach is termed 'Fit_Exp.'. As suggested by Barlat et al. (2005), the yield stress should be given a higher weight than the r -values in uniaxial tension, due to the smaller variation range of the normalized yield stress and higher fitting accuracy. Two sets of weights will be used for this fitting procedure, as shown in Table 2, where w^R has different values, and the resulting parameter sets will be called 'Fit_Exp.-1' and 'Fit_Exp.-2', respectively.

Table 2 Weights used for the different calibrations of Yld2004-18p.

Calibration	w^{YS}	w^R	w^{cp}	w^0
Fit_Exp.-1	1.0	0.25	0.0	10
Fit_Exp.-2	1.0	0.1	0.0	10
Fit_FC-Taylor	0.0	0.0	1.0	20
Fit_ALAMEL	0.0	0.0	1.0	20
Fit_ALAMEL Type III	0.0	0.0	1.0	20
Fit_VPSC	0.0	0.0	1.0	20
Fit_Exp.+FC-Taylor	1.0	0.25	0.04	10
Fit_Exp.+ALAMEL	1.0	0.25	0.04	10
Fit_Exp.+ALAMEL Type III	1.0	0.25	0.04	10
Fit_Exp.+VPSC	1.0	0.25	0.04	10

In the second approach, only the 201 stress states at yielding from the virtual experiments with the CP models are used to fit all 18 parameters of Yld2004-18p, i.e. anisotropic out-of-plane properties are assumed. This approach is termed ‘Fit_CP’, where CP could be FC-Taylor, ALAMEL, ALAMEL Type III or VPSC. The weights are also shown in Table 2 with the title ‘Fit_CP’.

The third fitting approach combines contributions from both the experimental and virtual experimental results, and is denoted ‘Fit_Exp.+CP’. The weights are shown in Table 2. The weights are determined so that the experimental and virtual experimental results will give similar contributions to the total error.

The exponent a is taken as 8 for the first fitting procedure, whereas for ‘Fit_CP’ and ‘Fit_Exp.+CP’ the exponent a takes the value that best fits the isotropic case with a random texture for the corresponding CP models.

3.2 The Facet method

Van Houtte et al. (2009) recently proposed an analytical expression describing the dual plastic potentials, known as the Facet method. It provides a yield surface description

$$\bar{\sigma}(\boldsymbol{\sigma}) \equiv \psi(\mathbf{S}) = \left(\sum_{k=1}^K \lambda_k (\mathbf{S} : \mathbf{D}_k^p)^n \right)^{1/n}, \quad \lambda_k \geq 0 \quad (28)$$

where the exponent n is an even integer and λ_k are weights to be determined. Here \mathbf{D}_k^p are plastic strain rates used for the K predictions that are applied to fit $\psi(\mathbf{S})$ at yielding. The weights λ_k can be determined uniquely, so that the yield surface fits all stress points \mathbf{S}_k for the corresponding strain rates \mathbf{D}_k^p (from the virtual experiments), and with a sufficiently large exponent n , all the weights λ_k remain positive. However, at lower exponents points are left out in order to have positive weights λ_k , i.e. a convex yield surface. The larger the angle between the stress tensors, the smaller the exponent can be, without loss of convexity (Van Houtte et al., 2009). Commonly the strain rates are prescribed as uniformly distributed, and then the stress points tend to cluster in the corners of the yield surface causing the need of a very high exponent. The result is a very faceted, poor yield surface. Hence, Van Houtte et al. (2009) proposed to first fit the dual plastic potential in the strain-rate space to the virtual experiments, and then fit the yield surface to this fitted potential. The dual strain-rate potential $\tilde{\psi}(\mathbf{D}^p)$ can be expressed by a similar Facet polynomial

$$\begin{aligned}\tilde{\psi}(\mathbf{D}^p) &= \left(\sum_{k=1}^K \tilde{\lambda}_k (\mathbf{S}_k : \mathbf{D}^p)^{\tilde{n}} \right)^{1/\tilde{n}}, \quad \tilde{\lambda}_k \geq 0 \\ \mathbf{S} &= \frac{\partial \tilde{\psi}}{\partial \mathbf{D}^p}\end{aligned}\quad (29)$$

The weights $\tilde{\lambda}_k$ can be uniquely fitted to the virtual experiments by a similar procedure as for the yield surface (Van Houtte et al., 2009). Since the strain rates are almost uniformly distributed, the exponent \tilde{n} , which is an even integer, can be chosen much smaller than for the direct fit in the stress space and still fit most of the virtual experiments. The weights $\tilde{\lambda}_k$ determine the contributions to the plastic potential from the stresses \mathbf{S}_k (Gawad et al., 2013a), and must be non-negative to guarantee convexity. Finally, an approximately uniform distribution of stress directions is used for the fit of the yield surface $\psi(\mathbf{S})$ to stresses derived from the plastic potential $\tilde{\psi}(\mathbf{D}^p)$. More details about parameter identification can be found in Van Houtte et al. (2009) and Gawad et al. (2013a).

In this paper, the FC-Taylor, ALAMEL, ALAMEL Type III and VPSC models are used to provide stress tensors at yielding for $K = 201$ strain modes as described in Section 2.5. After having calculated deviatoric stress points for the 201 strain-rate tensors, the plastic potential $\tilde{\psi}(\mathbf{D}^p)$ is first identified in the strain-rate space. Then, the Facet function in stress space $\psi(\mathbf{S})$ is fitted to 201 deviatoric stress points that are obtained from $\tilde{\psi}(\mathbf{D}^p)$.

The exponent \tilde{n} of $\tilde{\psi}(\mathbf{D}^p)$ with the same set of 201 strain-rate directions as presented here, was empirically suggested to be 6 (Van Houtte et al., 2009). The exponent will influence the shape of the Facet yield surface. From the work of Hosford (1972), it is known that the exponent of the yield function is material dependent. Hence, the exponents \tilde{n} and n should be optimised in a quantitative manner. The approach proposed here is that $\tilde{\psi}(\mathbf{D}^p)$ and $\psi(\mathbf{S})$ are first calibrated based on the 201 points. Different exponents \tilde{n} and n are tested. The potential $\psi(\mathbf{S})$ is then examined for a higher number of virtual experiments based on 1241 uniformly distributed \mathbf{D}^p . The optimal exponent n of $\psi(\mathbf{S})$ should minimize the error defined as

$$e(n) = \sum_{i=1}^{1241} |\psi(\mathbf{S}_i) - 1| \quad (30)$$

where the deviatoric stress tensors at yielding, S_i , here are normalized by the tensile yield stress in the RD in a virtual experiment. The exponents \tilde{n} and n are varied as even numbers in the range from 6 to 16 in this work. It is noted that $e(n)$ also depends on \tilde{n} due to the fitting procedure.

4. Material characterization

A commercial purity aluminium AA1050 sheet was studied. The microstructure, including texture, grain size and MDF, is used as input for CP calculations, while mechanical data are used for several purposes. Firstly, they are the basis for quantitative examinations of the capability of the CP models in predicting realistic plastic anisotropy. Secondly, these data are input to some of the fitting procedures used for the Yld2004-18p yield criterion, as described in Section 3.1.

The material was received as rolled sheets with length 2000 mm (along RD), width 1000 mm (along TD) and thickness 1.5 mm. The measured chemical composition is shown in Table 3. Uniaxial tensile samples at every 15° from RD to TD (seven directions) as well as samples for microstructure characterization were cut from the sheet. Before any tests or characterization, samples were annealed in salt bath at 390°C for 60 min to achieve a fully recrystallized state. A Zeiss ULTRA 55 FESEM equipped with a Nordif digital EBSD detector and TSL OIM4 EBSD software was used for characterization of the microstructure with a step size of $4\ \mu\text{m}$ covering approximately $15\ \text{mm}^2$. An EBSD scan of the microstructure is shown in Figure 4. The ODF is shown in Figure 5, where the cube texture is dominating with some Brass components present. The distribution of the misorientation across grain boundaries was also generated by the OIM software. The measured MDF is shown in Figure 6 with 5° binning steps. The average grain size determined from EBSD grain maps is $150\ \mu\text{m}$.

Table 3 Chemical composition of AA1050 (wt%).

Si	Fe	Zn	Ti	Al	Others
0.058	0.438	0.01	0.01	99.442	<0.043

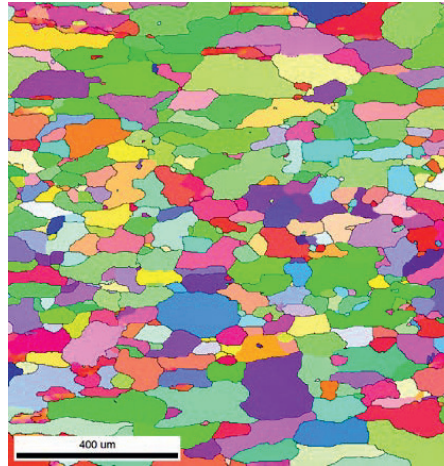


Figure 4 Microstructure of AA1050 sample after annealing, RD-ND section.

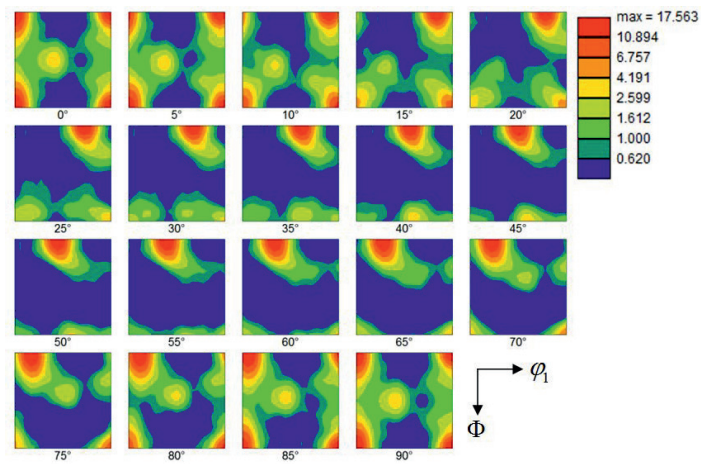


Figure 5 Orientation distribution function (ODF) (constant φ_2 sections) of commercial pure aluminium AA1050 after annealing, measured by EBSD technique.

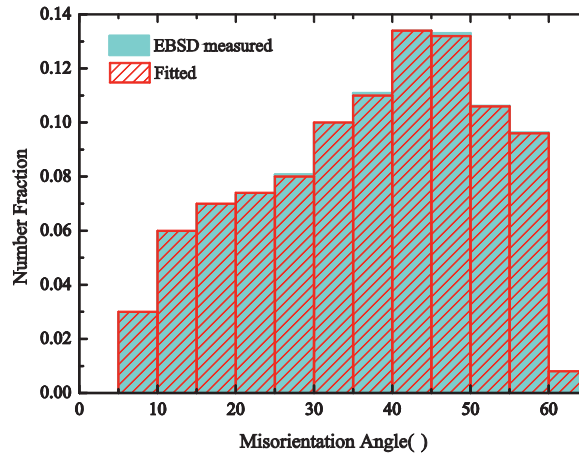


Figure 6 Misorientation distribution function (MDF) across grain boundaries measured by EBSD of fully recrystallized AA1050 sheet and MDF fitting for ALAMEL.

The uniaxial tensile samples have a uniform section with a gauge length of 50 mm and a width of 12.5 mm. The experiments were carried out at a nominal strain rate of $2 \times 10^{-4} \text{ s}^{-1}$. In the 0° (RD), 60° and 90° (TD) directions, two parallel tests were carried out, while the number of parallel tests was three in the other directions.

The r -value is determined following the ASTM Standard E517-00 (2010), i.e. it is measured using two extensometers: one attached in the longitudinal direction; and the other in the transverse direction. Employing the plastic incompressibility condition, the r -value is computed as

$$r = \frac{d\varepsilon_w}{d\varepsilon_t} = -\frac{d\varepsilon_w}{d\varepsilon_t + d\varepsilon_w} \quad (31)$$

where $d\varepsilon_l$, $d\varepsilon_w$ and $d\varepsilon_t$ are the true strain increments in the length, width and thickness direction of the sample.

5. Results

5.1 Uniaxial tension test data

Figure 7 illustrates the uniaxial tensile flow stress as a function of specific plastic work at seven directions as computed based on the experimental stress-strain curves. It is seen that the plastic anisotropy of the material changes over the investigated strain range. The normalized flow stress is defined as the ratio of the directional flow stress to the flow stress in the RD at the same level of specific plastic work. Figure 8 depicts the normalized flow stress versus sample orientation at specific plastic work equal to 0.2 MPa, 1 MPa, 5 MPa and 10 MPa, respectively. These levels of the specific plastic work correspond to plastic strains of about 0.4%, 2%, 8% and 14%, respectively. It should be noted that at each of these levels, the average value of the flow stress obtained from duplicate samples in the RD is used for normalization. At a specific plastic work of 0.2 MPa, a relatively larger scatter between duplicate tests is found. The reason for this is that flow stresses determined at small specific plastic work are sensitive to experimental errors, which may actually be very small. At higher specific plastic work, the spread reduces to become almost negligible.

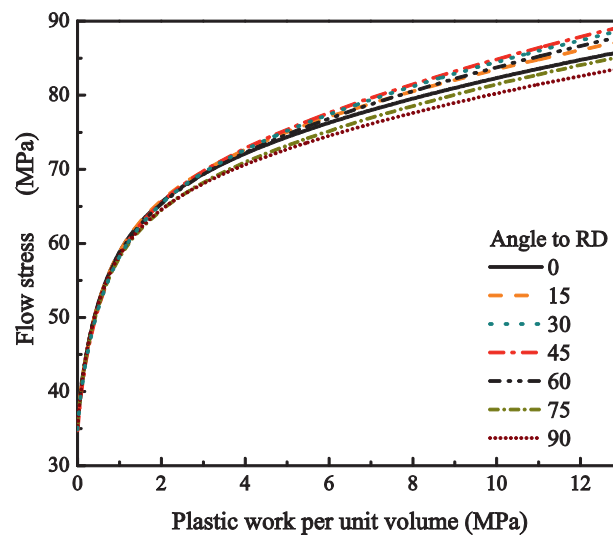


Figure 7 Uniaxial flow stress as a function of plastic work per unit volume for uniaxial tension in seven directions (all curves stop before necking) as obtained from the experiments.

In Figure 8, it is clearly seen that the strength anisotropy is weak. The maximum difference with respect to RD is below 3% for all cases. It is further illustrated that the strength anisotropy changes with increasing specific plastic work. At a specific plastic work equal to 0.2 MPa, the material is strongest in the RD and weakest in the 30° direction, but the difference is less than 2%. The strength anisotropy at 1 MPa specific plastic work has changed little compared with that at 0.2 MPa. At specific plastic work

equal to 5 and 10 MPa, the strength anisotropy has changed: the material is now strongest at 45° and weakest at 90° with a smooth change from the RD to TD.

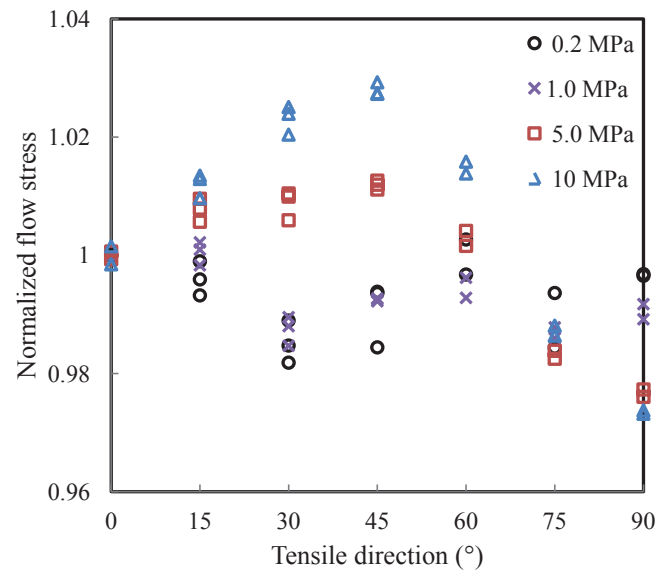


Figure 8 Normalized flow stress versus tensile direction at different specific plastic work levels as obtained from the experiments.

The r -values are determined at true strains between 2% and 15%, where the texture changes little and the elastic strain increments are relatively small as to not influence the results. Experimental r -values for different tensile directions are shown in Figure 10, where the results from CP simulations are also presented. The experiments show a variation of the r -value, which is an evidence of the anisotropy of the plastic flow of the material. The r -value is lowest in the 45° direction and highest at the RD and TD. In the actual strain range, the r -values in all directions show little variation with strains, which is in contrast to the behaviour of the normalized flow stress.

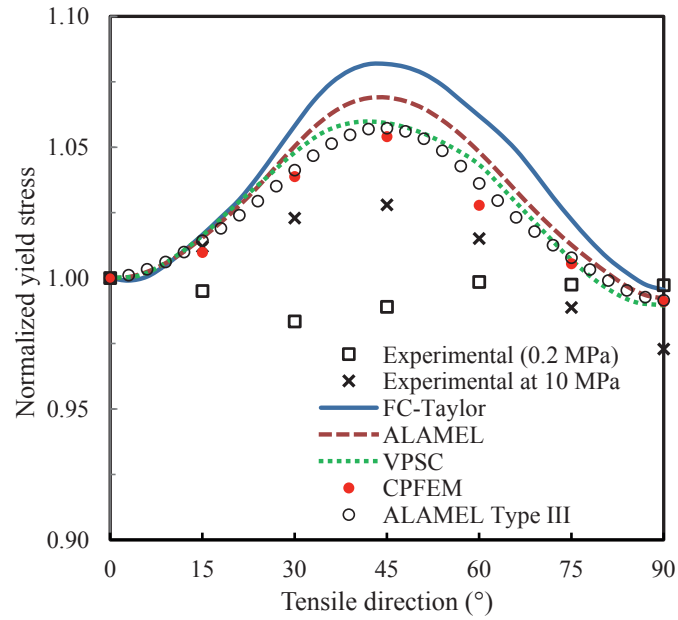


Figure 9 Normalized yield stress from experiments at 0.2 MPa and 10 MPa specific plastic work and predictions by the five CP models.

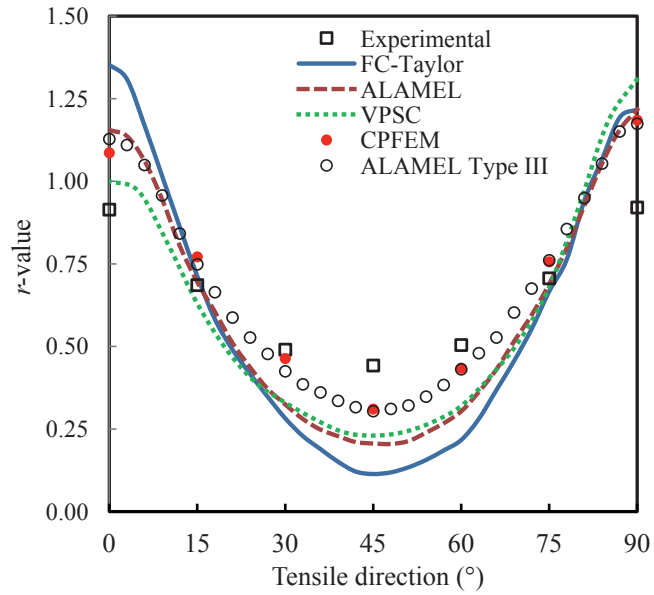


Figure 10 Plots of the r -value from experiments and predictions from the five CP models.

5.2 Prediction of mechanical anisotropy using crystal plasticity models

Modelling of pure tension along different angles from RD to TD was described in details in Section 2.5. Simulation results together with the experimental data are shown in Figure 9 and Figure 10. Simulations with CPFEM were made at every 15° from RD to TD, and at every 3° for simulations made with the other four CP models. The material is almost planar isotropic when it comes to yield stress measurements. As illustrated in Figure 9, all five CP models predict directional flow stress anisotropy, where the material is slightly stronger at 45° and weakest at 90°. The predictions differ from each other by the estimated maximum normalized yield stresses at 45°. At this direction, the FC-Taylor model gives the highest value of 1.08, ALAMEL gives an intermediate value, while ALAMEL Type III, VPSC and CPFEM give the lowest values which are similar and below 1.06. The CPFEM values are closest to the experimental results. It is interesting to note that at 10 MPa specific plastic work, which corresponds to a moderate strain level around 14% plastic strain, the experiments are closer to the crystal plasticity predictions.

It is interesting to compare the Taylor factor M predicted by the Taylor-type models with the CPFEM. The Taylor factors in uniaxial tension in the RD are given in Table 4, where the Taylor factor is estimated as $M = \sigma_y / \tau_0$ for VPSC and CPFEM¹; σ_y is the yield stress. This is a reasonable definition of the Taylor factor for low strain-rate sensitivity. The FC-Taylor model gives the largest value. The other models give lower M , and it is noted that CPFEM gives the lowest value.

Table 4 Taylor factors for AA1050 in uniaxial tension along the RD as computed by the different CP models.

FC-Taylor	ALAMEL	ALAMEL Type III	VPSC	CPFEM
2.81	2.65	2.58	2.58	2.55

The r -values obtained by experiments and CP predictions are shown in Figure 10. According to the experiments, the material has similar r -values at 0° and 90°, about 0.92, while the r -value has a minimum at 45° equal to 0.44. The r -values predicted from the five CP models have a similar trend as seen in the experiments. The r -value is high at 0°, decreases smoothly to a minimum at 45° and increases gradually again to a local maximum at 90°. However, none of the models gives quantitatively correct r -values. At

¹ In order to accurately capture the initial yield stress in CPFEM, the work hardening was deactivated and σ_y was then determined at the plateau in the stress-strain curve up to 1% elongation. This set-up was only employed for giving the results in Table 4.

0° and 90°, the CP models predict higher values than the experimental ones. The VPSC prediction is closest to the experiment at 0°, while the other four models give better predictions at 90°. However, the largest difference between experiments and predictions occurs at 45°, where FC-Taylor, ALAMEL and VPSC predicted values are less than one half of the experimental data. Note that CPFEM and ALAMEL Type III give much better predictions at 45°, with the value at 0.31, i.e. an error of only 25% compared to the experiments. Also in the other directions, except at 0°, the CPFEM and ALAMEL Type III models provide the best results. As can be seen from Figure 9 and Figure 10, the CPFEM and ALAMEL Type III models give almost identical results.

As shown in Figure 8, the in-plane directional variation of the flow stress in the experiments was found to change with the plastic strain. The texture evolution during uniaxial tension certainly contributes to the experimentally observed evolution of the strength anisotropy. To investigate this issue, the CPFEM model was employed to predict the strength anisotropy at different levels of specific plastic work where the texture evolution had been taken into consideration. The CPFEM calculations were conducted as described in section 2.5. Based on the predicted stress-strain curves for the seven tensile directions tested in the laboratory, the flow stresses at different levels of specific plastic work were recorded. The normalized flow stress was then obtained by normalization of the flow stress for each direction by the flow stress for the RD at the same level of specific plastic work.

Figure 11 presents for each tensile direction the change of the normalized flow stress from CPFEM calculations evaluated at specific plastic work equal to 1.0 MPa, 5 MPa and 10 MPa with respect to the normalized flow stress at specific plastic work equal to 0.2 MPa. The CPFEM model predicted an evolution of the strength anisotropy, i.e. the material gets stronger at the 30° and 45° directions (with respect to the RD) and weaker at the 75° and 90° directions as compared to the initial predictions shown in Figure 9. The largest change is predicted at the 45° direction, which indicates that the texture evolution is strongest in this direction under uniaxial tension. The predicted evolution of the strength anisotropy is in qualitative agreement with the experimental results, see Figure 8, but the predicted changes are severely underestimated and much smaller than the difference between the experiments and model predictions at the initial yielding. Changes estimated by the FC-Taylor model are very close to these CPFEM results.

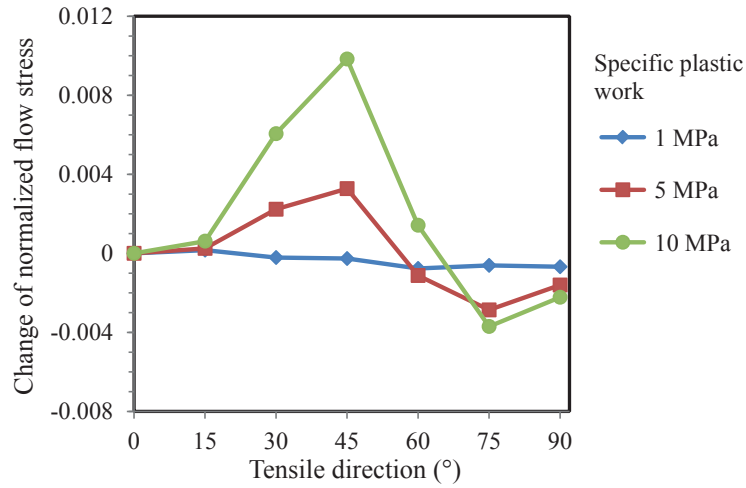


Figure 11 Change of normalized flow stress with specific plastic work predicted by CPFEM with respect to the calculations at initial yielding.

5.3 Calibration of the Yld2004-18 yield function

In this section, the initial yielding of the AA1050 sheet is described using the advanced yield function Yld2004-18p. The calibration methods of the Yld2004-18p yield function have been elaborated in Section 3.1. Equation (27) gives the error to be minimized using the values of the weighting factors given in Table 2. Since the initial yield surface is concerned here, the experimental normalized flow stresses at specific plastic work equal to 0.2 MPa, shown in Figure 8 and Figure 9, were used as the experimental yield stresses in the following. When the coefficients of the Yld2004-18p yield function are determined, the in-plane normalized yield stresses, r -values and sections of the yield surface, e.g. the $\sigma_{11} - \sigma_{22}$ yield locus, can be derived (Barlat et al., 2005), where σ_{11} and σ_{22} are the normalized stresses (by the stress at yielding along the RD) along RD and TD, respectively. Results are presented and discussed in the following.

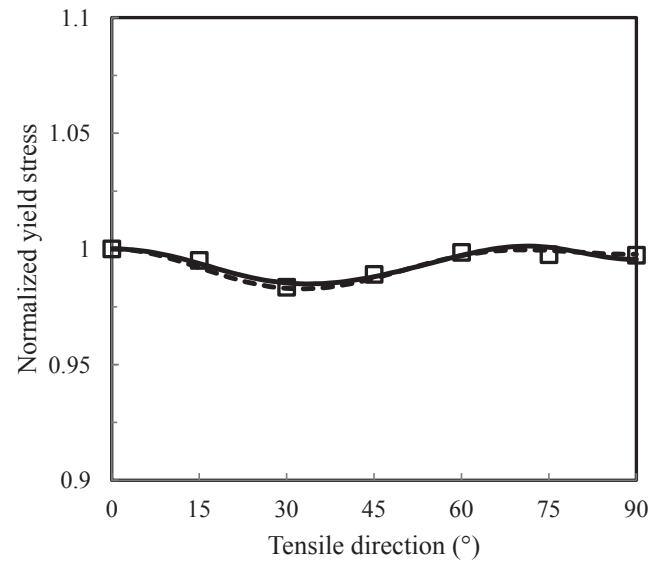
5.3.1 Using experimental data

As discussed in Section 3.1, Yld2004-18p was fitted only to uniaxial tension data from experiments, i.e. the normalized yield stresses and r -values for various in-plane directions. Following the work of Barlat et al. (2005) and Grytten et al. (2008), a is set as 8 when fitted to only or mainly mechanical experimental results. Mechanical isotropy was assumed for the out-of-plane directions by setting the coefficients governing the out-of-plane properties, i.e. c'_{44} , c'_{55} , c''_{44} , c''_{55} , equal to unity. The two experimental

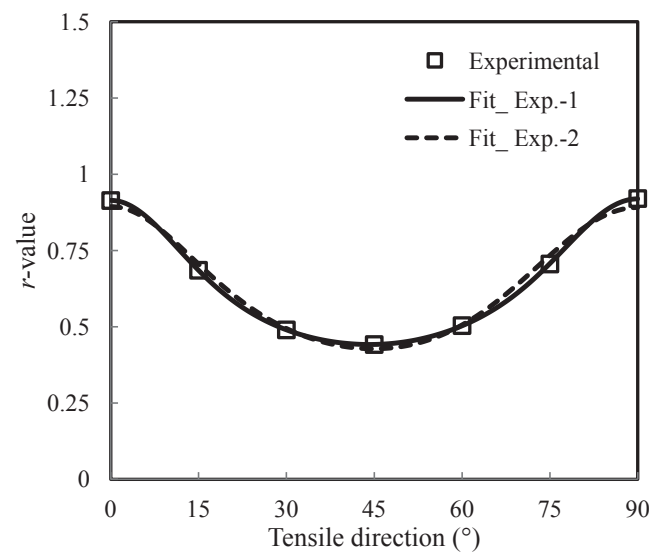
calibration methods, 'Fit_Exp.-1' and 'Fit_Exp.-2', are different in the weighting factors used for the r -value, which are 0.25 and 0.1, respectively.

As shown in Figure 12, the Yld2004-18p yield functions obtained from Fit_Exp.-1 and Fit_Exp.-2 capture the in-plane directional anisotropy in uniaxial tension with high accuracy. There is little difference between the two solutions. However, the two resulting yield loci are quite different, as shown in Figure 13. Especially in the equi-biaxial stress region, the two loci have distinct curvatures, which indicate distinct plastic flow directions owing to the normality rule.

The normalized equi-biaxial flow stress σ_b and the equi-biaxial r -value $r_b = D_{22}^p / D_{11}^p$ which can be determined by experiments or CP calculations, could be added into the error function in order to control the curvature of the yield locus. To illustrate this point, σ_b (normalized by the yield stress in RD) and r_b were calculated by the FC-Taylor model for the material. The resulting values were $\sigma_b = 1.027$ and $r_b = 1.000$. These two values were added to the error function for 'Fit_Exp.-1' and 'Fit_Exp.-2' in the same manner as the experimental data, using weighting factors equal to 0.05 and 0.01 for σ_b and r_b , respectively. Relatively small weights were applied, as suggested by Barlat (2005). The two resulting yield loci are also shown in Figure 13, with the legend 'Fit_Exp.-1 + Biaxial' and 'Fit_Exp.-2 + Biaxial', respectively. The two new yield loci are almost identical but different from the previously calculated yield loci.



(a)



(b)

Figure 12 Anisotropy of (a) normalized yield stress and (b) r -value for AA1050 measured and calculated with Yld2004-18p fitted to uniaxial tensile data.

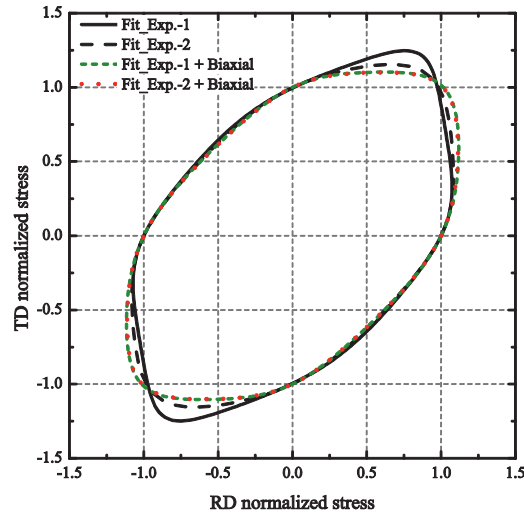


Figure 13 RD-TD section of the yield surface of Yld2004-18p fitted to uniaxial tensile data and fitted to uniaxial tensile data plus the equi-biaxial yield stress and r -value predicted by the FC-Taylor model. Different weighting factors were assigned to the ‘Exp.-1’ and ‘Exp.-2’ approaches.

5.3.2 Using data from crystal plasticity simulations

The calibration methods using virtual experiments by CP simulations were detailed in Section 3.1. Now, Yld2004-18p is fitted in the five-dimensional deviatoric stress space, using 201 stress points at yielding provided by the FC-Taylor, ALAMEL, ALAMEL Type III and VPSC models, respectively. The normal directions to the yield surface are given by the prescribed strain paths but are not included in the fitting procedure, which means that the curvature of the yield surface is only controlled by the 201 yield stress points. One prominent advantage of such a fitting method is that no real mechanical tests are needed.

Results for fitting of the exponent a of Yld2004-18p to a random texture are shown in Table 5, together with the Taylor factor M for tensile tests of this isotropic case. One can notice that, when fitting to the CP models, the FC-Taylor model gives the largest value of a , and hence has the yield surface with sharpest corners. When grain interactions are introduced either locally (ALAMEL and ALAMEL Type III) or in the long range (VPSC), the fitted exponent drops from 8.5 for the FC-Taylor model to around 6.5 for the other three CP models. Conventionally, the exponent of phenomenological yield functions takes an even integer. Thus, for the fitting of Yld2004-18p by the ‘Fit_CP’ and the ‘Fit_Exp.+CP’ methods, the exponent a is set as 8 when the FC-Taylor model is used as the lower-scale model, and as 6 when one of the other three CP models is employed. This is indicated in Table 5 by the values of a

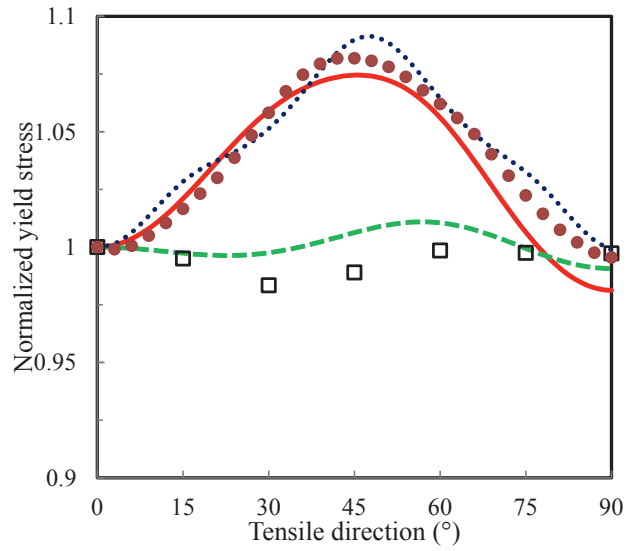
given in the parentheses. The result obtained for the FC-Taylor model is consistent with the work done by Hosford (1972) for a random FCC texture where the exponent was also found as 8.

Table 5 Taylor factor M in uniaxial tension along RD and estimated values of the exponent a of the Yld2004-18p yield function, based on CP simulations for random texture. The nearest even integer value of a is given in parenthesis.

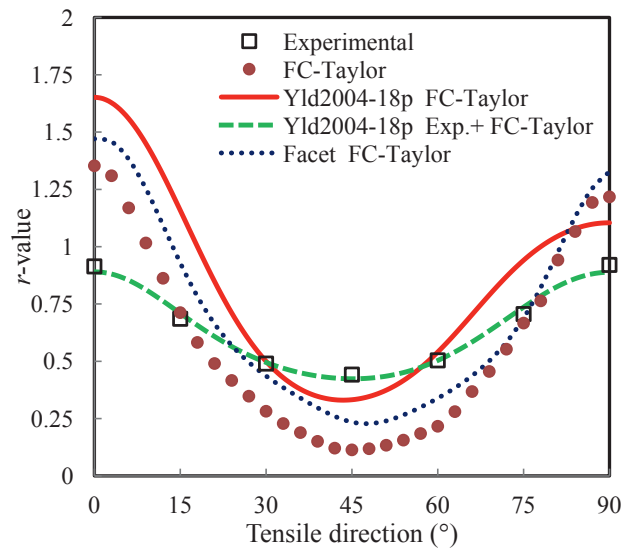
CP models	M	a
FC-Taylor	3.067	8.53 (8)
ALAMEL	2.826	6.60 (6)
ALAMEL Type III	2.732	6.46 (6)
VPSC	2.752	6.65 (6)

Normalized yield stresses and r -values could be calculated using the yield function fitted by the 201 FC-Taylor model predictions. In Figure 14 these are compared with experiments for different angles to the RD in the sheet and also with predictions by the FC-Taylor model. Compared to the FC-Taylor calculations, the Yld2004-18p yield function (denoted ‘Yld2004-18p FC-Taylor’ in the figure) captures the stress anisotropy well, while the r -value exhibits the same trend but with a moderately higher value at all angles except near the TD. Figure 15 shows good agreement between the yield locus obtained by Yld2004-18p and the in-plane yield stresses from the FC-Taylor calculations.

The Yld2004-18p yield function was also fitted to yield stresses computed by the ALAMEL, ALAMEL Type III and VPSC models. The results are shown in Figure 16 to Figure 21, where they are compared to the corresponding CP calculations and experimental data. The conclusions are the same as for the fitting based on FC-Taylor calculations. The Yld2004-18p yield function agrees well with the anisotropy determined by the underlying ALAMEL, ALAMEL Type III and VPSC calculations, respectively.



(a)



(b)

Figure 14 Plots of (a) normalized yield stress and (b) r -value obtained from experiments, FC-Taylor calculations, Yld2004-18p fitted to 201 FC-Taylor stress points, Yld2004-18p fitted to a combination of 201 FC-Taylor stress points and the tensile tests, and the Facet model fitted to 201 FC-Taylor stress points.

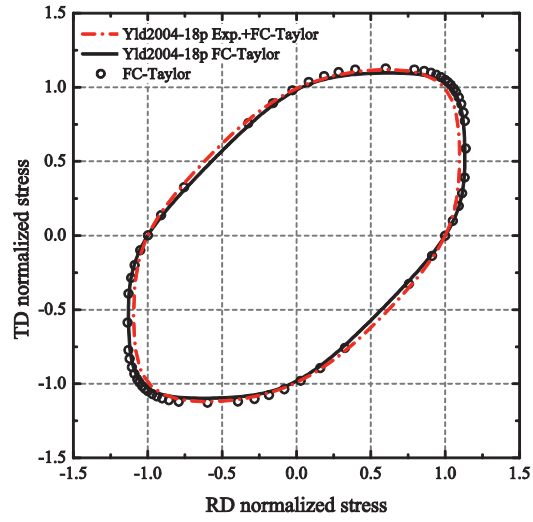
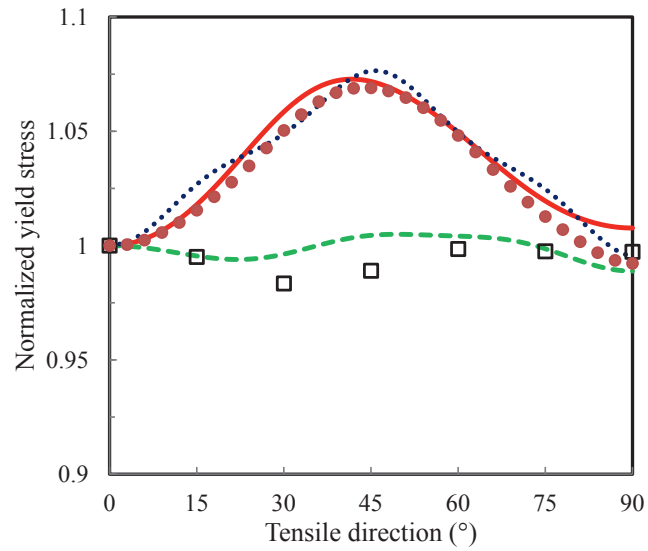
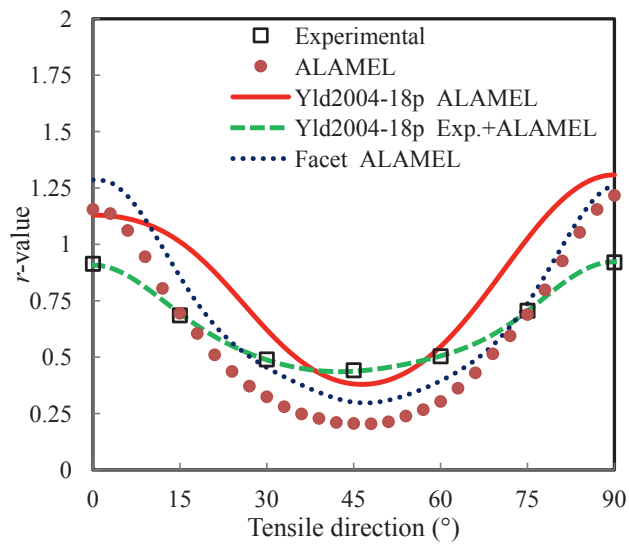


Figure 15 RD-TD section of the yield surface of Yld2004-18p fitted to 201 FC-Taylor stress points and fitted to a combination of both experiments and the 201 stress points, compared to the FC-Taylor model predictions.



(a)



(b)

Figure 16 Plots of (a) normalized yield stress and (b) r -value obtained from experiments, ALAMEL calculations, Yld2004-18p fitted to 201 ALAMEL stress points, Yld2004-18p fitted to a combination of 201 ALAMEL stress points and experiments, and Facet fitted to 201 ALAMEL stress points.

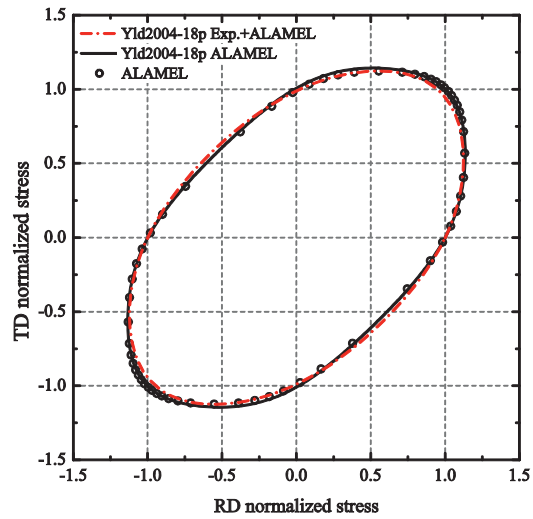
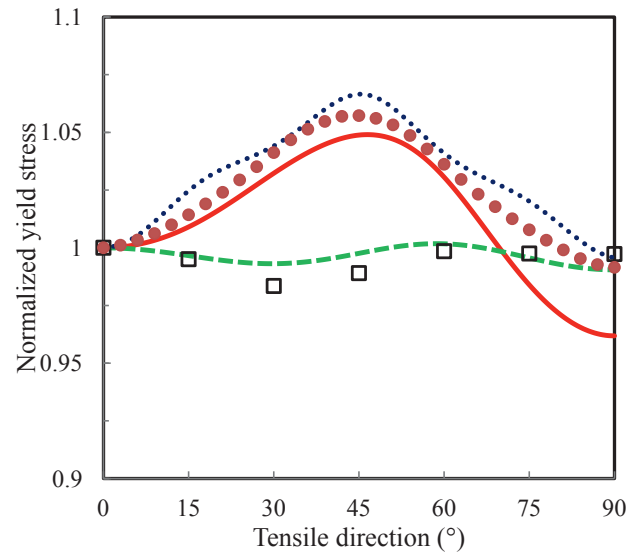
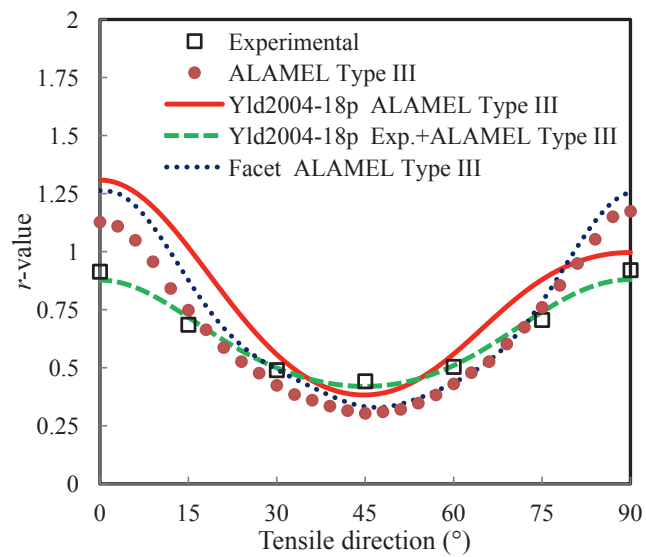


Figure 17 RD-TD section of the yield surface of Yld2004-18p fitted to 201 ALAMEL stress points and fitted to a combination of both experiments and the 201 stress points, compared to the ALAMEL model predictions.



(a)



(b)

Figure 18 Plots of (a) normalized yield stress and (b) r -value obtained from experiments, ALAMEL Type III calculations, Yld2004-18p fitted to 201 ALAMEL Type III stress points, Yld2004-18p fitted to a combination of 201 ALAMEL Type III stress points and experiments, and Facet fitted to 201 ALAMEL Type III stress points.

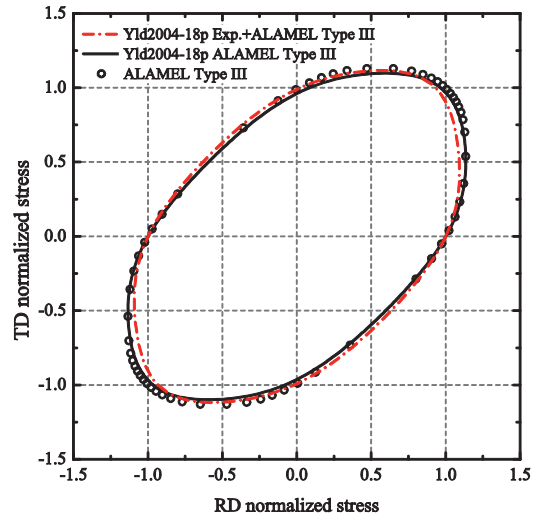
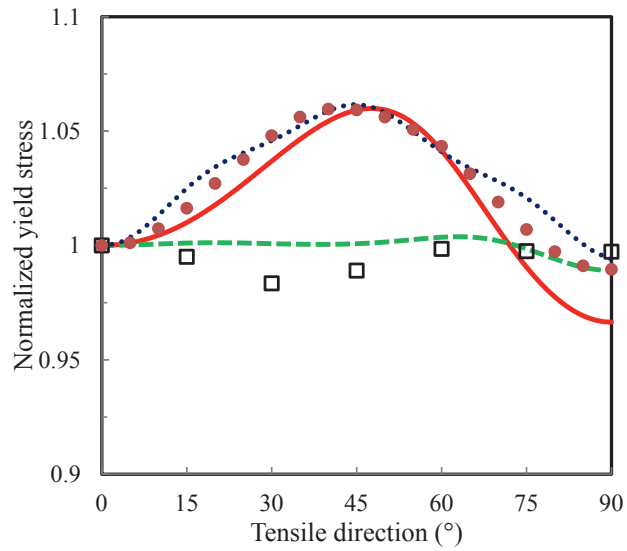
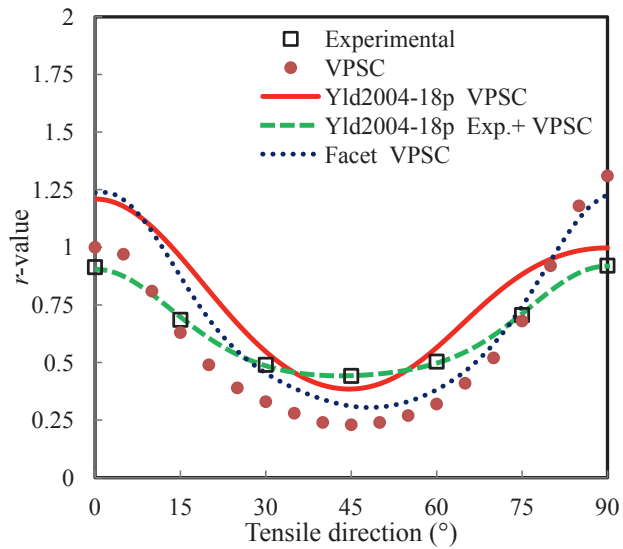


Figure 19 RD-TD section of the yield surface of Yld2004-18p fitted to 201 ALAMEL Type III stress points and fitted to a combination of both experiments and the 201 stress points, compared to the ALAMEL Type III model predictions.



(a)



(b)

Figure 20 Plots of (a) normalized yield stress and (b) r -value obtained from experiments, VPSC calculations, Yld2004-18p fitted to 201 VPSC stress points, Yld2004-18p fitted to a combination of 201 VPSC stress points and experiments, and Facet fitted to 201 VPSC stress points.

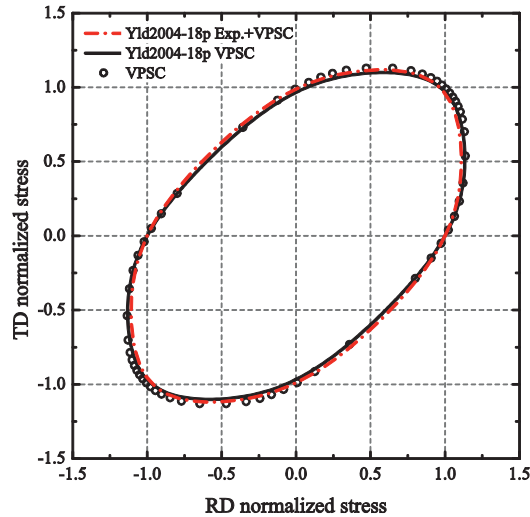


Figure 21 RD-TD section of the yield surface of Yld2004-18p fitted to 201 VPSC stress points and fitted to a combination of both experiments and the 201 stress points, compared to the VPSC model predictions.

5.3.3 Using combined data from experiments and crystal plasticity simulations

Data from experiments and CP calculations can be combined by various weighting in Eq. (27) to fit the Yld2004-18p yield function. The tension tests in seven directions provide the experimental data, and 201 yield stresses were computed by the chosen CP model along the same number of strain-rate directions. Weighting factors are given in Table 2. These factors were chosen to ensure similar contributions to the total error from all the experiments and from all the CP computations with the FC-Taylor, ALAMEL, ALAMEL Type III and VPSC model, respectively. All 18 parameters of Yld2004-18p are now calibrated, while values of the exponent a are referred to Table 5. The results are presented in Figure 14 to Figure 22.

It is clearly illustrated in Figure 14, Figure 16, Figure 18 and Figure 20 that yield functions calibrated using a combination of experimental data and CP simulations capture the experimentally observed in-plane anisotropy with a good accuracy. All calibrations reproduce the very weak stress anisotropy seen in the experiments. The results predicted by the yield function deviates less than 2% from the experimental data in all directions. The distribution of the r -value shows perfect agreement with the experiments in all the four cases. The yield loci correspond rather well with yield points calculated by the corresponding CP models, see Figure 15, Figure 17, Figure 19 and Figure 21. Even though the 201 points are spread in the five-dimensional space, the

yield loci show reasonable agreement with CP predictions near the corners of the equibiaxial stress region.

In the experimental fitting schemes, all parameters governing the out-of-plane behaviour were set to unity, while they were free in the calibrations discussed here. This will influence the shape of yield surface in the regions where out-of-plane stress components are involved. In Figure 22, the $\sigma_{11} - \sigma_{33}$ yield locus, based on the different calibration schemes discussed above, is shown for cases where $\sigma_{13} = 0$ and $\sigma_{13} = 0.3$, respectively. The differences in the yield loci relate to the way the out-of-plane yield stresses are calibrated.

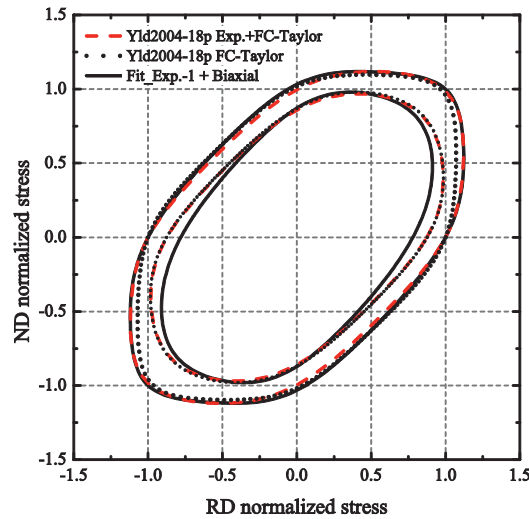


Figure 22 RD-ND sections of yield surface of Yld2004-18p: fitted to experimental data plus the equibiaxial yield stress and r -value calculated by the FC-Taylor model; fitted to 201 FC-Taylor stress points; fitted to a combination of experiments and the 201 FC-Taylor stress points. The sections with $\sigma_{13} = 0$ (outer ones) and $\sigma_{13} = 0.3$ (inner ones) are shown.

5.4 Calibration of the Facet yield surface

The Facet method is designed to be used in combination with multilevel models. The parameters are identified from stress states at yielding calculated for selected strain rates by CP models with texture as input. No experimental data, except for the measured texture, are needed or included in the identifications. In this work, 201 stress-strain rate pairs from the FC-Taylor, ALAMEL, ALAMEL Type III and VPSC models have been used for fitting the Facet yield surface, respectively.

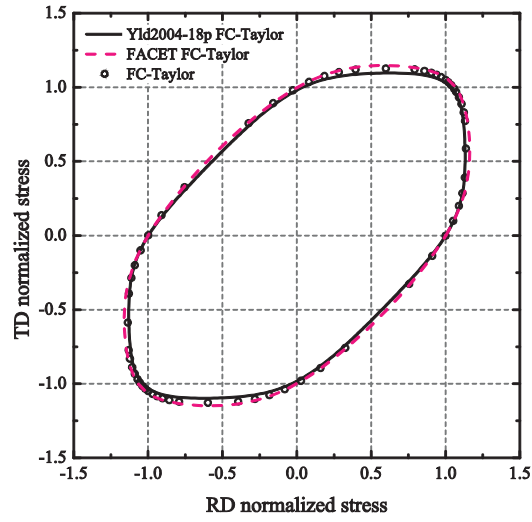
The error $e(n)$, defined in Eq. (30), was computed to determine the optimal Facet exponents for the considered material with different CP models. It was found that the number of points actually fitted by $\tilde{\psi}(\mathbf{D}^p)$ and $\psi(\mathbf{S})$ increases with larger exponents \tilde{n} and n , respectively. When the exponent is large enough, all the fitting points are exactly run through by the Facet yield function. Quantitative evaluations of calibrations to 201 points were made by comparison to another 1241 strain-rate directions and corresponding stress states from virtual experiments. It was found that optimal values for \tilde{n} and n exist, at which $e(n)$ reaches its minimum. Optimal exponents of the Facet yield functions for all CP models, and corresponding errors $e(n)$, are compiled in Table 6. The yield function $\psi(\mathbf{S})$ fitted with the optimal exponents in Table 6 is used to predict the plastic anisotropy of AA1050 and the results are described in the following.

Table 6 Optimal exponents \tilde{n} and n of the dual Facet potentials in strain-rate space and stress space, respectively, and the corresponding error $e(n)$ for the different CP models.

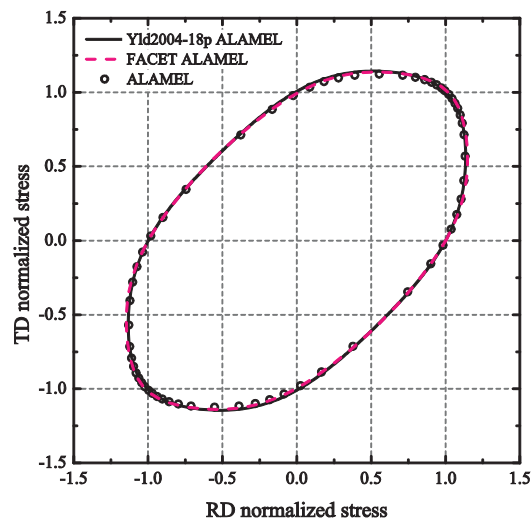
CP models	\tilde{n}	n	$e(n)$
FC-Taylor	12	14	9.13
ALAMEL	10	12	7.06
ALAMEL Type III	10	12	5.60
VPSC	10	10	8.73

Normalized yield stresses and r -values for in-plane uniaxial tensile tests could then be predicted for various angles to the RD, as shown in Figure 14, Figure 16, Figure 18 and Figure 20. The fitted Facet yield surface gives a precise representation of the in-plane anisotropy provided by the corresponding calculations by each of the four CP models. The Facet yield surface shows a slightly oscillating prediction of the in-plane stress anisotropy, but still the accuracy is good.

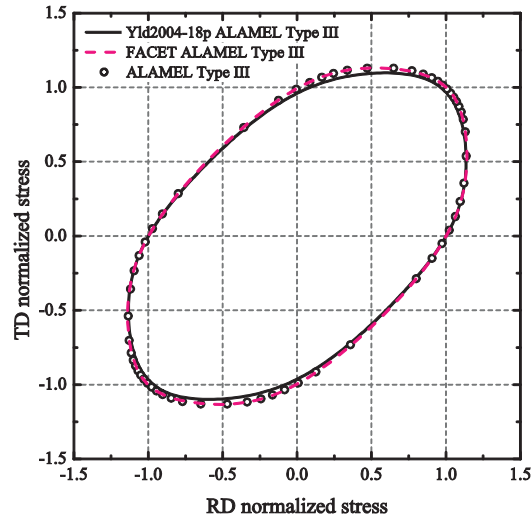
The yield loci of Facet and Yld2004-18p identified from virtual experiments using the four CP models are shown in Figure 23, where yield points computed by the CP models are also shown. As can be seen from the figure, the yield surface corners of the FC-Taylor based yield locus become too rounded by the Facet fit, whereas Yld2004-18p is slightly closer to the FC-Taylor calculations. For the other three CP models, both the Facet and the Yld2004-18p give results in good agreement with the corresponding CP-based yield loci, where in general the Facet fits are slightly better.



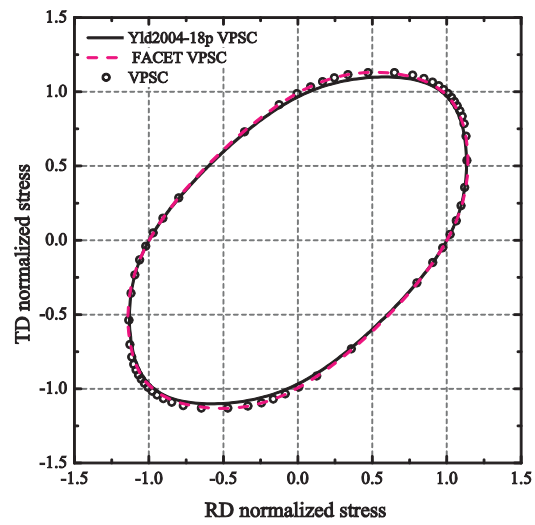
(a)



(b)



(c)



(d)

Figure 23 RD-TD sections of the yield surface of Facet and Yld2004-18p fitted to 201 stress points at yielding from (a) FC-Taylor, (b) ALAMEL, (c) ALAMEL Type III and (d) VPSC models, respectively, together with the in-plane stress points computed by each of the four models.

6. Discussion

The hierarchical modelling approach applied here, i.e. a two-scale scheme, uses analytical yield functions at the continuum scale and CP models at the mesoscale. The continuum yield functions implemented in finite element codes can be used in simulations of complex deformation processes at the engineering scale with relatively high computational efficiency, while the CP models provide stress-strain points at yielding to identify the advanced yield functions. However, the success of the hierarchical modelling approach depends crucially on the independent accuracy of models at both scales in representing the material behaviour and on the fitting method which bridges the models through the scales.

It is quite clear from the results that the FC-Taylor, VPSC and ALAMEL models are not capable of capturing the plastic anisotropy of the AA1050 sheet in a quantitative manner. The variation of the r -value is qualitatively correct, but especially with the FC-Taylor model the stress anisotropy is overestimated. Similar conclusions with respect to the FC-Taylor model, namely that it is only qualitatively correct in predicting mechanical anisotropy, have been made in other studies (Grytten et al., 2008; Delannay et al., 2009). The recent ALAMEL Type III model provides predictions that are very similar to CPFEM and these two models give results that are in better agreement with the experimental data than the other three models.

It is interesting to compare the Taylor factors, both for the case of a random texture in Table 5 and for the AA1050 cube texture in Table 4. The FC-Taylor model predicts the largest Taylor factor among the five CP models. The other models give lower values due to their strain constraint relaxations. The aggregate type of Taylor models considered here can be regarded as computationally efficient simplifications of a CPFEM model where both equilibrium and compatibility are achieved. Research on CPFEM texture predictions shows that increasing the in-grain mesh resolution can improve the agreement with experimental results (Zhao et al., 2007). Plastic anisotropy predicted by CPFEM is believed to be improved by a finer mesh, which is why a very fine mesh was used in this investigation. Attempts with a coarser mesh (not included here) gave results closer to the FC-Taylor model. It is interesting to note that CPFEM gives the lowest value of M for AA1050, and that the relaxed Taylor models are much closer to the stress predicted by CPFEM than by the FC-Taylor model, suggesting that strain relaxations are very important in stress calculations by aggregate models.

The in-plane directional variation of the flow stress in the experiments was found to change with the plastic strain. This change is not captured by the CP models, where only the texture-induced anisotropy is considered. According to the CPFEM calculations shown in Figure 11, the texture evolution contributes only to a minor part of the experimentally observed evolution of strength anisotropy. Other microstructural

features, possibly playing a role in defining the observed mechanical anisotropy, are neglected in the formulations of all CP models discussed in this work. Sources of microstructure-induced anisotropy could be aligned dislocation structures (Barlat et al., 2003b, Barlat et al., 2013, Holmedal et al., 2008), grain size (Delannay et al., 2012) and texture heterogeneity (Dumoulin et al., 2011). Furthermore, strain gradients and corresponding geometrically necessary dislocations are not accounted for. Keeping these simplifying assumptions in mind, the CP models do not seem capable of describing the plastic anisotropy of the material with high accuracy. The CP models predict the correct trends, but are not capable of accurately describing the directional variation of the flow stress and the r -value of the AA1050 sheet. The ALAMEL Type III and the CPFEM give the best results, but still with a 25% too small r -value at the 45° direction.

The results obtained with the calibrated Yld2004-18p and Facet yield functions in the present study show that both yield functions are capable of capturing the plastic anisotropy described by the underlying CP model with good accuracy. Only fitted to 201 yield stress points, the yield functions could still give r -values and reproduce the curvature and radius of the RD-TD section of the yield locus closely to what was predicted by the CP models. Since the 201 stress points were not chosen particularly to map the region of the stress space shown in Figure 23, one may expect similar quality of the fits to CP models by the Yld2004-18p or Facet yield surfaces in other regions of the stress space as well. However, one should always keep in mind that this approach is limited by the quality of the CP models in reproducing the experimentally observed mechanical anisotropy. When a realistic crystal plasticity model is available, both the Yld2004-18p and Facet yield surfaces seem capable of giving a realistic description of the plastic anisotropy exhibited by the material at hand.

FCC metals are challenging for the Facet yield surface, in particular when applying the FC-Taylor model, because the sharp corners of the yield surface require a much higher exponent than for the rounded BCC yield surfaces. This contributes to the largest error for the FC-Taylor model in Table 6. The relaxed constraint CP models predict a more rounded shape that may be described by lower exponents, similar as the decrease from 8 to 6 for the exponent a of Yld2004-18p in Table 5 for the case of random texture. It is desirable that as many as possible amongst the 201 points are included in the fitting procedure, but when the exponent is too low that is not possible by the non-negative least squares method, which is chosen because of uniqueness and high computational efficiency. On the other hand, if the exponent is too large the generic shape of the yield surface is wrong. As a compromise, the optimal fit was achieved with less than 201 points involved. A procedure for determining the exponent has been suggested here, with which minimum errors of the Facet surface can be achieved when a sufficiently large number of points has been used. The exponents obtained were larger than those suggested and applied earlier (Van Houtte et al., 2009, Gawad et al., 2013a). Note that

with another number of stress/strain-rate points or a different distribution of their directions, this procedure must be repeated to obtain suitable exponents.

The planar stress anisotropy as described by the Facet yield surface in Figure 14, Figure 16, Figure 18 and Figure 20, shows some oscillations. This is due to that among the 201 points, only a few are controlling the in-plane properties. Note that the oscillations would vanish with a lower exponent of the Facet function, but at the cost of a poorer overall fit. Of importance for formability predictions, a low exponent would also give a too rounded equi-biaxial region of the yield surface that would lead to non-conservative formability limit estimates.

Compared to the Yld2004-18p, results from the Facet model are somewhat closer to the CP calculations. An advantage of the Facet model is that it can be fitted unambiguously to the virtual experiments, but due to its many terms it is computationally more expensive in use. The reason for the slight difference between the fitted Yld2004-18p and the CP calculations can be twofold. Firstly, 201 stress points are not enough to fully represent the yield surface. Secondly, there are only 18 parameters in the Yld2004-18p yield function (not counting a), which limits its flexibility in adapting to complex surface shapes.

It is interesting to compare the calibration using only the 201 CP simulations, the one using a combination of experimental data and CP simulations, and the one using the experimental data in addition to one CP calculation providing the yield stress and r -value for the equi-biaxial stress state. As seen from Figure 22, the latter approach deviates significantly from the two first regarding the $\sigma_{11} - \sigma_{33}$ section of the yield surface with $\sigma_{13} = 0.3$. Without experimental data involving the out-of-plane stress components, it is difficult to assess the quality of these different yield loci, but the calibrations based on CP simulations in the full stress space clearly indicate the presence of additional out-of-plane anisotropy.

When isotropy is assumed for the out-of-plane mechanical properties of the material, 14 parameters remain to be fitted in Yld2004-18p. The uniaxial yield stresses and r -values in the seven directions in the plane of the sheet provide 14 data points, which is the minimum number required for fitting of the yield function. Using this approach, the in-plane directional tension properties could be reproduced with high accuracy. However, a small change of the weighting factors led to significant changes in the shape of the yield locus, especially in the equi-biaxial stress region, as shown in Figure 13. This effect may be weakened if biaxial data from CP models or experiments are used. Hence, fitting Yld2004-18p only to uniaxial tensile data in seven directions is not found to be a reliable and stable approach.

Despite the shortcomings of the CP models, it is suggested that advanced yield functions can be identified by using a combination of all the available experimental data, supplemented with the 201 yield stresses from CP simulations to span the five-dimensional deviatoric stress space. In the current case, the recent ALAMEL Type III model gave much better results than the FC-Taylor model, but since the mechanical anisotropy is not generally determined with satisfactory precision in the virtual experiments, adequate corrections are implicitly taken into consideration by the hybrid identification method. This method provides a good compromise between the qualitatively correct CP calculations and the experiment results for several stress states and material directions. Even if only uniaxial tension tests could be employed to provide the experimental data, additional tests, e.g. in shear, plane-strain tension or biaxial tension, are recommended to increase the accuracy and robustness of the identification (Lademo et al., 2009).

Methods for identifying the initial yield surface of aluminium alloys with a satisfactory accuracy have been described and discussed above. Plasticity models using the initial yield surface combined with isotropic or combined isotropic and kinematic hardening are widely used by the industry in forming simulations and have produced results in good agreement with experiments (Worswick and Finn, 2000; Yoon et al., 2004). However, the shape of the yield surface may change in the course of the forming operation, due to the evolution of the microstructure of the material. As a consequence, the coefficients of the anisotropic yield function should be updated to track the subsequent yield surfaces. Although the initial yield surface is the main concern in this paper, ways of tracking the subsequent yield surfaces are briefly discussed in the following with emphasis on employing the fitting procedures proposed above.

In a hierarchical multi-scale (HMS) model², Gawad et al. (2013a) included the evolution of crystallographic texture in the FACET yield function in simulations of plastic forming of polycrystalline metallic alloys. Similar methods were also reported by Neumann et al. (2005), Kowalczyk and Gambin (2004) and Gawad et al. (2013b). The HMS model could easily be extended to the Yld2004-18p yield function by use of crystal plasticity based fitting procedures. However, the prediction accuracy of such an

² In the HMS model, the crystallographic texture at each integration point is represented by a number of orientations. Initially, the texture is the same for all integration points. After certain plastic strains or strain-intervals, the texture is updated with the CP models and deformation history experienced by the integration point. With newly updated texture, virtual stress points are provided with CP models and then used to calibrate the new coefficients of the yield function.

approach would depend critically on the accuracy of the crystal plasticity model used to identify the yield surfaces. In the case of the AA1050 material, crystal plasticity simulations indicate that the experimentally observed evolution of strength anisotropy can only be partially attributed to texture evolution. Hence, the HMS model cannot capture accurately the observed distortion of the yield surface. The evolution of the shape of the yield surface can also be described by distortional hardening models (e.g., Aretz, 2008; Barlat et al., 2013; Shutov and Ihlemann, 2012), but these models are beyond the scope of this paper.

7. Conclusion

In this work, the mechanical anisotropy of an AA1050 sheet has been studied by experiments, crystal plasticity modelling and use of advanced yield functions. None of the five considered crystal plasticity models, namely the FC-Taylor model, the two variants of the ALAMEL model, the VPSC model and CPFEM, were able to perfectly describe the plastic anisotropy exhibited in uniaxial tension tests in the plane of the sheet. However, CPFEM and ALAMEL Type III provided the best agreement with experimental results for the AA1050 sheet. The ALAMEL Type III predictions showed as good accuracy as the CPFEM with a high resolution mesh. Since the computational efficiency of the ALAMEL Type III model is much higher than that of high resolution CPFEM, it is a promising candidate for hierarchical modelling.

The Yld2004-18p yield function and the Facet potential have been identified based on 201 distinct stress states on the yield surface computed by the FC-Taylor, ALAMEL, ALAMEL Type III and VPSC models. The results show that even though the Yld2004-18p yield surface has few parameters compared to the Facet surface, both yield functions are flexible and fit rather accurately the yield points as well as the yield surface predicted by the CP models. It is concluded that the exponent of the Facet polynomial should be carefully chosen and that the optimal values are higher than reported earlier. However, due to the inaccuracy of the CP models, the identifications of the yield functions could not represent the experimental data with high precision.

Identifying the Yld2004-18p yield function based on uniaxial tensile tests in seven directions with respect to RD is not a reliable method. More data points are required to properly define the equi-biaxial stress region of the yield locus. This is achieved by the hybrid calibration method adopted for the Yld20014-18p yield function, which takes both the experimental data and the yield stresses from the CP simulations into consideration in the parameter identification. By this approach the identified yield function shows good agreement with the experimental data as well as with the CP calculations. This method is suggested here for identifying the Yld20014-18p yield

function, as it gives a more robust determination of the yield surface in the whole of the five-dimensional deviatoric stress space.

Acknowledgements

T. Mánik is acknowledged for stimulating discussions on implementation of the Taylor-type crystal plasticity models. K. Huang is acknowledged for help on EBSD experiments. J. Gawad, A. Van Bael, P. Van Houtte gratefully acknowledge financial support of KU Leuven IOF via Knowledge Platform M2Form. Q. Xie is acknowledged for discussions on ALAMEL and FACET during K. Zhang's stay in Department MTM, KU Leuven.

References

- An, Y.G., Vegter, H., Carless, L., Lambriks, M., 2011. A novel yield locus description by combining the Taylor and the relaxed Taylor theory for sheet steels. *International Journal of Plasticity* 27, 1758-1780.
- Aretz, H., 2008. A simple isotropic-distortional hardening model and its application in elastic-plastic analysis of localized necking in orthotropic sheet metals. *International Journal of Plasticity* 24, 1457-1480.
- Aretz, H., Barlat F., 2013. New convex yield functions for orthotropic metal plasticity. *International Journal of Non-Linear Mechanics* 51, 97-111.
- Arul Kumar, M., Mahesh, S., Parameswaran, V., 2011. A 'stack' model of rate-independent polycrystals. *International Journal of Plasticity* 27, 962-981.
- ASTM Standards E517-00, 2010. Standard test method for plastic strain ratio r for sheet metal. ASTM International, West Conshohocken, PA, doi: <http://dx.doi.org/10.1520/E0517-00R10>, www.astm.org.
- Banabic, D., Kuwabara, T., Balan, T., Comsa, D.S., Julean, D., 2003. Non-quadratic yield criterion for orthotropic sheet metals under plane-stress conditions. *International Journal of Mechanical Sciences* 45, 797-811.
- Banabic, D., Aretz, H., Comsa, D.S., Paraianu, L., 2005. An improved analytical description of orthotropy in metallic sheets. *International Journal of Plasticity* 21, 493-512.
- Barlat, F., Lian, K., 1989. Plastic behavior and stretchability of sheet metals. Part I: A yield function for orthotropic sheets under plane stress conditions. *International Journal of Plasticity* 5, 51-66.
- Barlat, F., Lege, D.J., Brem, J.C., 1991. A six-component yield function for anisotropic materials. *International Journal of Plasticity* 7, 693-712.

- Barlat, F., Becker, R.C., Hayashida, Y., Maeda, Y., Yanagawa, M., Chung, K., Brem, J.C., Lege, D.J., Matsui, K., Murtha, S.J., Hattori, S., 1997. Yielding description for solution strengthened aluminum alloys. *International Journal of Plasticity* 13, 385-401.
- Barlat, F., Brem, J.C., Yoon, J.W., Chung, K., Dick, R.E., Lege, D.J., Pourboghrat, F., Choi, S.H., Chu, E., 2003a. Plane stress yield function for aluminum alloy sheets—part 1: theory. *International Journal of Plasticity* 19, 1297-1319.
- Barlat, F., Ferreira Duarte, J.M., Gracio, J.J., Lopes, A.B., Rauch E.F., 2003b. Plastic flow for non-monotonic loading conditions of an aluminum alloy sheet sample. *International Journal of Plasticity* 19, 1215-1244.
- Barlat, F., Aretz, H., Yoon, J.W., Karabin, M.E., Brem, J.C., Dick, R.E., 2005. Linear transformation-based anisotropic yield functions. *International Journal of Plasticity* 21, 1009-1039.
- Barlat, F., Yoon, J.W., Cazacu, O., 2007. On linear transformations of stress tensors for the description of plastic anisotropy. *International Journal of Plasticity* 23, 876-896.
- Barlat, F., Ha, H., Gracio, J.J., Lee, M.-G., Rauch E.F., Vincze, G., 2013. Extension of homogeneous anisotropic hardening model to cross-loading with latent effects. *International Journal of Plasticity* 46, 130-142.
- Bishop, J.F.W., Hill, R., 1951a. A theory of the plastic distortion of a polycrystalline aggregate under combined stresses. *Philosophical Magazine* 42, 414-427.
- Bishop, J.F.W., Hill, R., 1951b. A theoretical derivation of the plastic properties of a face-centred metal. *Philosophical Magazine* 42, 1298-1307.
- Chang, H.J., Han, H.N., Park, S.J., Cho, J.H., Oh, K.H., 2010. Texture evolution in FCC metals from initially different misorientation distributions under shear deformation. *Metals and Materials International* 16, 553-558.
- Crumbach, M., Pomana, G., Wagner, P., Gottstein, G., 2001. A Taylor type deformation texture model considering grain interaction and material properties. Part I – Fundamentals. In: Gottstein, G., Molodov, D.A. (Eds.), *Recrystallisation and Grain Growth, Proceedings of the First Joint Conference*. Springer, Berlin, pp. 1053-1060.
- Delannay, L., Melchior, M.A., Signorelli, J.W., Remacle, J.F., Kuwabara, T., 2009. Influence of grain shape on the planar anisotropy of rolled steel sheets – evaluation of three models. *Computational Materials Science* 45, 739-743.
- Delannay, L., Barnett, M.R., 2012. Modelling the combined effect of grain size and grain shape on plastic anisotropy of metals. *International Journal of Plasticity* 32–33, 70-84.
- Dumoulin, S., Hopperstad, O.S., Berstad, T., 2009. Investigation of integration algorithms for rate-dependent crystal plasticity using explicit finite element codes. *Computational Materials Science* 46, 785-799.
- Dumoulin, S., Friis, J., Gouttebroze, S., Holmedal, B., Marthinsen, K., 2011. 3D Crystal Plasticity Modelling of Complex Microstructures in Extruded Products. *AIP Conference Proceedings* 1383, 322-329.

- Eisenlohr, P., Diehl, M., Lebensohn, R.A., Roters, F., 2013. A spectral method solution to crystal elasto-viscoplasticity at finite strains. *International Journal of Plasticity* 46, 37-53.
- Engler, O., Randle, V., 2010. *Introduction to Texture Analysis: Macrotexture, Microtexture, and Orientation Mapping*, Second Edition. Taylor & Francis.
- Eshelby, J.D., 1957. The Determination of the Elastic Field of an Ellipsoidal Inclusion, and Related Problems. *Proceedings of the Royal Society of London. Series A. Mathematical and Physical Sciences* 241, 376-396.
- Gawad, J., Van Bael, A., Yerra, S.K., Samaey, G., Van Houtte, P., Roose, D., 2010. A Coupled Multiscale Model of Texture Evolution and Plastic Anisotropy. *AIP Conference Proceedings* 1252, 770-777.
- Gawad, J., Van Bael, A., Eyckens, P., Samaey, G., Van Houtte, P., Roose, D., 2013a. Hierarchical multi-scale modeling of texture induced plastic anisotropy in sheet forming. *Computational Materials Science* 66, 65-83.
- Gawad, J., Banabic, D., Comsa, D.S., Gologanu, M., Van Bael, A., Eyckens, P., Van Houtte, P., Roose, D., 2013b. Evolving texture-informed anisotropic yield criterion for sheet forming. *AIP Conference Proceedings* 1567, 350-355.
- Grytten, F., Holmedal, B., Hopperstad, O.S., Børvik, T., 2008. Evaluation of identification methods for YLD2004-18p. *International Journal of Plasticity* 24, 2248-2277.
- Hershey, A.V., 1954. The plasticity of an isotropic aggregate of anisotropic face centred cubic crystals. *Journal of Applied Mechanics* 21, 241-249.
- Hill, R., 1948. A Theory of the Yielding and Plastic Flow of Anisotropic Metals. *Proceedings of the Royal Society of London. Series A, Mathematical and Physical Sciences* 193, 281-297.
- Hill, R., 1965. Continuum micro-mechanics of elastoplastic polycrystals. *Journal of the Mechanics and Physics of Solids* 13, 89-101.
- Holmedal, B., Van Houtte, P., An, Y., 2008. A crystal plasticity model for strain-path changes in metals. *International Journal of Plasticity* 24, 1360-1379.
- Hosford, W.F., 1972. A Generalized Isotropic Yield Criterion. *Journal of Applied Mechanics* 39, 607-609.
- Hosford, W.F., 1979. On yield loci of anisotropic cubic metals. In: *Proceedings of the Seventh North American Metalworking Conference, Dearborn*, pp. 191-197.
- Hutchinson, J.W., 1976. Bounds and Self-Consistent Estimates for Creep of Polycrystalline Materials. *Proceedings of the Royal Society of London. A. Mathematical and Physical Sciences* 348, 101-127.
- Inal, K., Mishra, R.K., Cazacu, O., 2010. Forming simulation of aluminum sheets using an anisotropic yield function coupled with crystal plasticity theory. *International Journal of Solids and Structures* 47, 2223-2233.

- Karafillis, A.P., Boyce, M.C., 1993. A general anisotropic yield criterion using bounds and a transformation weighting tensor. *Journal of the Mechanics and Physics of Solids* 41, 1859-1886.
- Kocks, U.F., Chandra, H., 1982. Slip geometry in partially constrained deformation. *Acta Metallurgica* 30, 695-709.
- Kocks, U.F., Tomé, C.N., Wenk, H.R., 2000. *Texture and Anisotropy: Preferred Orientations in Polycrystals and Their Effect on Materials Properties*. Cambridge University Press.
- Kowalczyk, K., Gambin, W., 2004. Model of plastic anisotropy evolution with texture-dependent yield surface. *International Journal of Plasticity* 20, 19-54.
- Kröner, E., 1958. Berechnung der elastischen konstanten des vielkristalls aus den konstanten des einkristalls. *Zeitschrift Fur Physik* 151, 504-518.
- Lademo, O.G., Engler, O., Keller, S., Berstad, T., Pedersen, K.O., Hopperstad, O.S., 2009. Identification and validation of constitutive model and fracture criterion for AlMgSi alloy with application to sheet forming. *Materials & Design* 30, 3005-3019.
- Lebensohn, R.A., Tomé, C.N., 1993. A self-consistent anisotropic approach for the simulation of plastic deformation and texture development of polycrystals: Application to zirconium alloys. *Acta Metallurgica et Materialia* 41, 2611-2624.
- Lebensohn, R.A., Tomé, C.N., 1994. A self-consistent viscoplastic model: prediction of rolling textures of anisotropic polycrystals. *Materials Science and Engineering: A* 175, 71-82.
- Lebensohn, R.A., 2001. N-site modeling of a 3D viscoplastic polycrystal using Fast Fourier Transform. *Acta Materialia* 49, 2723-2737.
- Lebensohn, R.A., Tomé, C.N., Castañeda, P.P., 2007. Self-consistent modelling of the mechanical behaviour of viscoplastic polycrystals incorporating intragranular field fluctuations. *Philosophical Magazine* 87, 4287-4322.
- Lebensohn, R.A., Kanjarla, A.K., Eisenlohr, P., 2012. An elasto-viscoplastic formulation based on fast Fourier transforms for the prediction of micromechanical fields in polycrystalline materials. *International Journal of Plasticity* 32-33, 59-69.
- Livermore Software Technology Corporation (LSTC), 2007. *LS-DYNA Keyword User's Manual, Version 971*.
- Mánik, T., Holmedal, B., 2013. Additional relaxations in the Alamel texture model. *Materials Science and Engineering: A* 580, 349-354.
- Miodownik, M., Godfrey, A.W., Holm, E.A., Hughes, D.A., 1999. On boundary misorientation distribution functions and how to incorporate them into three-dimensional models of microstructural evolution. *Acta Materialia* 47, 2661-2668.
- Molinari, A., Canova, G.R., Ahzi, S., 1987. A self consistent approach of the large deformation polycrystal viscoplasticity. *Acta Metallurgica* 35, 2983-2994.
- Neumann, L., Kopp, R., Aretz, H., Crumbach, M., Goerdeler, M., Gottstein, G., 2005. Prediction of texture induced anisotropy by through-process modelling 495-497, 1657-1664.

- Patala, S., Mason, J.K., Schuh, C.A., 2012. Improved representations of misorientation information for grain boundary science and engineering. *Progress in Materials Science* 57, 1383-1425.
- Prakash, A., Lebensohn, R.A., 2009. Simulation of micromechanical behavior of polycrystals: finite elements versus fast Fourier transforms. *Modelling and Simulation in Materials Science and Engineering* 17, 064010.
- Peirce, D., Asaro, R.J., Needleman, A., 1982. An analysis of nonuniform and localized deformation in ductile single crystals. *Acta Metallurgica* 30, 1087-1119.
- Quey, R., Dawson, P.R., Barbe, F., 2011. Large-scale 3D random polycrystals for the finite element method: Generation, meshing and remeshing. *Computer Methods in Applied Mechanics and Engineering* 200, 1729-1745.
- Roters, F., Eisenlohr, P., Hantcherli, L., Tjahjanto, D.D., Bieler, T.R., Raabe, D., 2010. Overview of constitutive laws, kinematics, homogenization and multiscale methods in crystal plasticity finite-element modeling: Theory, experiments, applications. *Acta Materialia* 58, 1152-1211.
- Saai, A., Dumoulin, S., Hopperstad, O.S., Lademo, O.G., 2013. Simulation of yield surfaces for aluminium sheets with rolling and recrystallization textures. *Computational Materials Science* 67, 424-433.
- Sachs, G., 1928. Zur ableitung einer filebedingung. *Zeitschrift des Vereines Deutscher Ingenieure* 72, 734-736.
- Shutov, A.V., Ihlemann, J., 2012. A viscoplasticity model with an enhanced control of the yield surface distortion. *International Journal of Plasticity* 39, 152-167.
- Taylor, G.I., 1938. Plastic strain in metals. *Journal of the Institute of Metals* 62, 307-324.
- Tomé, C.N., 1999. Self-consistent polycrystal models: a directional compliance criterion to describe grain interactions. *Modelling and Simulation in Materials Science and Engineering* 7, 723-738.
- Toth, L.S. and Van Houtte, P., 1992. Discretization techniques for orientation distribution functions. *Textures and Microstructures* 19, 229-244.
- Tresca, H., 1864. Mémoire sur l'écoulement des corps solides soumis à de fortes pressions. *Comptes Rendus de l'Academie des Sciences, Paris* 59, 754-758.
- Van Houtte, P., 1982. On the equivalence of the relaxed Taylor theory and the Bishop-Hill theory for partially constrained plastic deformation of crystals. *Materials Science and Engineering* 55, 69-77.
- Van Houtte, P., 1988. A comprehensive mathematical formulation of an extended Taylor-Bishop-Hill model featuring relaxed constraints, the Renouard-Wintenberger theory and a strain rate sensitivity model. *Textures and Microstructures* 8, 313-350.
- Van Houtte, P., Delannay, L., Samajdar, I., 1999. Quantitative Prediction of Cold Rolling Textures in Low-Carbon Steel by Means of the Lamel Model. *Textures and Microstructures* 31, 109-149.

- Van Houtte, P., Delannay, L., Kalidindi, S.R., 2002. Comparison of two grain interaction models for polycrystal plasticity and deformation texture prediction. *International Journal of Plasticity* 18, 359-377.
- Van Houtte, P., Li, S., Seefeldt, M., Delannay, L., 2005. Deformation texture prediction: from the Taylor model to the advanced Lamel model. *International Journal of Plasticity* 21, 589-624.
- Van Houtte, P., Yerra, S.K., Van Bael, A., 2009. The Facet method: A hierarchical multilevel modelling scheme for anisotropic convex plastic potentials. *International Journal of Plasticity* 25, 332-360.
- Van Houtte, P., Gawad, J., Eyckens, P., Van Bael, A., Samaey, G., Roose, D., 2011. A full-field strategy to take texture-induced anisotropy into account during FE simulations of metal forming processes. *JOM: the Journal of the Minerals, Metals and Materials Society* 63, 37-43.
- Von Mises, R., 1913. *Mechanik der festen Körper im plastisch-deformablen Zustand*. Nachrichten von der Gesellschaft der Wissenschaften zu Göttingen, Mathematisch-Physikalische Klasse 1913, 582-593.
- Worswick, M.J., Finn, M.J., 2000. The numerical simulation of stretch flange forming. *International Journal of Plasticity* 16, 701-720.
- Yoon, J.-W., Barlat, F., Dick, R.E., Chung, K., Kang, T.J., 2004. Plane stress yield function for aluminum alloy sheets—part II: FE formulation and its implementation. *International Journal of Plasticity* 20, 495-522.
- Yoon, J.W., Barlat, F., Dick, R.E., Karabin, M.E., 2006. Prediction of six or eight ears in a drawn cup based on a new anisotropic yield function. *International Journal of Plasticity* 22, 174-193.
- Zhu, G., Mao, W., Yu, Y., 1999. Calculation of misorientation distribution between recrystallized grains and deformed matrix. *Scripta Materialia* 42, 37-41.
- Zhang, K., Holmedal, B., Manik, T., Zhao, Q., 2012. Crystal Plasticity Calculations of Mechanical Anisotropy of Aluminium Compared to Experiments and to Yield Criterion Fittings. ICAA13: 13th International Conference on Aluminum Alloys. John Wiley & Sons, Inc., pp. 915-920.
- Zhao, Z., Kuchnicki, S., Radovitzky, R., Cuitiño, A., 2007. Influence of in-grain mesh resolution on the prediction of deformation textures in fcc polycrystals by crystal plasticity FEM. *Acta Materialia* 55, 2361-2373.

Article 2

Use of plane-strain tension and shear tests to evaluate yield surfaces for AA1050 aluminium sheet

Kai Zhang^{1,a*}, Bjørn Holmedal^{1,b}, Odd Sture Hopperstad^{2,3,c}
and Stéphane Dumoulin^{4,d}

¹Department of Materials Science and Engineering, Norwegian University of Science and Technology, NO-7491 Trondheim, Norway

²Department of Structural Engineering, Norwegian University of Science and Technology, NO-7491 Trondheim, Norway

³Structural Impact Laboratory (SIMLab), Center for Research-based Innovation, Norwegian University of Science and Technology, NO-7491 Trondheim, Norway

⁴SINTEF Materials and Chemistry, NO-7465 Trondheim, Norway

^akai.zhang@ntnu.no, ^bbjorn.holmedal@ntnu.no, ^codd.hopperstad@ntnu.no,

^dStephane.Dumoulin@sintef.no

Accepted after peer-review for the **14th International Conference on Aluminium Alloys (ICAA14)**.

The conference proceeding will appear in the journal:
Materials Science Forum.

Use of plane-strain tension and shear tests to evaluate yield surfaces for AA1050 aluminium sheet

Abstract. Plane-strain tension and shear tests were carried out for a fully annealed AA1050 sheet. The tests were simulated numerically with a commercial finite element method (FEM) code using an anisotropic plasticity model including the Yld2004-18p yield function, the associated flow rule and isotropic hardening. The advanced yield function was calibrated by three different methods: using uniaxial tension data combined with FC-Taylor model predictions of the equibiaxial yield stress and r -value, using 201 virtual yield points in stress space, and using a combination of experimental data and virtual yield points (i.e., a hybrid method). The virtual stress points at yielding were provided by the recently proposed Alamel model with the so-called Type III relaxation (Alamel Type III model). FEM simulations of the tests were then made with parameters of Yld2004-18p identified by these three methods. Predicted force-displacement curves were compared to the experimental data, and the accuracy of the parameter identification methods for Yld2004-18p was evaluated based on these comparisons.

Keywords: Yld2004-18p, parameter identification, Alamel Type III model, multi-level modelling, finite element simulation

Introduction

The yield function is a key component for simulating plastic forming with FEM codes. Sheet metals commonly exhibit plastic anisotropy, i.e. direction-dependent strengths and flow patterns, which is mainly attributed to the crystallographic texture. Many advanced anisotropic yield functions that are capable of accurately describing the plastic anisotropy of aluminium alloys have been proposed in the last decade [1-3]. One example is the linear transformation-based Yld2004-18p yield function [2]. The parameters of an advanced yield function are conventionally identified by mechanical tests. However, the available mechanical tests are limited for sheet metals. Crystal plasticity (CP) calculations can be employed to facilitate the identification of anisotropic yield functions, i.e., using hierarchical multilevel modelling [4, 5].

In a recent work by the authors [5], the plastic anisotropy of a commercial pure aluminium sheet, AA1050, was measured by uniaxial tensile tests at every 15° from the rolling direction (RD) to the transverse direction (TD). With the measured texture as the main input, five different CP models were used to predict the anisotropic plastic behaviour. The Yld2004-18p yield function was identified by three methods: using uniaxial tension data combined with FC-Taylor model predictions of the equibiaxial yield

stress and r -value, using 201 virtual yield points in stress space, and using a combination of experimental data and virtual yield points.

As a continuation of [5], plane-strain tension and shear tests were conducted on the same material in this study. These tests were then simulated with the commercial FEM code LS-DYNA using an anisotropic plasticity model including the Yld2004-18p yield function, the associated flow rule and isotropic hardening. The Yld2004-18p yield function was identified by experiments and virtual equibiaxial yield stress and r -value, by virtual yield stress points provided by the Alamel Type III model [6, 7] and by a combination of experimental data and the virtual stress points, and then evaluated by comparison of experimental and predicted force-displacement curves.

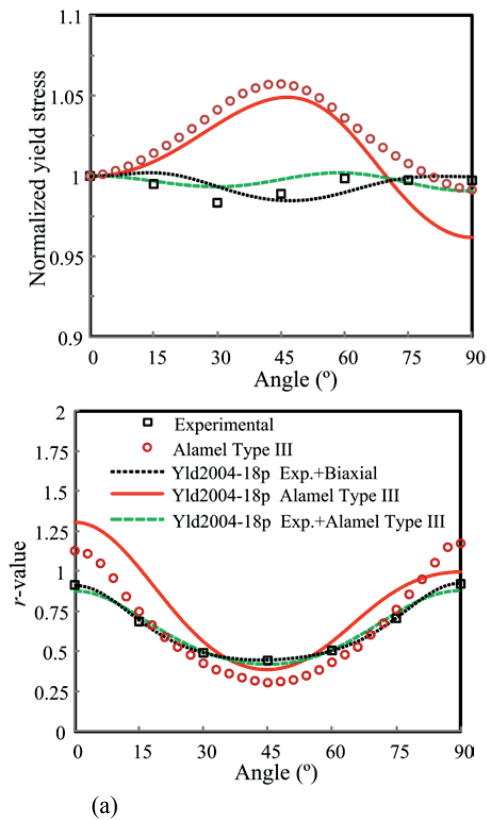


Figure 1 (a) Normalized yield stress and (b) r -value for AA1050 at different tensile directions with respect to RD obtained from experiments, the Alamel Type III model and predictions with Yld2004-18p calibrated by the three methods.

Material

The AA1050 sheet was of thickness 1.5mm. It was in a fully annealed state and the grain structure was almost equiaxed with a grain size of ~100 μm . The orientation distribution function (ODF) was measured by the EBSD technique. The cube orientation was the dominant texture component with a maximum intensity of about 18. Uniaxial tensile tests along 7 directions from RD to TD revealed that the material exhibits weak strength anisotropy but strong anisotropy in plastic flow, see Figure 1. Distortional hardening was observed from these tests, i.e. the strength anisotropy evolved with strain.

Parameter identification

The Yld2004-18p yield function and the parameter identification will be briefly described in this section, while the reader is referred to [5] for further details.

The Yld2004-18p yield function has an analytical expression as

$$\bar{\sigma}(\boldsymbol{\sigma}) = \frac{1}{4^{1/a}} \left(|S'_1 - S''_1|^a + |S'_1 - S''_2|^a + |S'_1 - S''_3|^a + |S'_2 - S''_1|^a + |S'_2 - S''_2|^a + |S'_2 - S''_3|^a + |S'_3 - S''_1|^a + |S'_3 - S''_2|^a + |S'_3 - S''_3|^a \right)^{1/a} \quad (1)$$

where $\bar{\sigma}$ is the equivalent stress; a is the exponent of the yield function; S'_i and S''_i , $i = 1, 2, 3$, are the principal values of the tensors $\mathbf{S}' = \mathbf{C}'\mathbf{S}$ and $\mathbf{S}'' = \mathbf{C}''\mathbf{S}$, where \mathbf{S} is the deviatoric stress tensor and \mathbf{C}' and \mathbf{C}'' are fourth-order tensors containing all the 18 parameters of the yield function.

The Yld2004-18p yield function was employed to describe the yield surface of the AA1050 material. The coefficients of the yield function were identified by three methods. Firstly, it was fitted to normalised yield stresses and r -values from uniaxial tensile tests along 7 directions. The experimental equi-biaxial flow stress and r -value were not available. Instead, they were provided by FC-Taylor calculations. The exponent was set to 8 following conventions for FCC metals. This method was denoted *Fit_Exp. + biaxial*. Secondly, the yield function was fitted to 201 yield stress points provided by Alamel Type III calculations. This method was denoted *Fit_Alamel Type III*. Thirdly, the experimental data (7 yield stresses and 7 r -values) and the 201 virtual stress points at yielding were combined to identify the parameters. The last method represents a hybrid fitting method and was termed *Fit_Exp. + Alamel Type III*.

When all coefficients of the Yld2004-18p equal unity, the yield function reduces to Hershey's isotropic yield function [8]. Optimized exponents of the isotropic

Yld2004-18p yield function for a randomly textured FCC polycrystal were identified for the FC-Taylor model, Alamel type models and the VPSC model along 1241 strain-paths [5]. It was found that when the exponent was 8 (nearest even integer), the isotropic yield function fitted best to the FC-Taylor stress points, while the exponent was 6 for the Alamel type models and the VPSC model. Hence, the exponent for the identifications *Fit_Alamel Type III* and *Fit_Exp. + Alamel Type III* was set to 6, while a value of 8 was used for the *Fit_Exp. + biaxial* identification, following the conventions for purely experimental fitting. The FC-Taylor model was chosen to provide the equal-biaxial data points because the FC-Taylor based isotropic yield function also has the same value of the exponent. Details about the parameter identifications, e.g. the error function, weighting factors and the fitting algorithm, can be found in [5]. As the identified coefficients were not shown in [5], they are compiled in Table 1.

The measured normalized yield stresses and r -values for the AA1050 sheet at different directions are plotted in Figure 1, where predicted results by the Alamel Type III model and by the Yld2004-18p yield function with parameters compiled in Table 1 are also shown.

Table 1 Yld2004-18p coefficients identified by three methods.

	Fit_Exp.+	Fit_Alamel	Fit_Exp.+	Fit_Exp.+	Fit_Alamel	Fit_Exp. +	
	Biaxial	Type III	Alamel Type III	Biaxial	Type III	Alamel Type III	
c'_{12}	0.6675	1.0893	1.3952	c''_{12}	0.6827	0.9232	0.5741
c'_{13}	0.9842	1.2371	1.5374	c''_{13}	0.8491	0.2354	-0.6093
c'_{21}	1.3155	0.5741	0.809	c''_{21}	0.7963	1.1698	0.7892
c'_{23}	1.2477	0.931	0.7741	c''_{23}	-0.032	1.192	1.1262
c'_{31}	0.0459	0.7879	0.928	c''_{31}	1.0476	0.9533	0.3695
c'_{32}	1.0818	0.8374	0.8402	c''_{32}	0.9001	1.0169	0.6886
c'_{44}	1.0	0.5453	0.5612	c''_{44}	1.0	1.1363	1.132
c'_{55}	1.0	1.1614	1.247	c''_{55}	1.0	0.5515	0.3961
c'_{66}	1.1455	1.0503	1.1333	c''_{66}	0.6563	0.6403	0.5924
a	8	6	6	-	-	-	-

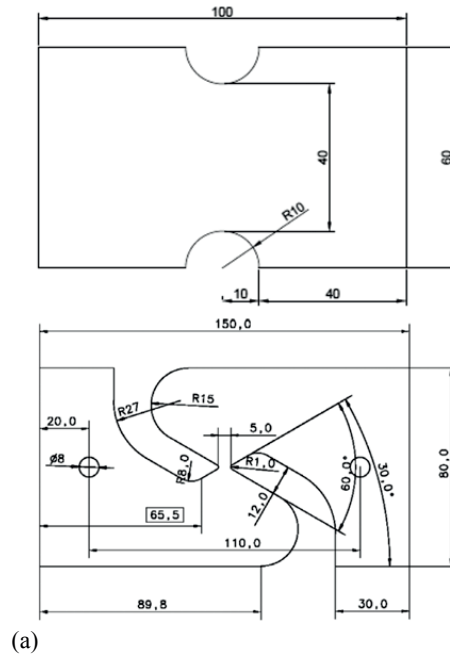


Figure 2 Geometries of test samples for (a) plane-strain tension and (b) shear [9].

Plane-strain tension and shear tests

The geometries of the plane-strain tension and shear test samples are illustrated in Figure 2. The samples were machined with the longitudinal directions being parallel with RD. The tests were carried out on a Zwick/Roell Z030 testing machine. During the plane-strain tension tests, the samples were clamped at 10 mm distances from the groove edges, while the cross-head speed was 0.6 mm/min. The displacement was recorded by an extensometer with a gauge length of 30 mm. During shear testing, the samples were mounted to the testing machine at the two outermost holes with bolts of a similar diameter [9]. The same loading speed was applied as in the plane-strain tension tests, and an extensometer with a gauge length of 70 mm was used to record displacements. The force was also recorded during testing. Each test was carried out two times. The measured force-displacement curves for the plane-strain tension and shear tests are shown in Figure 3 and Figure 4, respectively.

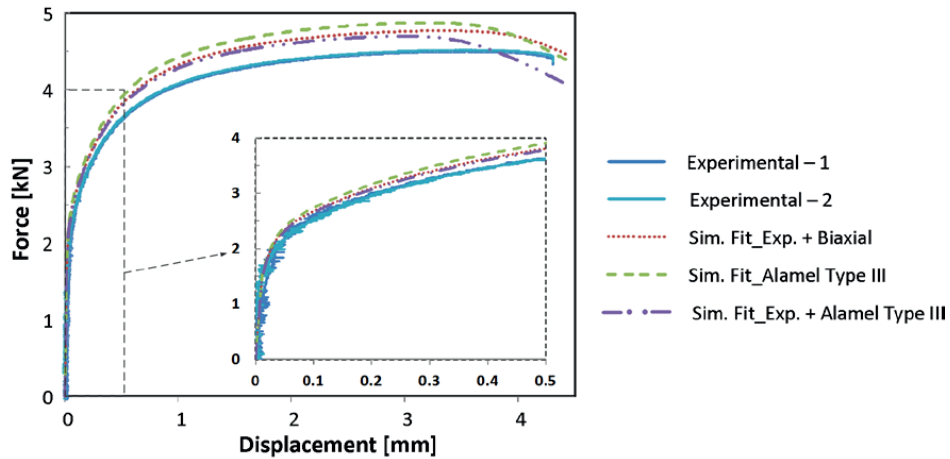


Figure 3 Force-displacement curves in plane-strain tension along RD from tests and FEM simulations.

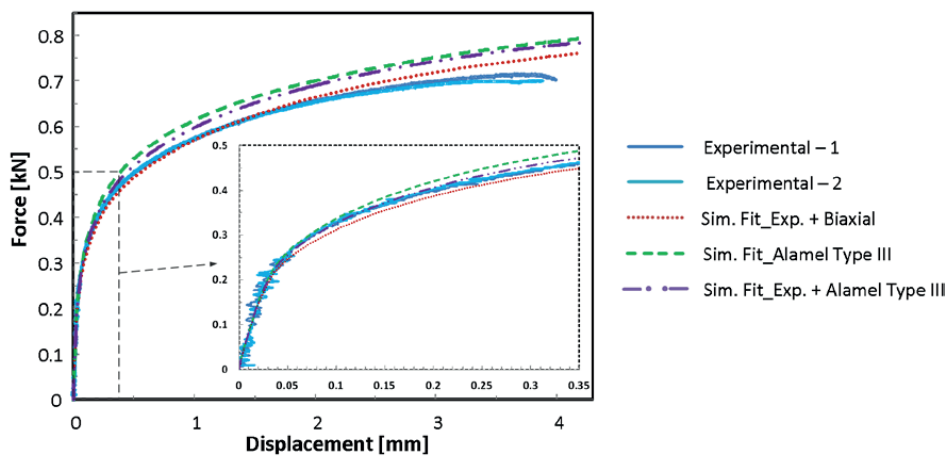


Figure 4 Force-displacement curves in shear along RD from tests and FEM simulations.

FEM simulations

An anisotropic plasticity model including the Yld2004-18p yield function, the associated flow rule and isotropic hardening has been implemented into LS-DYNA through a user-defined material subroutine (UMAT) [4]. The plane-strain tension and shear tests were simulated in LS-DYNA using solid elements. Isotropic hardening was described using the extended Voce rule, i.e.

$$\sigma_Y(\bar{\varepsilon}) = \sigma_0 + \sum_{i=1}^3 Q_i \left[1 - \exp\left(-\frac{\theta_i}{Q_i} \bar{\varepsilon}\right) \right] \quad (2)$$

where $\bar{\varepsilon}$ is the equivalent plastic strain, σ_0 is the yield stress in the reference direction, and Q_i and θ_i are hardening parameters. The hardening parameters and σ_0 were identified against the true stress vs. plastic strain curve (up to a plastic strain of 0.3) for the uniaxial tensile test in the RD of AA1050, using a least-squares fitting method. The fitted hardening parameters are compiled in Table 2. Uniaxial tension tests in RD were simulated in LS-DYNA with the parameters compiled in Table 1 and Table 2, and the predicted stress-strain curves accurately matched the experimental one (not included here). The same parameters were used for simulating the plane-strain tension and shear tests.

Table 2 Work-hardening parameters for AA1050 [MPa].

σ_0	Q_1	θ_1	Q_2	θ_2	Q_3	θ_3
19.51	12.92	21905	28.91	1924.4	52.17	187.7

FEM meshes for the plane-strain tension and shear test samples are illustrated in Figure 5. Only the unclamped part of the plane-strain tension sample was discretized. Solid elements with one integration points were used for both models, while there were 3 elements and 6 elements through the thickness direction for the plane-strain tension and shear test models, respectively. Constant velocities were applied at the loading points. The relative displacement between nodes N1 and N2 in Figure 5 (a) and nodes N3 and N4 in Figure 5 (b) were assumed to be equivalent to the measured displacements by the extensometers for respective tests. Forces were recorded at a cross-section of the FEM model during the simulation.

The predicted force-displacement curves obtained in the FEM simulations with different parameters of the Yld2004-18p yield function are shown in Figure 3 for the plane-strain tension test and in Figure 4 for the shear test. Curves at the initial loading/yielding are shown as inserts in both figures.

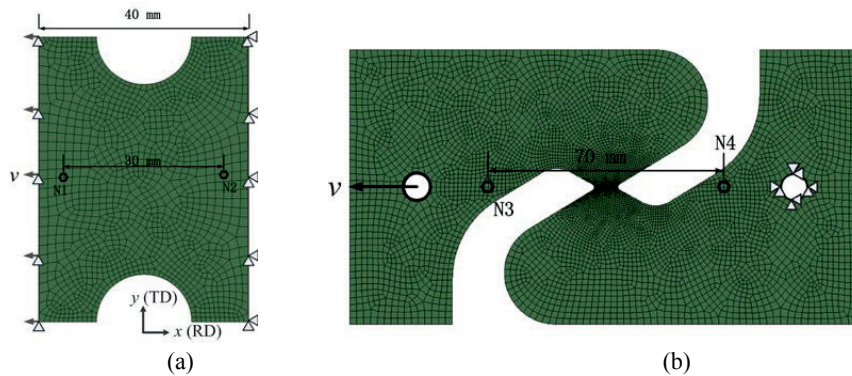


Figure 5 FEM models for (a) the plane-strain tension test and (b) the shear test. Triangular markers and arrows indicate the boundary conditions.

Discussion and conclusion

The directional normalized yield stresses and r -values obtained from experiments, the Alamel Type III model and the Yld2004-18p yield function with different identification methods are shown in Figure 1. The Yld2004-18p yield function identified by the uniaxial tensile tests and biaxial data points from a FC-Taylor simulation captures the experimental data accurately. The yield function fitted by the hybrid method gives very similar results, while the identification based solely on simulations with the Alamel Type III model is less accurate.

The experimental and predicted force-displacement curves for the plane-strain tension test are shown in Figure 3. The effective plastic strain at a displacement of 4 mm was about 0.5 in the FEM simulations. All simulations predicted higher forces than found in the experiments, but the prediction using the yield function obtained with the hybrid identification method is closest to the experiments. The prediction with the yield function identified solely from Alamel Type III simulations is the least accurate.

Figure 4 shows the results for the shear test. The effective plastic strains at displacements of 0.25 mm and 4 mm are about 0.05 and 1.0, respectively. Up to 0.25 mm displacement, the yield function identified with the hybrid method captured the experimental data with greatest accuracy, while for displacements larger than 2 mm all simulations predicted higher force levels than what was observed experimentally.

Based on results of the FEM simulations, the yield function identified by the hybrid method was most accurate for small displacements, while all identification methods led to too high force levels for large deformations. There are at least three possible explanations for the latter observation. First, the isotropic hardening rule was fitted up to necking in

uniaxial tension but used in the simulations up to significantly larger strains. Second, the distortional hardening of the material which was neglected in the simulations, may also contribute to the overestimation of the force level. Third, there may be an influence of the mesh size and element aspect ratio on the predictions.

The yield function obtained with the hybrid identification method and exponent $a = 6$ performed very well in terms of capturing the experimental uniaxial tensile data and the force-displacement curves of the plane-strain tension and shear tests at strains smaller than about 5%. Compared to the hybrid identification method, the yield function identified mainly to the uniaxial tensile results performed similarly for the plane-strain tension test and even better at large strains for the shear test. The yield functions identified mainly or partially to the experimental data performed better than the yield function identified solely by CP simulations.

References

- [1] F. Barlat, H. Aretz, J.W. Yoon, M.E. Karabin, J.C. Brem and R.E. Dick, Linear transformation-based anisotropic yield functions, *Int. J. Plast.*, 21 (2005) 1009-1039.
- [2] D. Banabic, H. Aretz, D.S. Comsa and L. Paraianu, An improved analytical description of orthotropy in metallic sheets, *Int. J. Plast.*, 21 (2005) 493-512.
- [3] H. Aretz and F. Barlat, New convex yield functions for orthotropic metal plasticity, *Int. J. Nonlin. Mech.*, 51 (2013) 97-111.
- [4] F. Grytten, B. Holmedal, O.S. Hopperstad and T. Børvik, Evaluation of identification methods for YLD2004-18p, *Int. J. Plast.*, 24 (2008) 2248-2277.
- [5] K. Zhang, B. Holmedal, O.S. Hopperstad, S. Dumoulin, J. Gawad, A. Van Bael and P. Van Houtte, Multi-level Modelling of Mechanical Anisotropy of Commercial Pure Aluminium Plate: Crystal Plasticity Models, Advanced Yield Functions and Parameter Identification, *Int. J. Plast.*, (2014). doi: 10.1016/j.ijplas.2014.02.003
- [6] P. Van Houtte, S. Li, M. Seefeldt and L. Delannay, Deformation texture prediction: from the Taylor model to the advanced Lamel model, *Int. J. Plast.*, 21 (2005) 589-624.
- [7] T. Mánik and B. Holmedal, Additional relaxations in the Alamel texture model, *Mater. Sci. Eng., A*, 580 (2013) 349-354.
- [8] A. Hershey, The plasticity of an isotropic aggregate of anisotropic face centred cubic crystals, *Journal of Applied Mechanics*, 21 (1954) 241-249.
- [9] A. Reyes, M. Eriksson, O.G. Lademo, O.S. Hopperstad and M. Langseth, Assessment of yield and fracture criteria using shear and bending tests, *Materials & Design*, 30 (2009) 596-608.

Article 3

A robust and efficient substepping scheme for the explicit numerical integration of a rate-dependent crystal plasticity model

K. Zhang¹, O.S. Hopperstad^{2,3}, B. Holmedal¹, S. Dumoulin⁴

1. Department of Materials Science and Engineering, Norwegian University of Science and Technology, NO-7491 Trondheim, Norway

2. Department of Structural Engineering, Norwegian University of Science and Technology, NO-7491 Trondheim, Norway

3. Structural Impact Laboratory (SIMLab), Center for Research-based Innovation, Norwegian University of Science and Technology, NO-7491 Trondheim, Norway

4. SINTEF Materials and Chemistry, NO-7465 Trondheim, Norway

International Journal for Numerical Methods in Engineering, 2014

DOI: 10.1002/nme.4671

A robust and efficient substepping scheme for the explicit numerical integration of a rate-dependent crystal plasticity model

Abstract

This paper describes the development of efficient and robust numerical integration schemes for rate-dependent crystal plasticity models. A forward Euler integration algorithm is first formulated. An integration algorithm based on the modified Euler method with an adaptive substepping scheme is then proposed, where the substepping is mainly controlled by the local error of the stress predictions within the time step. Both integration algorithms are implemented in a stand-alone code with the Taylor aggregate assumption and in an explicit finite element code. The robustness, accuracy and efficiency of the substepping scheme are extensively evaluated for large time steps, extremely low strain-rate sensitivity, high deformation rates and strain-path changes using the stand-alone code. The results show that the substepping scheme is robust and in some cases one order of magnitude faster than the forward Euler algorithm. The use of mass scaling to reduce computation time in crystal plasticity finite element simulations for quasi-static problems is also discussed. Finally, simulation of Taylor bar impact test is carried out to show the applicability and robustness of the proposed integration algorithm for the modelling of dynamic problems with contact.

Keywords: crystal plasticity, forward Euler method, modified Euler method, adaptive substepping, stability, dynamic problems

1. Introduction

The mechanisms of plastic deformation of metals, e.g. slip and twinning, are well described by single crystal plasticity models. Slip is the dominant mechanism in face centred cubic (FCC) and body centred cubic (BCC) metals and can be described either by rate-independent or rate-dependent single crystal plasticity models, see Mánik and Holmedal [1] for a review. Rate-dependent crystal plasticity (RDCP) models commonly assume viscoplasticity, i.e. that all slip systems are active during plastic deformation and that the slip activity is determined via a power-law type equation [2, 3]. Since most metals exhibit weak rate dependence at room temperature, the RDCP models with power-law type crystallographic flow rules are highly non-linear and could lead to numerical instabilities in the temporal integration [4]. Many research efforts have been made to propose efficient and robust integration algorithms for various RDCP models [5-13]. Ling *et al.* [13] and Dumoulin *et al.* [14] evaluated several implicit and explicit

constitutive update schemes for RDCP models, and found that the explicit schemes are much more time efficient than the implicit ones but are only conditionally stable.

The combination of crystal plasticity with the finite element method (CPFEM) opens up for a wide range of applications [15]. In many applications, such as in impact dynamics, explicit finite element methods are most often used, in which the stable time step is determined by the Courant-Freidrichs-Lewy criterion [16]. The stable time step is then found to depend on the element size and the speed of sound in the material, and to achieve large deformations in the material with fine resolution of the stress and strain fields a large number of time steps are required.

In classical explicit integration schemes for differential equations, the accuracy depends significantly on the size of the selected time step. Sloan [17] proposed an automatic time stepping with error control for temporal integration of the elastic-plastic constitutive relations. This numerical technique, widely used in the field of numerical analysis, is based on extrapolation procedures using for instance the modified Euler method or the Runge-Kutta method. The use of automatic substepping and time stepping algorithms with error control overcomes the main limitation of explicit techniques, since the system adapts as the estimated error changes [18]. Substepping schemes for integrating RDCP models also exist. van der Giessen and Neale [19] proposed an adaptive time stepping method to ensure that the increments of several pertinent quantities remain within user-defined bounds, but this method was particularly proposed for simulating the torsion of a cylindrical bar or tube. Kuchnicki *et al.* [8] proposed an explicit integration method with a subcycling algorithm in order to work around the maximal time step limitation of their explicit model, but apparent stress oscillations occurred when large time increments were applied. Besides, both substepping methods mentioned above have no estimate of the error during the integration process. Substepping is very important for contact problems since the contact algorithm might introduce large strain increments and strain rates locally.

In this work, we extend the adaptive substepping scheme based on the modified Euler method [17] to integrate RDCP models in time. The accuracy, efficiency and stability of the substepping scheme is extensively investigated, considering large time steps, extremely low strain-rate sensitivity in the power-law type flow rules, large strain rates and strain-path changes. The mass scaling technique is also discussed for CPFEM with the purpose of speeding up explicit finite element simulations of quasi-static deformation processes. Simulation of the Taylor bar impact test is conducted to illustrate the extremely good stability of the substepping scheme in a problem involving large deformations, high strain rates and contact.

The paper is organized as follows. The crystal plasticity models are described in section 2. In section 3, the new explicit integration scheme is presented and procedures of adaptive substepping based on the modified Euler method are proposed. The integration

algorithms are evaluated for simple cases in section 4, using a stand-alone code based on the full-constraint Taylor hypothesis, while CPFEM is used to evaluate the algorithms for more complex cases in section 5. The conclusions of the research work are found in section 6.

2. Crystal plasticity model

The mathematical formulation of the crystal plasticity model is described in this section. The model is developed for metals and alloys, assuming that plastic deformation occurs via slip on crystallographic slip systems. It is further assumed that the elastic deformations are infinitesimal, while plastic deformations and rotations may be finite.

2.1. Single crystal plasticity

In addition to the global or sample coordinate system (or frame) with basis \mathbf{e}_i^g , $i = 1, 2, 3$, two additional coordinate systems will be employed for defining vector and tensor components. The first one is the initial lattice frame with basis \mathbf{e}_i that coincides with the three orthogonal axes of the cubic lattice at the beginning of deformation. The other is the co-rotational lattice frame with basis $\hat{\mathbf{e}}_i$ which coincides with the lattice after deformation. The rotation of the lattice is defined by an orthogonal rotation tensor \mathfrak{R} . The sample and initial lattice frames are stationary, while the co-rotational frame changes as the deformation proceeds. The coordinate transformation between the initial and co-rotational lattice frames reads

$$\hat{\mathbf{v}} = \mathfrak{R}^T \cdot \mathbf{v}, \quad \mathbf{v} = \mathfrak{R} \cdot \hat{\mathbf{v}} \quad (1)$$

$$\hat{\mathbf{T}} = \mathfrak{R}^T \cdot \mathbf{T} \cdot \mathfrak{R}, \quad \mathbf{T} = \mathfrak{R} \cdot \hat{\mathbf{T}} \cdot \mathfrak{R}^T \quad (2)$$

where \mathbf{v} is a vector and \mathbf{T} is a second-order tensor with components referred to the initial lattice frame. Hence, $\hat{\mathbf{v}}$ is the same vector as \mathbf{v} but with components referred to the co-rotational coordinate system. The same convention is used for tensors. The transformation matrix \mathbf{Q} from the global frame to the current co-rotational lattice frame is determined as:

$$\mathbf{Q} = \mathfrak{R}^T \cdot \mathbf{Q}_0 \quad (3)$$

where \mathbf{Q}_0 is the transformation matrix from the sample frame to the initial lattice frame. Then

$$\hat{\mathbf{v}} = \mathbf{Q} \cdot \mathbf{v}^g, \quad \mathbf{v}^g = \mathbf{Q}^T \cdot \hat{\mathbf{v}} \quad (4)$$

$$\hat{\mathbf{T}} = \mathbf{Q} \cdot \mathbf{T}^g \cdot \mathbf{Q}^T, \quad \mathbf{T}^g = \mathbf{Q}^T \cdot \hat{\mathbf{T}} \cdot \mathbf{Q} \quad (5)$$

where the notation \mathbf{v}^g and \mathbf{T}^g implies that the components of the vector and tensor are referred to the sample frame.

The velocity gradient \mathbf{L} can be additively decomposed into symmetric and skew-symmetric parts:

$$\mathbf{L} = \mathbf{D} + \mathbf{W} \quad (6)$$

where \mathbf{D} is the symmetric deformation rate tensor and \mathbf{W} is the skew-symmetric spin tensor. The tensors \mathbf{D} and \mathbf{W} can be further decomposed into lattice and plastic parts:

$$\mathbf{D} = \mathbf{D}^e + \mathbf{D}^p \quad (7)$$

$$\mathbf{W} = \mathbf{W}^e + \mathbf{W}^p \quad (8)$$

where \mathbf{D}^e represents the elastic deformation rate of the lattice and \mathbf{D}^p is the plastic deformation rate caused by crystallographic slip. The rigid spin of the lattice is represented by \mathbf{W}^e , while \mathbf{W}^p is the spin due to slip activities. The elastic spin is negligible since infinitesimal elastic deformation is assumed. The tensors \mathbf{D}^p and \mathbf{W}^p can be expressed by the shear rates $\dot{\gamma}^\alpha$ on all slip systems:

$$\mathbf{D}^p = \sum_{\alpha=1}^N \dot{\gamma}^\alpha \mathbf{P}^\alpha \quad (9)$$

$$\mathbf{W}^p = \sum_{\alpha=1}^N \dot{\gamma}^\alpha \mathbf{\Omega}^\alpha \quad (10)$$

where N is the number of slip systems, and \mathbf{P}^α and $\mathbf{\Omega}^\alpha$ are the symmetric and skew-symmetric parts of the Schmid tensor \mathbf{M}^α , respectively:

$$\mathbf{M}^\alpha = \mathbf{m}^\alpha \otimes \mathbf{n}^\alpha \quad (11)$$

where \mathbf{m}^α is the unit vector defining slip direction, while \mathbf{n}^α is the unit slip plane normal vector, for the slip system α (where $\alpha=1-12$ for FCC metals). Thus

$$\mathbf{P}^\alpha = \frac{1}{2} (\mathbf{m}^\alpha \otimes \mathbf{n}^\alpha + \mathbf{n}^\alpha \otimes \mathbf{m}^\alpha) \quad (12)$$

$$\mathbf{\Omega}^\alpha = \frac{1}{2} (\mathbf{m}^\alpha \otimes \mathbf{n}^\alpha - \mathbf{n}^\alpha \otimes \mathbf{m}^\alpha) \quad (13)$$

The unit vectors \mathbf{m}^α and \mathbf{n}^α are not affected by crystallographic slip, and are defined by

$$\mathbf{m}^\alpha = \mathfrak{R} \cdot \hat{\mathbf{m}}^\alpha, \quad \mathbf{n}^\alpha = \mathfrak{R} \cdot \hat{\mathbf{n}}^\alpha \quad (14)$$

where $\hat{\mathbf{m}}^\alpha$ and $\hat{\mathbf{n}}^\alpha$ define the slip system in the co-rotational frame, and the orthogonal rotation tensor \mathfrak{R} is defined by the differential equation

$$\dot{\mathfrak{R}} = \mathbf{W}^* \cdot \mathfrak{R} \quad (15)$$

The Schmid tensor $\hat{\mathbf{M}}^\alpha$ with respect to the co-rotational frame is then defined as

$$\hat{\mathbf{M}}^\alpha = \hat{\mathbf{m}}^\alpha \otimes \hat{\mathbf{n}}^\alpha \quad (16)$$

while $\hat{\mathbf{P}}^\alpha$ and $\hat{\mathbf{Q}}^\alpha$ are the symmetric and skew-symmetric parts of $\hat{\mathbf{M}}^\alpha$, respectively. Using Eq. (11), (14) and (16), we get

$$\mathbf{M}^\alpha = \mathfrak{R} \cdot \hat{\mathbf{M}}^\alpha \cdot \mathfrak{R}^\top \quad (17)$$

The vectors $\hat{\mathbf{m}}^\alpha$ and $\hat{\mathbf{n}}^\alpha$ refer to the co-rotational frame and have constant components, and so does the Schmid tensor $\hat{\mathbf{M}}^\alpha$.

The resolved shear stress τ^α on the slip system α can be expressed as:

$$\tau^\alpha = \boldsymbol{\sigma} : \mathbf{P}^\alpha = \hat{\boldsymbol{\sigma}} : \hat{\mathbf{P}}^\alpha \quad (18)$$

where $\boldsymbol{\sigma}$ and $\hat{\boldsymbol{\sigma}}$ are the Cauchy stress tensor expressed in the initial and co-rotational lattice frames, respectively.

In the co-rotational lattice frame, Hooke's law can be expressed in the rate form as:

$$\dot{\hat{\boldsymbol{\sigma}}} = \hat{\mathbf{C}} : \hat{\mathbf{D}}^e \quad (19)$$

where $\hat{\mathbf{C}}$ is a fourth-order elastic modulus tensor and $\hat{\mathbf{D}}^e$ is the elastic deformation rate tensor, both in the co-rotational frame. The fourth-order tensor $\hat{\mathbf{C}}$ accounts for the elastic anisotropy of the cubic lattice. It is assumed to be invariant to plastic deformation and is kept constant in the co-rotational lattice frame. Expressed in the orthonormal basis associated with the crystal lattice, it reads (in Voigt notation):

$$\hat{\mathbf{C}} = \begin{bmatrix} c_{11} & c_{12} & c_{12} & 0 & 0 & 0 \\ c_{12} & c_{11} & c_{12} & 0 & 0 & 0 \\ c_{12} & c_{12} & c_{11} & 0 & 0 & 0 \\ 0 & 0 & 0 & c_{44} & 0 & 0 \\ 0 & 0 & 0 & 0 & c_{44} & 0 \\ 0 & 0 & 0 & 0 & 0 & c_{44} \end{bmatrix} \quad (20)$$

where c_{11} , c_{12} and c_{44} are three independent elastic constants. The elastic deformation rate tensor $\hat{\mathbf{D}}^e$ is computed according to Eq. (7) with the tensors expressed in the corotational lattice frame. The Jaumann stress rate $\sigma^{\nabla J}$ is then defined by transforming $\dot{\hat{\sigma}}$ into the initial lattice frame, i.e.

$$\sigma^{\nabla J} = \mathfrak{R} \cdot \dot{\hat{\sigma}} \cdot \mathfrak{R}^T \quad (21)$$

Finally, the material time derivative of the Cauchy stress tensor is obtained as

$$\dot{\sigma} = \sigma^{\nabla J} + \mathbf{W}^* \cdot \sigma - \sigma \cdot \mathbf{W}^* \quad (22)$$

The shear rate on the slip systems is calculated using a power-law equation:

$$\dot{\gamma}^\alpha = \dot{\gamma}_0 \left| \frac{\tau^\alpha}{g^\alpha} \right|^{\frac{1}{m}} \text{sgn}(\tau^\alpha) \quad (23)$$

where $\dot{\gamma}_0$ is a reference shearing rate, m is the instantaneous strain-rate sensitivity and g^α represents the slip resistance which evolves during the plastic deformation according to the hardening law. The hardening law used here assumes that the critical resolved shear stress g^α , which is initially equal to g_0 , evolves through

$$\dot{g}^\alpha = \sum_{\beta=1}^N h^{\alpha\beta} |\dot{\gamma}^\beta| \quad (24)$$

where $h^{\alpha\beta}$ is the instantaneous strain hardening matrix. In this work, $h^{\alpha\beta}$ is described phenomenologically by a saturation-type law [5]:

$$h^{\alpha\beta} = h_0 [q + (1-q)\delta^{\alpha\beta}] [1 - g^\beta / g_{sat}]^a \text{sgn}[1 - g^\beta / g_{sat}] \quad (25)$$

where $\delta^{\alpha\beta}$ is the Kronecker delta function; h_0 , g_{sat} and a are material parameters, representing the reference self-hardening coefficient, the saturation values of slip resistance and the hardening exponent, respectively. The parameter q represents latent hardening.

Other single crystal models, in terms of flow rules and work hardening laws, exist in the literature, e.g. Cuitino and Ortiz [6] and Buchheit *et al.* [20].

2.2. Polycrystal plasticity

Most engineering metals are polycrystalline and the constitutive model described above can be applied to polycrystal plasticity by use of CPFEM, where the grains are explicitly resolved. Alternatively, less time consuming, simplified Taylor-type of

models [21] are applied, for which a statistical aggregate of grain orientations is considered.

The Cauchy stress at the material point, here denoted $\boldsymbol{\sigma}^g$, because it is most often expressed in the sample frame, is the volume-averaged stress of all the grains. If all grains are assumed to have the same volume, the volume-averaged stress may be expressed as:

$$\boldsymbol{\sigma}^g = \frac{1}{N_g} \sum_{i=1}^{N_g} \boldsymbol{\sigma}_i^g \quad (26)$$

where N_g is the number of grains.

3. Temporal integration schemes

Two explicit integration schemes are proposed in this work for the RDCP model described above. The first one is a fully explicit method based on the first-order forward Euler method, while the second one is featured with adaptive substepping and employs the modified Euler method within each substep. The modified Euler method is an extension of the forward Euler method into a two-stage, second-order Runge-Kutta method [22].

3.1. Forward Euler method

A fully explicit integration algorithm based on the forward Euler method with application to the RDCP model in section 2 is proposed here. The main steps of this scheme are summarized below. It is assumed that all variables at time t_n are known in the initial lattice frame and the task is to determine the same variables at time $t_{n+1} = t_n + \Delta t$.

- a) Compute the deformation rate tensor $\mathbf{D}_n = \frac{1}{2}(\mathbf{L}_n + \mathbf{L}_n^T)$ and the spin tensor $\mathbf{W}_n = \frac{1}{2}(\mathbf{L}_n - \mathbf{L}_n^T)$, which are assumed to be constant during the time step Δt .
- b) Compute the stress tensor $\hat{\boldsymbol{\sigma}}_n = \boldsymbol{\mathfrak{R}}_n^T \cdot \boldsymbol{\sigma}_n \cdot \boldsymbol{\mathfrak{R}}_n$ and deformation rate tensor $\hat{\mathbf{D}}_n = \boldsymbol{\mathfrak{R}}_n^T \cdot \mathbf{D}_n \cdot \boldsymbol{\mathfrak{R}}_n$ in the co-rotational lattice frame.
- c) Compute the resolved shear stresses $\tau_n^\alpha = \hat{\boldsymbol{\sigma}}_n : \hat{\mathbf{P}}^\alpha$ and the shearing rates $\dot{\gamma}_n^\alpha = \dot{\gamma}_0 \left| \tau_n^\alpha / g_n^\alpha \right|^{1/m} \text{sgn}(\tau_n^\alpha)$ on all slip systems.

- d) Compute the plastic and elastic deformation rate tensors $\hat{\mathbf{D}}_n^p = \sum_{\alpha=1}^N \dot{\gamma}_n^\alpha \hat{\mathbf{P}}^\alpha$ and $\hat{\mathbf{D}}_n^e = \hat{\mathbf{D}}_n - \hat{\mathbf{D}}_n^p$, and the plastic spin tensor $\hat{\mathbf{W}}_n^p = \sum_{\alpha=1}^N \dot{\gamma}_n^\alpha \hat{\mathbf{\Omega}}^\alpha$, all in the co-rotational lattice frame.
- e) Compute the plastic spin tensor $\mathbf{W}_n^p = \mathfrak{R}_n \cdot \hat{\mathbf{W}}_n^p \cdot \mathfrak{R}_n^T$ and the lattice spin tensor $\mathbf{W}_n^* = \mathbf{W}_n - \mathbf{W}_n^p$ in the initial lattice frame.
- f) Compute the Jaumann stress rate: $\dot{\boldsymbol{\sigma}}_n^{\nabla J} = \mathfrak{R}_n \cdot \dot{\hat{\boldsymbol{\sigma}}}_n \cdot \mathfrak{R}_n^T = \mathfrak{R}_n \cdot (\hat{\mathbf{C}} : \hat{\mathbf{D}}_n^e) \cdot \mathfrak{R}_n^T$
- g) Compute the material time derivative of the stress tensor in the initial lattice frame as $\dot{\boldsymbol{\sigma}}_n = \boldsymbol{\sigma}_n^{\nabla J} + \mathbf{W}_n^* \cdot \boldsymbol{\sigma}_n - \boldsymbol{\sigma}_n \cdot \mathbf{W}_n^*$ and update the stress tensor according to

$$\boldsymbol{\sigma}_{n+1} = \boldsymbol{\sigma}_n + \dot{\boldsymbol{\sigma}}_n \Delta t \quad (27)$$

- h) Update the critical resolved shear stresses according to $g_{n+1}^\alpha = g_n^\alpha + \dot{g}_n^\alpha \Delta t$, where $\dot{g}_n^\alpha = \sum_{\beta=1}^N h^{\alpha\beta} |\dot{\gamma}_n^\beta|$ and $h^{\alpha\beta}$ is calculated according to Eq. (25)
- i) Update the rotation tensor \mathfrak{R}_{n+1} using a second-order scheme [23] as

$$\mathfrak{R}_{n+1} = \left(\mathbf{I} - \frac{1}{2} \mathbf{W}_n^* \Delta t \right)^{-1} \cdot \left(\mathbf{I} + \frac{1}{2} \mathbf{W}_n^* \Delta t \right) \cdot \mathfrak{R}_n \quad (28)$$

where \mathbf{I} is the identity tensor.

- j) Update the grain orientation matrix as $\mathbf{Q}_{n+1} = \mathfrak{R}_{n+1}^T \cdot \mathbf{Q}_0$.

This integration scheme is theoretically equivalent to the one proposed by Zhang *et al.* [11] where formulations of the same RDCP model are mainly expressed and integrated in the initial lattice frame. The vectors \mathbf{m}^α and \mathbf{n}^α as well as the Schmid tensor \mathbf{M}^α then need to be continuously updated at every time step, while this is not required in the current scheme. Hence, the forward Euler scheme proposed here should have the same accuracy and somewhat higher efficiency than the one proposed by Zhang *et al.* [11].

It is well known that the forward Euler integration scheme is only conditionally stable. If the time step exceeds a critical value Δt_{crit} , which is also called the stable time step, the solution will grow unboundedly. For RDCP models, the flow rules, such as Eq. (23), are very stiff. The reason is the low strain-rate sensitivity of metals at room temperature, and $\dot{\gamma}^\alpha$ can readily attain very high values even if τ^α is only slightly greater than g^α , which might lead to instabilities in the integration algorithm. In practice, instability is detected when

$$\dot{\gamma}^\alpha \Delta t \geq \Delta \gamma_{crit} \quad (29)$$

where $\Delta\gamma_{crit}$ is a critical shear increment. Eq. (29) was employed also in the work by van der Giessen and Neale [19] in order to estimate the stable time step when integrating the RDCP model, where $\Delta\gamma_{crit}$ was set to a small value, 0.0025. It should be noted that limiting the shear increment per step to a small value cannot always ensure a stable integration. In addition to the constraint set by Eq. (29), other criteria [19] or advanced integration schemes should be used to keep the stability when integrating RDCP models.

3.2. Modified Euler method with adaptive substepping

Following the work of Sloan [17], a modified Euler method with adaptive substepping and error control is proposed here for temporal integration of the RDCP model. The Adaptive Sub-Stepping scheme with the Modified Euler method is denoted the ASSME method in the following. The substepping in the ASSME is controlled by the shear increment and by the error of the stress increment, while the second criterion plays the main role.

All variables at time t_n are known in the initial lattice frame and variables at $t_{n+1} = t_n + \Delta t$ are going to be determined. Instead of integrating directly over Δt in one step as in the forward Euler method proposed in section 3.1, the interval will be subdivided into NS ($NS \geq 1$) substeps. NS is equal to one at the beginning of Δt and will increase monotonically as the substepping proceeds. The velocity gradient \mathbf{L}_n is constant over Δt and all the substeps within it. Each substep has a time increment $\Delta t_{(i)} = \alpha_{(i)} \Delta t$, where $\alpha_{(i)}$ is a substep time factor for substep number i ($i = 1, 2, \dots, NS$) and is defined according to

$$\begin{cases} 0 < \alpha_{(i)} \leq 1 \\ \sum_{i=1}^{NS} \alpha_{(i)} = 1 \end{cases} \quad (30)$$

It is noted that $\alpha_{(i)}$ is not necessarily the same for all substeps.

For each substep, the modified Euler method is used to integrate the constitutive equations. The modified Euler method involves two forward Euler integration steps, where the forward Euler method proposed in section 3.1 is used for each step. The adaptive substepping scheme will be illustrated by describing the procedure for substep $i+1$ between t_n and t_{n+1} . All variables are known at the end of the last substep, or equivalently at the beginning of the current substep, which starts at time $t_{(i)} = t_n + \sum_{j=1}^i \alpha_{(j)} \Delta t = t_n + \sum_{j=1}^i \Delta t_{(j)}$. It is noted that $t_{(0)} = t_n$, which corresponds to the

beginning of the first substep within Δt . The updated variables at $t_{(i+1)}$ are computed as follows.

- A. The velocity gradient is assumed constant and equal to \mathbf{L}_n during the time increment $\Delta t = t_{n+1} - t_n$. The provisional time step is $\Delta t_{(i+1)} = \alpha_{(i+1)} \Delta t$. Use the forward Euler scheme with rates at $t_{(i)}$, e.g. $\dot{\boldsymbol{\sigma}}_{(i)}$, $\dot{\boldsymbol{g}}_{(i)}^s$, $\dot{\boldsymbol{\gamma}}_{(i)}^s$ and $\mathbf{W}_{(i)}^*$, to compute intermediate variables at time $t_{(i+1)}$, e.g. $\tilde{\boldsymbol{\sigma}}_{(i+1)}$, $\tilde{\boldsymbol{\mathfrak{R}}}_{(i+1)}$ and $\tilde{\boldsymbol{g}}_{(i+1)}^s$.
- B. Based on these intermediate variables, compute rates at time $t_{(i+1)}$, e.g. $\tilde{\dot{\boldsymbol{\sigma}}}_{(i+1)}$, $\tilde{\dot{\boldsymbol{g}}}_{(i+1)}^s$, $\tilde{\dot{\boldsymbol{\gamma}}}_{(i+1)}^s$ and $\tilde{\mathbf{W}}_{(i+1)}^*$.
- C. Check the stability of the integration according to Eq. (29), and if $\tilde{\dot{\boldsymbol{\gamma}}}_{(i+1)}^s \Delta t_{(i+1)} > \Delta \gamma_{crit}$, decrease the time factor as

$$\alpha_{(i+1)} \leftarrow 0.5 \cdot \alpha_{(i+1)} \quad (31)$$

Return to step A.

- D. Else, compute the relative error in the stress increment based on the two steps, defined here as

$$ERR = \frac{\left\| \tilde{\boldsymbol{\sigma}}_{(i+1)} - \dot{\boldsymbol{\sigma}}_{(i)} \right\| \Delta t_{(i+1)}}{\left\| \dot{\boldsymbol{\sigma}}_{(i)} + (\tilde{\dot{\boldsymbol{\sigma}}}_{(i+1)} + \dot{\boldsymbol{\sigma}}_{(i)}) \frac{\Delta t_{(i+1)}}{2} \right\|} \quad (32)$$

- E. If $ERR > TOL$ (typical range is $10^{-2} \sim 10^{-5}$), decrease the time factor as

$$\alpha_{(i+1)} \leftarrow \lambda \cdot \alpha_{(i+1)} \quad (33)$$

where [17]

$$\lambda = \max \left\{ 0.1, 0.8 \left[\frac{TOL}{ERR} \right]^{1/2} \right\} \quad (34)$$

Return to step A.

- F. If $ERR \leq TOL$, calculate rates at the midpoint of $\Delta t_{(i+1)}$ as

$$\begin{aligned} \dot{\boldsymbol{\sigma}}_{(i+1/2)} &= (\tilde{\dot{\boldsymbol{\sigma}}}_{(i+1)} + \dot{\boldsymbol{\sigma}}_{(i)}) / 2 \\ \dot{\boldsymbol{g}}_{(i+1/2)}^s &= (\tilde{\dot{\boldsymbol{g}}}_{(i+1)}^s + \dot{\boldsymbol{g}}_{(i)}^s) / 2 \\ \dot{\boldsymbol{\gamma}}_{(i+1/2)}^s &= (\tilde{\dot{\boldsymbol{\gamma}}}_{(i+1)}^s + \dot{\boldsymbol{\gamma}}_{(i)}^s) / 2 \\ \mathbf{W}_{(i+1/2)}^* &= (\tilde{\mathbf{W}}_{(i+1)}^* + \mathbf{W}_{(i)}^*) / 2 \end{aligned} \quad (35)$$

and update variables at $t_{(i+1)}$ according to

$$\begin{aligned}
\boldsymbol{\sigma}_{(i+1)} &= \boldsymbol{\sigma}_{(i)} + \dot{\boldsymbol{\sigma}}_{(i+1/2)} \Delta t_{(i+1)} \\
\boldsymbol{g}_{(i+1)}^s &= \boldsymbol{g}_{(i)}^s + \dot{\boldsymbol{g}}_{(i+1/2)}^s \Delta t_{(i+1)} \\
\gamma_{(i+1)}^s &= \gamma_{(i)}^s + \dot{\gamma}_{(i+1/2)}^s \Delta t_{(i+1)} \\
\boldsymbol{\mathfrak{R}}_{(i+1)} &= \left(\mathbf{I} - \frac{1}{2} \mathbf{W}_{(i+1/2)}^* \Delta t_{(i+1)} \right)^{-1} \cdot \left(\mathbf{I} + \frac{1}{2} \mathbf{W}_{(i+1/2)}^* \Delta t_{(i+1)} \right) \cdot \boldsymbol{\mathfrak{R}}_{(i)}
\end{aligned} \tag{36}$$

- G. If $\sum_{j=1}^{i+1} \alpha_{(j)} < 1.0$, record the variables at $t_{(i+1)}$, update the number of substeps, $NS \leftarrow NS + 1$, and estimate the time factor for the next substep as

$$\alpha_{(i+2)} = \min \left\{ \chi \cdot \alpha_{(i+1)}, \left[1 - \sum_j^{i+1} \alpha_{(i+1)} \right] \right\} \tag{37}$$

where χ is an adaptive factor of substep size.

Return to step A.

- H. If $\sum_{j=1}^{i+1} \alpha_{(j)} = 1.0$, the integration over the time step Δt is complete.

Some comments to the above integration procedure are added in the following. As a first attempt, the initial value of the time factor $\alpha_{(1)}$ was set equal unity. However, a better estimate of $\alpha_{(1)}$ is obtained by

$$\alpha_{(1)} = \min \left\{ \frac{2}{NS_n}, 1.0 \right\} \tag{38}$$

where NS_n is the number of substeps from last time increment. Using Eq. (38) to define the initial value of $\alpha_{(1)}$ was found, in most cases, to reduce the number of trials required to find a value of $\alpha_{(1)}$ that fulfils the error tolerance. Thus, Eq. (38) will be used as default to estimate the initial value of $\alpha_{(1)}$. The value of $\Delta \gamma_{crit}$ in Eq. (29) was set to 10 to indicate numerical instability of some sort. This value is many order of magnitudes larger than $\dot{\gamma}_0 \Delta t_{(i+1)}$, and will not control the accuracy of the integration algorithm. The tolerance used to control the error is in the range $10^{-2} \leq TOL \leq 10^{-5}$, while the default value of TOL is taken as 10^{-3} . The minimum value of λ equal to 0.1 is introduced in Eq. (34) to avoid exceedingly small substeps. The adaptive factor between substeps, χ in Eq. (37), can be determined according to

$$\chi = \min \left\{ 0.8 \left[\frac{TOL}{ERR} \right]^{1/2}, 2.0 \right\} \tag{39}$$

which was suggested by Sloan [17]. However, $\chi = 1.0$ is found here to be a better choice, since a valid time factor will usually work also for the next several substeps when the time step is not excessively large. Finally, the efficiency of the ASSME algorithm can be further improved by some practical techniques, such as changing from the ASSME algorithm to the forward Euler algorithm when no substepping is needed and vice versa.

For a given strain increment, the forward Euler method has a local truncation error of order $O(\Delta t^2)$, whereas the local truncation error in the modified Euler method is of order $O(\Delta t^3)$. The substepping is controlled by the error estimated from the stress rates calculated from the two steps of the modified Euler method. By controlling the local relative error for each substep, we aim to control the global relative error in the overall solution.

The proposed integration schemes have been implemented in a stand-alone code using the Taylor assumption for the polycrystal, and as a user-defined material subroutine (UMAT) in the commercial finite element code LS-DYNA [24]. Boundary conditions, crystallographic texture and material parameters are the main input of both codes, while the stress response and the texture evolution are predicted. The accuracy, efficiency and stability of the forward Euler and ASSME methods will be evaluated in sections 4 and 5.

It should be noted that the ASSME method proposed here can be extended to hyperelastic formulations of rate-dependent crystal plasticity, e.g. by adopting the forward Euler scheme proposed by Grujicic and Batchu [7].

4. Evaluation of forward Euler and ASSME methods using the stand-alone code

The robustness, efficiency and stability of the two temporal integration schemes for the RDCP model, and especially the ASSME method, are now evaluated using the stand-alone code. It is not intended to compare with any experimental results here. All the simulations made by the stand-alone code were run on a computer with a 3.2GHz processor. Only a single thread was employed for each simulation.

4.1. Primary verification of integration schemes

Simulations of uniaxial compression and simple shear for oxygen-free high conductivity (OFHC) copper with random texture have been used by many researchers as a benchmark for accuracy evaluation of RDCP models. It will also be employed here as a primary verification of the two integration schemes. To assess the accuracy, another

verified implementation [14] of the explicit integration scheme for RDCP models proposed by Grujicic and Batchu [7] has been used as a reference here.

A total of 500 almost random orientations are used and the corresponding pole figure is shown in Figure 1, while material parameters are compiled in Table 1 [5]. The velocity gradient imposed for uniaxial compression is

$$\mathbf{L}^g = |\dot{\epsilon}_{33}^g| \cdot \begin{bmatrix} 0.5 & 0 & 0 \\ 0 & 0.5 & 0 \\ 0 & 0 & -1 \end{bmatrix} \quad (40)$$

while for simple shear the velocity gradient is

$$\mathbf{L}^g = 2\dot{\epsilon}_{12}^g \cdot \begin{bmatrix} 0 & 1 & 0 \\ 0 & 0 & 0 \\ 0 & 0 & 0 \end{bmatrix} \quad (41)$$

where $\dot{\epsilon}_{33}^g$ and $\dot{\epsilon}_{12}^g$ indicate the axial compression and shear strain rates, respectively. The strain rates used in this section are $|\dot{\epsilon}_{33}^g| = 10^{-2} \text{ s}^{-1}$ and $\dot{\epsilon}_{12}^g = 0.5 \cdot 10^{-2} \text{ s}^{-1}$. The loading time is 120 s and the time step is set to 10^{-4} s for the fully explicit methods and $2 \cdot 10^{-2}$ s for the simulations with the ASSME method. It is noted that Δt_{crit} for both explicit schemes is only around $5 \cdot 10^{-4}$ s with the current set-up of the simulations.

The predicted stress-strain curves are shown in Figure 2, while the CPU time is presented in Table 2. Here ‘‘FE’’ refers to the forward Euler integration scheme proposed in this work, whereas ‘‘FE-GB’’ refers to the explicit integration scheme proposed by Grujicic and Batchu [7] and implemented by Dumoulin *et al.* [14].

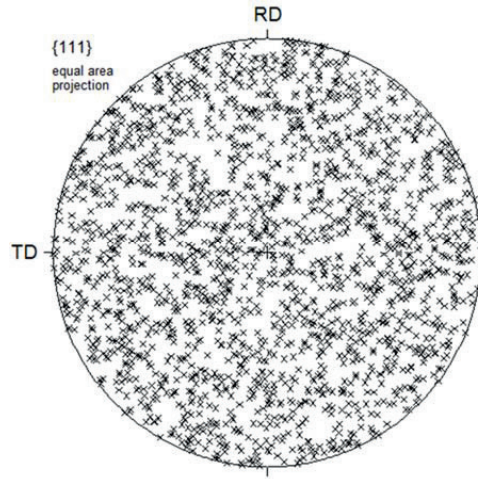


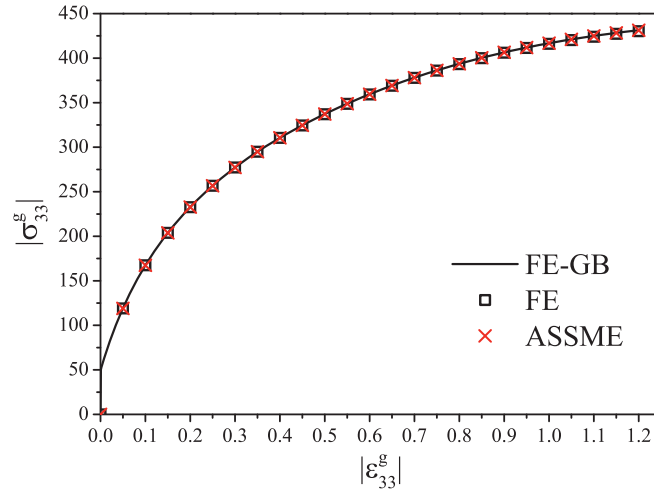
Figure 1 {111} equal area pole figure of the 500 orientations.

Table 1 Model parameters for OFHC copper

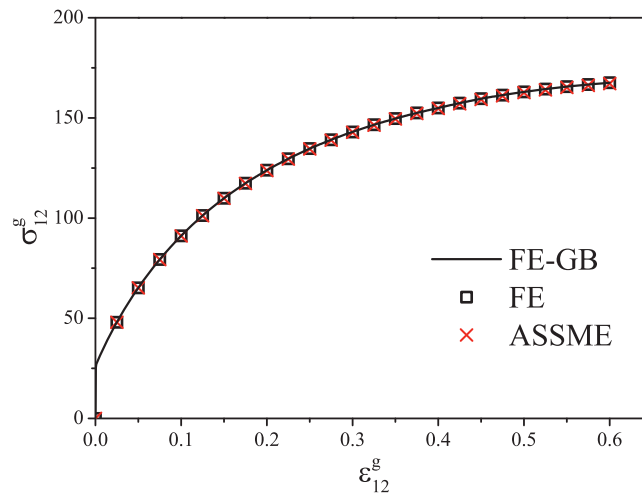
$\dot{\gamma}_0$	m	g_0	g_{sat}	h_0	a	q	c_{11}	c_{12}	c_{44}
(s^{-1})	-	(MPa)	(MPa)	(MPa)	-	-	(GPa)	(GPa)	(GPa)
10^{-3}	0.012	16	148	180	2.25	1.4	186	93	46.5

Table 2 CPU time (s) for simulations of uniaxial compression and shear using the different integration schemes.

	FE-GB	FE	ASSME
Uniaxial compression	8533	7369	906
Shear	9099	7934	639



(a)



(b)

Figure 2 Stress-strain curves in (a) uniaxial compression and (b) simple shear calculated by different integration algorithms.

As illustrated in Figure 2, the stress predictions are visually identical. The stresses predicted with the current FE method deviate only slightly from those obtained with the FE-GB method with relative errors less than 0.3% for both deformation cases. The

ASSME method has the same accuracy as the FE method, although a much larger time step was used. The CPU time shown in Table 2 demonstrates the computational efficiency of the FE method compared with the FE-GB method; in both cases, the FE method is around 15% faster. The ASSME method is around 10 times faster than the two fully explicit methods, but still the accuracy is retained.

4.2. Evaluation of the ASSME method

The robustness, efficiency and accuracy of the ASSME method are now evaluated for large time increments, extremely low strain-rate sensitivity, high strain rates, and strain-path changes, using the stand-alone code. These conditions are known to be very challenging for the stability of integration schemes for RDCP models.

4.2.1. Large time steps

Two arbitrarily chosen FCC single crystals, denoted grain A and grain B respectively, will be employed for the investigations. The Euler angles of grain A are $(212^\circ, 58^\circ, 51^\circ)$ in Bunge's notation, while they are $(115^\circ, 15^\circ, 53^\circ)$ for grain B. The material parameters correspond to copper [5] and take the values given in Table 1. Both grains will be deformed separately with the strain path specified by Eq. (40) with $|\dot{\varepsilon}_{33}^g| = 10^{-2} \text{ s}^{-1}$, to a logarithmic strain of -1.2 along the compression direction.

Details on the simulation programme and extensive simulation statistics are compiled in Table 3 and Table 4 for grain A and grain B, respectively, where the time step Δt and the tolerance TOL of the ASSME method were varied and by which the performance of the integration schemes can be evaluated. In the tables, $\max(NS)$, $\min(NS)$ and $\text{avg}(NS)$ mean the maximum, minimum and average number of substeps per time step, respectively. The average substep size is then given by $\text{avg}(\Delta t_{(i)}) = \Delta t / \text{avg}(NS)$. The tables also present the CPU time of each simulation. To assess the accuracy of the stress prediction, the relative error of the stress state $\boldsymbol{\sigma}$ is defined as

$$\text{err}(\boldsymbol{\sigma}) = \frac{\|\boldsymbol{\sigma} - \boldsymbol{\sigma}^*\|}{\|\boldsymbol{\sigma}^*\|} \quad (42)$$

where $\boldsymbol{\sigma}^*$ is a reference stress obtained by the ASSME method with $TOL = 10^{-3}$ and a very fine step, i.e. $\Delta t = 10^{-6} \text{ s}$. The relative stress error $\text{err}(\boldsymbol{\sigma})$ is calculated at intervals of axial strain $|\varepsilon_{33}^g|$ equal to 10^{-3} except for the two cases with large time step, $\Delta t = 1 \text{ s}$ and $\Delta t = 10 \text{ s}$, where it is measured at each step. The maximum value of $\text{err}(\boldsymbol{\sigma})$ during

the simulation, which is denoted $\max \text{err}(\boldsymbol{\sigma})$, is then listed in the tables. Note that the initial value of $\alpha_{(1)}$ was set to 1.0 in all simulations.

Using the forward Euler (FE) algorithm for grain A and grain B, the CPU time changes inversely proportional to the time step Δt . With a time step $\Delta t = 10^{-4}$ s, it is found that $\max \text{err}(\boldsymbol{\sigma})$ has the same magnitude as Δt , which indicates good accuracy, while for larger time steps $\max \text{err}(\boldsymbol{\sigma})$ increases faster than Δt and eventually the critical time step Δt_{crit} is reached, at which the algorithm fails to converge. It is noted that Δt_{crit} is markedly lower for grain A than for grain B, which is important for a polycrystal since it is the lowest value of Δt_{crit} for all grains that will limit the time step.

The influence on stability, accuracy and efficiency of the time step Δt and the tolerance TOL used with the ASSME method is seen for grain A in Table 3 and for grain B in Table 4. Six cases for each grain are shown where $TOL = 10^{-3}$ and the time step Δt varies from 10^{-4} s to 10 s. Even with the largest time step, the ASSME method was stable. No sign of instability was found in the other cases with higher or lower TOL , except for the cases in which the tolerance was set to the exceedingly large value $TOL = 1$. It is noted that Sloan [17] suggested the typical range of the tolerance as $TOL \in [10^{-2}, 10^{-5}]$ for the substepping algorithm based on the modified Euler method.

The accuracy of various stress calculations for grain A and B with respect to the corresponding high precision reference case, can be assessed by considering the value of $\max \text{err}(\boldsymbol{\sigma})$ in Table 3 and Table 4. It is seen that for all combinations of time step and tolerance giving stable solutions, the maximum relative error of the stress is about one order of magnitude lower than the tolerance. The following phenomenological relationship can be found

$$\max \text{err}(\boldsymbol{\sigma}) \approx 10^{-1} \cdot TOL \quad (43)$$

This indicates that the accuracy of the ASSME method is rather independent on Δt but depends on TOL ; the smaller the value of TOL , the higher the accuracy. Hence, a good accuracy of the ASSME method can be obtained even for extremely large time steps, as shown in Table 3 and Table 4.

The orientation evolution of grain A and B at intervals of $|\varepsilon_{33}^g|$ equal to 0.1 is shown in Figure 3. Both the forward Euler and ASSME methods predict the same orientation change, and the orientation evolution obtained with the ASSME method is independent on the time step.

The efficiency of the integration schemes can be assessed from the CPU time tabulated in Table 3 and Table 4. Since each substep in the ASSME method involves two forward

Euler updates, the ASSME method with no substepping ($\max(NS) = 1$) should be two times more expensive than the forward Euler method. Comparison between the calculations with $\Delta t = 10^{-4}$ s in Table 3 for grain A and Table 4 for grain B shows that this is indeed the situation. Substepping is initiated ($\max(NS) > 1$) only when $\Delta t \geq 10^{-3}$, as shown in Table 3 and Table 4. The values of $\max(NS)$ and $\text{avg}(NS)$ vary in the same way as the time step Δt , which means that more substeps are needed when larger time steps are used. The increase by a factor of 10 of the time step from the case with $\Delta t = 10^{-4}$ s to the case with $\Delta t = 10^{-3}$ s ($TOL = 10^{-3}$) leads to a decrease of 10 times of the CPU time, both for grain A and B, which implies that substepping here contributes little to the efficiency, since only a few substeps are made. However, when the time step Δt is increased to 10^{-2} s and further to 10^{-1} s, the improved efficiency is attributed to the substepping, since these time steps are far beyond the critical time step Δt_{crit} of the forward Euler method. By comparing the cases with $\Delta t = 10^{-3}$ s and $\Delta t = 10^{-1}$ s, keeping $TOL = 10^{-3}$, it is seen that $\text{avg}(\Delta t_{(i)})$ becomes only five times larger when Δt is increased by two orders of magnitude. By further increasing the time step, the CPU time starts to increase again, which shows that there is an optimal time step size for the substepping algorithm.

It is also noted that the difference between $\text{avg}(NS)$ and $\max(NS)$ becomes more apparent with larger Δt . This indicates that the degree of substepping is not constant during the simulation. Since the substepping is controlled by the relative error in stress rate measured between the two forward Euler steps, defined in Eq. (32) and denoted ERR , adaptive substepping means that ERR is not constant. To illustrate this, the evolutions of NS and ERR at the beginning of each step, i.e. ERR computed with Δt as the substep size, denoted $ERR_{\Delta t}$, are shown in Figure 4 and Figure 5 with $TOL = 10^{-3}$ and $\Delta t = 10^{-2}$ s for grain A and B, respectively. The data are plotted at intervals of $|\varepsilon_{33}^g|$ equal to 10^{-4} when $|\varepsilon_{33}^g| \leq 10^{-2}$ and 10^{-3} otherwise. As illustrated in Figure 4 and Figure 5, $NS = 1$ and $ERR_{\Delta t} \ll 10^{-3}$ for the first two or three time steps. After these time steps, both NS and $ERR_{\Delta t}$ increase abruptly to reach a global maximum. The slip activity in the first few steps, as described by $\sqrt{\sum_{\alpha=1}^N (\dot{\gamma}^{\alpha})^2}$, is illustrated in Table 5. It shows that during the first few steps, $\sqrt{\sum_{\alpha=1}^N (\dot{\gamma}^{\alpha})^2} < 10^{-11} \text{ s}^{-1}$, which demonstrates no or infinitesimal plastic slip on the slip systems. The deformation is then nearly elastic and a small value of $ERR_{\Delta t}$ is expected, hence no substepping is needed at all. When $\sqrt{\sum_{\alpha=1}^N (\dot{\gamma}^{\alpha})^2} > 10^{-5} \text{ s}^{-1}$, the slip activity is not negligible any more. This corresponds to initial yielding in the RDCP model, and a very small time step should then be used to accurately capture the ‘elastic-plastic’ transition. Ideally, the ASSME method behaves

in this manner and a maximum value of NS occurs in the ‘elastic-plastic’ transition. Then as the monotonic deformation proceeds, both NS and $ERR_{\Delta t}$ decrease, see Figure 4 and Figure 5. This trend can be explained as follows. Firstly, the work-hardening leads to a higher stress level, thus increasing the denominator in Eq. (32) and making $ERR_{\Delta t}$, and thus the number of substeps, smaller. Secondly, the work-hardening rate will generally decrease at increasing strain levels. For a small or near constant work-hardening rate, relatively large time steps can be used while still keeping a good accuracy. The decrease of NS and $ERR_{\Delta t}$ at increasing strain levels also leads to an increase of the substep size. As a result, the simulation will speed-up at increasing strain levels. Ideally, the ASSME method will run with a maximum substep size which fulfils the accuracy requirement at each step or substep. The substep size will increase during the simulation and is much larger than the critical time step Δt_{crit} of the forward Euler scheme, since this is typically set by the ‘elastic-plastic’ transition. In polycrystalline materials, each grain can run at its own substep size without any limitations from the other grains. The above factors all explain the improvement of the computational efficiency of the ASSME method compared with the forward Euler scheme when large time steps are used. Since the average substep size in the ASSME method for a polycrystal could be many times larger than Δt_{crit} (which is the minimum value for all grains throughout the loading process), the ASSME method could be an order of magnitude faster than the forward Euler method. This emerges from the simulations made in section 4.1, where Table 2 shows that the ASSME method is nearly 10 times faster than the forward Euler method for the polycrystal in uniaxial compression and shear. A comparison between the FE-GB scheme [7] and a fully implicit integration scheme [6, 13] has been done by Dumoulin *et al.* [14], where the FE-GB scheme was found to be more than 50 times faster than that implicit integration scheme. Together with the data shown in Table 2, it is then expected that the ASSME method could be two orders of magnitude faster than the fully implicit integration scheme for some cases.

Table 3 Statistics of simulations for grain A with the ASSME and forward Euler (FE) methods using different settings.

Method	TOL	Δt (s)	$\max(NS)$	$\text{avg}(NS)$	$\text{avg}(\Delta t_{(i)})$ ($\times 10^{-3}$ s)	CPU time (s)	$\max \text{err}(\sigma)$	
ASSME	10^{-3}	10^{-4}	1	1	0.1	28.92	$3.48 \cdot 10^{-5}$	
		10^{-3}	6	1.01	0.99	3.15	$2.73 \cdot 10^{-4}$	
		10^{-2}	30	3.33	3.03	1.40	$3.23 \cdot 10^{-4}$	
		10^{-1}	255	19.78	5.21	0.73	$4.61 \cdot 10^{-4}$	
		1	3703	310.53	3.22	0.98	$1.53 \cdot 10^{-4}$	
		10	41663	6289.92	1.59	2.01	$3.26 \cdot 10^{-5}$	
	10^{-4}	10^{-2}	89	3.35	2.99	1.42	$7.11 \cdot 10^{-5}$	
		10^{-1}	717	23.12	4.32	0.78	$7.10 \cdot 10^{-5}$	
	10^{-2}	10^{-2}	23	3.23	3.09	1.40	$5.05 \cdot 10^{-3}$	
		10^{-1}	169	19.88	5.03	0.61	$4.79 \cdot 10^{-3}$	
	10^{-1}	10^{-2}	182	2.99	3.34	1.17	$5.18 \cdot 10^{-2}$	
		10^{-1}	3858	31.81	3.14	1.03	$4.72 \cdot 10^{-2}$	
		1	10^{-2}	Unstable				
	FE		10^{-4}				14.06	$7.6 \cdot 10^{-5}$
		$5 \cdot 10^{-4}$				2.79	$2.69 \cdot 10^{-4}$	
		$8.5 \cdot 10^{-4}$	Δt_{crit}					

Table 4 Statistics of simulations for grain B with the ASSME and forward Euler (FE) methods using different settings.

Method	TOL	Δt (s)	$\max(NS)$	$\text{avg}(NS)$	$\text{avg}(\Delta t_{(i)})$ ($\times 10^{-3}$ s)	CPU time (s)	$\max \text{err}(\sigma)$	
ASSME	10^{-3}	10^{-4}	1	1	0.1	28.42	$4.30 \cdot 10^{-5}$	
		10^{-3}	11	1.01	0.99	2.92	$2.14 \cdot 10^{-4}$	
		10^{-2}	44	4.08	2.45	1.67	$2.24 \cdot 10^{-4}$	
		10^{-1}	507	23.23	4.30	0.80	$5.18 \cdot 10^{-4}$	
		1	6170	371.31	2.69	1.19	$5.52 \cdot 10^{-5}$	
		10	56913	8279.92	1.13	2.65	$4.77 \cdot 10^{-6}$	
	10^{-4}	10^{-2}	102	4.05	2.47	1.62	$6.59 \cdot 10^{-5}$	
		10^{-1}	1515	27.98	3.57	0.94	$6.81 \cdot 10^{-5}$	
	10^{-2}	10^{-2}	25	3.86	2.59	1.54	$3.82 \cdot 10^{-3}$	
		10^{-1}	267	22.82	4.38	0.75	$4.90 \cdot 10^{-3}$	
	10^{-1}	10^{-2}	32	3.63	2.75	1.29	$4.52 \cdot 10^{-2}$	
		10^{-1}	2761	73.26	1.37	2.25	$6.50 \cdot 10^{-2}$	
		1	10^{-1}	Unstable				
	FE		10^{-4}				13.95	$1.41 \cdot 10^{-4}$
		$5 \cdot 10^{-4}$				2.85	$6.87 \cdot 10^{-4}$	
		$1 \cdot 10^{-3}$				1.42	$3.13 \cdot 10^{-2}$	
		$1.7 \cdot 10^{-3}$	Δt_{crit}					

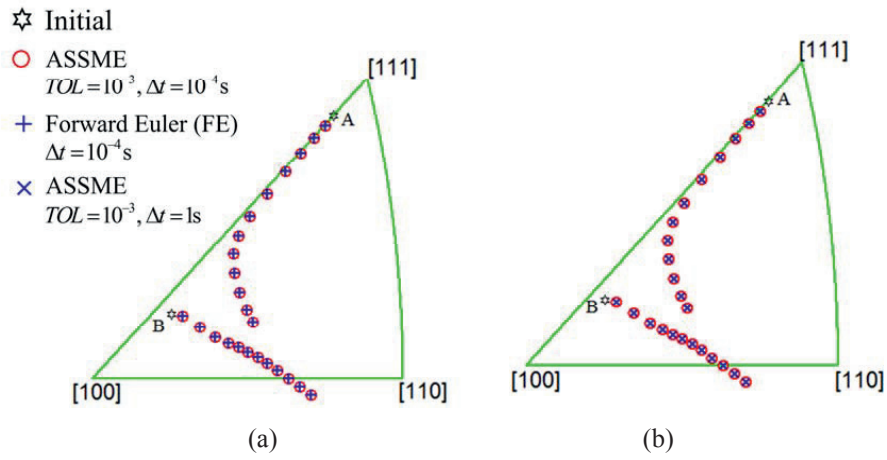
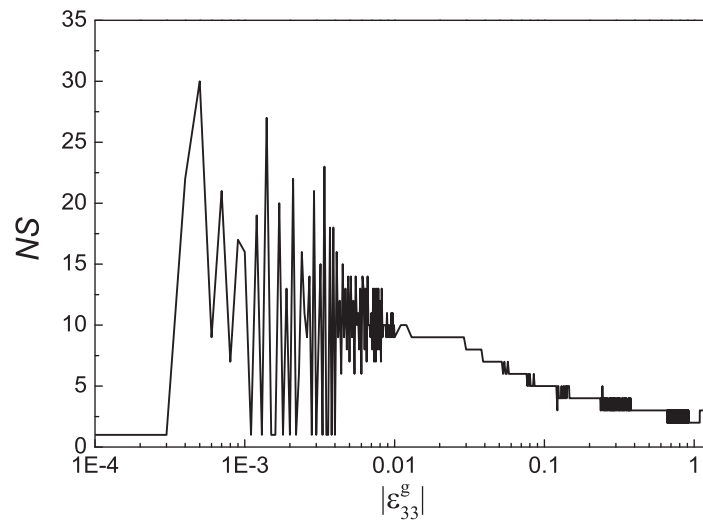


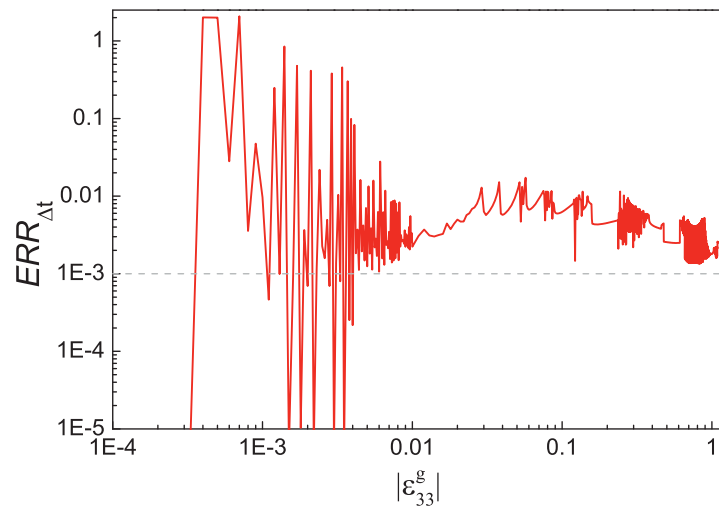
Figure 3 Standard triangular inverse pole figure showing the orientation change of grain A and grain B at strain intervals of 0.1 in terms of $|\epsilon_{33}^e|$.

Table 5 Slip activity of the first 5 time steps for ASSME results with $TOL = 10^{-3}$ and $\Delta t = 10^{-2} \text{ s}$.

$ \epsilon_{33}^e (\times 10^{-4})$	$\sqrt{\sum_{\alpha=1}^N (\dot{\gamma}^{\alpha})^2} (\text{s}^{-1})$	
	Grain A	Grain B
1	$5.55 \cdot 10^{-52}$	$1.19 \cdot 10^{-38}$
2	$6.76 \cdot 10^{-27}$	$1.45 \cdot 10^{-13}$
3	$3.19 \cdot 10^{-12}$	$5.72 \cdot 10^{-5}$
4	$3.09 \cdot 10^{-5}$	$1.64 \cdot 10^{-4}$
5	$1.46 \cdot 10^{-4}$	$2.72 \cdot 10^{-4}$

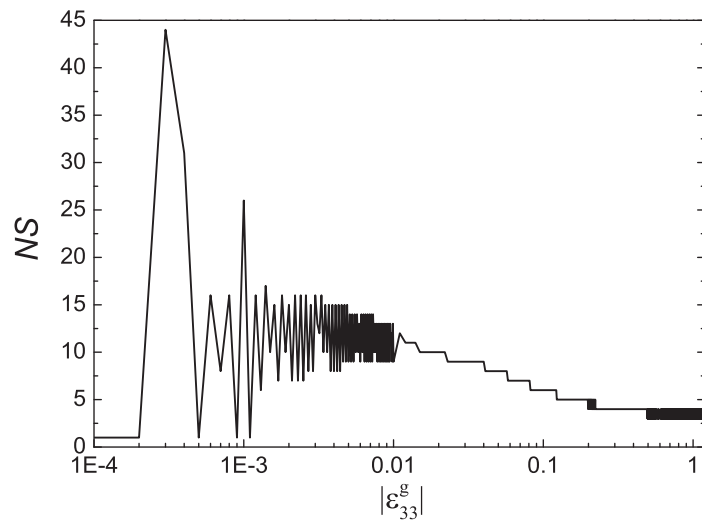


(a)

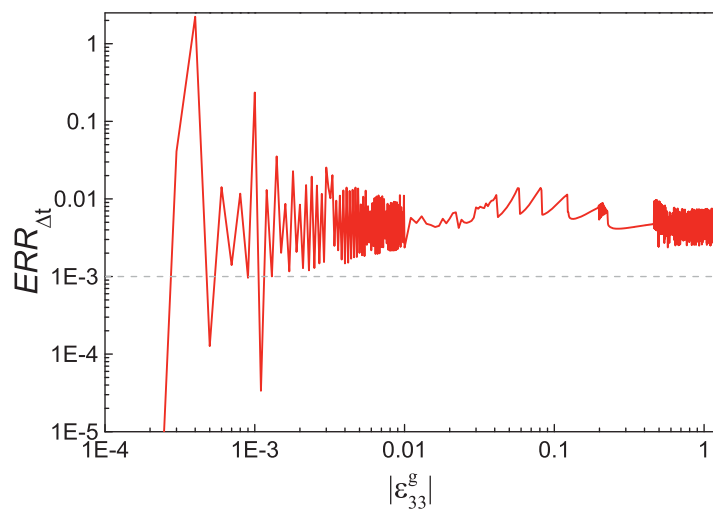


(b)

Figure 4 For grain A: (a) Number of substeps NS and (b) relative error $ERR_{\Delta t}$ at the beginning of each time step vs. magnitude of true axial strain for ASSME results with $TOL = 10^{-3}$ and $\Delta t = 10^{-2}$ s.



(a)



(b)

Figure 5 For grain B: (a) Number of substeps NS and (b) relative error $ERR_{\Delta t}$ at the beginning of each time step vs. magnitude of true axial strain for ASSME results with $TOL = 10^{-3}$ and $\Delta t = 10^{-2}$ s.

4.2.2. Low strain-rate sensitivity

The visco-plastic flow rule adopted in the RDCP model becomes very stiff with a low rate sensitivity, i.e. for small values of the exponent m . In the following, the stability of the ASSME method is evaluated for values of m equal to 10^{-4} , 10^{-3} , 10^{-2} and 10^{-1} , which represent very low to rather high rate sensitivity.

Simulations of the copper single crystal with cube orientation are made, where it is deformed in uniaxial compression, i.e. according to Eq. (40) with $|\dot{\epsilon}_{33}^g| = 10^{-2} \text{ s}^{-1}$. All material parameters, except m , take the values compiled in Table 1. The deformation is up to an axial logarithmic strain of -1.2 and the time step is set to 10^{-2} s . The default settings of the ASSME method are used, i.e. $TOL = 10^{-3}$ and Eq. (38) is used to define $\alpha_{(1)}$. Figure 6 shows the predicted stress-strain response. More simulations were made with other setting of m and TOL , and the statistics from all these simulations are compiled in Table 6.

It is clearly shown that the simulation with high strain-rate sensitivity, i.e. $m = 10^{-1}$, gives a higher stress level than the simulations with lower m . Simulations made with $m \leq 10^{-2}$ give quite similar stress responses. Especially when $m = 10^{-3}$ and $m = 10^{-4}$, the stress predictions show no visible difference. As suggested by Rashid and Nemat-Nasser [4], a nearly rate-independent response can be recovered from RDCP models by making $m = 5 \cdot 10^{-3}$ or smaller. The simulations with $m = 10^{-3}$ and $m = 10^{-4}$ correspond to the nearly rate-independent cases.

As already mentioned, the statistics shown in Table 6 cover a wide range of values for m and TOL . The ASSME method is stable even when m is as low as 10^{-5} , but $\max(NS)$, $\text{avg}(NS)$ and the CPU time increase when decreasing m , which suggests higher levels of substepping at smaller strain-rate sensitivities. A smaller value of TOL should be used when employing extremely small m , otherwise a numerical instability could occur due to the increased stiffness of the equation system. As an example, the integration scheme becomes unstable when $TOL = 10^{-2}$ and $m = 10^{-5}$. The critical time step of the forward Euler method when simulating uniaxial compression of the single crystal with different m is shown in Figure 7. One can notice that $\log(\Delta t_{crit})$ decreases almost linearly with $\log(m)$, and the relation $\Delta t_{crit} = 0.118 \cdot m^{0.897} \text{ s}$ is obtained by a least square linear fitting of the data. It is noted that the relation between Δt_{crit} and m depends on grain orientation and deformation rate.

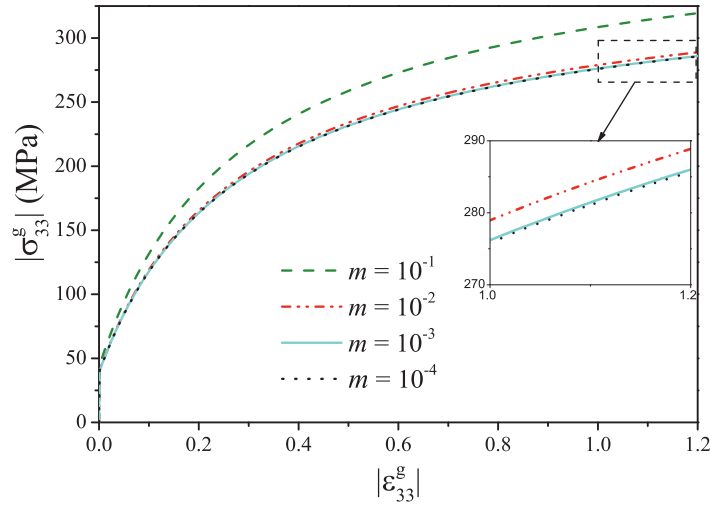


Figure 6 Uniaxial stress-strain response with different strain-rate sensitivity values and $TOL = 10^{-3}$.

Table 6 Statistics of simulations run with different m and TOL

m	TOL	max (NS)	avg (NS)	CPU time (s)
10^{-1}	10^{-3}	23	1.01	0.34
10^{-2}		26	3.82	1.62
10^{-3}		204	35.77	10.59
10^{-4}		3165	348.62	98.61
10^{-4}	10^{-2}	3605	279.68	85.55
10^{-5}	10^{-4}	137122	4942.91	2134

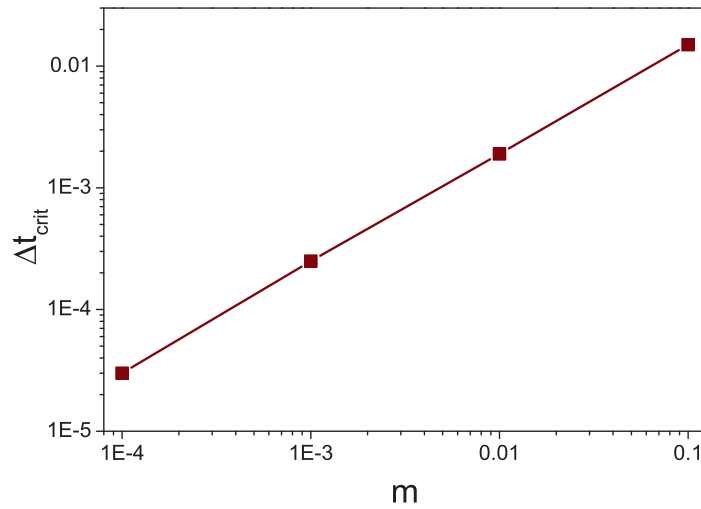


Figure 7 Critical time step of the forward Euler method at different values of the strain-rate sensitivity m in simulation of copper single crystal with cube orientation under uniaxial compression.

4.2.3. High strain rates

The performance of the ASSME method at different strain rates is studied in this section. Except for the strain-rate sensitivity m and the deformation rates, the set-up of the simulations is the same as in section 4.2.2. The value of m will be set to 10^{-2} and 10^{-3} , and for each of these values, four levels of the strain rate in Eq. (40) will be used, namely 10^{-2} , 1, 10^2 and 10^4 s^{-1} for $|\dot{\epsilon}_{33}^g|$. The time step Δt also takes varying values so that the strain increment per step $|\dot{\epsilon}_{33}^g| \Delta t$ equals 10^{-4} ; i.e., Δt equals 10^{-2} , 10^{-4} , 10^{-6} and 10^{-8} s for the four strain rates, respectively. Totally, there are 8 cases simulated.

Statistics related to the above simulations are shown in Table 7. It is very interesting to note that the CPU times are almost the same for each of the two values of m . Also, $\max(NS)$ is barely influenced by the strain rate, especially for the case of lower strain-rate sensitivity. The reason is that the strain increment per time step is the same for all simulations. High strain rates will not really challenge the integration schemes with a proper strain increment, i.e. smaller time steps for high strain rates. This also holds for the forward Euler scheme.

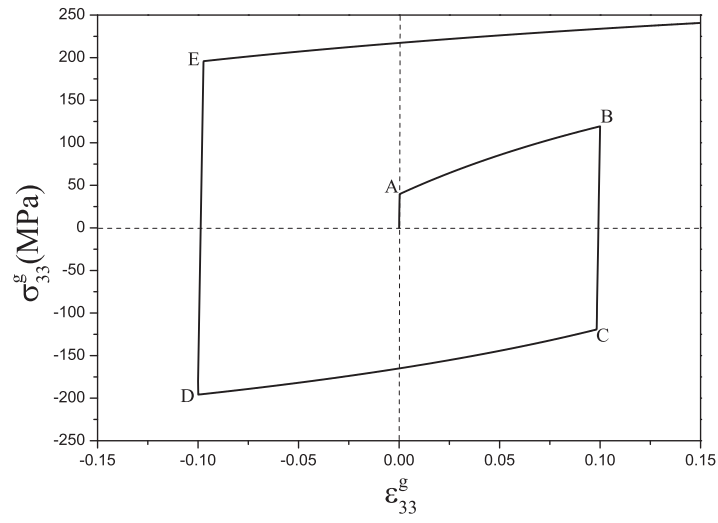
Table 7 Statistics of the simulation with different strain rate $|\dot{\epsilon}_{33}^g|$ and strain-rate sensitivity parameter m

$ \dot{\epsilon}_{33}^g $ (s^{-1})	$m=10^{-2}$			$m=10^{-3}$		
	max (NS)	avg (NS)	CPU time (s)	max (NS)	avg (NS)	CPU time (s)
10^{-2}	26	3.82	1.62	204	35.77	10.70
10^0	86	3.65	1.51	198	35.61	10.73
10^2	61	3.48	1.44	207	35.43	10.64
10^4	54	3.36	1.36	194	35.28	10.69

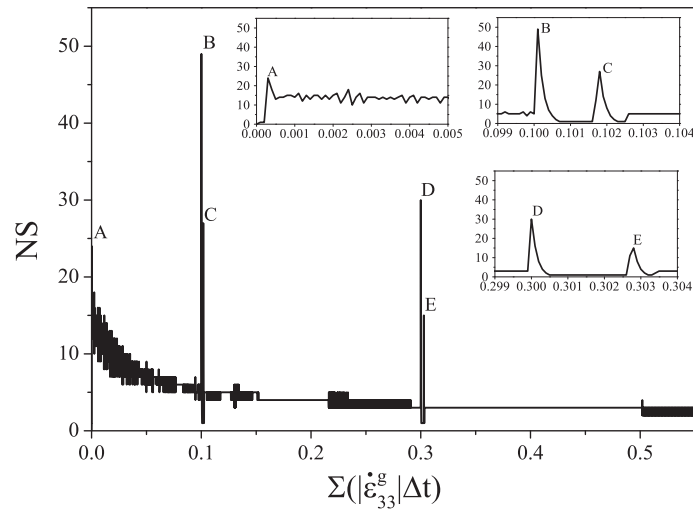
4.2.4. Strain-path change

In forming operations and impact events, the loading process often involves strain-path changes of some sort. Loading and unloading occurring during strain-path changes will challenge the stability of the numerical integration scheme. The performance of the ASSME method under strain-path changes is investigated here. The copper single crystal with cube orientation is studied. The material parameters take values as given in Table 1. The velocity gradient is given by Eq. (40) with $|\dot{\epsilon}_{33}^g| = 10^{-2} s^{-1}$. The single crystal will be first stretched to a logarithmic strain of 0.1, then compressed to a logarithmic strain of -0.1 and finally stretched to a logarithmic strain of 0.15. The default settings of the ASSME method are used with a time step of $\Delta t = 10^{-2} s$.

The stress response is shown Figure 8 (a), while the number of substeps per time step is shown in Figure 8 (b). The stress-strain curve shows the elastic loading, unloading and reloading. The evolution of the number of substeps NS shows an abrupt increase at points of plastic loading (A), elastic unloading (B/D) and plastic reloading (C/E). The increase of NS helps to accurately capture the elastic-plastic transition points.



(a)



(b)

Figure 8 Single crystal with cube orientation. (a) Predicted stress-strain response and (b) the evolution of NS during the simulation. Points A to E indicate plastic loading/reloading and elastic unloading. Inserts in (b) are enlarged views near loading, reloading and unloading points.

5. CPFEM simulations

The two integration schemes have also been implemented into the commercial finite element code LS-DYNA through a user-defined material subroutine (UMAT). The explicit solver of LS-DYNA applies the explicit central difference method to solve for velocities and accelerations from the momentum balance equations. This integration procedure is only conditionally stable, and the stable time increment of the central difference scheme is estimated as:

$$\Delta t_{crit}^{FE} = \min \left(\frac{l_e}{c_d} \right) \cong \sqrt{\frac{\rho}{E}} \cdot \min l_e \quad (44)$$

where l_e is the characteristic element length and c_d is the dilatational elastic wave speed in the material; c_d approximately equals $\sqrt{E / \rho}$, where ρ is the specific mass density and E is the Young's modulus. In CPFEM, single grains are usually represented by one element or more. Hence, l_e approximately equals the grain size. In the case of aluminium or copper with 100 μm grain size, Δt_{crit}^{FE} is in the order of 10^{-8} s.

Time and mass scaling are two common methods to speed up explicit finite element simulations. However, the RDCP models are deformation rate sensitive, especially for relatively large values of m , as shown in Figure 6. Thus, reducing the time scale of the loading process is not a valid way of speeding up CPFEM simulations. Mass scaling can be used, but may introduce undesirable dynamic effects that originate from the inertia forces of the governing equations. Hence, the influence of mass scaling on the accuracy and efficiency of CPFEM simulations is worthy of investigation.

5.1. Mass scaling in quasi-static problem

Uniaxial tension of the same copper single crystal with cube orientation is simulated, but with different mass scaling factors (MSF) by CPFEM, run on the same computer as described in section 4 with a single thread. For the CPFEM model, a cube of volume $1 \times 1 \times 1 \text{ mm}^3$ is considered as the representative volume element (RVE), which is meshed using $4 \times 4 \times 4$ uniform cubic elements with one integration point. The face with normal vector $-\mathbf{e}_1^g$ is constrained in the x_1^g direction, while the opposite face with normal vector \mathbf{e}_1^g is subjected to a motion in the x_1^g direction to stretch the RVE. The nodes belonging to these two faces are free to move along the x_2^g and x_3^g directions, whereas the other four faces are free of any constraints. The loading speed increases smoothly from zero to 0.02 mm/s in one second and is then kept constant. The total process time is 21 seconds and the final elongation is 41%. Simulation results were recorded at every 0.25 seconds. The density of copper is 8.96 g/mm³ and five different MSF values are evaluated, namely 1 (no mass scaling), 10^4 , 10^8 ,

10^{10} and 10^{12} . The ASSME method is used to integrate the constitutive equations, except for the no mass-scaling case where the forward Euler method is used instead. The forward Euler method is used to reduce the CPU time but it is unstable for large MSF. Predicted stress-strain curves are shown in Figure 9, while some statistics of the simulations running are shown in Table 8, where $E_{kinetic}$ and E_{total} represent the kinetic and total energy of the system, respectively.

The stress prediction with no mass scaling is taken as a reference. The maximum relative errors of the stress prediction is $1.7 \cdot 10^{-5}$ and $2.8 \cdot 10^{-3}$ for MSF equal to 10^4 and 10^8 , respectively. The differences are so small that the stress predictions can be said to be identical for these three cases. When MSF equals 10^{10} , a 4.1% relative error occurs at the initial loading stage, as shown in the insert of Figure 9. As the deformation proceeds, the relative error decreases rapidly to smaller values. It is only around 10^{-3} or less when the true strain is larger than $5.0 \cdot 10^{-3}$. When further increasing MSF to 10^{12} , non-physical peaks and some oscillations of the stress-strain curve are observed, indicating that dynamic effects have been introduced in the solutions, see Figure 9.

As illustrated in Table 8, the average time step determined by the finite element code changes with the MSF according to Eq. (44). If MSF is no larger than 10^8 , no substepping is initiated, and the maximum value of NS is one. Beyond this value of MSF, substepping is required to control the accuracy of the time integration. The CPU time drops dramatically when increasing MSF. Without mass scaling, $E_{kinetic}$ is negligible compared with E_{total} , but $E_{kinetic}$ increases almost linearly with MSF, due to the artificially added mass. The ratio $E_{kinetic} / E_{total}$ changes near linearly with MSF. A large value of this ratio indicates a transition from quasi-static to dynamic deformation.

The main conclusion of this section is that mass scaling is a valid technique to speed up the CPFEM simulation for quasi-static problems. The ratio $E_{kinetic} / E_{total}$ should always be checked to make sure that the deformation can still be considered as quasi-static. Based on the results here, the kinetic effect introduced by mass scaling for a quasi-static problem is negligible by keeping the ratio between the kinetic and the total energy $E_{kinetic} / E_{total}$ less than 10^{-2} . Further, a critical strain increment, about 10^{-5} here, is normally needed to initiate the substepping in the ASSME method. This critical increment depends on the material and the prescribed tolerance TOL .

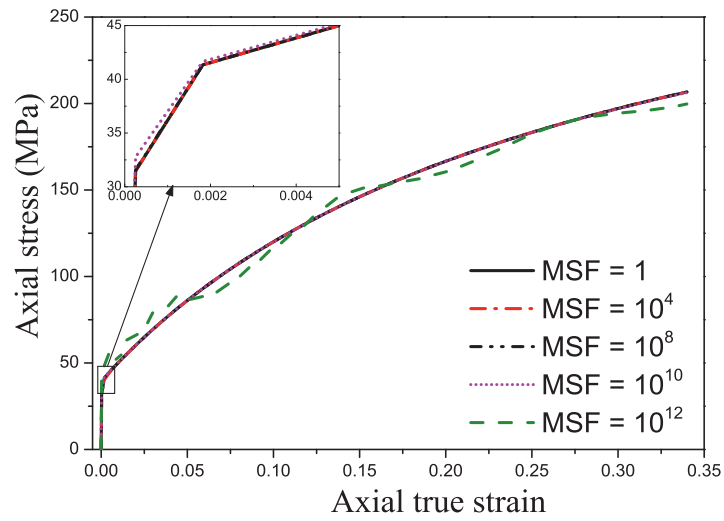


Figure 9 Stress-strain responses predicted with CPFEM and different mass scaling factors (MSF). The curves with the three lowest values of MSF coincide throughout the loading process.

Table 8 Statistics of CPFEM simulations with different MSF

MSF	avg(Δt) (s)	CPU time (s)	max(NS)	avg(NS)	max $\left(\frac{E_{kinetic}}{E_{total}}\right)$	avg $\left(\frac{E_{kinetic}}{E_{total}}\right)$
1	$4.31 \cdot 10^{-8}$	195780	1	1	$3.51 \cdot 10^{-12}$	$2.00 \cdot 10^{-13}$
10^4	$4.31 \cdot 10^{-6}$	4383	1	1	$3.51 \cdot 10^{-8}$	$2.00 \cdot 10^{-9}$
10^8	$4.31 \cdot 10^{-4}$	44.76	1	1	$3.51 \cdot 10^{-4}$	$2.00 \cdot 10^{-5}$
10^{10}	$4.19 \cdot 10^{-3}$	21.45	13	3.6	$3.40 \cdot 10^{-2}$	$1.97 \cdot 10^{-3}$
10^{12}	$4.09 \cdot 10^{-2}$	17.64	299	39.9	$6.27 \cdot 10^{-1}$	$9.46 \cdot 10^{-2}$

5.2. Dynamic problem

In this section, the Taylor bar impact test will be simulated with CPFEM. The purpose is to validate the robustness of the ASSME method under highly dynamic deformations with contact.

The material of the Taylor bar is assumed to be OFHC copper with random texture. Hence, material parameters except m take the values compiled in Table 1. The instantaneous strain-rate sensitivity m is set to 0.005 to have a nearly rate-independent stress-strain response.

The Taylor bar in the analysis has a length of 32 mm and a diameter of 6.4 mm. The finite element model consists of 5184 eight-node solid elements with one integration point, using the standard hourglass control in LS-DYNA, see Figure 10. Each element is given an orientation out of 5184 random orientations, and hence each element represents one grain. The impact velocity is 190 m/s and the interface between the bar and the rigid wall is assumed to be frictionless. The deformation time is 30 μ s. The ASSME method is used to integrate the constitutive equations with $TOL = 10^{-4}$.

The simulation was run using the shared memory parallel (SMP) version of LS-DYNA on a computer with two 2.4 GHz Quad-Core CPUs, i.e. using 8-equivalent CPUs. The average time step was $2.65 \cdot 10^{-2} \mu$ s and the CPU time was 3310 s. The final deformation shape with fringes of effective plastic strain $\varepsilon^p = \int_0^t \sqrt{2/3 \mathbf{D}^p : \mathbf{D}^p} dt$ is shown in Figure 11.

The simulation captures the flat, bulged shape at the contact surface where the maximum plastic strain occurs while the rear part of the bar shows no plastic strains at all. The irregular element shape at the contact surface after deformation is due to the plastic anisotropy exhibited by elements which are assigned with different grain orientations. The number of substeps per time step for the elements marked with crosses in Figure 10 (b) is shown in Figure 12. It clearly shows that due to contact, the elements at the front of the impact bar experience high levels of substepping, while the rear ones need no substepping at all.

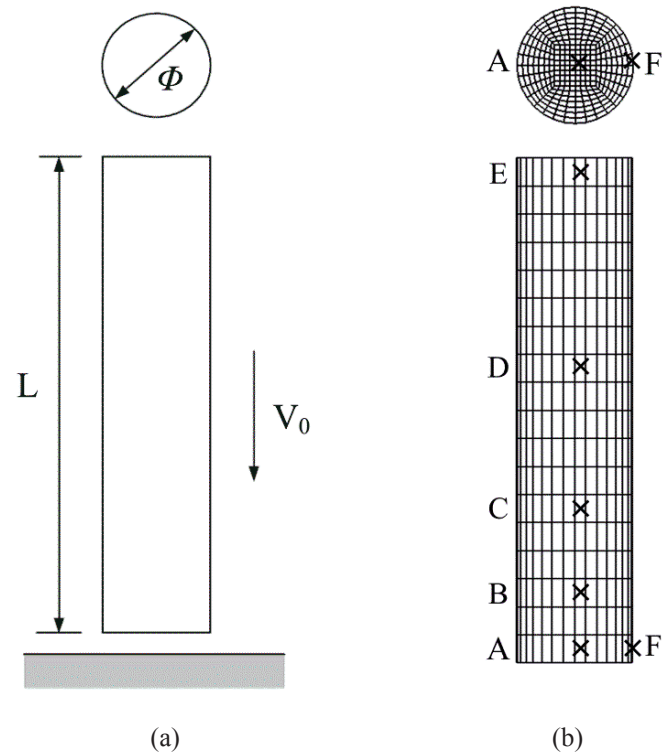


Figure 10 (a) Sketch of Taylor bar impact test and (b) finite element model. The crosses indicate selected history elements and are labelled A-F.

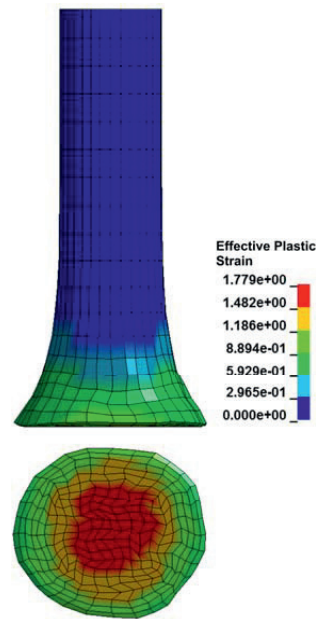


Figure 11 Final shape of the Taylor bar with fringes of effective plastic strain simulated by CPFEM. The side view and the contact surface of the bar are shown.

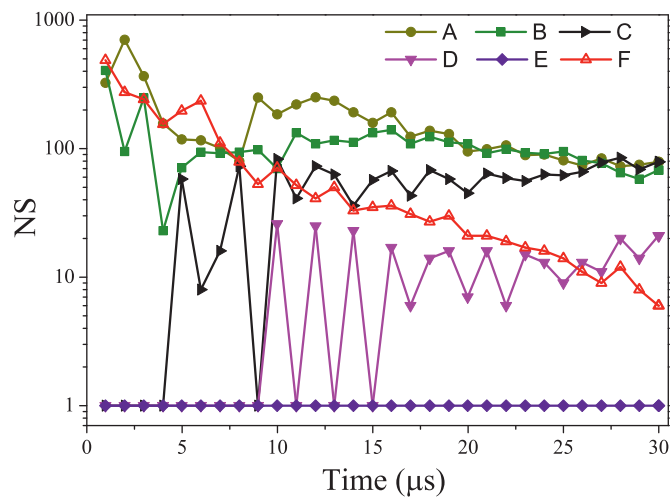


Figure 12 Number of substeps per time step for elements A to F marked with crosses in Figure 10 (b) versus time for the simulation of the Taylor bar impact test by CPFEM.

6. Conclusions

A robust and efficient substepping scheme based on the modified Euler method has been proposed for time integration of hypo-elastic RDCP models and denoted the ASSME method. Based on the numerical tests, the accuracy and stability of the ASSME method are found independent on the time step, but depend on the substepping control parameter, which governs the relative error of stress prediction between the two steps of the modified Euler method. The substepping is not influenced by other grains in the polycrystal, and accordingly each grain can run at its own maximum substep size. The ASSME method is in some cases one order of magnitude faster than the forward Euler method, and shows excellent stability for large time steps, exceedingly small strain-rate sensitivity, high strain rates and strain-path changes. The effect of mass scaling, used to speed up quasi-static CPFEM simulations, has been investigated. It was found that when the ratio of the kinetic to total energy is small, say less than 10^{-2} , there is almost no effect of the mass scaling on the stress prediction for the case studied here. Simulation of the Taylor bar impact test shows that the ASSME method works well even for highly dynamic problems involving large deformations, high strain rates and contact.

Acknowledgement

Dr. Torodd Berstad is gratefully acknowledged for discussions on the implementation and evaluation of the crystal plasticity UMAT in LS-DYNA.

References

1. Mánik T and Holmedal B. Review of the Taylor ambiguity and the relationship between rate-independent and rate-dependent full-constraints Taylor models. *International Journal of Plasticity* 2013.
2. Hutchinson JW. Bounds and self-consistent estimates for creep of polycrystalline materials. *Proceedings of the Royal Society of London. A. Mathematical and Physical Sciences* 1976; **348**: 101-127.
3. Peirce D, Asaro RJ and Needleman A. Material rate dependence and localized deformation in crystalline solids. *Acta Metallurgica* 1983; **31**: 1951-1976.
4. Rashid MM and Nemat-Nasser S. A constitutive algorithm for rate-dependent crystal plasticity. *Computer Methods in Applied Mechanics and Engineering* 1992; **94**: 201-228.
5. Kalidindi SR, Bronkhorst CA and Anand L. Crystallographic texture evolution in bulk deformation processing of fcc metals. *Journal of the Mechanics and Physics of Solids* 1992; **40**: 537-569.

6. Cuitino AM and Ortiz M. Computational modelling of single crystals. *Modelling and Simulation in Materials Science and Engineering* 1993; **1**: 225.
7. Grujicic M and Batchu S. Crystal plasticity analysis of earing in deep-drawn ofhc copper cups. *Journal of Materials Science* 2002; **37**: 753-764.
8. Kuchnicki SN, Cuitiño AM and Radovitzky RA. Efficient and robust constitutive integrators for single-crystal plasticity modeling. *International Journal of Plasticity* 2006; **22**: 1988-2011.
9. Li HW, Yang H and Sun ZC. A robust integration algorithm for implementing rate dependent crystal plasticity into explicit finite element method. *International Journal of Plasticity* 2008; **24**: 267-288.
10. Rossiter J, Brahme A, Simha MH, Inal K and Mishra R. A new crystal plasticity scheme for explicit time integration codes to simulate deformation in 3d microstructures: Effects of strain path, strain rate and thermal softening on localized deformation in the aluminum alloy 5754 during simple shear. *International Journal of Plasticity* 2010; **26**: 1702-1725.
11. Zhang K, Holmedal B, Dumoulin S and Hopperstad OS. An explicit integration scheme for hypo-elastic viscoplastic crystal plasticity. *Transactions of Nonferrous Metals Society of China* 2014; **To be published**.
12. Miehe C. Exponential map algorithm for stress updates in anisotropic multiplicative elastoplasticity for single crystals. *International Journal for Numerical Methods in Engineering* 1996; **39**: 3367-3390.
13. Ling X, Horstemeyer MF and Potirniche GP. On the numerical implementation of 3d rate-dependent single crystal plasticity formulations. *International Journal for Numerical Methods in Engineering* 2005; **63**: 548-568.
14. Dumoulin S, Hopperstad OS and Berstad T. Investigation of integration algorithms for rate-dependent crystal plasticity using explicit finite element codes. *Computational Materials Science* 2009; **46**: 785-799.
15. Roters F, Eisenlohr P, Hantcherli L, Tjahjanto DD, Bieler TR and Raabe D. Overview of constitutive laws, kinematics, homogenization and multiscale methods in crystal plasticity finite-element modeling: Theory, experiments, applications. *Acta Materialia* 2010; **58**: 1152-1211.
16. Belytschko T, Liu WK and Moran B. *Nonlinear finite elements for continua and structures*. Wiley, 2000.
17. Sloan SW. Substepping schemes for the numerical integration of elastoplastic stress-strain relations. *International Journal for Numerical Methods in Engineering* 1987; **24**: 893-911.
18. Luccioni LX, Pestana JM and Taylor RL. Finite element implementation of non-linear elastoplastic constitutive laws using local and global explicit algorithms with automatic error control. *International Journal for Numerical Methods in Engineering* 2001; **50**: 1191-1212.
19. van der Giessen E and Neale KW. Analysis of the inverse swift effect using a rate-sensitive polycrystal model. *Computer Methods in Applied Mechanics and Engineering* 1993; **103**: 291-313.

20. Buchheit TE, Wellman GW and Battaile CC. Investigating the limits of polycrystal plasticity modeling. *International Journal of Plasticity* 2005; **21**: 221-249.
21. Taylor GI. Plastic strain in metals. *Journal of Institute of metals* 1938; **62**: 307-324.
22. Lambert JD. *Numerical methods for ordinary differential systems: The initial value problem*. John Wiley & Sons Ltd: Chichester, U.K., 1991.
23. Hughes TJR and Winget J. Finite rotation effects in numerical integration of rate constitutive equations arising in large-deformation analysis. *International Journal for Numerical Methods in Engineering* 1980; **15**: 1862-1867.
24. LSTC. *Ls-dyna keyword user's manual, version 971*. Livermore Software Technology Corporation, 2007.

Article 4

Modelling the Plastic Anisotropy of Aluminium Alloy 3103 Sheets by Polycrystal Plasticity Models

K. Zhang¹, B. Holmedal¹, O.S. Hopperstad^{2,3}, S. Dumoulin⁴

1. Department of Materials Science and Engineering, Norwegian University of Science and Technology, NO-7491 Trondheim, Norway

2. Department of Structural Engineering, Norwegian University of Science and Technology, NO-7491 Trondheim, Norway

3. Structural Impact Laboratory (SIMLab), Center for Research-based Innovation, Norwegian University of Science and Technology, NO-7491 Trondheim, Norway

4. SINTEF Materials and Chemistry, NO-7465 Trondheim, Norway

Submitted to the journal:

Modelling and Simulation in Materials Science and Engineering.

Modelling the Plastic Anisotropy of Aluminium Alloy 3103 Sheets by Polycrystal Plasticity Models

Abstract

The plastic anisotropy of AA3103 sheets in the cold-rolled condition (H18 temper) and in the fully annealed condition (O temper) was studied experimentally and numerically in this work. The microstructure and texture of the two materials were characterized and the anisotropic plastic behaviour was measured by in-plane uniaxial tension tests along every 15° from the rolling direction to the transverse direction of the sheet. Five polycrystal plasticity models, namely the full-constraint Taylor model, the Alamel model, the Alamel Type III model, the visco-plastic self-consistent crystal plasticity model and the crystal plasticity finite element method (CPFEM), were employed to predict the plastic anisotropy in the plane of the sheet. Experimentally observed grain shapes have been taken into consideration. In addition, a multi-level modelling method was employed where the advanced yield function Yld2004-18p was calibrated to stress points provided by CPFEM simulations along 89 strain-paths, and the plastic anisotropy was then produced by the yield function. Based on comparisons between the experimental and the predicted results, the multi-level fitting method is considered as the most accurate way of describing the plastic anisotropy. The Alamel Type III and Alamel models are also recommended as accurate and time-efficient models for predicting the plastic anisotropy of the AA3103 sheets in H18 and O tempers.

Keywords: Plastic anisotropy, crystal plasticity models, Yld2004-18p, multi-level modelling, AA3103

1. Introduction

Due to their thermo-mechanical history, sheet metals commonly feature a crystallographic orientation distribution which is termed crystallographic texture – or texture for short. The significance of texture lies in the plastic anisotropy, i.e. direction-dependent strengths and flow patterns, which is mainly attributed to the texture. In a forming process, the plastic anisotropy of the material greatly influences the final shapes and dimensions of the products. Hence, proper description of the plastic anisotropy is of importance for the design and optimization of forming processes. Crystal plasticity (CP) models and anisotropic yield functions are two principal approaches to describe the plasticity, and its anisotropy, of engineering metallic alloys [1]. Due to higher computational efficiency than the CP models, anisotropic yield functions are widely applied in finite element (FE) simulations of forming processes.

In the last decade, many advanced yield functions have been proposed that are capable of accurately describing the plastic anisotropy of aluminium alloys [2-5]. These yield

functions are generally calibrated by mechanical tests, e.g. uniaxial tensile tests and biaxial tension/compression tests. However, most of the stress space is left unexplored when fitting the parameters of the yield function due to severe experimental limitations, and biaxial tension/compression testing is not universally accessible. To overcome these limitations, many researchers have employed CP models to facilitate the fitting of anisotropic yield functions, i.e. a hierarchical multi-level modelling. This can be done by conducting all or part of the required experimental tests virtually using CP models [2, 6, 7]. Alternatively, the yield functions can also be calibrated against the stress points at yielding provided by CP models in the stress space [1, 8-11]. As pointed out by Zhang et al. [12], the success of the hierarchical multi-level modelling critically depends on the accuracy of the lower-scale CP models in representing the materials' plastic anisotropy. Hence, quantitative evaluations of the performance of CP models for predicting plastic anisotropy are of great value for the research on and applications of the hierarchical multi-level modelling.

Over the past few decades, materials scientists have become more aware of the important role played by the distribution and connectivity of different grain boundary types in governing various mechanical and functional properties of materials [13]. It has been shown that the grain boundary can be of importance to texture and microstructure evolution during deformation [14, 15]. The plastic anisotropy predicted by CP models is also influenced by the grain morphology [15]. Hence, the grain morphology should be taken into consideration when conducting CP calculations, and thus make the predictions more physically reasonable.

In this work, the plastic anisotropy of AA3103 sheets, in a cold-rolled state (H18 temper, denoted AA3103-H18 in the following) and in a fully annealed state (denoted AA3103-O in the following), were investigated by experiments and by various CP models. Uniaxial tensile tests at every 15° from the rolling direction (RD) to the transverse direction (TD) were carried out to get the directional normalized yield stresses and Lankford coefficients (r -values). Five different crystal plasticity models, namely the full-constraint (FC) Taylor model [16-18], the Alamel model [19] and the variant with Type III relaxation (Alamel Type III) [20], the visco-plastic self-consistent (VPSC) model [21] and the crystal plasticity finite element method (CPFEM) [22], were employed to simulate the uniaxial tension tests. Besides the texture, the grain shape of the material has also been taken into consideration in the CP models, except for the FC-Taylor model. Due to the non-equiaxed grain structures of the AA3103 sheets (especially AA3103-H18), the in-plane uniaxial tensile tests along directions other than the RD and TD are difficult to perform by the CPFEM while keeping a realistic grain structure in the representative volume element (RVE). Instead, a hierarchical multi-level modelling method is used, i.e. fitting the advanced yield function Yld2004-18p [2] by CPFEM stress points for different in-plane loadings. The numerical results are compared with the experiments to evaluate the performance of the different CP models.

In Section 2 of this paper, the procedures for microstructure characterization and uniaxial tensile testing are described along with the experimental results. The five CP models and the virtual uniaxial tensile tests are described in Section 3. The methods adopted for considering the grain morphology in the different CP models are described in the same section. Section 4 deals with the hierarchical multi-level modelling of plastic anisotropy, including the Yld2004-18p yield function and CPFEM calculations. All the numerical results are presented and discussed in Section 5, while the main conclusions of the study are provided in Section 6.

2. Experimental methods and results

The AA3103-H18 and AA3103-O sheets were provided by the R&D Center of Hydro Aluminium in Bonn, Germany. Starting from a 4.1 mm thick hot-rolled strip, the AA3103-H18 sheets were produced by cold-rolling to a final thickness of 1.2 mm, i.e. corresponding to a 71% thickness reduction. The AA3103-O was then prepared through a simulated batch anneal of the AA3103-H18 sheets with a holding time of 2 hours at a peak metal temperature of 350 °C. The chemical composition is shown in Table 1.

The microstructure in both RD-ND and TD-ND sections (ND being the normal direction) of the two variants of the AA3103 sheets were measured by electron back scatter diffraction (EBSD) in a Zeiss Ultra/Supra 55 field emission scanning electron microscope (FESEM) equipped with the TSL software. The scanned area in the RD-ND and TD-ND sections of the AA3103-O material were $1.0 \times 1.6 \text{ mm}^2$ and $0.8 \times 1.2 \text{ mm}^2$, respectively, with a step size of 2 μm . In the case of the AA3103-H18 material, the scanned area in both sections was $0.3 \times 0.3 \text{ mm}^2$ with a step size of 0.5 μm . The orientation distribution functions (ODF) were then generated using all scanning points by the series expansion method with $l_{\text{max}} = 22$ and $\psi_0 = 5^\circ$. In order to get EBSD diffraction patterns with a higher quality, the EBSD samples of the AA3103-H18 material were put in an air-circulated oven, which had been pre-heated to 250 °C, and held for 10 minutes, before water quenching. Textures of the AA3103-H18 samples before and after the flash annealing at 250 °C were also measured by X-ray diffraction, which confirmed that there was little influence on the texture. The constitutive particles were characterized by back-scattered electrons (BSE) in the FESEM while the area fraction and size of constitutive particles were analysed by quantitative metallography.

Uniaxial tensile tests at every 15° from the RD to the TD (a total of seven directions) were conducted to measure the anisotropy in strength and plastic flow of the two AA3103 materials. The tensile direction with respect to RD is represented with the angle α , i.e., $\alpha = 0^\circ$ for the RD and $\alpha = 90^\circ$ for the TD. The uniaxial tensile samples had a uniform section with a gauge length of 50 mm and a width of 12.5 mm. The experiments were carried out with a cross-head speed of 2 mm per minute until fracture. At least two samples were tested in each direction. Extensometers were attached in the

longitudinal and transverse directions to record the respective deformations. The r -value was then determined from the recorded deformations employing the plastic incompressibility condition. Elastic deformations were calculated based on the longitudinal true stress, Young's modulus and Poisson's ratio and were deducted from the total deformations when calculating the r -value [23]. The r -values were calculated in the uniform plastic deformation region with logarithmic strain between $\sim 0.5\%$ and 2.0% for the AA3103-H18 sheet and between 3% and 15% for the AA3103-O sheet. The yield stresses were determined at 0.2% plastic strain.

EBSD orientation maps of the AA3103-H18 and AA3103-O sheets are shown in Fig. 1. The RD-ND section of AA3103-H18 shows a typical cold-rolling structure, i.e. fibrous grain shapes, whereas the pancake grain shape can be seen in the TD-ND section. Due to the large deformation, the grain size and aspect ratio along three orthotropic directions of the AA3103-H18 sheet are difficult to measure accurately. Instead, they can be estimated according to the thickness reduction and the grain morphology before the cold-rolling, i.e. a partially recrystallized grain structure after hot-rolling. The AA3103-O sheet shows a fully recrystallized grain structure where a slightly smaller grain size along ND can be observed. Grain sizes along the RD, TD and ND directions are measured using the line intercept method. The aspect ratios along the three orthotropic directions of the sheet were then determined based on the measurements and are compiled in Table 2.

The BSE micrographs in Fig. 2 further reveal that the AA3103 alloys contain a large fraction of micron-sized second-phase particles. The size and area fraction of these particles were analysed by quantitative metallography and are summarized in Table 2.

Crystallographic textures of the two AA3103 sheets are illustrated in Fig. 3 by means of ODFs. The β -fibre which consists of the copper, S and brass components is clearly recognized in the ODF of the AA3103-H18 material. The main texture components for the AA3103-O material are the cube and P orientations together with the Goss orientation at a lower intensity. The AA3103 alloy in both tempers exhibit quite weak textures, which are attributed to the high fraction of second-phase particles [24].

In Fig. 4, experimental stress-strain curves of the two AA3103 materials are shown. Due to the pre-cold-rolling, the A3103-H18 sheet has small uniform elongations before necking, only $\sim 1.5\%$. In contrast, the AA3103-O sheets have uniform deformations of $\sim 25\%$ engineering strain. The yield stress along the RD for the AA3103-H18 and the AA3103-O sheets is 201.6 MPa and 39.8 MPa, respectively. The yield stress along the RD was taken as a reference to normalize the yield stress along the other directions. The anisotropy in strength and plastic flow is plotted in Fig. 5. The AA3103-H18 sheet shows weak strength anisotropy. The maximum deviation from the reference value occurs at $\alpha = 45^\circ$ where the yield strength is only about 3% lower. The strength anisotropy of the AA3103-O sheet is different and significantly stronger. The maximum

deviation from the reference value occurs in the TD ($\alpha = 90^\circ$) where the yield strength is about 8% lower. The directional variation of the r -value of the AA3103-H18 sheet is strong with a minimum of about 0.5 in the RD and a maximum of about 1.5 at $\alpha = 45^\circ$. The AA3103-O sheet exhibits less and somewhat different variation of the r -value. The maximum value of about 0.9 occurs at $\alpha = 30^\circ$, while the minimum value, about 0.4, is found in the TD. Within the investigated strain ranges, only minor changes in the anisotropy in strength and plastic flow of the AA3103 materials were found.

Table 1 Chemical composition of the AA3103 alloy (in wt%).

Si	Fe	Cu	Mn	Mg	Cr	Zn	Ti	Al
0.063	0.53	0.0027	1.03	0.01	0.0006	0.0054	0.006	Rest

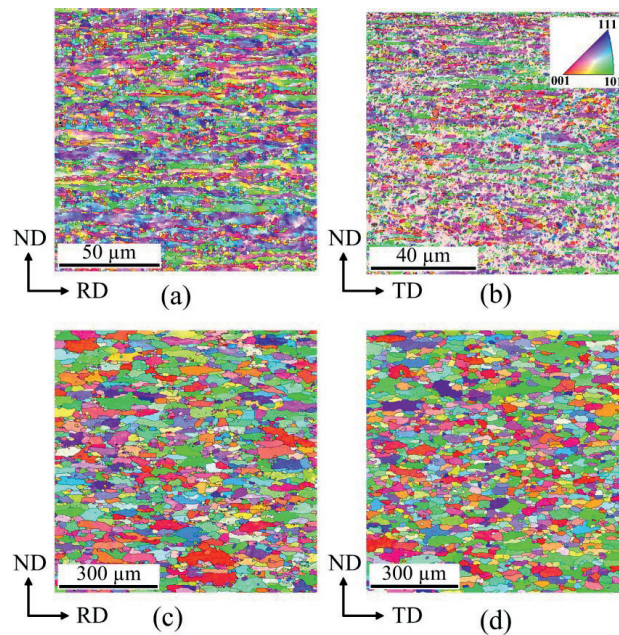
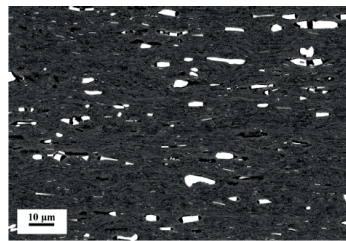


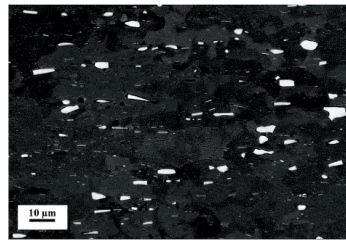
Fig. 1 EBSD maps for (a, b) the AA3103-H18 material and for (c, d) the AA3103-O material.

Table 2 Measured grain size, estimated aspect ratios of grains, constituent particle size (mean diameter of an equivalent circle) and area fraction of constituent particles.

	AA3103-H18	AA3103-O
Grain size	—	RD: $38.4 \pm 4.3 \mu\text{m}$
	—	TD: $30.8 \pm 3.1 \mu\text{m}$
	ND: $\sim 5 \mu\text{m}$	ND: $15.0 \pm 1.7 \mu\text{m}$
Aspect ratio (RD: TD: ND)	5 : 1 : 0.2	2.5 : 2 : 1
Particle size	$2.6 \pm 0.14 \mu\text{m}$	$2.6 \pm 0.15 \mu\text{m}$
Area fraction	$3.5 \pm 0.3 \%$	$3.2 \pm 0.29 \%$



(a)



(b)

Fig. 2 BSE images of the constituent particles of the AA3103 sheets (a) in the H18 temper and (b) in the O temper.

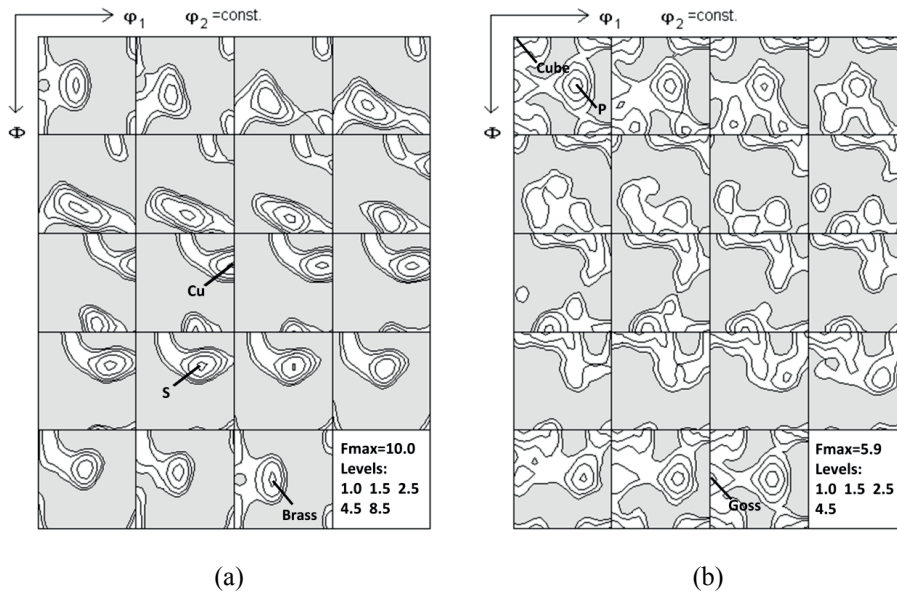


Fig. 3 ODFs for (a) the AA3103-H18 and (b) the AA3103-O sheets.

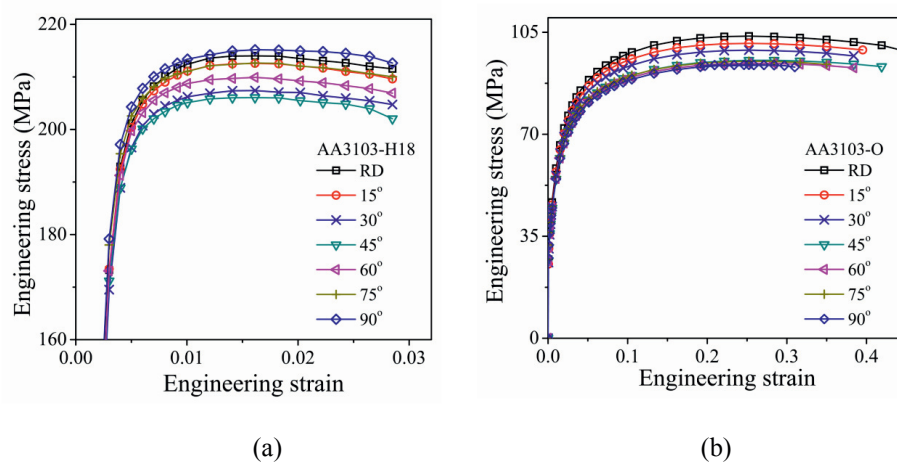


Fig. 4 Stress-strain curves from uniaxial tensile tests along seven in-plane directions of the AA3103 sheets: (a) H18 temper and (b) O temper.

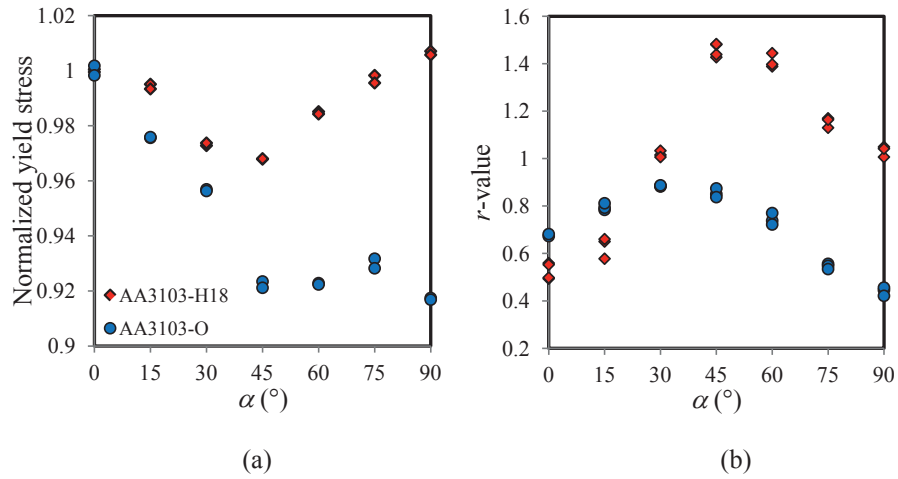


Fig. 5 Plastic anisotropy of the AA3103 sheets based on tensile tests in seven in-plane directions with respect to the RD: (a) normalized yield stress and (b) r -values.

3. Crystal plasticity modelling of plastic anisotropy

The five CP models employed in this work will be briefly introduced in Section 3.1, while the virtual uniaxial tension tests performed with the Taylor-type and VPSC models are described in Section 3.2. Section 3.3 deals with the CPFEM simulations.

3.1. Crystal plasticity models

It is assumed that the plastic deformation is caused by crystallographic slip on the $\{111\}\langle 110\rangle$ slip systems, as is usually assumed for face-centred-cubic (FCC) metals.

The FC-Taylor model assumes that each grain experiences the same deformation as the aggregate, and the deformation is accommodated by at least five slip systems according to the principle of maximum plastic work or the complementary minimum principle, which follows from the yield criteria of the slip systems. Based on the active slip systems, the stress state is found in one of the 56 vertices of the yield surface of each FCC crystal. The stress state of the aggregate is defined as the volume average over all grains.

In the Alamel-type models, a pair is assembled by two grains and their common grain boundary. Local interactions between the two grains in the pair are considered by means of relaxations of constraints of the shear strain components of the prescribed deformation. Stress tensors in each crystal of one pair are calculated from the yield criteria of the slip systems and the equilibrium conditions of the shear stress

components [12, 25]. The Taylor-type models studied here, i.e. the FC-Taylor and Alamel-type models, are rate-independent.

The VPSC model regards each grain of the polycrystal as an ellipsoidal inclusion embedded in a homogeneous effective medium whose mechanical response corresponds to the volumetric average of all grains. Grains in the CPFEM are represented by single or multiple elements and both stress equilibrium and strain compatibility are fulfilled.

The rate-dependent VPSC and CPFEM models assume that all slip systems are active and that the slip activity is determined by a power-law type equation

$$\dot{\gamma}^\alpha = \dot{\gamma}_0 \left| \frac{\tau^\alpha}{g^\alpha} \right|^{\frac{1}{m}} \text{sgn}(\tau^\alpha) \quad (1)$$

where $\dot{\gamma}_0$ is a reference shearing rate, m is the instantaneous strain-rate sensitivity, g^α represents the slip resistance which evolves during the plastic deformation according to the hardening law, and τ^α is the resolved shear stress calculated from the current stress-state and crystallographic orientation.

The hardening law employed in the CPFEM simulations in this work assumes that the critical resolved shear stress g^α , which is initially equal to g_0 , evolves through

$$\dot{g}^\alpha = \sum_{\beta=1}^N h^{\alpha\beta} |\dot{\gamma}^\beta| \quad (2)$$

where $h^{\alpha\beta}$ is the instantaneous strain hardening matrix; α and β are indices referring to slip systems; and N is the number of slip systems. In this work, $h^{\alpha\beta}$ is described phenomenologically by a Voce-type law:

$$h^{\alpha\beta} = \left[\theta_1 + \left(\theta_0 - \theta_1 + \frac{\theta_0 \theta_1}{g_1} \Gamma \right) \exp\left(-\frac{\theta_0}{g_1} \Gamma \right) \right] \left[q + (1-q) \delta^{\alpha\beta} \right] \quad (3)$$

where θ_0 is the initial hardening rate, while θ_1 and g_1 describe the asymptotic hardening. The accumulated plastic shear strain Γ is defined by

$$\dot{\Gamma} = \sum_{\alpha} |\dot{\gamma}^\alpha| \quad (4)$$

The parameter q represents latent hardening, while $\delta^{\alpha\beta}$ is the Kronecker delta function.

3.2. Set-up of Taylor-type and VPSC calculations

Grain orientations are the necessary input for all of the CP models mentioned above. A total of 2500 orientations were randomly selected from the EBSD scanning points, i.e. an aggregate of 2500 grains, for both the AA3103-H18 and AA3103-O materials. The quality of the selected orientations in representing the measured texture is evaluated by the normalized difference texture index [19], defined as

$$ID_N = \frac{\oint (f_{selected}(g) - f_{exp}(g))^2 dg}{\oint (f_{exp}(g))^2 dg} \quad (5)$$

where $f(g)$ is the ODF. Values of ID_N for the grain selections of AA3103-H18 and AA3103-O are 0.39% and 1.13%, respectively, which indicates a rather good representation of the experimental ODF for both materials.

The 2500 orientations were randomly assembled into 3750 Alamel pairs for the AA3103-H18 sheet, such that each grain was reused three times. These pairs were then considered by the Alamel and the Alamel Type III models. The cold-rolled AA3103-H18 sheet shows extensively elongated grain shapes, as illustrated in Fig. 1 and estimated by the grain aspect ratio compiled in Table 2. To reflect such rolling grain structure in the Alamel-type models, grain boundaries in all Alamel pairs were assumed parallel with the RD-TD plane, which reduces the Alamel-type models into Lamel-type models [25], i.e. the Lamel model and the Lamel Type III model.

The same number of Alamel pairs was considered for AA3103-O as for AA3103-H18. To account for the non-equiaxed grain morphology, a deformation gradient tensor \mathbf{F} of a hypothetical deformation was constructed, corresponding to the transformation of a sphere (the ‘basic’ equiaxed grain) into an ellipsoid with the same aspect ratio as the average one estimated in Table 2. Each grain boundary segment, out of a total of 1875, was first assigned a random orientation. Then it was deformed by the tensor \mathbf{F} , leading to a rotation of its plane normal, i.e. modifying the grain boundary orientation distribution. The ratio between the new and the original area of each grain boundary segment was taken as a weighting factor for its corresponding Alamel pair. More details about the methodology for considering grain shapes in Alamel-type models can be found in the literature [15, 19].

The VPSC code reads the grain aspect ratio to define the initial lengths of the three ellipsoid axes. The aspect ratios shown in Table 2 for AA3103-H18 and AA3103-O were then input into the VPSC code for their respective calculations. The instantaneous strain-rate sensitivity m was set as 0.01 to represent the low strain-rate sensitivity of the materials under study. Several formulations exist for the interaction equation that linearly relates stress and strain rate in the grain with the overall stress and strain rate of the effective medium. The intermediate approximation with one adjustable parameter

$n^{eff} = 10$ was used [26]. This approximation approach gives a response of the polycrystal which lies in-between the stiff secant and the compliant tangent approaches.

Virtual in-plane uniaxial tensile tests were carried out along every 3° from the RD to the TD for the Taylor-type and VPSC models. The global strain-rate components were applied and iteratively adjusted until the average stress of the aggregate was uniaxial along the tensile axis. Only the strain-rate components were iterated for the FC-Taylor and Alamel-type models when determining r -values [27, 28], whereas both strain-rate and stress components entered the iteration procedure in the VPSC model.

3.3. Direct CPFEM simulations of tensile tests

To conduct CPFEM simulations of the AA3103-H18 material, Voronoi tessellation [29] was first utilized to generate 2500 grains of random structure in a cuboid volume of size 0.8 mm, 4 mm and 4.8 mm along the RD, TD and ND, respectively. About 26 grains were resolved along the ND while only about 4 grains along the RD. This equiaxed tessellation was then scaled according to the grain aspect ratio shown in Table 2 to obtain a final RVE of $4.0 \times 4.0 \times 0.96 \text{ mm}^3$. The RVE was finally meshed with $89 \times 89 \times 21 = 166341$ cubic solid elements with one integration point, i.e., under-integrated elements with hourglass control. In average, each grain is represented by 67 elements and holds the experimentally observed grain shape, see Fig. 6 (a).

The RVE of AA3103-O material was made in a similar manner, but the final RVE size was $2 \times 2 \times 1 \text{ mm}^3$. The RVE was meshed into 131072 elements. With such a fine mesh, each grain in the RVE is represented by about 52 elements in average and holds qualitatively the general experimental grain shape, see Fig. 6 (b).

Particles were not represented in the CPFEM mesh. Periodic boundary conditions were applied to the nodes located on the faces of the RVE in order to ensure periodicity in displacements and minimize constraint effects [8].

The same value of the strain-rate sensitivity parameter as in the VPSC calculations was adopted in the CPFEM simulations, i.e. $m = 0.01$; the latent hardening parameter q is set to 1.4 as commonly used for FCC metals [30, 31]. The elastic constants c_{11} , c_{12} and c_{44} were set to 106 GPa, 60.4 GPa and 28.2 GPa, respectively. The calibration of other material parameters in Eqs. (1) and (3) were carried out with the design optimization tool LS-OPT [32]. The calibration was made against the experimental uniaxial tensile stress-strain curves along the RD. Since the initial plastic anisotropy is of main concern in this work, the calibration was made in a relatively small deformation range, i.e. up to 1.5% elongation for AA3103-H18 and up to 9.5% elongation for AA3103-O. The calibrated values of the coefficients are compiled in Table 3.

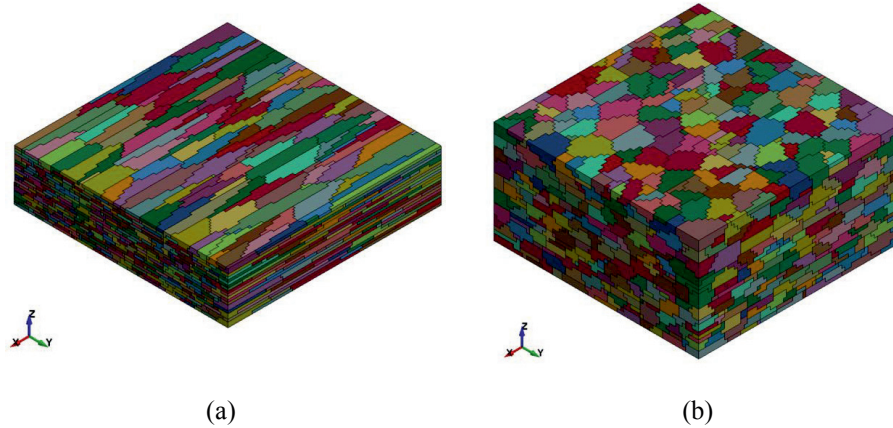


Fig. 6 The RVE used in the CPFEM simulations for (a) the AA3103-H18 and (b) the AA3103-O sheets; the x , y and z axes coincide with the RD, TD and ND, respectively.

Uniaxial tension tests were simulated for AA3103-O by CPFEM for the seven experimentally investigated directions. Tension along the RD was simulated by stretching along the RD with a constant speed. The final elongation for AA3103-O materials was 9.5%. Yield stresses were determined at a constant plastic work per unit volume, namely 0.07 MPa, corresponding to 0.2% plastic strain along the RD for AA3103-O. The r -value was determined from 2% plastic strain to the final deformation. For uniaxial tension in other directions than RD and TD, a technically convenient ‘texture rotation’ method [6, 31] was applied, i.e. fixing the RVE and boundary conditions used for uniaxial tension along the RD while the texture was rotated through decreasing the first Euler angle by the tensile angle α . The ‘texture rotation’ method could be employed since the AA3103-O exhibits nearly equiaxed grain shapes in the RD-TD plane. Uniaxial tension along the TD was simulated by stretching the RVE along this direction.

Uniaxial tension tests for AA3103-H18 were simulated by CPFEM only for the RD and TD, where the RVE was stretched along the respective directions with a constant speed until a final elongation of 1.5%. Yield stresses were determined at a constant plastic work per unit volume, namely 0.36 MPa, corresponding to 0.2% plastic strain along the RD for AA3103-H18. The r -value was determined from 0.4% plastic strain to the final deformation. Simulations were not performed for directions between RD and TD, since the distinctly elongated grain shapes cannot be properly represented by the ‘texture rotation’ method.

Simulation of uniaxial tensile tests in other directions than RD and TD is not simple for non-equiaxed grain structures. Instead, a multi-level modelling method is proposed in the next section.

Table 3 Model parameters used in the CPFEM simulations.

	m	q	$\dot{\gamma}_0$ (s ⁻¹)	g_0 (MPa)	θ_0 (MPa)	g_1 (MPa)	θ_1 (MPa)
AA3103-H18	0.01	1.4	0.001	66.52	3000	9.49	10.98
AA3103-O	0.01	1.4	0.0021	12.02	467.64	15.59	27.76

4. Multi-level modelling by Yld2004-18p and CPFEM

A two-scale modelling scheme was used to describe the plastic anisotropy. The lower scale (meso-scale) model is the grain aggregate consisting of 2500 grains. Stress points at yielding are provided by CPFEM for a number of prescribed in-plane deformations. The macroscopic yield surface is described by the advanced yield function Yld2004-18p which is fitted to these stress points at yielding. The generation of the plane stress states at yielding by CPFEM follows the method proposed by Saai et al. [8]. For the sake of completeness, the method is briefly described in the following.

The RVE has four master nodes, which are numbered 0, 1, 2 and 3 and shown by full black circles in Fig. 7. The axes x , y and z coincide with RD, TD and ND, respectively. Master node 0 was always fixed. A constant velocity v_1^x was applied to the master node 1 along the RD, while master node 2 was given a constant velocity v_2^y along the TD for normal loading and/or a constant velocity v_2^x in the RD for shear loading. Master node 3 was free to move along the ND to adapt the incompressibility of the deformation.

The stress states on the yield surface were generated by controlling the three velocities of master nodes 1 and 2. Three sets of deformation were prescribed, namely

$$v_1^x = v^0, v_2^y = \rho v^0, v_2^x = \lambda v^0 \quad (6)$$

$$v_1^x = \rho v^0, v_2^y = v^0, v_2^x = \lambda v^0 \quad (7)$$

$$v_1^x = 0, v_2^y = 0, v_2^x = v^0 \quad (8)$$

where v^0 is a constant reference velocity, the variable ρ was varied between -1 and 1 with increment $\Delta\rho$, and the variable λ was varied between 0 and 3 with increment $\Delta\lambda$. The deformation according to Eq. (8) corresponds to pure in-plane shear. CPFEM simulations were made for each deformation condition until the volume-weighted average of the plastic work among all integration points reached a critical value. The

Cauchy stress tensor $\boldsymbol{\sigma}$ of the RVE was defined as a volume-weighted average of the stress tensors of all integration points. Since all deformations were prescribed in the sheet plane, the stress components σ_{13} , σ_{23} and σ_{33} were negligibly small compared to the three in-plane stress components, i.e., the averaged stress tensor $\boldsymbol{\sigma}$ corresponded to a state of plane stress.

In this study, the increments $\Delta\rho$ and $\Delta\lambda$ were set to 0.2 and 1.0, respectively. To obtain stress states near initial yielding of each material, the critical plastic work was taken as the plastic work per unit volume at 0.2% plastic strain calculated with the experimental stress-strain curves for tensions along the RD. The value was found to be 0.36 MPa for AA3103-H18 and 0.07 MPa for AA3103-O. With the described settings, a total of 89 stress points at yielding were obtained for each material. The stress component σ_{11} obtained at the critical plastic work for uniaxial tension along the RD was considered as the reference yield stress of the material.

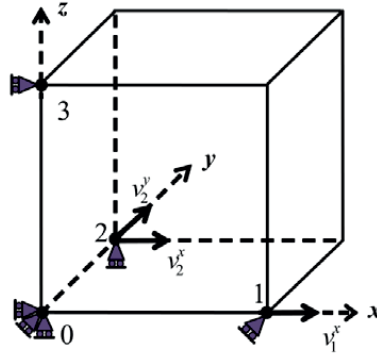


Fig. 7 Boundary conditions applied to the RVE; grey marks at nodes show the constraints of translation motions along axes.

The analytical yield function, denoted Yld2004-18p, was proposed by Barlat et al. [2] as

$$\bar{\sigma}(\boldsymbol{\sigma}) = \frac{1}{4^{1/a}} \left(|S'_1 - S_1''|^a + |S'_1 - S_2''|^a + |S'_1 - S_3''|^a + |S'_2 - S_1''|^a + |S'_2 - S_2''|^a + |S'_2 - S_3''|^a + |S'_3 - S_1''|^a + |S'_3 - S_2''|^a + |S'_3 - S_3''|^a \right)^{1/a} \quad (9)$$

where $\bar{\sigma}$ is the equivalent stress; a is the exponent of the yield function; S'_i and S''_i , $i = 1, 2, 3$, are the principal values of the tensors $\mathbf{S}' = \mathbf{C}'\mathbf{S}$ and $\mathbf{S}'' = \mathbf{C}''\mathbf{S}$, where \mathbf{S} is the deviatoric stress tensor; \mathbf{C}' and \mathbf{C}'' are fourth-order tensors containing all the 18 parameters of the yield function. The exponent a is usually set to 8 for FCC materials. The yield function is then fitted to the stress points at yielding provided by the CPFEM. Among the 18 parameters of Yld2004-18p, there are four related to the through-

thickness stress components. Since only plane stress states are considered here, these four parameters were set to unity, which is the value for an isotropic material. The other 14 parameters were identified by calibration to the 89 stress points at yielding computed by CPFEM. It is noted that these 89 stress points were normalized by the yield stress along the RD before entering into the calibration procedure.

More details about the yield function and associated parameter identification procedures can be found in the literature [1, 2, 12, 33].

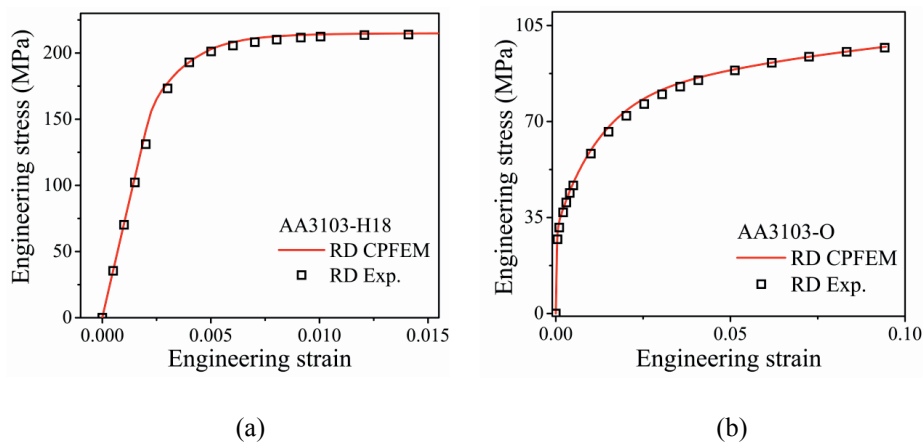


Fig. 8 Comparisons between the experimental stress-strain curves and the CPFEM predictions with calibrated material coefficients.

5. Numerical results and discussion

Stress-strain curves for uniaxial tension in the RD predicted by CPFEM with the parameters compiled in Table 3 are compared to the experimental data in Fig. 8. The predicted curves for both materials show perfect match with the experiments, thus validating the parameter calibration.

The $\sigma_{11} - \sigma_{22}$ yield loci derived from the fitted Yld2004-18p for both materials are plotted in Fig. 9, where also the CPFEM stress points at yielding in biaxial tension, i.e. loading with $\lambda = 0$ in Eq. (6) and (7), are shown. Fig. 9 shows good agreement between the yield loci and the CPFEM stress points. Since all 89 stress points were equally weighted in the calibration procedure, the same accuracy of the Yld2004-18p yield surface in representing the CPFEM calculations is expected for other plane stress states.

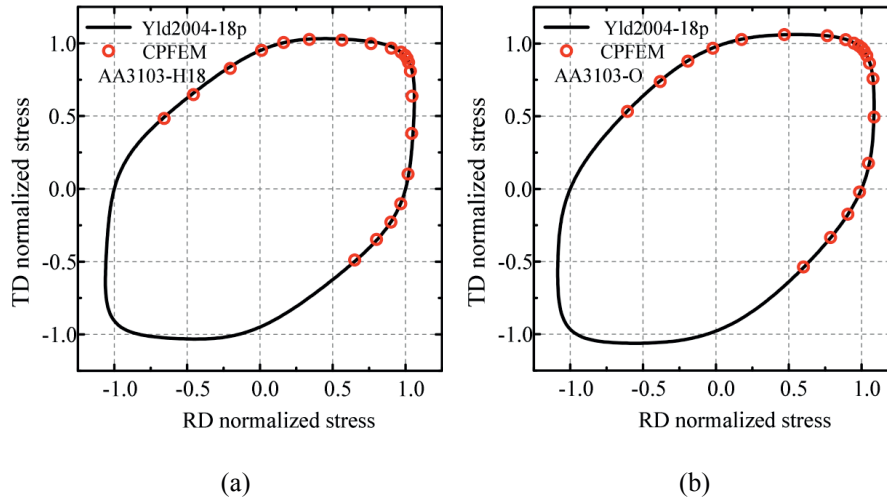
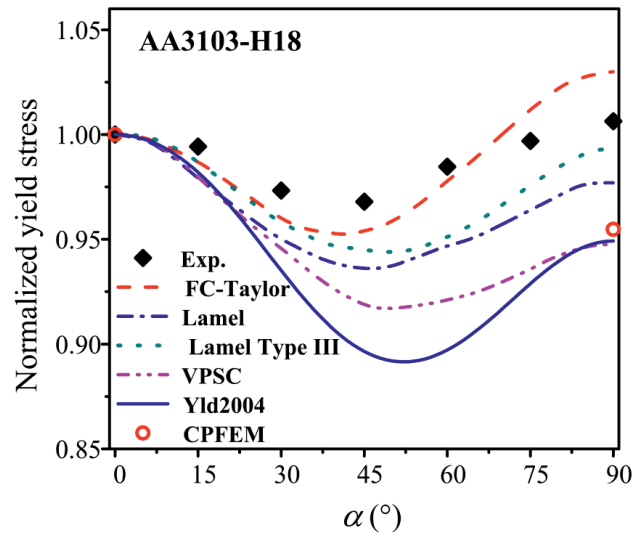


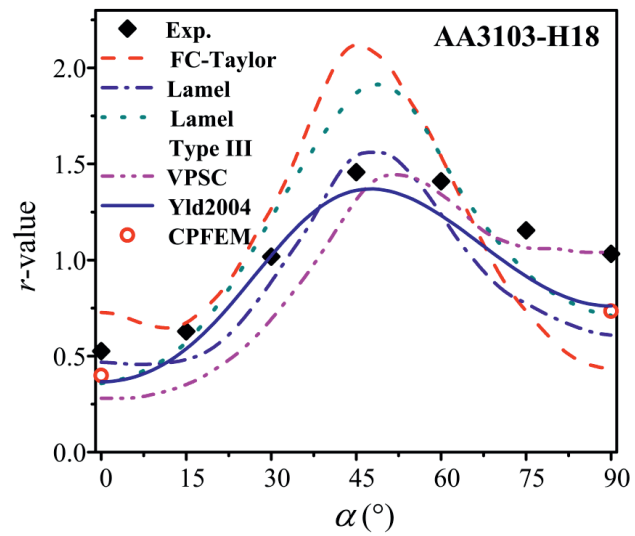
Fig. 9 Yld2004-18p yield loci for (a) the AA3103-H18 and (b) the AA3103-O material, including the stress points at yielding in biaxial tension from the CPFEM calculations.

The predicted anisotropy of the normalized yield stress and the r -value by all the CP models described above is shown in Fig. 10 and Fig. 11 for AA3103-H18 and AA3103-O, respectively. The average of duplicate experimental tests is shown in these figures to evaluate the quality of predictions.

As shown in Fig. 10 for AA3103-H18, all CP models and the Yld2004-18p yield surface calibrated to CPFEM stress points predict weak anisotropy in strength but strong anisotropy in plastic flow. The trends of the experimental data are well captured by all CP models and the yield surface, but there are some quantitative differences. The FC-Taylor model gives the most accurate prediction of the anisotropy in the normalized yield stress, and gives results within 2% of the experimental values. The other CP models consistently predict lower normalized yield stresses. Note that for all CP models the normalized yield stress equals unity in the RD owing to the normalization. The Lamel and Lamel-type III models give similar predictions but the latter model performs slightly better. The predictions obtained with the VPSC model and the CPFEM calibrated Yld2004-18p yield function are similar, but less accurate.



(a)



(b)

Fig. 10 Plastic anisotropy of the AA3103-H18 material predicted by different CP models and the CPFEM-fitted Yld2004-18p yield surface: (a) normalized yield stress and (b) r -value.

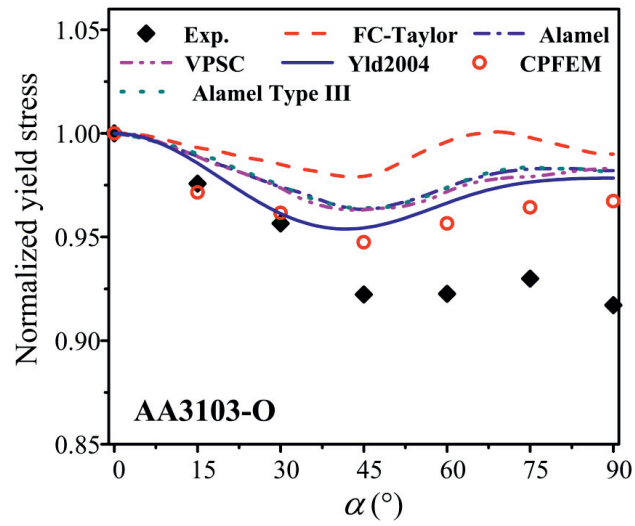
Concerning the r -value at the RD, the Lamel-type models and the CPFEM-calibrated Yld2004-18p yield function give reasonable predictions, while the FC-Taylor and VPSC models are 25% higher and 50% lower than the experimental data, respectively. At $\alpha = 45^\circ$, the FC-Taylor and Lamel Type III models give about 30% higher r -value than the experiments, whereas the predictions with the Lamel and VPSC models and the Yld2004-18p yield function are close to the experiments. At the TD, only the prediction with the VPSC model agrees well with the experiment, while the other predictions are lower than the experimental results. In particular, the FC-Taylor model underestimated the r -value severely at the TD.

In Fig. 10, the CPFEM points at RD and TD are close to the predictions by the Yld2004-18p yield function fitted to 89 distributed yield points in the stress space, which indicates a good precision of this calibration. In summary, the CPFEM-calibrated Yld2004-18p yield surface gives the best overall description of the variation of the r -value, whereas the Lamel Type III model works slightly better than other aggregate models when considering both the variation of the normalized yield stress and the r -value.

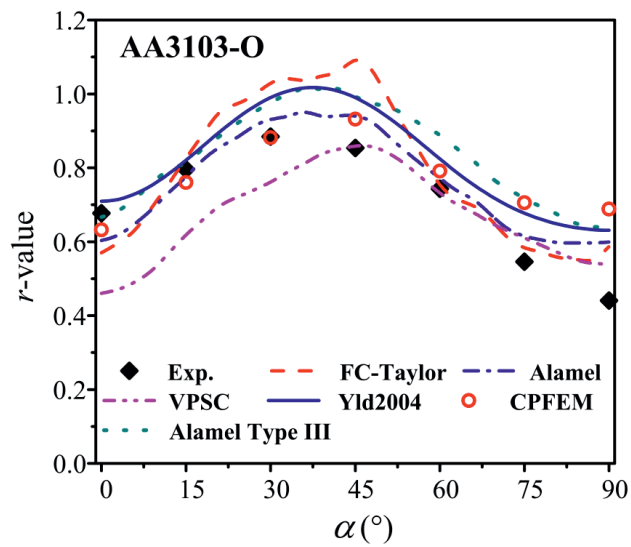
Simulations were also made by Alamel-type models where the grain morphology was represented by fictitiously deforming a random grain structure according to the measured grain aspect ratio of the AA3103-H18 sheet. The results were very similar to the Lamel-type calculations, confirming that the assumption made with respect to the grain boundary in the Lamel-type models is reasonable for the heavily cold rolled H18 condition.

The predicted anisotropy in normalized yield stress and r -value for AA3103-O is presented in Fig. 11. All models show similar variations of both the normalized yield stress and the r -value, but there are some quantitative differences. The lower strengths exhibited in the experiments for $\alpha \in [45^\circ, 90^\circ]$ is not captured by any of the models. The predictions obtained with CPFEM, either with direct calculations or the fitted yield surface, are closest to the experiments, only 3% and 6% higher values of the normalized yield stress than in the experiments at α equal to 45° and 90° , respectively. The predictions of the normalized yield stress by the Alamel, Alamel Type III and VPSC models are nearly identical and slightly higher than the CPFEM results, while the FC-Taylor model gives the least accurate predictions.

The variation of r -values predicted by all CP models and the CPFEM-calibrated Yld2004-18p yield function agrees well with the experimental results. The predictions obtained with the Alamel model, CPFEM and its calibrated Yld2004-18p yield surface are closest to the experimental r -values.



(a)



(b)

Fig. 11 Plastic anisotropy of the AA3103-O material predicted by different CP models and the CPFEM-fitted Yld2004-18p yield surface: (a) normalized yield stress and (b) r -value.

In Fig. 11, small discrepancies can be observed between the CPFEM calculations and the calibrated Yld2004-18p yield function with respect to predictions of the directional normalized yield stresses and r -values. These differences indicate the errors of the calibration procedure of the Yld2004-18p yield surface. In other directions than RD or TD, the non-equiaxed shape of the grains may also contribute to the differences. Since the differences are small, it can be concluded that the multi-level modelling method can accurately capture the plastic anisotropy predicted from CPFEM calculations. This conclusion is supported by the similarity of the predictions in Fig. 9 and Fig. 10.

In summary, the Alamel model, CPFEM and the CPFEM-calibrated Yld2004-18p yield surface perform slightly better than other models in predicting the in-plane plastic anisotropy of the AA3103-O in uniaxial tension.

Even the simple FC-Taylor model was found to give reasonable predictions of the plastic anisotropy of the AA3103-H18 and AA3103-O sheets based solely on the texture. This indicates that the plastic anisotropy exhibited by the two materials is mainly due to their respective textures. The predictions of the Alamel-type models, the VPSC model and CPFEM are generally better than those of the FC-Taylor model. In these advanced CP models, the strain constraints imposed in the FC-Taylor model are relaxed to various extents, rendering these models somehow more physically reasonable. The grain morphology is to some extent considered in these advanced CP models in addition to the texture. Despite their differences in handling the grain morphology and grain interactions, the performance of these CP models in predicting plastic anisotropy and its evolution is improved, even though not significantly.

As mentioned above, the ‘texture rotation’ method has been employed in the CPFEM simulations of uniaxial tension tests in directions between the RD and TD for AA3103-O. It should be noted that the ‘texture rotation’ method is physically meaningful for equiaxed grain structures. For elongated grain structures as studied here, however, the grain boundary configurations change with the tensile direction. As an example, the number density of grain boundaries along the RD differs significantly from that along the TD of the AA3103-H18 material, see Fig. 6. As a consequence, different RVEs should be prepared for uniaxial tension along different directions. Unfortunately, preparing such RVEs for directions other than the three orthotropic axes is rather complex and inconvenient. Alternatively, the hierarchical multi-level modelling method described in Section 4 can be used, where uniaxial tension is no longer the only desired deformation mode. Instead, a number of virtual deformation modes are prescribed to obtain stress states on the yield surface. The flexible yield function Yld2004-18p is then calibrated against these stress points at yielding and used to represent the yield surface of the material. In these CPFEM simulations, the effect of the grain shape has been considered implicitly, since all the deformations are prescribed with respect to the same RVE. Another distinct advantage of this multi-level method is that the plastic anisotropy

is known for any stress direction once the calibration is done. The yield loci shown in Fig. 9 are such examples. Furthermore, the virtually fitted yield surface can be used in large-scale FE simulations of forming processes.

As shown in Fig. 10 and Fig. 11, the CPFEM-calibrated Yld2004-18p yield surface cannot capture the experimental data in a quantitative manner. This is mainly attributed to the inaccuracy of the underlying CPFEM calculations compared with the experimental results. The Yld2004-18p yield surface can also be calibrated to both experimental data and virtual stress points at yielding from CPFEM calculations, following the hybrid fitting procedure proposed in [12]. As concluded by Zhang et al. [12], based on results for a commercially pure aluminium alloy, the hybrid-fitted Yld2004-18p yield function can capture the experimental results and at the same time ensure a good fit to the anisotropy in the full stress space predicted by the crystal plasticity models. Procedures for calibrating the Yld2004-18p yield surface against the virtual stress points at yielding provided by the FC-Taylor, Alamel, Alamel-type III and VPSC models, respectively, can also be found in [12].

The FC-Taylor, Alamel-type and VPSC models showed a similar computational efficiency when simulating the uniaxial tensile tests. Each of these models can calculate a tensile test up to a strain of 10% in only a few seconds using one single CPU, whereas the CPFEM takes a few hours running 4 parallel CPUs on the same computer. Thus, roughly estimated, applying the CPFEM is three orders of magnitude more computationally expensive than the Taylor-type and VPSC models.

The current materials feature large fractions of constituent particles which were ignored in all the simulations made in this work. During cold-rolling, back-stresses can be introduced due to these non-shearable particles [34]. The back-stress may contribute to the weak strength anisotropy observed in the AA3103-H18 material. For the fully annealed material, the back-stress should have completely vanished during the recrystallization, and there should then be little influence of particles on the observed initial strength anisotropy. Other micro-structural features besides the texture and grain morphology, such as aligned dislocation structures [35-37] and grain size [38], may also be the sources of mechanical anisotropy. Taking particles and other micro-structural information into consideration by CP models is beyond the scope of this paper.

6. Conclusion

The anisotropic plastic behaviour of AA3103 sheets in cold-rolled and fully recrystallized states has been investigated experimentally by uniaxial tensile tests and virtually by five different CP models and a hierarchical multi-level modelling method. The experimentally observed grain shapes have been taken into consideration in the computations. All the five CP models give reasonable predictions of the directional

normalized yield stresses and r -values for both materials when compared to the experiments, but the Alamel-type models and the multi-level fitting method that involves CPFEM calculations and the Yld2004-18p yield function perform slightly better than the other CP models.

In the multi-level modelling method, the yield surface of the material was represented by the Yld2004-18p yield function and calibrated to stress points at yielding obtained with CPFEM. This method makes it possible to predict plastic anisotropy while considering the real grain shapes even for non-equiaxed grain structures in the CPFEM simulations. The Yld2004-18p yield surface was able to represent quite accurately the plastic anisotropy determined from CPFEM calculations under this multi-level modelling scheme. Based on the results presented in this work, the multi-level fitting method used here is considered to be the most accurate method for predicting the plastic anisotropy in the considered two cases. Since high-resolution CPFEM calculations are very time-expensive, the Alamel-type models are good alternatives for predicting the plastic anisotropy of the considered AA3103 sheets.

Reference

- [1] Grytten F, Holmedal B, Hopperstad O S and Børvik T 2008 Evaluation of identification methods for YLD2004-18p *Int. J. Plast.* 24 2248-2277.
- [2] Barlat F, Aretz H, Yoon J W, Karabin M E, Brem J C and Dick R E 2005 Linear transformation-based anisotropic yield functions *Int. J. Plast.* 21 1009-1039.
- [3] Banabic D, Kuwabara T, Balan T, Comsa D S and Julean D 2003 Non-quadratic yield criterion for orthotropic sheet metals under plane-stress conditions *Int. J. Mech. Sci.* 45 797-811.
- [4] Aretz H and Barlat F 2013 New convex yield functions for orthotropic metal plasticity *Int. J. Nonlin. Mech.* 51 97-111.
- [5] Barlat F, Brem J C, Yoon J W, Chung K, Dick R E, Lege D J, Pourboghraat F, Choi S H and Chu E 2003 Plane stress yield function for aluminum alloy sheets—part 1: theory *Int. J. Plast.* 19 1297-1319.
- [6] Inal K, Mishra R K and Cazacu O 2010 Forming simulation of aluminum sheets using an anisotropic yield function coupled with crystal plasticity theory *Int. J. Solids. Struct.* 47 2223-2233.
- [7] Gawad J, Banabic D, Comsa D S, Gologanu M, Van Bael A, Eyckens P, Van Houtte P and Roose D 2013 Evolving texture-informed anisotropic yield criterion for sheet forming *AIP Conf. Proc.* 1567 350-355.
- [8] Saai A, Dumoulin S, Hopperstad O S and Lademo O G 2013 Simulation of yield surfaces for aluminium sheets with rolling and recrystallization textures *Comput. Mater. Sci.* 67 424-433.
- [9] Gawad J, Van Bael A, Eyckens P, Samaey G, Van Houtte P and Roose D 2013 Hierarchical multi-scale modeling of texture induced plastic anisotropy in sheet forming *Comput. Mater. Sci.* 66 65-83.

- [10] Barlat F and Richmond O 1987 Prediction of tricomponent plane stress yield surfaces and associated flow and failure behavior of strongly textured f.c.c. polycrystalline sheets *Mater. Sci. Eng.* 95 15-29.
- [11] Zhang K, Holmedal B, Manik T and Zhao Q, Crystal Plasticity Calculations of Mechanical Anisotropy of Aluminium Compared to Experiments and to Yield Criterion Fittings, ICAA13: 13th International Conference on Aluminum Alloys, John Wiley & Sons, Inc., 2012, pp. 915-920.
- [12] Zhang K, Holmedal B, Hopperstad O S, Dumoulin S, Gawad J, Van Bael A and Van Houtte P 2014 Multi-level Modelling of Mechanical Anisotropy of Commercial Pure Aluminium Plate: Crystal Plasticity Models, Advanced Yield Functions and Parameter Identification *Int. J. Plast.*
- [13] Patala S, Mason J K and Schuh C A 2012 Improved representations of misorientation information for grain boundary science and engineering *Prog. Mater. Sci.* 57 1383-1425.
- [14] Chang H J, Han H N, Park S J, Cho J H and Oh K H 2010 Texture evolution in FCC metals from initially different misorientation distributions under shear deformation *Met. Mater. Int.* 16 553-558.
- [15] Xie Q, Eyckens P, Vegter H, Moerman J, Van Bael A and Van Houtte P 2013 Polycrystal plasticity models based on crystallographic and morphologic texture: Evaluation of predictions of plastic anisotropy and deformation texture *Mater. Sci. Eng., A* 581 66-72.
- [16] Taylor G I 1938 Plastic strain in metals *J. Inst. Metals.* 62 307-324.
- [17] Bishop J F W and Hill R 1951 CXXVIII. A theoretical derivation of the plastic properties of a polycrystalline face-centred metal *Philos. Mag.* S7 42 1298-1307.
- [18] Bishop J F W and Hill R 1951 XLVI. A theory of the plastic distortion of a polycrystalline aggregate under combined stresses *Philos. Mag.* S7 42 414-427.
- [19] Van Houtte P, Li S, Seefeldt M and Delannay L 2005 Deformation texture prediction: from the Taylor model to the advanced Lamel model *Int. J. Plast.* 21 589-624.
- [20] Mánik T and Holmedal B 2013 Additional relaxations in the Alamel texture model *Mater. Sci. Eng., A* 580 349-354.
- [21] Lebensohn R A and Tomé C N 1993 A self-consistent anisotropic approach for the simulation of plastic deformation and texture development of polycrystals: Application to zirconium alloys *Acta Metall. Mater.* 41 2611-2624.
- [22] Zhang K, Hopperstad O S, Holmedal B and Dumoulin S 2014 A robust and efficient substepping scheme for the explicit numerical integration of a rate-dependent crystal plasticity model *Int. J. Numer. Meth. ENG.* To be published.
- [23] An Y G, Vegter H, Melzer S and Romano Triguero P 2013 Evolution of the plastic anisotropy with straining and its implication on formability for sheet metals *J. Mater. Process. Technol.* 213 1419-1425.
- [24] Engler O, Crumbach M and Li S 2005 Alloy-dependent rolling texture simulation of aluminium alloys with a grain-interaction model *Acta Mater.* 53 2241-2257.
- [25] Van Houtte P, Delannay L and Samajdar I 1999 Quantitative Prediction of Cold Rolling Textures in Low-Carbon Steel by Means of the Lamel Model *Textures Microstruct.* 31 109-149.
- [26] Tomé C N 1999 Self-consistent polycrystal models: a directional compliance criterion to describe grain interactions *Modell. Simul. Mater. Sci. Eng.* 7 723.
- [27] Bunge H J 1970 Some applications of the Taylor theory of polycrystal plasticity *Kristall und Technik* 5 145-175.

- [28] Li S, Engler O and Van Houtte P 2005 Plastic anisotropy and texture evolution during tensile testing of extruded aluminium profiles *Modell. Simul. Mater. Sci. Eng.* 13 783.
- [29] Quey R, Dawson P R and Barbe F 2011 Large-scale 3D random polycrystals for the finite element method: Generation, meshing and remeshing *Comput. Method, Appl. M.* 200 1729-1745.
- [30] Kalidindi S R, Bronkhorst C A and Anand L 1992 Crystallographic texture evolution in bulk deformation processing of FCC metals *J. Mech. Phys. Solids* 40 537-569.
- [31] Dumoulin S, Engler O, Hopperstad O S and Lademo O G 2012 Description of plastic anisotropy in AA6063-T6 using the crystal plasticity finite element method *Modell. Simul. Mater. Sci. Eng.* 20 055008.
- [32] Stander N, Roux W, Goel T, Eggleston T and Craig K 2012 *LS-OPT User's Manual* Version 4.2 Livermore Software Technology Corporation California
- [33] Yoon J W, Barlat F, Dick R E and Karabin M E 2006 Prediction of six or eight ears in a drawn cup based on a new anisotropic yield function *Int. J. Plast.* 22 174-193.
- [34] Zhao Q, Holmedal B and Li Y 2013 Influence of dispersoids on microstructure evolution and work hardening of aluminium alloys during tension and cold rolling *Philos. Mag.* 93 2995-3011.
- [35] Holmedal B, Houtte P V and An Y 2008 A crystal plasticity model for strain-path changes in metals *Int. J. Plast.* 24 1360-1379.
- [36] Juul Jensen D and Hansen N 1990 Flow stress anisotropy in aluminium *Acta Metall. Mater.* 38 1369-1380.
- [37] Barlat F, Ha J, Grácio J J, Lee M-G, Rauch E F and Vincze G 2013 Extension of homogeneous anisotropic hardening model to cross-loading with latent effects *Int. J. Plast.* 46 130-142.
- [38] Delannay L and Barnett M R 2012 Modelling the combined effect of grain size and grain shape on plastic anisotropy of metals *Int. J. Plast.* 32-33 70-84.

Appendix

Article A-1

An explicit integration scheme for hypo-elastic viscoplastic crystal plasticity

K. ZHANG¹, B. HOLMEDAL¹, S. DUMOULIN², O.S. HOPPERSTAD^{3,4}

¹ Department of Materials Science and Engineering, Norwegian University of Science and Technology, NO-7491 Trondheim, Norway

² SINTEF Materials and Chemistry, NO-7465 Trondheim, Norway

³ Department of Structural Engineering, Norwegian University of Science and Technology, NO-7491 Trondheim, Norway

⁴ Structural Impact Laboratory (SIMLab), Center for Research-based Innovation, Norwegian University of Science and Technology, NO-7491 Trondheim, Norway

Presented at the conference: **1st Asian Conference on Aluminum Alloys (ACAA-2013)**.

Accepted after peer-review for publication in the journal:

Transactions of Nonferrous Metals Society of China

An explicit integration scheme for hypo-elastic viscoplastic crystal plasticity

Abstract: An explicit integration scheme for rate-dependent crystal plasticity (CP) has been developed in this work. Additive decomposition of the velocity gradient tensor into lattice and plastic parts is adopted for describing the kinematics; the Cauchy stress is calculated by using a hypo-elastic formulation, applying the Jaumann stress rate. This CP scheme has been implemented into a commercial finite element code (CPFEM). Uniaxial compression and rolling processes were simulated. The results show good accuracy and reliability of the integration scheme. The results were compared to simulations using one hyper-elastic CPFEM implementation which involves multiplicative decomposition of the deformation gradient tensor. It is found that the hypo-elastic implementation is only slightly faster and has a similar accuracy as the hyper-elastic formulation.

Keywords: crystal plasticity; hypo-elasticity; hyper-elasticity; forward Euler integration

1. Introduction

Crystal plasticity (CP) models originate from the physical aspect of plastic deformation, i.e. slip dominated plastic deformation [1]. Constitutive laws of single crystals together with homogenization methods across polycrystalline aggregates define the polycrystal plasticity model [2, 3]. Mechanical properties, texture evolution and other material phenomena can be simulated using CP models [2-5]. The main inputs into CP models are initial texture and material parameters.

One key component of a crystal plasticity model at single grain level is the determination of shear strains or shear strain rates on slip systems, which can generally be solved using two different approaches, either rate-independent or rate-dependent. For the rate-independent method, the shear strain is determined to accommodate the prescribed plastic deformation using a minimum dissipation energy assumption [1]. Only the slip systems for which the resolved shear stress equals the critical resolved shear stress are considered to be active. It can be implemented numerically by solving linear equations or using e.g. the Simplex method with high computational efficiency [6]. However, due to the Taylor ambiguity, an additional criterion is needed [7]. The rate-dependent crystal plasticity (RDCP) model assumes that all slip systems are active and uses a viscoplastic flow rule. Although without Taylor ambiguity, RDCP could lead to numerical instabilities of integration, because most metals exhibit a weak rate dependence at room temperature [8]. Since first introduced by PEIRCE et al [9], the crystal plasticity theory implemented in the finite element method (CPFEM) has matured into a whole family of constitutive and numerical formulations that have been applied to a broad variety of crystal

mechanical problems [3]. CPFEM has both theoretical and practical advantages. First, grains are represented by single or multiple elements while both stress equilibrium and strain compatibility can be fulfilled at boundaries. Second, complex boundary conditions are easily specified in the FEM code. Hence, CPFEM is applicable to simulations of engineering processes. The main drawback of CPFEM is the huge computational cost and the numerical instabilities [2]. Thus, robust and efficient integration schemes are required to reduce computational cost and improve the stability [2, 8, 10-14].

DUMOULIN et al [2] implemented and evaluated three different integration schemes for RDCP, including two forward Euler methods and one implicit integration method. Multiplicative decomposition of the deformation gradient tensor \mathbf{F} was used to describe the kinematics and a hyper-elastic formulation was used for the calculation of the Cauchy stress. Rotation of the crystal lattice was obtained by polar decomposition of the elastic deformation gradient tensor \mathbf{F}^e . Among those three integration methods, the forward Euler integration scheme proposed by GRUJICIC and BATCHU (GB) [14] proved to be stable, accurate and the fastest. The RDCP model together with the GB forward Euler integration scheme has also been implemented into a commercial finite element code, LS-DYNA [15], via a user defined subroutine UMAT. This model implementation is referred to as hyper-CPFEM in the following since hyper-elasticity is assumed.

In the current work, a new explicit integration scheme for rate-dependent viscoplastic crystal plasticity has been developed. Different from the constitutive models employed by DUMOULIN et al [2], additive decomposition of the velocity gradient tensor \mathbf{L} is employed for the kinematics; hypo-elasticity is assumed for the material and Jaumann stress rate is applied. In the crystal plasticity theory, the hyper- and hypo- elastic formulations should give the same results in terms of the plastic deformation. There is small difference in the elastic part while details about the hypo-elastic and hyper-elastic theories can be found in the literature [16]. The hypo-elastic theory is commonly applied in the continuum plasticity for metals and alloys due to their small elastic strains. Compared with the hyper-elastic crystal plastic framework, the hypo-elastic counterpart has a simpler mathematical formulation and is easier to implement. Hence, the hypo-elastic crystal plasticity model has a potential to speed up the calculations. However, the accuracy and reliability of stress calculation and texture prediction should be evaluated due to the different formulation employed.

The kinematics, kinetics and crystal plasticity models are described in section 2. A new explicit integration scheme is proposed in section 3. The RDCP model has been implemented into LS-DYNA and is termed hypo-CPFEM in the following. The accuracy and efficiency of this new integration scheme are evaluated through numerical simulations and a comparison with the hyper-CPFEM which are shown in section 4, while general conclusions are made in section 5.

2. Kinematics and crystal plasticity models

The model employed in this work is briefly given here while more details can be found in the literature [17, 18]. It includes anisotropic elastic deformation and assumes that all plastic deformation occurs via dislocation slip on $\{111\} \langle 110 \rangle$ crystallographic systems for face centred cubic (FCC) crystal metals.

2.1. Kinematics

All the equations described in the following are formulated in the initial crystal frame unless specified otherwise. The imposed velocity gradient \mathbf{L} can be additively decomposed into symmetric and skew-symmetric parts:

$$\mathbf{L} = \mathbf{D} + \mathbf{W} \quad (1)$$

where \mathbf{D} is the symmetric deformation rate tensor and \mathbf{W} is the skew-symmetric spin tensor. Deformation of single crystals has been attributed to a combination of plastic flow due to crystallographic slips and lattice distortion. Lattice distortion includes elastic distortion and rigid body rotation of the crystal lattice. Thus, for single crystals, the deformation rate \mathbf{D} and spin \mathbf{W} can be further decomposed into lattice and plastic parts as follows:

$$\mathbf{D} = \mathbf{D}^e + \mathbf{D}^p \quad (2)$$

$$\mathbf{W} = \mathbf{W}^* + \mathbf{W}^p \quad (3)$$

where \mathbf{D}^e represents the elastic deformation rate of the lattice, while \mathbf{D}^p is the plastic deformation rate caused by crystallographic slip. \mathbf{W}^* represents the lattice rigid spin, while \mathbf{W}^p is the spin due to slip activities. \mathbf{D}^p and \mathbf{W}^p can be expressed by the shear rates $\dot{\gamma}^s$ on all slip systems:

$$\mathbf{D}^p = \sum_{s=1}^{12} \dot{\gamma}^s \mathbf{P}^s \quad (4)$$

$$\mathbf{W}^p = \sum_{s=1}^{12} \dot{\gamma}^s \mathbf{\Omega}^s \quad (5)$$

with

$$\mathbf{P}^s = \frac{1}{2} (\mathbf{m}^s \otimes \mathbf{n}^s + \mathbf{n}^s \otimes \mathbf{m}^s) \quad (6)$$

$$\mathbf{\Omega}^s = \frac{1}{2} (\mathbf{m}^s \otimes \mathbf{n}^s - \mathbf{n}^s \otimes \mathbf{m}^s) \quad (7)$$

where \mathbf{m}^s is the unit vector defining slip direction, while \mathbf{n}^s is the unit slip plane normal vector, for the slip system s (where $s = 1-12$ for FCC metals). \mathbf{m}^s and \mathbf{n}^s are not affected by crystallographic slip but will be rotated by the lattice spin \mathbf{W}^* as:

$$\dot{\mathbf{m}}^s = \mathbf{W}^* \cdot \mathbf{m}^s \quad (8)$$

$$\dot{\mathbf{n}}^s = \mathbf{W}^* \cdot \mathbf{n}^s \quad (9)$$

2.2. Kinetics

The resolved shear stress τ^s on the slip system s can be expressed as:

$$\tau^s = \boldsymbol{\sigma} : \mathbf{P}^s \quad (10)$$

where $\boldsymbol{\sigma}$ is the Cauchy stress tensor. For rate-dependent crystal plasticity, the shear rate on slip systems is often calculated using a power-law type equation:

$$\dot{\gamma}^s = \dot{\gamma}_0 \cdot \text{sgn}(\tau^s) \cdot \left| \frac{\tau^s}{g^s} \right|^{\frac{1}{m}} \quad (11)$$

where $\dot{\gamma}_0$ is a reference shearing rate, m is the instantaneous strain rate sensitivity and g^s represents the slip resistance which evolves during the plastic deformation of single grains. The evolution laws of g^s or hardening models will be discussed in section 2.3.

During distortion of single crystals, a coordinate system attached to the lattice will co-rotate with the lattice. The co-rotational lattice frame is related to the fixed lattice frame by a rotation tensor \mathfrak{R} which is orthogonal and updated by the lattice spin tensor \mathbf{W}^* :

$$\dot{\mathfrak{R}} = \mathbf{W}^* \mathfrak{R} \quad (12)$$

In the co-rotational frame, Hooke's law can be expressed in the rate form as:

$$\dot{\hat{\boldsymbol{\sigma}}} = \hat{\mathbf{C}} : \hat{\mathbf{D}}^e \quad (13)$$

where $\hat{\mathbf{C}}$ is a fourth-order elastic modulus tensor and $\hat{\mathbf{D}}^e$ is the elastic deformation rate tensor, both in the co-rotational frame. The fourth-order tensor $\hat{\mathbf{C}}$ accounts for the elastic anisotropy of the cubic lattice. It is assumed to be invariant to plastic deformation and is kept constant in the co-rational lattice frame. Expressed in the orthonormal basis associated with the crystal lattice, it reads (in Voigt notation):

$$\hat{\mathbf{C}} = \begin{bmatrix} c_{11} & c_{12} & c_{12} & 0 & 0 & 0 \\ c_{12} & c_{11} & c_{12} & 0 & 0 & 0 \\ c_{12} & c_{12} & c_{11} & 0 & 0 & 0 \\ 0 & 0 & 0 & c_{44} & 0 & 0 \\ 0 & 0 & 0 & 0 & c_{44} & 0 \\ 0 & 0 & 0 & 0 & 0 & c_{44} \end{bmatrix} \quad (14)$$

where c_{11} , c_{12} and c_{44} are three independent elastic constants. $\hat{\mathbf{D}}^e$ can be computed by transforming \mathbf{D}^e from the fixed lattice frame to the co-rotational frame as:

$$\hat{\mathbf{D}}^e = \mathfrak{R}^T \mathbf{D}^e \mathfrak{R} \quad (15)$$

where the upper script T means transpose of a tensor or matrix. Then Jaumann stress rate, $\sigma^{\nabla J}$, is now defined by transforming $\hat{\dot{\sigma}}$ into the fixed coordinate system:

$$\sigma^{\nabla J} = \mathfrak{R} \hat{\dot{\sigma}} \mathfrak{R}^T \quad (16)$$

Finally, the material time derivative of the stress tensor is obtained:

$$\dot{\sigma} = \sigma^{\nabla J} + \mathbf{W}^* \sigma - \sigma \mathbf{W}^* \quad (17)$$

2.3. Hardening model

Material hardening is captured at slip system level through g^s in Eq. (11). The hardening law used in this work assumes that the critical resolved shear stress, g^s , initially equals g_0 , evolves through:

$$\dot{g}^s = \sum_{n=1}^{12} h^{sn} |\dot{\gamma}^n| \quad (18)$$

where h^{sn} is the instantaneous strain hardening matrix; s and n are indices referring to slip systems. In this work, h^{sn} is described phenomenologically by a saturation-type law [8, 19]:

$$h^{sn} = h_0 [q + (1-q) \delta^{sn}] [1 - g^n / g_{sat}]^a \operatorname{sgn}[1 - g^n / g_{sat}] \quad (19)$$

where $\delta^{sn} = 1$ for $s = n$ and otherwise zero; h_0 , g_{sat} and a are material parameters, representing the reference self-hardening coefficient, the saturation values of slip resistance and the hardening exponent, respectively. The parameter q represents latent hardening.

2.4. Update of grain orientations and the texture

If the velocity gradient \mathbf{L}' is prescribed in the sample frame, \mathbf{L} in the initial lattice frame is obtained by the transformation

$$\mathbf{L} = \mathbf{Q}_0 \mathbf{L}' \mathbf{Q}_0^T \quad (20)$$

where the transformation matrix \mathbf{Q}_0 depends on the Euler angles $(\varphi_1, \Phi, \varphi_2)$. The transformation matrix \mathbf{Q} from the global frame to the current co-rotational lattice frame is updated by:

$$\mathbf{Q} = \mathfrak{R}^T \mathbf{Q}_0 \quad (21)$$

Euler angles of single grains during deformation can be calculated from \mathbf{Q} and are used to represent the texture.

3. Integration algorithm

The crystal plasticity model described above has been implemented into LS-DYNA through a user defined material subroutine. The key input includes material parameters and initial grain orientations. Mechanical response and deformation texture can then be predicted.

For the time integration, a fully explicit scheme based on the forward Euler method is adopted. This method is simple, robust but only conditionally stable and requires small time steps. The main steps of the explicit scheme are summarized below, where all variables at time t_n are known and the variables at $t_{n+1} = t_n + \Delta t$ are to be determined.

- a) Compute the resolved shear stress τ_n^s on each slip system using Eq. (10)
- b) Compute the slip rate $\dot{\gamma}_n^s$ using Eq. (11)
- c) Compute \mathbf{D}_n^p and \mathbf{W}_n^p using Eq. (4) and Eq. (5)
- d) Compute \mathbf{D}_n^c and \mathbf{W}_n^* using Eq. (2) and Eq. (3), where \mathbf{D} and \mathbf{W} are constant during the current time step
- e) Compute the Jaumann stress rate $\dot{\boldsymbol{\sigma}}_n^{\text{vJ}}$ using Eq. (13), Eq. (15) and Eq. (16)
- f) Compute $\dot{\boldsymbol{\sigma}}_n$ using Eq. (17) and update $\boldsymbol{\sigma}_{n+1}$:

$$\boldsymbol{\sigma}_{n+1} = \boldsymbol{\sigma}_n + \dot{\boldsymbol{\sigma}}_n \Delta t \quad (22)$$

- g) Update \mathfrak{R}_{n+1} using a second-order scheme [20] as:

$$\mathfrak{R}_{n+1} = \left(\mathbf{I} - \frac{1}{2} \mathbf{W}_n^* \Delta t \right)^{-1} \left(\mathbf{I} + \frac{1}{2} \mathbf{W}_n^* \Delta t \right) \mathfrak{R}_n \quad (23)$$

- h) Update internal variables and update the critical resolved stress g_{n+1}^s using equations described in section 2.3
- i) Update slip direction vectors, \mathbf{m}_{n+1}^s , and slip plane normal vectors, \mathbf{n}_{n+1}^s , using the second-order method:

$$\mathbf{m}_{n+1}^s = \left(\mathbf{I} - \frac{1}{2} \mathbf{W}_n^* \Delta t \right)^{-1} \left(\mathbf{I} + \frac{1}{2} \mathbf{W}_n^* \Delta t \right) \mathbf{m}_n^s \quad (24)$$

$$\mathbf{n}_{n+1}^s = \left(\mathbf{I} - \frac{1}{2} \mathbf{W}_n^* \Delta t \right)^{-1} \left(\mathbf{I} + \frac{1}{2} \mathbf{W}_n^* \Delta t \right) \mathbf{n}_n^s \quad (25)$$

- j) Compute \mathbf{P}_{n+1}^s and $\mathbf{\Omega}_{n+1}^s$ from \mathbf{m}_{n+1}^s and \mathbf{n}_{n+1}^s using Eq. (6) and Eq. (7)
- k) Update the grain orientation matrix \mathbf{Q}_{n+1} using Eq. (21)

4. Numerical study and discussion

To evaluate the hypo-elastic formulation used here and the integration algorithm proposed in this work, two numerical studies have been conducted. The first one is the simulation of uniaxial compression of OFHC copper with initially random texture while the second one is the texture prediction after rolling of the same material. The hyper-CPFEM model implemented by DUMOULIN et al [2] with the GB integration scheme has also been used for the above simulation cases. Predicted results from the two CPFEM formulations will be compared in order to evaluate their performance in terms of accuracy and efficiency.

The material parameters are given similar values as reported in the work of KALIDINDI et al [18], as shown in Table 1. 1000 random orientations are used to represent the initial texture of the material and the $\{111\}$ pole figure is shown in Fig. 1. The representative volume (RVE) has a size of $2\text{mm} \times 2\text{mm} \times 2\text{mm}$. The RVE is meshed with 1000 equal-sized 8 integration point solid elements and each element is assigned one orientation and hence represents one grain, as shown in Fig. 2. Mass scaling is used to speed up the simulations with a scaling factor of 10^8 . All simulations were performed on a work-station with Intel Xeon E5620 CPU (2.4 GHz) and 12G memory, and 8 threads were used simultaneously for each simulation.

Table 1 Model parameters used in the simulations.

$\dot{\gamma}_0$	m	g_0	g_{sat}	h_0	a	q	c_{11}	c_{12}	c_{44}
		(MPa)	(MPa)	(MPa)			(GPa)	(GPa)	(GPa)
10^{-3}	0.012	16	148	180	2.25	1.4	186	93	46.5

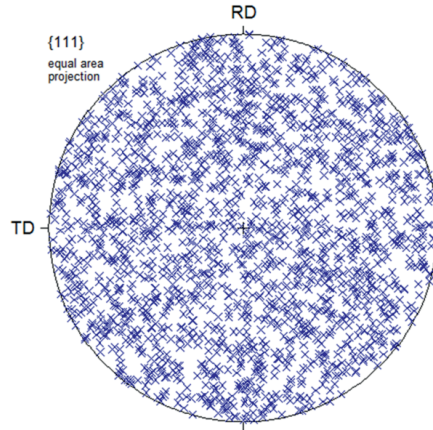


Fig. 1 Initial {111} equal area pole figure of the 1000 orientations.

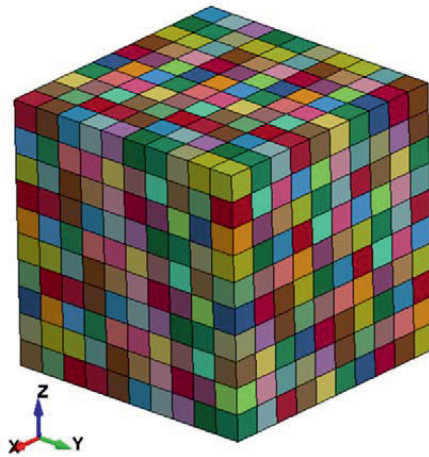


Fig. 2 RVE with 1000 grains.

4.1. Uniaxial compression

The RVE is compressed along the x -direction with a speed of 0.01 mm/s to 70% thickness reduction, i.e. the deformation time is 140 seconds. The surfaces along y - and z - directions are free to move.

The stress-strain curves from simulations using the hypo-CPFEM and the hyper-CPFEM respectively are shown in Fig. 3, where the experimental data from literature [19] is also shown. It can be seen that the hypo-CPFEM and the hyper-CPFEM give

the same stress versus strain response. The agreement between the predicted curves and the experiment is reasonable. The CPU time is shown in Table 2. Both CPFEM models have similar time efficiency, but the hypo-CPFEM is slightly faster.

The good agreement between the predictions by the two CPFEM models validates accuracy and reliability of the crystal plasticity formulations as well as the integration method used for the hypo-CPFEM. Moreover, the fact that the hypo-CPFEM and the hyper-CPFEM give identical stress predictions illustrates that both hypo-elasticity and hyper-elasticity are valid assumptions for crystal plasticity models of metals.

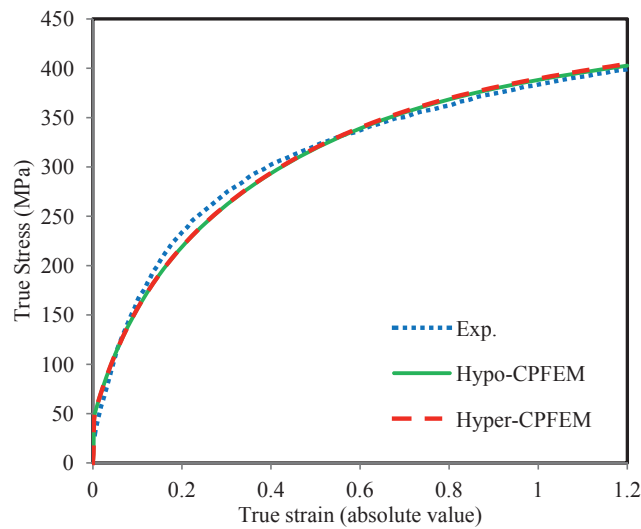


Fig. 3 Stress-strain curves from CPFEM simulations and experiment.

Table 2 CPU time for the simulations using two CPFEM models.

Problem time (s)	Hypo-CPFEM (s)	Hyper-CPFEM (s)
140	12580	13971

4.2. Rolling texture prediction

For the rolling simulation, periodic boundary conditions were applied on all faces of the RVE. The RVE was compressed along the z -axis with a speed of 0.02 mm/s to a thickness reduction of 70%. It was allowed to move along the x -axis freely while the deformation along the y -direction was constrained. The Euler angles after deformation

in all integration points were output into files, and the orientation distribution function (ODF) were computed using the series expansion method with $l_{\max} = 22$ and $\psi_0 = 7.5^\circ$.

Fig. 4 shows the ODFs predicted by both hypo-CPFEM and hyper-CPFEM after rolling to 70% thickness reduction, while the corresponding CPU times are shown in Table 3. The ODF shows a typical rolling texture of FCC metals made of Brass, Goss, S, and Copper texture components [18] which qualitatively validates the correctness of the texture updating algorithms employed. Furthermore, the ODFs from the two simulations show excellent agreement with each other. It is reminded that the texture is updated by the tensor \mathbf{R}^e which is obtained from the polar decomposition of the elastic deformation gradient tensor in the hyper-CPFEM. However, \mathfrak{R} which is updated using \mathbf{W}^* is employed for updating the texture in the hypo-CPFEM. The excellent agreement between the texture predictions demonstrates that both texture updating methods are equally accurate. Similar to the uniaxial compression case, the hypo-CPFEM is slightly faster ($\sim 10\%$) than the hyper-CPFEM, as shown in Table 3.

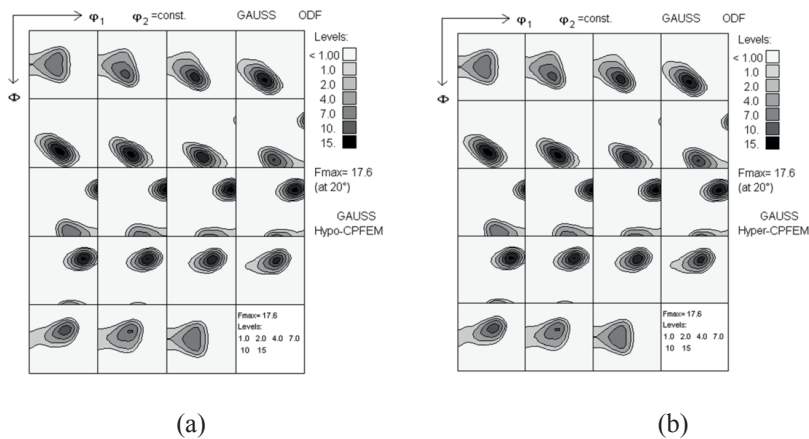


Fig. 4 Orientation distribution function (ODF) after 70% thickness reduction in rolling predicted by (a) hypo-CPFEM, (b) hyper-CPFEM.

Table 3 CPU time for rolling using two CPFEM models.

Problem time (s)	Hypo-CPFEM (s)	Hyper-CPFEM (s)
70	12958	14669

5. Conclusion

- (1) A new forward Euler integration scheme is proposed for rate-dependent crystal plasticity, which employs the additive decomposition of the velocity gradient and uses a hypo-elasticity formulation for the stress calculation. The RDCP model with the new integration scheme has been implemented into the commercial finite element code LS-DYNA.
- (2) This implementation is validated by comparison with a hyper-elastic formulation through two numerical tests. It is shown that the hypo-CPFEM is accurate for stress predictions, and the numerical algorithm for updating texture is validated by comparison to hyper-CPFEM predictions.
- (3) Comparison of predictions by the hypo-CPFEM and by the hyper-CPFEM shows that the two models have equal accuracy when predicting stress and texture while the hypo-CPFEM is slightly more efficient.
- (4) Finally, the current forward Euler integration method, and thereby the hypo-CPFEM, can be further improved without loss of accuracy, through e.g. sub-stepping; this is part of an on-going work.

References

- [1] TAYLOR G I. Plastic strain in metals [J]. *Journal of Institute of Metals*, 1938, 62: 307–324.
- [2] DUMOULIN S, HOPPERSTAD O S, BERSTAD T. Investigation of integration algorithms for rate-dependent crystal plasticity using explicit finite element codes [J]. *Computational Materials Science*, 2009(4), 46: 785-799.
- [3] ROTERS F, EISENLOHR P, HANTCHERLI L, TJAHAJANTO D D, BIELER T R, RAABE D. Overview of constitutive laws, kinematics, homogenization and multiscale methods in crystal plasticity finite-element modeling: Theory, experiments, applications [J]. *Acta Materialia*, 2010, 58(4): 1152-1211.
- [4] CHENG Li-dong, WANG Zhen-long. Scale effect mechanism on micro rod upsetting deformation analyzed by crystal plasticity model [J]. *Transactions of Nonferrous Metals Society of China*, 2012, 22(10): 2444-2450.
- [5] LI Sai-yi. Application of crystal plasticity modeling in equal channel angular extrusion [J]. *Transactions of Nonferrous Metals Society of China*, 2013, 23(1): 170-179.
- [6] VAN HOUTTE P. A comprehensive mathematical formulation of an extended Taylor–Bishop–Hill model featuring relaxed constraints, the Renouard–Wintenberger theory and a strain rate sensitivity model [J]. *Textures and Microstructures*, 1989, 8–9: 313–350.
- [7] DELANNAY L, KALIDINDI S R, VAN HOUTTE P. Quantitative prediction of textures in aluminium cold rolled to moderate strains [J]. *Materials Science and Engineering: A*, 2002, 336(1-2): 233-244.

-
- [8] ZHANG H, DONG X, WANG Q, ZENG Z. An effective semi-implicit integration scheme for rate dependent crystal plasticity using explicit finite element codes [J]. *Computational Materials Science*, 2012, 54: 208-218.
- [9] PEIRCE D, ASARO R J, NEEDLEMAN A. An analysis of nonuniform and localized deformation in ductile single crystals [J]. *Acta Metallurgica*, 1982, 30(6): 1087-1119.
- [10] LING X, HORSTEMEYER M F, POTIRNICHE G P. On the numerical implementation of 3d rate-dependent single crystal plasticity formulations [J]. *International Journal for Numerical Methods in Engineering*, 2005, 63(4): 548-568
- [11] KUCHNICKI S N, CUITIÑO A M, RADOVITZKY R A. Efficient and robust constitutive integrators for single-crystal plasticity modeling [J]. *International Journal of Plasticity*, 2006, 22(10): 1988-2011.
- [12] LI H W, YANG H, SUN Z C. A robust integration algorithm for implementing rate dependent crystal plasticity into explicit finite element method [J]. *International Journal of Plasticity*, 2008(2), 24: 267-288.
- [13] KUCHNICKI S N, RADOVITZKY R A, CUITIÑO A M. An explicit formulation for multiscale modeling of bcc metals [J]. *International Journal of Plasticity*, 2008, 24(12): 2173-2191
- [14] GRUJICIC M, BATCHU S. Crystal plasticity analysis of earing in deep-drawn OFHC copper cups [J]. *Journal of Materials Science*, 2002, 37(4): 753-764.
- [15] HALLQUIST J O. LS-DYNA Keyword User's Manual Version 971 [M]. California: Livermore Software Technology Corporation, 2007.
- [16] BELYTSCHKO T, LIU W K, MORAN B. *Nonlinear Finite Elements for Continua and Structures* [M]. New York: John Wiley, 2000.
- [17] BUCHHEIT T E, WELLMAN G W, BATTAILE C C. Investigating the limits of polycrystal plasticity modeling [J]. *International Journal of Plasticity*, 2005, 21(2): 221-249.
- [18] KOCKS U F, TOMÉ C N, WENK H R. *Texture and Anisotropy: Preferred Orientations in Polycrystals and their effect on Materials Properties* [M]. Cambridge: Cambridge University Press, 2000.
- [19] KALIDINDI S R, BRONKHORST C A, ANAND L. Crystallographic texture evolution in bulk deformation processing of fcc metals [J]. *Journal of the Mechanics and Physics of Solids*, 1992, 40(3): 537-569.
- [20] HUGHES TJR, WINGET J. Finite rotation effects in numerical integration of rate constitutive equations arising in large-deformation analysis [J]. *International Journal for Numerical Methods in Engineering*, 1980, 15(12): 1862-1867.

Article A-2

Crystal Plasticity Calculations of Mechanical Anisotropy of Aluminium Compared to Experiments and to Yield Criterion Fittings

Kai Zhang, Bjørn Holmedal, Tomas Manik, Qinglong Zhao

Department of Materials Science and Engineering, Norwegian University of Science and Technology, Alfred Getz vei 2, N-7491 Trondheim, Norway

Presented at the conference: **13th International Conference on Aluminum Alloys (ICAA -13)**.

ICAA13: 13th International Conference on Aluminum Alloys (eds H. Weiland, A. D. Rollett and W. A. Cassada), John Wiley & Sons, Inc., Hoboken, NJ, USA.
doi: 10.1002/9781118495292.ch137

Crystal Plasticity Calculations of Mechanical Anisotropy of Aluminium Compared to Experiments and to Yield Criterion Fittings

Abstract

Mechanical anisotropy of a sheet was studied by experiments as well as crystal plasticity calculations. The material is a 99.999% high purity Aluminum with additions of 0.066%Fe and 0.068%Si. Uniaxial tensile tests at every 15° from the rolling to the transverse direction were conducted. Yield stresses were measured and also the r -values for the uniaxial tensile tests. The anisotropic Yld2004-18p yield function for fully three-dimensional stress state was fitted to the experiments. Crystallographic orientation data were measured by EBSD and used as input for the full-constraint Taylor model. The yield locus was calculated by the Taylor model and compared to the Yld2004-18p criterion fitted to the experiments. Since the number of possible mechanical tests is limited and the experimental errors can be a challenge, it would be desirable to replace the mechanical tests by one texture measurement and virtual experiments by crystal plasticity calculations. The reliability of this approach is discussed for the case of pure aluminium.

Keywords: mechanical anisotropy, yielding condition, mechanical testing, crystal plasticity

Introduction

The yield condition for polycrystalline metallic materials can be described by two principal approaches. The first one is to use a polycrystalline plasticity model, like the full-constraint Taylor model [1,2,3]. This approach is based on the physical aspects of plastic deformation and on averaging the response over the grain aggregates. The second approach is to use a phenomenological yield functions which are based on the classical theory of plasticity. A fundamental problem with this approach is that when fitting parameters of the phenomenological models most of the stress space is left unexplored, due to the severe experimental limitations. The only realistic way to span the space is by fitting advanced phenomenological models to match virtual experiments using crystal plasticity calculations [4,5].

The Yld2004-18p yield criterion is a linear transformation-based yield function which was proposed by Barlat et al. [6] for the fully three-dimensional stress state. It has 18 anisotropy parameters and an exponent that can be varied. Yoon et al. [7] used results from uniaxial tensile and equiaxial tensile tests to determine the properties in plane, while crystal plasticity calculation were used to determine four parameters governing out-of-plane properties. Grytten et al.[4] explored different identification methods for

Yld2008-18p: only using experimental data, solely based on Taylor model calculations and their combination for the aluminium alloy AA5083-H116. Tikhovskiy et al. [8], Von Houtte et al. [9] and An et al. [10] used other crystal plasticity models (CPFEM, RC-Taylor, ALAMEL) to identify the parameters of different yield criterions.

In this paper, the mechanical anisotropy of sheet material, a 99.999% high purity Aluminum with additions of 0.066%Fe and 0.068%Si, is studied. Yield stress and r -values at seven directions are measured by uniaxial tensile tests. The FC-Taylor model is employed to calculate the stress states in 242 strain directions. The Yld2004-18p criterion is fitted to the experimental data and also to the calculated points. The two yield function fittings are discussed.

Yield criterion

The yield function Yld2004-18p is adopted. The effective stress is

$$\bar{\sigma} = \left(\frac{1}{4}\phi\right)^{\frac{1}{m}} \quad (1)$$

where

$$\begin{aligned} \phi = \phi(\tilde{\mathbf{S}}', \tilde{\mathbf{S}}'') &= |\tilde{S}'_1 - \tilde{S}''_1|^m + |\tilde{S}'_1 - \tilde{S}''_2|^m + |\tilde{S}'_1 - \tilde{S}''_3|^m + |\tilde{S}'_2 - \tilde{S}''_1|^m + |\tilde{S}'_2 - \tilde{S}''_2|^m \\ &+ |\tilde{S}'_2 - \tilde{S}''_3|^m + |\tilde{S}'_3 - \tilde{S}''_1|^m + |\tilde{S}'_3 - \tilde{S}''_2|^m + |\tilde{S}'_3 - \tilde{S}''_3|^m \end{aligned} \quad (2)$$

In Eq. (2), $\tilde{\mathbf{S}}'$ and $\tilde{\mathbf{S}}''$ represent the principal values of the stress deviators $\tilde{\mathbf{s}}'$ and $\tilde{\mathbf{s}}''$, which are defined by two linear transformations of the deviator of the Cauchy stress tensor. The two linear transformations provide 18 coefficients that can be used to capture materials' anisotropy. The details are not listed here but can be found in Barlat et al. [6].

Virtual experiments by the full-constraint Taylor model

A strain-rate independent full-constraint Taylor model is applied, more details might be found in Van Houtte et al. [5,11]. The measured texture and prescribed rate-of-deformation tensors are input into the FC-Taylor model. The texture was measured by EBSD. In this work, $N = 1000$ representative grains were chosen. In order to make this representative aggregate inherit the overall texture characteristics, the total scanned area was divided into N regions of equal areas, and one orientation was randomly picked from each such area.

For incompressible materials, the yield surface is in a five dimensional stress space. A good resolution of points on this surface was obtained by a procedure described by Grytten et al. [4]. Contracting the stress and strain tensors into five dimensional vectors, a distribution of strain-rate points on the five-dimensional unity hyper-sphere can be used to create the rate-of-deformation tensor as input for each Taylor model calculation. A resolution of 3 points on each axis, i.e. 1, 0 and -1, gave 242 calculated stress points on the yield surface. These results were used to calibrate the phenomenological Yld2004-18p yield surface.

Experiments

The material is a 99.999% high purity Aluminum with additions of 0.066%Fe and 0.068%Si (denoted Al5NFeSi), which makes it a well defined 99.8% purity alloy with most of the Fe and Si in the constituent particles. A flat extrusion profile, 70mm wide, 5mm thick and about 1000mm long was rolled into a 1mm thick sheet, from which tensile specimens at every 15° from the rolling to the transverse direction (7 directions) were machined. These samples were then annealed at salt bath at 375°C for 30min, intended to achieve a fully recrystallized state. The geometry of the specimens used in these tests is shown in Fig. 1.

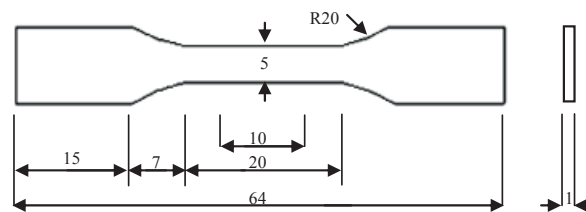


Fig. 1. Uniaxial tensile test specimen (in mm)

A Zeiss ULTRA 55 FESEM equipped with a Nordif digital EBSD detector and TSL OIM4 EBSD software were used, with a step size of 10 μm covering approximately 4 mm^2 . The orientation distribution function (ODF) is shown in Fig. 2, from which strong Goss and Cube orientations can be seen.

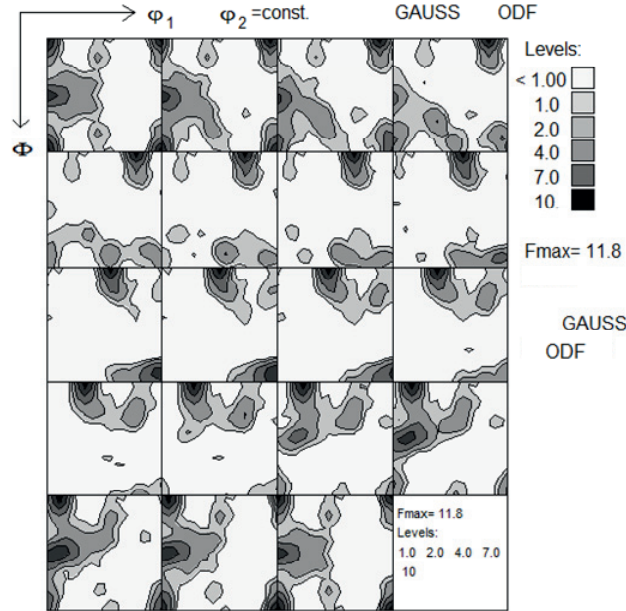


Fig. 2. Orientation distribution function (ODF) of aluminium alloy Al5NFeSi

Uniaxial tensile tests at every 15° from the rolling to the transverse direction were performed in a MTS 810 universal testing machine at a crosshead speed of 1mm/min, i.e. a strain rate $\sim 10^{-3}\text{s}^{-1}$. The tests were stopped at a strain of 0.15. An extensometer with 10mm gauge length was used to record the elongation automatically, while the specimen width before and after tests was measured manually using a caliper of 10^{-2}mm accuracy. From the stress-strain curves, the yield stresses were determined and r -values at 15% elongation were calculated according to ASTM E517

$$r = \frac{\ln(w_0 / w_f)}{\ln(l_f w_f / l_0 w_0)} \quad (3)$$

where l_0 , l_f and w_0 , w_f are original and final lengths and widths respectively. The measured yield stresses normalized by the average yield stress in the rolling direction (σ_0) and the corresponding r -values at every 15° from the rolling to the transverse direction are shown in Fig. 3 and Fig.4.

Parameter identification

A least squares method was used to identify the 18 parameters of Yld2004-18p yield function. A yield criterion exponent $m=8$ was applied, corresponding to the case of a

random FCC texture [12]. In the following, two procedures for fitting the anisotropy parameters will be tested and evaluated.

The first approach, ‘Fit 1’ is to use only the seven measured yield stresses and r -values to fit the parameters. The coefficients governing the out-of-plane properties, i.e. c'_{55} , c'_{66} , c''_{55} and c''_{66} were set to 1 as they are not easily measured for sheet materials.

The function to be minimized is

$$\sum_{i=1}^N \left[w'_i \left(\frac{\bar{\sigma}_i}{\sigma_0} - 1 \right)^2 + w''_i \left(\frac{\bar{r}_i}{r_i} - 1 \right)^2 \right] = \min \quad (4)$$

where N is the number of available fitting data points; $w'_i = 1$ and $w''_i = 0.01$ are weight factors for ‘Fit 1’. $\bar{\sigma}$ is the effective stress defined by Eq. (2) while r_i and \bar{r}_i are r -values that experimentally measured and predicted by the fitted yield function, respectively.

The second approach, ‘Fit 2’, is fitted to the 242 stress states calculated by the FC-Taylor model based on the measured texture. In this case, also the out of plane coefficients c'_{55} , c'_{66} , c''_{55} and c''_{66} were fitted. The fitted parameters are all listed in Table I. The normalized yield stress (σ/σ_0) and r -values from rolling to transverse direction are calculated by ‘Fit 1’ and ‘Fit 2’ yield functions and the results are shown in Fig. 3 and Fig. 4, together with the experimental results and the Taylor model predictions.

Table I. Fitted parameters of Yld2004-18p yield function (m=8).

	Fit1	Fit 2		Fit1	Fit 2
c'_{12}	0.9807	0.5027	c''_{12}	1.2446	1.1973
c'_{13}	0.9482	0.8921	c''_{13}	0.8541	1.0862
c'_{21}	0.9129	0.9112	c''_{21}	0.8346	0.8242
c'_{23}	1.0479	1.0214	c''_{23}	1.4175	0.6757
c'_{31}	1.0813	1.0331	c''_{31}	1.1571	0.9099
c'_{32}	1.1372	1.0136	c''_{32}	1.0064	0.7189
c'_{44}	1.0082	0.4899	c''_{44}	1.1211	1.0775
c'_{55}	1.0000	0.5875	c''_{55}	1.0000	1.0805
c'_{66}	1.0000	1.0806	c''_{66}	1.0000	0.7478

Discussion and conclusions

Measured, calculated and fitted yield stresses and r -values of Al5NFeSi at every 15° degrees from rolling to transverse direction are shown in Fig. 3 and Fig. 4. The difference between the maximum measured yield stress in the rolling direction and the

minimum one at 75° is around 15%, which reveals a moderately strong anisotropy. The experiments show a complex and stronger variation of r -values than the yield strength variation, which is evidence of a planar anisotropy in the plastic flow.

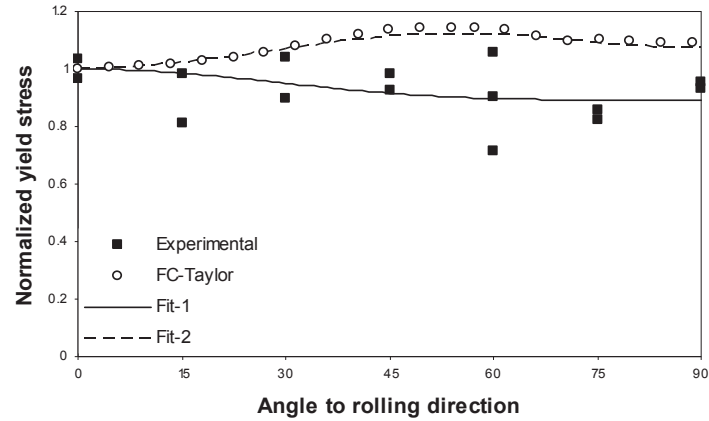


Fig. 3. Normalized yield stress versus angle to the rolling direction obtained from experiments, FC-Taylor calculation and fitted surfaces.

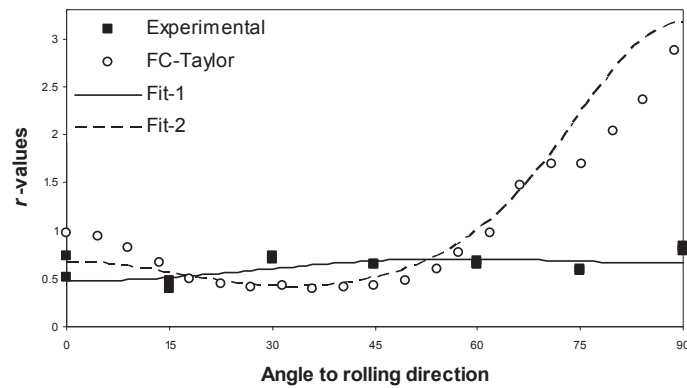


Fig. 4. r -values versus angle to the rolling direction obtained from experiments, FC-Taylor calculation and fitted surfaces.

Table I lists the yield surface parameters found for the studied anisotropic material of the two different fitting approaches. The two sets of fitted parameters are significantly different between 'Fit 1' and 'Fit 2'. In Fig. 3 and Fig. 4 it can be observed that 'Fit 1',

i.e. only fitted to the tensile tests, could capture the complex flow anisotropy and the general change of the yield strength. On the other hand, 'Fit2' fits well the r -values and tensile stresses predicted by the FC-Taylor model. However, the FC-Taylor model calculated virtual experimental stress states deviate significantly both with respect to yield strength anisotropy and flow anisotropy as compared to the tensile tests.

From the discussion, we can conclude that the Yld2004-18p yield function could be very well fitted to tensile tests in seven directions in the aluminium sheet plane. Furthermore, by using the 18 parameters of this yield surface to fit 242 stress points uniformly distributed in the general five-dimensional stress space still resulted in a very good fit to the planar variation of FC-Taylor model predicted yield stresses and r -values. Unfortunately, the FC-Taylor model was not capable of predicting the measured mechanical anisotropic properties of the considered Al5N-FeSi sheet. In particular the r -value predictions for tensile tests near the transverse direction were way off. More complex crystal plasticity models than the FC-Taylor model is required. A natural starting point would be to consider generalized Taylor type of models that account for interactions between neighboring grains.

References

1. Taylor, G., "Plastic strain in metals," *Journal of Institute of Metals*, 62 (1938), 307–324.
2. Bishop, J.F.W., Hill, R., "A theory of the plastic distortion of a polycrystalline aggregate under combined stresses," *Phil. Mag.*, 42 (1951), 414-427.
3. Bishop, J.F.W., Hill, R., "A theoretical derivation of the plastic properties of a polycrystalline facecentred metal," *Phil. Mag.*, 42 (1951), 1298-1307.
4. Grytten, F. et al., "Evaluation of identification methods for YLD2004-18p," *Int. J. Plasticity*, 24 (2008), 2248–2277.
5. Van Houtte, P. et al., "Multiscale modelling of the plastic anisotropy and deformation texture of polycrystalline materials," *Eur. J. Mech. A/Solids*, 25 (2006), 634–648.
6. Barlat, F. et al., "Linear transformation-based anisotropic yield functions," *Int. J. Plasticity*, 21 (2005), 1009–1039.
7. Yoon, J.W et al., "Prediction of six or eight ears in a drawn cup based on a new anisotropic yield function," *Int. J. Plasticity*, 22 (2006), 174–193.
8. Tikhovskiy I, Raabe D, Roters F, "Simulation of earing during deep drawing of an Al-3% Mg alloy (AA 5754) using a texture component crystal plasticity FEM," *J Mater Process Technol*, 183 (2007), 169–175.
9. Van Houtte, P. et al., "The Facet method: A hierarchical multilevel modelling scheme for anisotropic convex plastic potentials," *Int. J. Plasticity*, 25 (2009) 332-360.

10. An, Y. et al., "A novel yield locus description by combining the Taylor and the relaxed Taylor theory for sheet steel," *Int. J. Plasticity*, 27 (2011), 1758–1780.
11. Van Houtte, P. et al., "Deformation texture predictions: from the Taylor model to the advance Lamel model," *Int. J. Plasticity*, 21 (2005), 589–624.
12. Hosford, W.F., "A generalized isotropic yield criterion," *J. Appl. Mech. Trans. ASME*, 39 (1972), 607–609.